ALMA MATER STUDIORUM - UNIVERSITÀ DI BOLOGNA

DOTTORATO DI RICERCA IN INGEGNERIA CIVILE, CHIMICA, AMBIENTALE E DEI MATERIALI

XXXI CICLO

Settore Scientifico Disciplinare ICAR/08
Settore Concorsuale 08/B2

ADVANCES IN COMPUTATIONAL ANALYSIS OF MASONRY STRUCTURES

Autore:
Antonio Maria D'Altri

Coordinatore di Dottorato:
Prof. Luca Vittuari

Relatore:
Prof. Stefano de Miranda

Correlatore:
Giovanni Castellazzi

Esame finale anno 2019

ABSTRACT

Nowadays, numerical models aid significantly the engineers in the structural assessment of ordinary and monumental existing masonry buildings. Indeed, these models can be used to predict the structural response to extraordinary loads, and so to evaluate the main weaknesses and the safety of a masonry structure. Nevertheless, given the deep complexities and uncertainties which characterize the geometry of historic buildings and the mechanical response of masonry, the computational analysis of masonry structures is still a challenging task.

In this thesis, some recent advances in computational analysis of masonry structures are presented. Essentially, after a comprehensive review of the existing modeling strategies for masonry structures, the advancements pursued in the framework of (i) mesh generation procedures for historic monumental buildings, (ii) analysis of seismically interacting structures, (iii) analysis of leaning historic structures, and (iv) block-based modeling of masonry structures, are shown and discussed.

Particularly, with reference to the first point, two mesh generation procedures are proposed to transform 3D point clouds into 3D solid finite element models of historic monumental buildings. The first novel approach proposed, called CLOUD2FEM, consists in the slicing and subsequent stacking of the geometry, which can also be extremely complex. The resulting mesh contains all the information to be used within the finite element method, guaranteeing the semi-automatic generation of a reliable model. The second approach proposed, called watertight meshing, considers the structure as a watertight surface and eventually fills the volume through existing mesh processing tools. This approach represents a very fast solution for the direct and fully automatic mesh generation of a geometrically irregular masonry buildings, even though not always applicable, e.g. in case of inner spaces, rooms, furniture, etc.

Concerning the second point, a computational procedure based on the use of nonlinear static analyses is developed to assess the response of seismically interacting historic masonry structures. This procedure firstly requires the execution of a modal analysis on a 3D finite element model of the whole structure to define the modes which involve the dynamic response of each unit and their modal shapes. The latter are then fitted to define the load patterns to be applied on each unit through pushover analyses.

Regarding the third point, a computational procedure based on upper-bound finite element limit analysis is developed to undertake stability analysis of geometrically complex leaning historic masonry structures. This procedure permits to estimate the structural health condition of a historic structure by comparing the critical inclination angle against the actual one.

Finally, a damaging block-based model formulated in the context of contact mechanics is developed for the computational analysis of masonry structures. The

model is validated through the comparison against in-plane and out-of-plane experimental tests on masonry walls, as well as cyclic pushover tests on a full-scale masonry house. In addition, the developed block-based model is also used to investigate the response of historic barrel vaults undergoing differential settlements.

PUBLICATIONS

Some ideas and figures presented in this thesis have been previously published or submitted for publication in the following journal articles:

1. Castellazzi, G., D'Altri, A. M., Bitelli, G., Selvaggi, I., & Lambertini, A. (2015). From Laser Scanning to Finite Element Analysis of Complex Buildings by Using a Semi-Automatic Procedure. Sensors, 15(8), 18360–18380.

2. Castellazzi, G., D'Altri, A. M., de Miranda, S., & Ubertini, F. (2017). An innovative numerical modeling strategy for the structural analysis of historical monumental buildings. Engineering Structures, 132, 229–248.

3. D'Altri, A. M., Milani, G., de Miranda, S., Castellazzi, G., & Sarhosis, V. (2018). Stability analysis of leaning historic masonry structures. Automation in Construction, 92, 199–213.

4. D'Altri, A. M., de Miranda, S., Castellazzi, G., & Sarhosis, V. (2018). A 3D detailed micro-model for the in-plane and out-of-plane numerical analysis of masonry panels. Computers & Structures, 206, 18–30.

5. D'Altri, A. M., Messali, F., Rots, J., Castellazzi, G., & de Miranda, S. (2019) A damaging block-based model for the analysis of the cyclic behaviour of full-scale masonry structures. Engineering Fracture Mechanics (In press).

6. Degli Abbati, S., D'Altri, A. M., Ottonelli, D., Castellazzi, G., Cattari, S., De Miranda, S., & Lagomarsino, S. (2019) Seismic assessment of interacting structural units in complex historic masonry constructions by nonlinear static analyses. Computers & Structures (In press).

7. D'Altri, A. M., de Miranda, S, Castellazzi, G., Sarhosis, V., Hudson, J., & Theodossopoulos, D. Historic barrel vaults undergoing differential settlements. Submitted for publication.

8. D'Altri, A. M., Sarhosis, V., Milani, G., Rots, J., Cattari, S., Lagomarsino, S., Sacco, E., Tralli, A., Castellazzi, G., & de Miranda, S. Modeling strategies for the computational analysis of unreinforced masonry structures: Review and classification. Submitted for publication.

ACKNOWLEDGMENTS

CONTENTS

ACRONYMS

BBM Block-Based Models

BVP Boundary Value Problem

CAD Computer-Aided Design

CM Continuum Models

CSM Capacity Spectrum Method

CT Computed Tomography

DDA Discontinuous Deformation Analysis

DEM Distinct (or Discrete) Element Method

DOF Degree Of Freedom

FDEM Finite-Discrete Element Method

FE Finite Element

FELA Finite Element Limit Analysis

FEM Finite Element Method

FRP Fiber-Reinforced Polymer

FRCM Fiber-Reinforced Cementitious Matrix

GBM Geometry-Based Models

GIS Geographic Information System

LA Limit Analysis

LP Load Pattern

MDOF Multi-Degree Of Freedom

MM Macroelement Models

NLDA Nonlinear Dynamic Analyses

NLP Nonlinear Programming

NLSA Nonlinear Static Analyses

NSCD Non-Smooth Contact Dynamics

NURBS Non-Uniform Rational B-Spline

RBSM Rigid Body Spring Model

RC Reinforced Concrete

RVE Representative Volume Element

SDOF Single-Degree Of Freedom

SLP Sequential Linear Programming

TFA Transformation Field Analysis

TIN Triangular Irregular Network

TLS Terrestrial Laser Scanner

TNA Thrust Network Analysis

URM Unreinforced Masonry

VP Viscosity Parameter

XFEM Extended Finite Element Method

INTRODUCTION

Masonry structures represent a large part of the existing constructions in the world. A great part of the historic architectural heritage consists of monumental masonry structures (buildings, towers, castles, churches, mosques, temples, etc.). Furthermore, ordinary residential buildings are typically made of masonry in several countries. As it can be noted in Figure 1, considerable differences appear between monumental and ordinary buildings, in terms of material, geometry and structural details.

| (a) | (b) |

Figure 1: Examples of (a) monumental and (b) ordinary masonry structures.

It is well known that unreinforced masonry (URM) structures, although classically suitable to withstand gravitational loads, are sensibly vulnerable if subjected to extraordinary actions such as earthquakes. Indeed, the structural response to this kind of actions is often characterized by the arising of cracks in the masonry and/or partial (or even full) collapses even for seismic events of moderate intensity if compared to other structural typologies like as reinforced concrete or steel buildings. Given the heterogeneity of masonry, made of blocks usually bonded with mortar, cracks typically run along the mortar joints, even if the case of cracked blocks is possible as well depending on the relative strength properties of the two basic components (i.e. mortar and blocks). Indeed, alternative solutions to the unreinforced one have been developed over the centuries, aimed at improving the properties of ductility and dissipation as well as the strength, as the confined or reinforced masonry. Despite that, this thesis focuses only to the unreinforced masonry solution.

In the last half-century, the scientific community devoted a consistent effort to the computational analysis of masonry structures. The main objective at the basis of this topic is that, if a mechanical model is found to be able to simulate the

structural response of masonry structures, it can be used to predict the structural response to extraordinary loads and, therefore, to evaluate the main weaknesses and safety of a masonry building. Although new masonry buildings can be designed and computationally analyzed, this approach has been mainly oriented to the assessment of the near-collapse behavior of existing masonry buildings, given their widespread dissemination and their weak structural response.

However, given the deep complexities and uncertainties which characterize the geometry of buildings (especially historic ones) and the mechanical response of masonry, the computational analysis of masonry structures is still a challenging task. Indeed, several open issues arise when dealing with numerical modeling of masonry structures. Among them, the following open issues appear particularly stimulating:

(i) How to create the mesh of a structure if its geometry is extremely complex and irregular, as for historic masonry buildings?

(ii) How to perform the seismic analysis of historic masonry buildings which are typically composed of several interacting units?

(iii) How to evaluate the stability of leaning masonry structures with irregular geometries?

(iv) How to accurately and efficiently represent the complex mechanical behavior of masonry?

In such framework, this thesis proposes some wide-ranging advances in the computational analysis of masonry structures to fill the aforementioned gaps. Essentially, the advancements pursued in the framework of mesh generation procedures for historic monumental buildings, analysis of seismically interacting structures, analysis of leaning historic structures, and block-based modeling of masonry structures, are shown and discussed.

Firstly, a comprehensive review of the existing modeling strategies for masonry structures is given in Chapter 2, together with a novel classification of these strategies, which proposes four main categories: block-based models, continuum models, geometry-based models, and macroelement models. Each category is comprehensively reviewed and the future challenges of computational analysis of masonry structures are also discussed.

Then, two mesh generation procedures are proposed in Chapter 3 to transform 3D point clouds into 3D solid finite element models of historic monumental buildings. The first novel approach proposed, called CLOUD2FEM, consists in the slicing and subsequent stacking of the geometry, which can also be extremely complex. The resulting mesh contains all the information to be used within the finite element method, guaranteeing the semi-automatic generation of a reliable model. The procedure is applied on a real case study (a medieval masonry fortress damaged by an earthquake) and validated. The second approach proposed, called watertight meshing, considers the structure as a watertight surface and eventually fills the volume through existing mesh processing tools. This approach represents

a very fast solution for the direct and fully automatic mesh generation of a geometrically irregular masonry buildings, even though not always applicable, e.g. in case of inner spaces, rooms, furniture, etc. The procedure is applied on a medieval ruined masonry leaning tower. The accuracy of the geometry of the mesh generated appears suitable for structural purposes.

Additionally, a computational procedure based on the use of nonlinear static analyses is presented in Chapter 4 to assess the response of seismically interacting historic masonry structures. The proposed procedure firstly requires the execution of a modal analysis on the 3D finite element model of the whole structure to define the modes which involve the dynamic response of each unit and their modal shapes. The latter are then fitted to define the load patterns to be applied on each unit through pushover analyses. The pushover curves obtained for each unit are then converted into capacity curves to finalize the seismic assessment. The effectiveness of the proposed procedure is shown through an application to a medieval fortress significantly damaged by an earthquake.

Furthermore, a computational procedure based on upper-bound finite element limit analysis is presented in Chapter 5 to undertake stability analysis of leaning historic masonry structures. This outcome permits to estimate the structural health condition of a historic structure by comparing the critical inclination angle against the actual one. To demonstrate the effectiveness of the automated procedure, a medieval ruined masonry leaning tower is investigated, evaluating the failure mechanisms with collapse inclination angles.

Finally, a damaging block-based model formulated in the context of contact mechanics is presented in Chapter 6 for the computational analysis of masonry structures. The model is validated through the comparison against in-plane and out-of-plane experimental tests on masonry walls, as well as cyclic pushover tests on a full-scale masonry house. In addition, the developed block-based model is also used to investigate the response of historic barrel vaults undergoing differential settlements.

On a final note, it has to be pointed out that the wide-range advances carried out in this thesis, even though unconnected at first glance, can be linked together to obtain an innovative framework for the numerical analysis of masonry structures. Indeed, the mesh generation approaches developed in Chapter 3 can be utilized within the structural analysis procedures proposed in Chapter 4 and Chapter 5. Moreover, although merely used on rather simple structures so far, the block-based model presented in Chapter 6 could be utilized, in theory, within the structural analysis procedures developed in Chapter 4 and Chapter 5 for monumental historic buildings.

2

MODELING STRATEGIES FOR MASONRY STRUCTURES

In this chapter, a comprehensive review of the existing modeling strategies for masonry structures, as well as a novel classification of these strategies are presented. Although a fully coherent collocation of all the modeling approaches is substantially impossible due to the peculiar features of each solution proposed, this classification attempts to put in order the wide scientific production on this field. The modeling strategies are herein classified into four main categories: block-based models, continuum models, geometry-based models, and macroelement models. Each category is comprehensively reviewed. The future challenges of computational analysis of masonry structures are also discussed.

2.1 INTRODUCTION

In this chapter, a comprehensive review of the existing modeling strategies for masonry structures is presented and a classification of these strategies is proposed. This classification of modeling strategies for masonry structures consists of the four following categories (Figure 2): block-based models (BBM), continuum models (CM), geometry-based models (GBM), and macroelement models (MM). This classification, although a fully coherent collocation of all the modeling approaches is substantially impossible due to the peculiar features of each solution proposed, attempts to put in order the wide scientific production on this field.

Firstly, the main mechanical and geometrical challenges of masonry structures are briefly discussed in Section 2.2. Then, the limitations and possibilities of analysis approaches (i.e. step-by-step analysis and limit analysis) for masonry structures are pointed out in Section 2.3. The proposed classification of modeling strategies for masonry structures is presented in Section 2.4. Each category is then comprehensively reviewed (BBM in Section 2.5, CM in Section 2.6, GBM in Section 2.7, and MM in Section 2.8) and the limitations and possibilities of each strategy are deeply discussed. In the conclusions (Section 2.9), a summary of the pros and cons of each category is given and a discussion on future challenges of computational analysis of masonry structures is held.
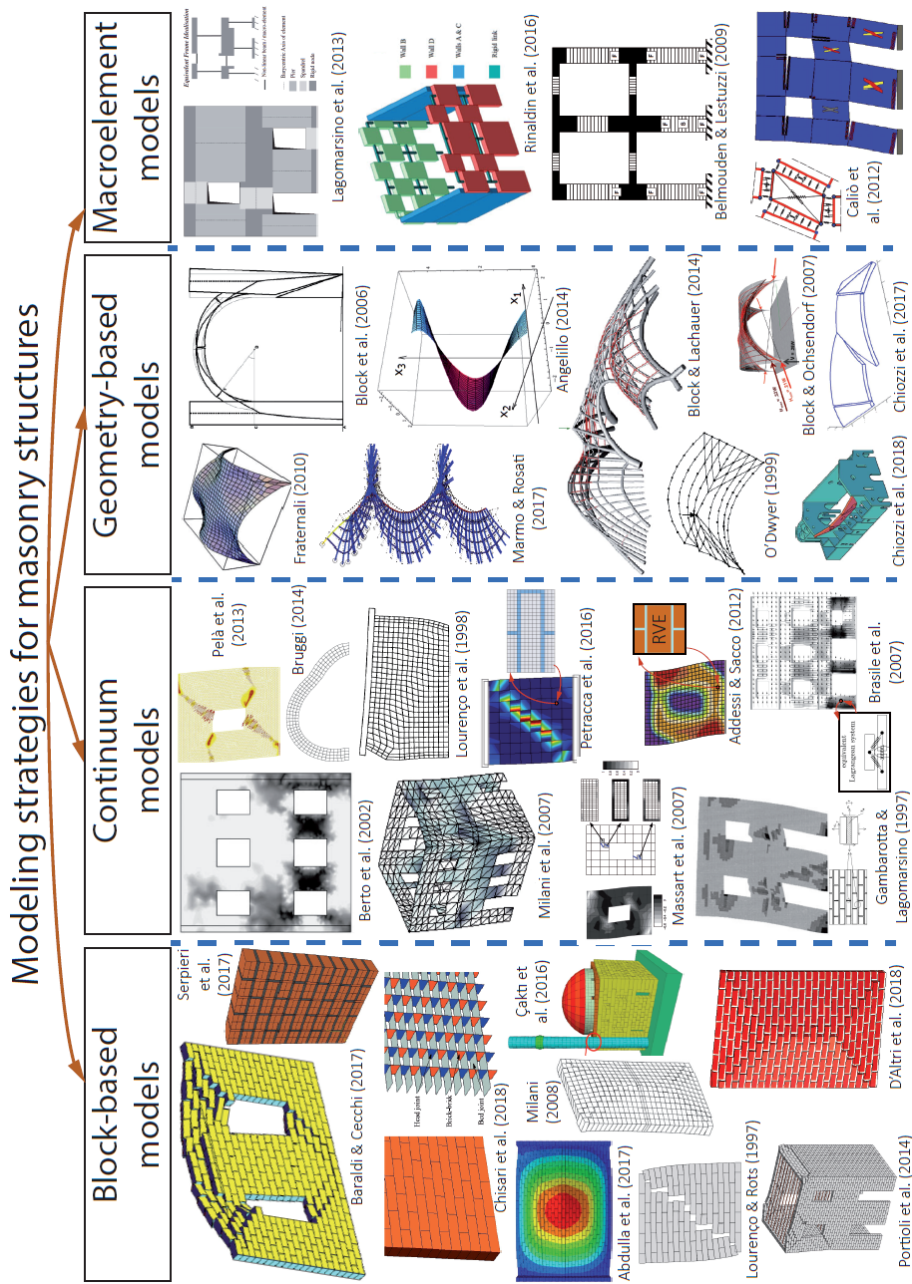
Figure 2: Modeling strategies for masonry structures.

2.2 MECHANICAL AND GEOMETRICAL CHALLENGES

A reliable simulation of the mechanical response of an existing masonry structure should be based on reliable mechanical properties characterized through experimental tests and on detailed geometrical and structural surveys.

This section aims to briefly highlight the main mechanical and geometrical challenges which arise when dealing with masonry structures. Further aspects on this topic can be found in [1, 2].

2.2.1 *Masonry mechanical behavior*

Masonry is a very complex material from a mechanical point of view. It is composed of blocks usually bonded with mortar. Blocks are typically made of quasi-brittle materials such as building stones, fired and non-fired bricks. Blocks are assembled with a certain pattern, which is called "bond". This makes masonry an heterogeneous material. As highlighted in [1], the term "masonry" actually refers to a very wide category of building materials (Figure 3), with different mechanical features and peculiarities.

| (a) | (b) | (c) |
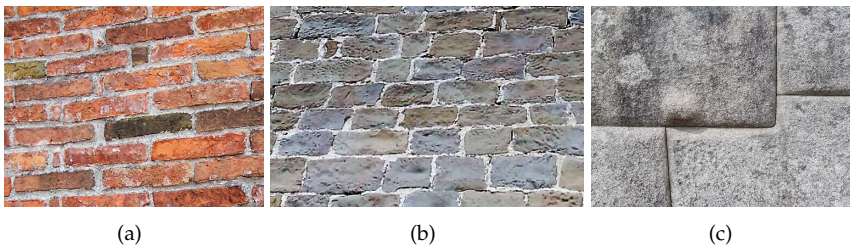
Figure 3: Examples of masonry: (a) brick masonry, (b) stone masonry and (c) Inca's masonry (dry stone masonry).

The overall masonry response is governed by the mechanical properties of its components (block and mortar) and the bond between them. Masonry components are generally characterized by a quasi-brittle response in tension and compression. In particular, the compressive behavior is characterized by much higher values of strength and fracture energy with respect to the tensile behavior. Beyond the nonlinearity showed by the masonry components, the bond between blocks and mortar is usually very weak, characterized by a normal stress-dependent cohesive-frictional behavior in shear and a cohesive behavior in tension (with essentially irrelevant cohesion in case of dry stone masonry) [2]. Therefore, the overall response of masonry is highly nonlinear.

Masonry is an anisotropic material [3]. Anisotropy can be observed in the elastic behavior (elastic anisotropy), in the strength properties (beyond the difference between compressive and tensile strengths, distinctive of quasi-brittle materials, it shows also different strengths along with different directions, i.e. strength ani-

sotropy), and in the post-peak response (brittleness anisotropy). In particular, regular brick masonry usually shows significant anisotropic properties. Conversely, anisotropy in random stone masonry, although a significant difference in compressive and tensile strengths is always observed, could be less significant (e.g. in terms of elasticity, strengths, and brittleness) than in regular brick masonry, given the lack of periodicity in the material.

The interpretation of the mechanical behavior of masonry could be based on different scales, typically the scale of the material [3, 4, 5] and the scale of the structural element [6, 7, 8, 9, 10]. For both cases, the description of the mechanical behavior has to be generally defined in terms of stiffness, strength and ductility. Figure 4 shows the limit strength domains of masonry at the scale of the material (Figure 4(a)) and at the scale of the pier (Figure 4(b)) for plane stress states.

(a)   (b)
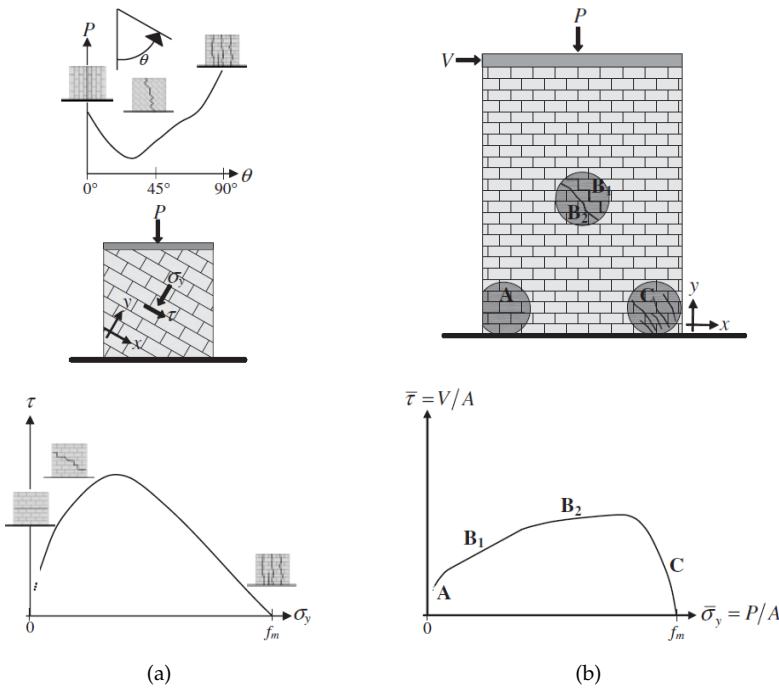
Figure 4: Failure modes and limit domains of masonry: (a) scale of the material and (b) scale of the pier, from [7].

Failure mechanisms in masonry are usually complex and articulated. Typical failure modes of masonry at a two-block masonry assemblage scale are sketched in Figure 5. At a structural scale, some examples of masonry failure are depicted in Figure 6.
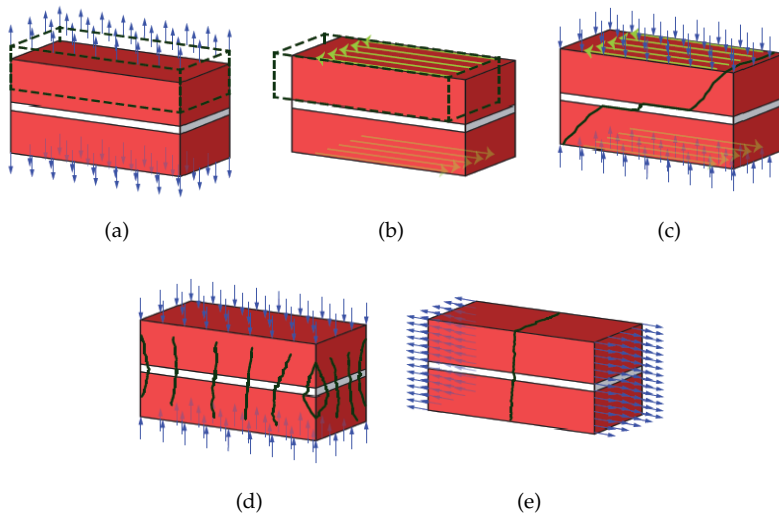
Figure 5: Masonry failure mechanisms (at a two-block masonry assemblage scale, from [11]): (a) block-mortar bond tensile failure, (b) block-mortar bond shear sliding, (c) diagonal masonry cracking, (d) masonry crushing, and (e) block and mortar tensile cracking.

2.2.2 *Experimental characterization of masonry*

The experimental characterization of masonry mechanical properties is still a challenging task. Indeed, although several experimental tests and set-ups have been proposed in the last decades, their reliability and reproducibility are still object of debate [13, 14].

Basically, the experimental characterization of masonry could be done at different scales, as shown in Figure 7: masonry components (block, mortar and block-mortar bond), wallets (small masonry assemblages), panels (real-scale masonry walls), and buildings (full-scale masonry structures).

When dealing with existing masonry buildings, in-situ tests should be used to mechanically characterize the structure [16, 17]. However, in-situ testing is usually characterized by larger difficulties and limitations than laboratory testing. This leads, in general, to greater uncertainties on the characterized mechanical properties. Even, merely non-destructive tests could be used in historic monumental buildings to guarantee their conservation and authenticity [18, 19]. To limit the invasiveness, together with experimental tests, also indirect methods have been proposed in the literature [20] to assign mechanical properties to masonry which are based on a qualitative interpretation of its main features (such as quality of mortar joints, effectiveness of in-plane and transversal interlocking, bond). Anyway, a limited mechanical information can be generally obtained on this kind of masonry structures.
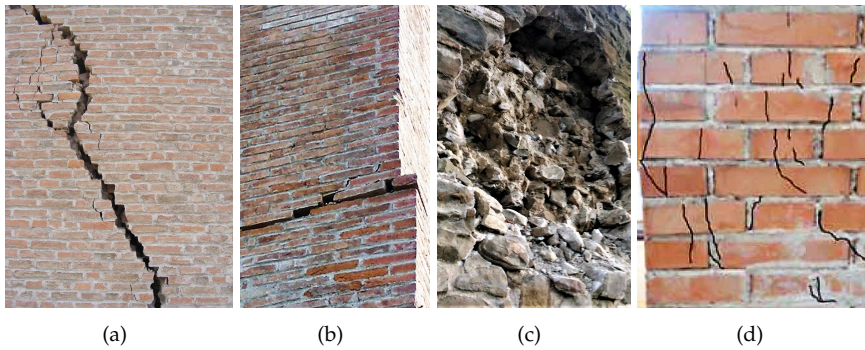
Figure 6: Masonry failure mechanisms (at a structural scale): (a) diagonal cracking, (b) sliding, (c) crumbling, and (d) crushing (from [12]).
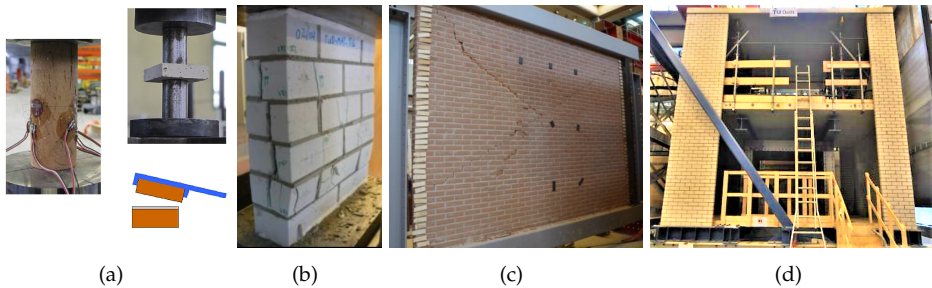
Figure 7: Experimental characterization of masonry at different scales: (a) masonry components testing (from [13]), (b) wallets testing (from [15]), (c) panels testing (from [15]), and (d) building testing (from [15]).

2.2.3 *Structural details*

In masonry structures, structural details play a fundamental role in the mechanical response. Indeed, the toothing between orthogonal walls (Figure 8), the quality of connection with horizontal diaphragms, the flexibility of horizontal diaphragms, the interaction with adjacent buildings, etc., could considerably affect the structural behavior of masonry buildings [21].

In general, the structural details also depend on the historical evolution of the building, in terms of restorations, additions of parts, destination changes, damages and repairs, etc. The knowledge of these aspects could be challenging for historic structures, as they are the result of a subsequent superimposition of modifications along with the centuries. Indeed, the setting up of an effective knowledge procedure when dealing with masonry cultural heritage assets is related not only to the cost-benefit optimization (with respect to the reliability of the final outcome), but also to the minimization of invasiveness on the construction, with the aim of its conservation [22]. Beyond the traditional approaches proposed
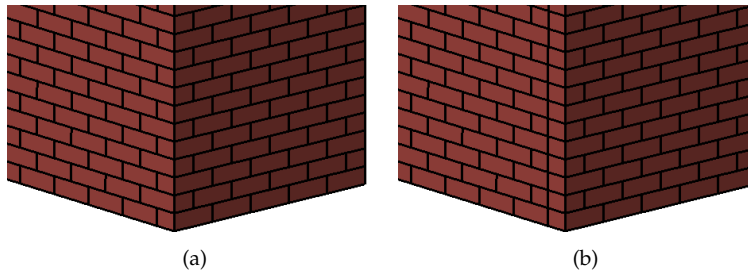
Figure 8: Example of corner between two orthogonal masonry walls (one leaf running bond walls): (a) toothing texture, and (b) without-toothing texture of the corner.

in standards or guidelines for the seismic assessment of existing buildings (e.g. at international levels, Eurocode 8 - Part 3 [23] and ASCE/SEI 41/06) or, more specifically, of heritage structures [24, 25], literature proposals to improve the knowledge phase have been recently developed [26, 27].

2.2.4 *Geometrical challenges*

In some cases, the definition of the geometry of the structure could be challenging as well, especially for historic monumental buildings characterized by complex and irregular geometries. In these cases, an accurate geometrical and structural survey is required.

One first issue concerns the identification of the structure (i.e. the load-bearing system) within the building geometry. This non-trivial operation has to be carried out by the analyst basing on the knowledge of the building.

Another issue regards the employability of the geometry in structural analysis purposes. The geometry of these structures can be manually drawn on a computer-aided design (CAD) environment basing on the geometric survey. The CAD-based geometry can be directly used within simplified structural analysis frameworks, such as the one proposed in [28]. However, the employability of this CAD-based geometry in mesh-based structural analysis could be problematic. Indeed, the discretization process of these geometries is usually accompanied by mesh errors, compatibility problems, excessively refined meshes, etc. Several approaches which use as input 3D point clouds for the automatic mesh generation of historic building have been recently proposed in [29, 30, 31, 32] to deal with the aforementioned issues. The development and the optimization of these methods is still an on-going process.

2.3 ANALYSIS APPROACHES

The collapse or near-collapse response of masonry structures can be investigated following two main ways: (i) incremental-iterative analyses and (ii) limit analysis-

based solutions. In this section, the main features of these two analysis approaches are briefly recalled.

2.3.1   *Incremental-iterative analyses*

In incremental-iterative analysis procedures, the evolution of the equilibrium conditions of a structure subjected to certain actions is investigated step-by-step. The loading and the structural response are divided into a sequence of intervals, increments or "steps". Iterations are hence carried out to reach equilibrium within each step. These procedures allows to account for mechanical nonlinearity, which is fundamental and mandatory to be considered for a reliable assessment of the collapse and near-collapse behavior of masonry structures. Although few examples of linear elastic models have been developed for the preliminary assessment of historic masonry structures [33, 34], their effectiveness in investigating the failure mode and the safety of these structure is substantially limited.

As the aim of these analyses consists in studying the collapse behavior of masonry structures, large displacements could occur and, therefore, geometrical nonlinearity could play a non-marginal role and should be included in the computations.

Incremental-iterative analyses could be classified in nonlinear static and nonlinear dynamic (time history) analyses:

(i) *Nonlinear static analysis*. In nonlinear static analyses, the structure is step-by-step subjected to certain actions until its critical and post-critical conditions. The pseudo-time in which the structural response evolves does not represent any physical characteristics. Simulations can be performed in either load control or displacement control, and in event-by-event damage control (e.g. sequentially linear analysis [35, 36]).

Given the mechanical nonlinearity assumed for the material, nonlinear differential equations have to be solved. These equations can be transformed in nonlinear algebraic equations and solved within a numerical framework. Typically, the nonlinear equations are step-wise linearized and resolved following an iterative procedure. Among the most famous iterative procedures are: the Picard iteration (or direct iteration) method, the Newton-Raphson iteration methods, and the Riks methods (the interested reader is referred to [37] for more information about iterative procedures).

These kind of analyses are typically used to simulate quasi-static experimental tests on masonry structures and to perform the so-called pushover analysis. Pushover analysis is a very common and standardized procedure to assess the seismic behavior of a masonry structure, which is subjected to a monotonically increasing displacement of a control node given a load pattern of horizontal forces kept constant in shape during the analysis.

(ii) *Nonlinear dynamic (time history) analysis*. In nonlinear time history analysis (also called transient nonlinear analysis), the structure is step-by-step sub-

jected to time-dependent actions and the structural response evolves in the actual time, accounting for inertial and damping effects as well.

Time integration methods are employed to approximately satisfy the equations of motion during each time step of the analysis. These methods may be classified as either explicit or implicit [38]. An explicit method is labeled as one in which the new response values calculated at each step depend only on quantities obtained in the previous step. Conversely, in an implicit method the expressions giving the new values for a given step include values which pertain to that same step. Therefore, trial values of the unknowns must be assumed and refined by successive iterations. Among the most famous time integration methods are the following: Euler-Gauss procedure, Newmark Beta methods, second central difference formulation, linear acceleration procedures [38]. In any case, a large body of literature has been written on this topic and the interested reader is referred to [38] for more details.

Nonlinear time history analyses can simulate the effects of dynamic actions (e.g. earthquakes, impacts, explosions, etc.) on masonry structures. Indeed, the possibility to account for time-dependent loads allows to simulate the response of the structure against, for instance, a real accelerogram. Shaking table experimental tests on masonry structures can be analyzed as well. Occasionally, dynamic analysis can be also used for simulating quasi-static tests and processes, by applying, for example, loads in a very slow way.

2.3.2 *Limit analysis-based solutions*

Heyman [39] firstly applied limit theorems of plasticity to masonry structures, adopting the following three hypotheses:

(i) masonry has no tensile strength,

(ii) the compressive strength of masonry is infinite,

(iii) sliding of one masonry block upon another cannot occur.

These hypotheses, together with the negligibility of elastic strains, allowed the formulation of the static theorem (lower-bound limit analysis) and the kinematic theorem (upper-bound limit analysis) for masonry structures.

The smart Heyman's rigid no-tension model has been widely used and fruitfully applied in analyzing the stability of masonry systems [40]. Firstly, these assumptions allowed simple graphic statics solutions for the stability analysis of masonry vaults [41], and kinematic analysis of common seismic failure modes of masonry buildings [42]. Secondly, the Heyman's hypotheses established a solid base for the formulation of modern computational limit analysis-based methods. These numerous methods (that will be discussed in the following) are based on either the static theorem [43] or the kinematic theorem [44], and the problem can be formulated as solution of an optimization problem (using or not genetic

algorithms), of nonlinear differential equations, of linear or sequential linear programming, etc.

One of the main disadvantages of limit analysis-based solutions consists in the fact that their output is limited to the collapse multiplier and the collapse mechanism, and no information is available on the ultimate displacement and/or post-peak response, which appear fundamental in widely adopted displacement-based seismic assessment procedures for masonry structures.

2.4 MODELING STRATEGIES

In this section, a classification of the modeling strategies for masonry structures is proposed. This classification is focused on the ways masonry and/or masonry structures are modeled. Therefore, the analysis approaches discussed in Section 2.3 can be, in principle, applied to each modeling strategy category.

Each modeling strategy has some peculiar appealing features, which, in general, could have a specific area of application. Furthermore, depending on the scale of representation conceived in the numerical strategy, different scales of material testing (Figure 7) could be used to calibrate the mechanical parameters of the model, see Section 2.2.2.

Although each modeling solution which can be found in the scientific literature presents original and peculiar features, making the classification non-trivial and non-fully coherent, our aim consists in trying to make some order on the wide scientific production on this field [45, 46, 47].

The present classification proposes four main categories of modeling strategies for masonry structures (Figure 2):

(i) *Block-based models*. Masonry is block-by-block modeled and, therefore, the actual masonry bond can be accounted for. The block behavior can be considered rigid or deformable, whereas their interaction can be mechanically represented by means of several suitable formulations, that are reviewed in Section 2.5.

(ii) *Continuum models*. The masonry material is modeled as a continuum deformable body. The nonlinear constitutive law adopted for the material can be defined either through (i) *direct approaches*, i.e. by means of constitutive laws calibrated, for example, on experimental tests, or through (ii) *homogenization procedures and multi-scale approaches*, where the constitutive law of the material (considered as homogeneous in the structural-scale model) is deduced from an homogenization process which relates the structural-scale model to a material-scale model (representing the main masonry heterogeneities) of a representative volume element (RVE) of the structure. In this cases, the solution of structural-scale problems could be formulated in a multi-scale framework. These continuum models are reviewed in Section 2.6.

(iii) *Geometry-based models*. The structure is modeled as a rigid body. The geometry of the structure represents the main (or even the only) input of these modeling strategies. The structural equilibrium and/or collapse are investigated through different procedures. Typically, these methods implement limit analysis-based solutions (see Section 2.3.2), which can be based on either static or kinematic theorems. Although these models could, in some respects, be considered as continuum models (see category (ii)), it should be remarked that the present category is based on the assumption of rigid body. The geometry-based models are reviewed in Section 2.7.

(iv) *Macroelement models*. The structure is idealized into panel-scale structural components (macroelements) with a phenomenological or mechanical-based nonlinear response. Typically, two main structural components may be identified: piers and spandrels. The subdivision of the structure into panel-scale portions is an *a priori* operation made by the analyst who interprets the structural conception of the building. Although these models could, in some respects, be considered continuum approaches, the main difference with the models in (ii) is that the constitutive law of macroelements attempts to reproduce the mechanical response of panel-scale structural components, while the constitutive law of the models in (ii) tries to reproduce the mechanical behavior of the masonry material. Macroelement models are reviewed in Section 2.8.

In the following, each category is comprehensively reviewed, showing the limitations and possibilities of each approach, accounting for new and recently proposed solutions. In this spirit, the following sections could be seen as an updating of well-known review papers [45, 46] on this field.

2.5 BLOCK-BASED MODELS

Block-based models represent the masonry behavior at the scale of the main heterogeneity of the material, characterized by blocks assembled by mortar (or dry) joints, which governs the main aspects of its mechanical and failure response. Indeed, these models can account for the actual masonry bond, which substantially controls the anisotropy and the failure pattern of the material.

The first example of nonlinear block-based model dates probably back to 1978, thanks to the pioneering work by Page [48], where masonry is considered as an assemblage (that will be called "textured continuum" in the following) of elastic brick elements acting in conjunction with linkage elements simulating the mortar joints which have limited shear strength depending upon the bond strength and the level of compression. From that work, several block-based models have been developed and proposed.

The main positive features of the block-based modeling strategy category can be summarized as:

- Representation of the actual masonry bond and many structural details (e.g. toothing of corners between orthogonal walls, see Figure 8);

- Easy mechanical characterization from small-scale experimental tests;

- Clear representation of the failure modes, which do not need demanding interpretation. Indeed, detailed insights on the weakest parts of the structure can be found, helping the designing of strengthening devices;

- Anisotropy intrinsically accounted for in the definition of the actual masonry bond;

- 3D models can account for, at the same time, the in-plane and out-of-plane responses of masonry walls (and their interactions [49]);

- The interaction between orthogonal walls if subjected to horizontal loads (in terms, for example, of vertical reaction transfer) is intrinsically accounted for in 3D models.

Conversely, the main negative features of the block-based models can be summarized as:

- The main issue of these models resides in their huge computational demand. This well-known problem [45, 46], typically limits the applicability of these modeling strategies to panel-scale structures. Indeed, few examples of applications on full-scale masonry structures can be found in the literature [50, 51]. However, given the continuous power increment of the computational facilities, this problem could be less significant in the near future;

- 2D models unlikely show a reliable out-of-plane response;

- The actual bond of existing masonry structures is often non-completely know. Therefore, the block-by-block discretization could be approximated in those cases;

- The assembly of the model is usually a time-consuming and complex operation, which limits the use of these modeling strategies to academic studies and very few high-level consultancy groups.
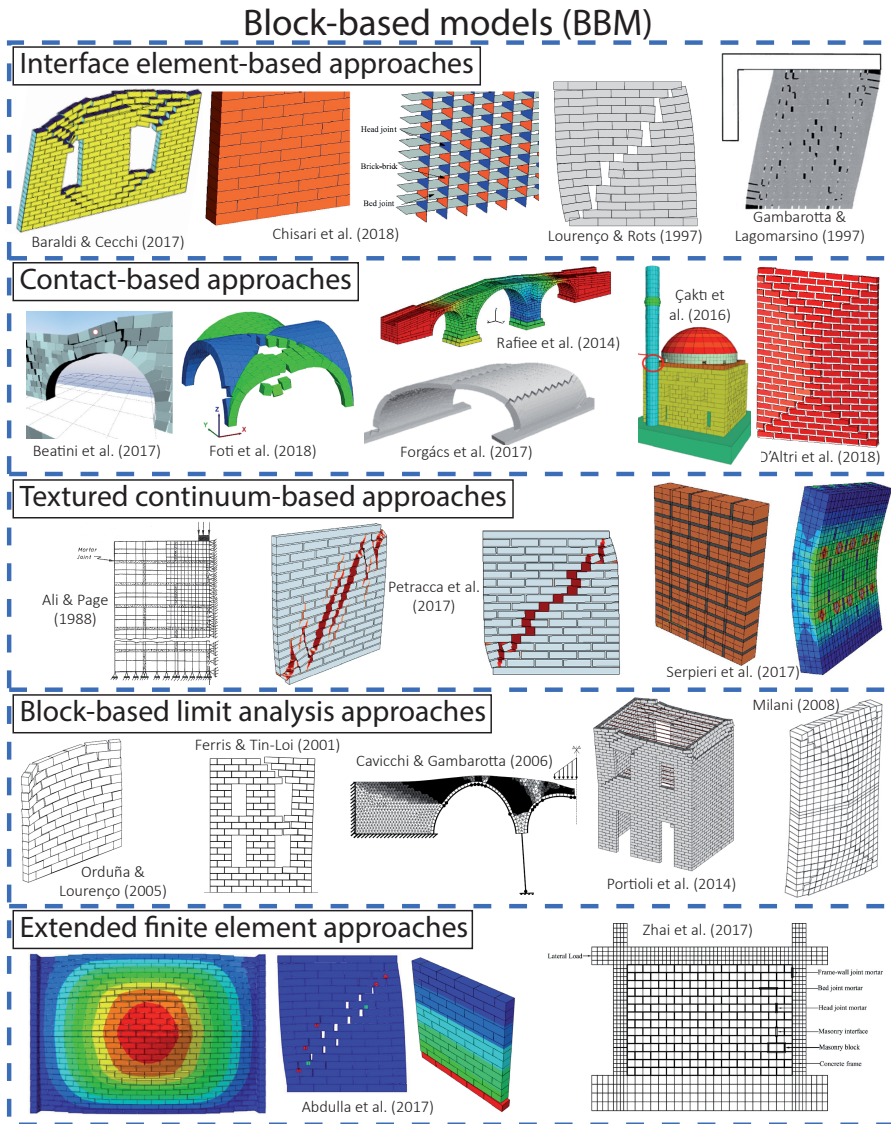
Figure 9: Examples of block-based models.

In this section, block-based models are classified into different subcategories depending on the way the interaction between blocks is formulated (Figure 9):

1. Interface element-based approaches;

2. Contact-based approaches;

3. Textured continuum-based approaches;

4. Block-based limit analysis approaches;

5. Extended finite element approaches.

Each subcategory is then exhaustively reviewed in the following.

2.5.1 *Interface element-based approaches*

A first nonlinear interface-based model to simulate the collapse behavior of masonry structures appeared in [52], where the mortar joints were modeled with zero-thickness interface elements and the masonry units (which were considered as expanded to account for the geometry of the mortar joints) were modeled with smeared crack elements, within a FE approach (Figure 10). In particular, a dilatant interface plasticity-based constitutive model capable of simulating the initiation and propagation of interface fracture under combined normal and shear stresses was developed.
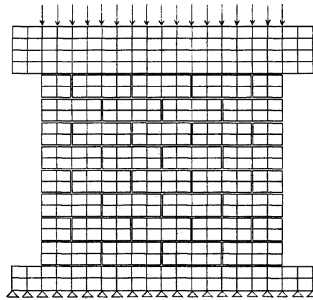
Figure 10: Example of a pioneering interface-based model [52].

An important improvement of this approach has been proposed by Lourenço & Rots [53]. In particular, they developed a multi-surface interface-based model in which all the nonlinearities (including also crushing) were concentrated in the interfaces. This permitted to increase the efficiency of the model, in the framework of softening plasticity. Such a model [53] has been diffusely used in the years that followed, and is still today utilized for many applications on masonry structures [54, 55]. For example, an interesting application of this interface model has been conducted in [56] for historic non-regular stone masonry shear walls. Furthermore, an extension of the interface model developed in [53] to the cyclic behavior

of masonry shear walls has been presented and validated in [57], fully-based on the plasticity theory.

A cyclic mortar joint interface model based on damage mechanics has been developed by Gambarotta & Lagomarsino [58]. In particular, the constitutive equation of the interface is postulated in terms of two internal variables representing the frictional sliding and the mortar joint damage. The interface model exhibits a brittle response under tensile stresses and is characterized by frictional dissipation together with stiffness degrading under compressive stresses (Figure 9).

Other approaches, based on cohesive interfaces with damage and friction have been presented in [59, 60, 61], which were suitable for the simulation of masonry shear walls.

Additionally, several strategies have been based on the assumption of rigid blocks which interact through nonlinear springs simulating the response of masonry joints as well as crushing. This is the case, for example, of the model developed by Malomo et al. [62] within the framework of the so-called applied element method. Although similar, in principle, to the rigid body spring model (RBSM) developed by Casolo [63] (which is, however, used without accounting for the actual masonry bond and, so, the spring linear and nonlinear properties have to be homogenized), in [62] the block-by-block modeling is pursued for the analysis of the in-plane cyclic behavior of masonry walls.

All references described up unto this point are conceived for the analysis of 2D problems, typically in-plane problems. This aspect, as discussed above, considerably limits the applicability of the modeling strategies to real problems. To overcome this issue, several 3D models have been developed [64, 65, 66] to deal with real case studies as well. Primarily, two different interface elements have been developed specifically for 3D analysis of masonry structures.

Firstly, an extension of the Lourenço & Rots [53] multi-surface interface model to the 3D case, accounting also for geometrical nonlinearity, has been developed by Macorini and Izzudin [67]. In particular, a co-rotational approach has been employed in [67] for the interface element, which shifts the treatment of geometric nonlinearity to the level of discrete entities, and enables the consideration of material nonlinearity within a simplified local framework employing first-order kinematics (Figure 9). This approach has been extensively used for real applications [68, 69] by using partitioning routines [70, 71]. Moreover, the interface model presented in [67] has been further developed for simulating the cyclic response of masonry structures [50] by using a damage-plasticity approach.

Secondly, another interface constitutive model has been developed in [72] and coupled with elasto-plastic block elements for the explicit cyclic analysis of 3D masonry walls. This interface model has been broadly used for studying several aspects of the mechanics of masonry walls [73, 74, 49, 75].

2.5.2 *Contact-based approaches*

Block-based modeling strategies based on contact mechanics are widely used for the accurate modeling of masonry structures. Basically, rigid or deformable (linear or nonlinear) blocks interact following a frictional or cohesive-frictional contact definition. Although several in-house formulations have been developed and validated (see for instance [76, 77]), three main families of contact-based approaches can be found.

Firstly, a wide family of modeling approaches has been based on the distinct element method (DEM), also called discrete element method in the literature [78], originally proposed by Cundall & Stack [79] for the analysis of granular assemblies and implemented in the UDEC code [80]. DEM approaches are based on contact penalty formulations and explicit integration schemes. In this context, several applications have been conducted on real masonry structures [81, 82, 83, 84, 85, 86, 87, 88, 89, 90] using rigid or linear elastic blocks (Figure 9).

Secondly, an implicit approach which considers the deformability of blocks is the so-called discontinuous deformation analysis (DDA) [91]. DDA fulfills constraints of no tension between blocks and no penetration of one block into another. Also, Coloumb's law is fulfilled at all contact positions for both static and dynamic computations [92].

Thirdly, another family is based on the non-smooth contact dynamics (NSCD) method, developed by Jean [93] and Moreau [94] and characterized by a direct contact formulation, in its non-smooth form, implicit integrations schemes, and energy dissipation due to blocks' impacts. This approach, although successfully applied to several real case studies [95, 96, 97, 98], appears limited to dry stone masonry structures, as it seems still not capable in representing cohesive responses of the mortar joints.

Although the approaches belonging to the aforementioned three families are generally rather fast and permit full-scale applications as well, they cannot properly account for masonry crushing, which can be, in some cases, crucial in the mechanical response of masonry structures. To this aim, other approaches have been developed to account for block nonlinearity in tension and compression (Figure 11).

In the framework of the so-called finite-discrete element method (FDEM) [99], Smoljanović et al. [100] developed a code for the computational analysis of dry stone masonry structures [100] and extended it to 3D structures in [101]. Additionally, they implemented the nonlinear response of blocks in [102] to account for masonry crushing and block fragmentation (Figure 11(a)).

Finally, a very recent 3D block-based model with contacting damaging blocks has been developed and validated in [11], where the mortar layers are explicitly modeled in the block mesh. This model, based on implicit integration schemes, contact penalty method, compressive and tensile damage for the blocks, and rigid-cohesive-frictional contact behavior, provided very accurate results for the in-plane and out-of-plane response of masonry panels. Moreover, the model pre-

sented in [11] has been extended to the cyclic behavior of full-scale masonry structures (Figure 11(b)) in [51].

(a)   (b)
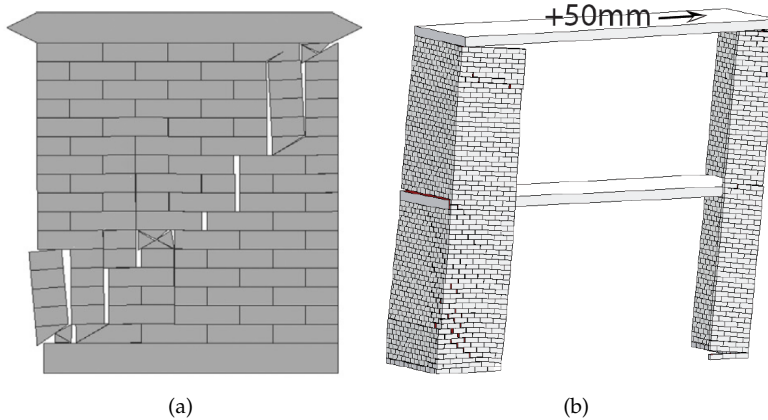
Figure 11: Examples of contact-based approaches which include masonry crushing [102, 51].

2.5.3 *Textured continuum-based approaches*

The main idea of block-based textured continuum models [48] is to have, in a FEM framework with nonlinear elements, blocks and joints modeled separately without any interface between them, allowing for nonlinear deformation characteristics of the two materials as well as failure of the blocks, the mortar, or the mortar joints by bond.

An example of a pioneering mesh discretization of this kind of approaches is shown in Figure 9 (see Ali & Page [103]), in which the FEs with block properties are distinguished from the ones with mortar (or more correctly mortar joint) properties. In particular, the model used in [103] uses a strength criterion for crack initiation and propagation, and the smeared crack modeling technique for reproducing the effects of the crack.

More recently, a block-based textured continuum model which discretizes both units and mortar-joints with continuum elements, making use of a tension/compression damage model, has been developed in [104]. Particularly, in [104] the damage model has been refined to properly reproduce the nonlinear response under shear and to control the dilatancy. Another solution, based on a enriched kinematic damage model, has been proposed in [105].

A very innovative approach to mechanically model the nonlinear response of mortar joints has been lately presented in [106], where a microstructured 3D composite interphase formulation based on a multiplane cohesive-zone model has been proposed. Basically, a multiscale modeling strategy for the constitutive

law of mortar joints has been adopted, allowing to conduct a consistent and reproducible calibration procedure of the mortar joint parameters.

2.5.4 *Block-based limit analysis approaches*

Block-based limit analysis represents an accurate and robust approach for the prediction of collapse load and failure mechanism of masonry structures. Several 2D and 3D approaches have been developed along the last two decades (Figure 9), generally based on either static or kinematic theorems of limit analysis, even if the implementation of friction in the computations is usually non-conservative with respect to the limit analysis theorems.

The first block-based limit analysis approach applied to masonry assemblages is probably the one developed by Baggio & Trovalusci [107], where the solution of the limit analysis problem in the presence of friction at interfaces between rigid blocks, i.e. a nonlinear programming problem, is obtained by solving a preliminary problem of linear programming, corresponding to a linearized limit analysis in the presence of dilatancy at the interfaces [108].

Another approach has been developed by Ferris & Tin-Loi [109], where the computation of the collapse loads of discrete rigid block systems, characterized by nonassociative friction and tensionless contact interfaces, is formulated and solved as a special constrained optimization problem, i.e. the so-called mathematical program with equilibrium constraints.

Furthermore, Sutcliffe et al. [110] developed a technique for computing the lower bound limit loads in unreinforced masonry shear walls under conditions of plane strain. By using a Mohr–Coulomb approximation of the yield surfaces, the numerical procedure proposed in [110] computes a statically admissible stress field via linear programming and finite elements. By imposing equilibrium, an expression of the collapse load is formed by imposing equilibrium, and the solution obtained is a rigorous lower bound on the actual collapse load.

Later, Orduña & Lourenço [111, 112] proposed a solution procedure for the non-associated limit analysis of rigid block masonry assemblages, incorporating non-associated flow rules and a coupled yield surface.

Moreover, a formulation for limit analysis of masonry block structures with non-associative frictional joints, using linear programming, has been proposed in [113], extended to 3D structures accounting for torsional effects in [114], and optimized using cone programming in [115]. In these approaches, rigid blocks interact via no-tension contact surfaces with Coulomb friction.

Conversely, the approach proposed and developed by Milani [116], based on 3D FE upper bound limit analyses of in- and out-of-plane loaded masonry walls, implements interfaces with a Mohr–Coulomb failure criterion with tension cut-off and cap in compression for mortar joints, whereas a Mohr–Coulomb failure criterion is adopted for bricks. Therefore, mortar joint cohesion and masonry crushing are accounted for in this approach. Other direct applications of this

model can be found in [117, 118], whereas applications within homogenization procedures are going to be discussed in the following section.

Although block-based limit analysis approaches have been also applied to real structures, e.g. masonry bridges in [119], their computational demand appears particularly high, preventing their use for large-scale masonry structures.

2.5.5 *Extended finite element approaches*

Very recently, few block-based models formulated in the framework of the extended finite element method (XFEM) have been proposed [120, 121] (Figure 9).

Particularly, Abdulla et al. [120] proposed a 3D model which includes surface-based cohesive behavior to capture the elastic and plastic behavior of masonry joints and a Drucker-Prager plasticity model to simulate crushing of masonry under compression (Figure 9).

Furthermore, XFEM is adopted in [121] to model the cracking behavior and the compressive failure of masonry in infill panels, and the discrete interface element is employed to simulate the behavior of the masonry mortar joints and the joints at the frame-to-infill interface (Figure 9).

Although only two models have been proposed so far in this subcategory, these approaches can represent a powerful alternative for block-based analysis of masonry structures.

2.6 CONTINUUM MODELS

In continuum approaches, masonry is modeled as a continuum deformable body (Figure 12). This category of modeling strategies has the advantage that the mesh discretization does not have to describe the main heterogeneities of masonry, and, hence, can have dimensions which can be significantly greater than the block size. So, the computational effort of these approaches is, in general, lower than block-based approaches. However, given the complexities of masonry from a mechanical point of view (Section 2.2), the definition of suitable homogeneous constitutive laws for masonry is a challenging task, and can be pursued either through (i) *direct approaches*, i.e. by means of constitutive laws calibrated, for example, on experimental tests, or through (ii) *homogenization procedures and multi-scale approaches*, where the constitutive law of the material (considered as homogeneous in the structural-scale model) is derived from an homogenization process which relates the structural-scale model to a material-scale model (representing the main masonry heterogeneities). The homogenization process is typically based on refined modeling strategies (e.g. block-based models) of a representative volume element (RVE) of the structure.
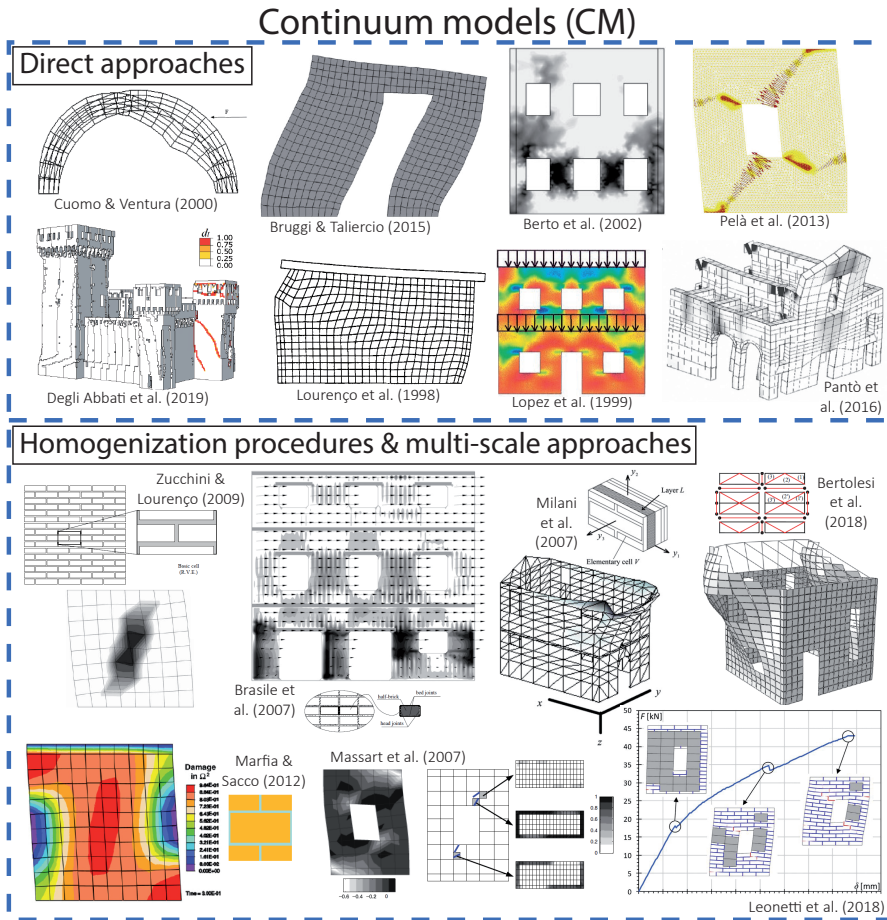
Figure 12: Examples of continuum models.

2.6.1 *Direct approaches*

Direct continuum models rely on continuum constitutive laws which can, some-
how, approximate the overall mechanical response of masonry. In these approaches,
the mechanical properties (elastic parameters, strength domain, etc.) could be
calibrated through experimental tests or other data (e.g. experimentally-derived
analytical strength domains), without resorting to RVE-based homogenization
procedures.

Several formulations, with different levels of approximation, have been devel-
oped and tested on real applications. Indeed, although the mechanical properties
of the homogeneous model should be, in theory, rigorously deduced from homog-
enization theories, many simplified approaches have been successfully applied on
interesting case studies.

One first family of direct approaches consists in a drastic idealization of the masonry mechanical behavior, i.e. masonry is conceived as a perfectly *no-tension* material. Generally, perfectly no-tension material means an isotropic medium incapable of sustaining tensile stresses but, otherwise, linear-elastic [122]. This radical hypothesis, although sustained by the fact that the mechanical characterization of masonry is very challenging especially in the tensile regime, can be a valuable basis for preliminary structural analyses [123]. Nevertheless, the hypothesis of no-tension material has been widely used in the analysis of the stability of masonry vaults and domes [39, 40], in the framework of geometry-based models (Section 2.7).

In [123], an approximate, piecewise-linear description of perfectly no-tension material behavior has been developed, leading to a very simple formulation of the discretized boundary value problem in finite terms. Later, Angelillo [124] proposed a FE solution based on a complementary energy theorem for elastic no-tension bodies. The solution relies on a problem of minimization of a quadratic function with equality and inequality constraints. Starting from an elementary stress field, an optimal approximate solution (safe in the spirit of limit analysis) is reached. Other solutions of the FE analysis of no-tension structures can be found in [125, 126, 127]. More recently, Bruggi [128] proposed a FE analysis of no-tension structures as a topology optimization problem. Then, Bruggi & Taliercio [129] proposed a non-incremental energy-based algorithm to define the distribution and the orientation of an equivalent orthotropic material, minimizing the potential energy so that to achieve a compression-only state of stress.

Although the cited no-tension approaches represent elegant solutions for such a complex problem, their applicability to real case studies is still limited. Indeed, all the aforementioned approaches are limited to 2D problems and only very recently 3D no-tension structures have been investigated [130]. However, these approaches cannot simulate the post-peak behavior of masonry structures, which is a strong limitation in the field of seismic assessment of structures. Moreover, although the assumption of null tensile strength can be considered, in general, conservative, this could lead to failure mechanisms which are not coherent with the ones experimentally observed, given that in reality the tensile strengths of masonry are non-zero.

Other direct continuum models for masonry structures rely on continuum nonlinear constitutive laws based either on fracture mechanics (smeared crack models), on damage mechanics, or on plasticity theory. Several smeared crack [131, 132], plastic [133], damage [134], and plastic-damage [135, 136] models have been primarily developed for the FE analysis of concrete structures. However, their usability for the simulation of the collapse or near collapse behavior of masonry structures presents some limitations, mainly due to the multi-level anisotropy (elastic, strength and brittleness anisotropies, see Section 2.2) of masonry and its heterogeneity introduced by mortar joints. A pioneering test of the accuracy of smeared crack models for masonry structures is reported in [137]. While the model adopted in [137] showed good performance with respect to flexure-

dominated behavior, it showed problems in capturing the brittle shear behavior of masonry panels.

Although non-fully coherent with masonry mechanics, smeared crack and isotropic damage and plastic-damage models have been extensively used for analyzing masonry structures [138], mainly due to their efficiency, their diffusion in commercial FE codes, and the relatively few mechanical parameters to characterize.

Particularly, the utilization of these nonlinear models has been found especially indicated for the analysis of historic monumental structures, given their limited computational effort and their capability to represent complex and large-scale 3D geometries. In addition, historic buildings are usually characterized by multi-leaf irregular randomly-assembled masonries, which are often impossible to represent block-by-block and to mechanically characterize, given also the strict limitations for destructive in situ tests on historic buildings [139]. Indeed, poor information is usually available on the mechanical properties of historic masonries, favoring the use of isotropic nonlinear models. Many applications of isotropic smeared crack, damage and plastic-damage models have been successfully conducted on historic towers [140, 141, 142, 142], churches and temples [143, 144, 145, 146], palaces [147, 148, 30, 149], and masonry bridges [150, 151]. In particular, most of the applications on historic monumental structures rely on 3D models (Figure 13), as the structural behavior is rarely representable by 2D models, given the complex and irregular geometries of these buildings (Section 2.2).

(a)   (b)   (c)

(d)
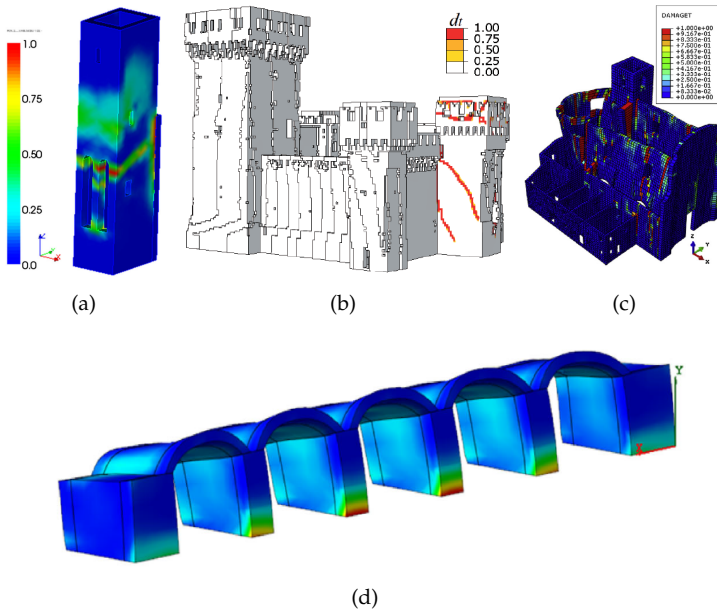
Figure 13: Examples of direct continuum isotropic approaches applied on historic monumental structures [140, 149, 144, 151].

Although each reliable damage model has to conceive a regularization of the fracture energy, which is usually normalized on a characteristic dimension of the element, very coarse meshes could lead to unsafe results as they are not able to essentially represent the damage pattern and the stress redistribution. An enhancement of the aforementioned constitutive models could be represented by the use of crack-tracking algorithms, originating from the analysis of localized cracking in quasi-brittle materials, which ensure mesh-bias independency of the numerical results and the realistic representation of propagating cracks in the numerical simulation of fracture in quasi-brittle materials [152, 153].

However, when dealing with periodic well-organized masonry, the assumption of only one tensile strength value (that governs the tensile response in each direction) risks to be too simplistic. To this aim, some orthotropic nonlinear constitutive laws have been developed and applied on masonry structures.

A first example of orthotropic plasticity model with softening has been proposed in [154], while in [155] the ability of that continuum model to represent the inelastic behavior of orthotropic materials is shown, and a set of experimental tests to characterize the constitutive behavior of masonry is proposed, demonstrating the capability of the model to reproduce the strength behavior of different masonry types.

Successively, the effect of anisotropy has been introduced in [156] by means of fictitious isotropic stress and strain spaces. The material properties in the fictitious isotropic spaces are mapped into the actual anisotropic space by means of a consistent fourth-order tensor. The advantage of the model is that the classical theory of plasticity can be used to model the nonlinear behavior in the isotropic spaces.

Later, an orthotropic damage model specifically developed for the analysis of brittle masonry subjected to cyclic in-plane loading has been described in [157]. Different elastic and inelastic properties have been assumed along the two natural axes of the masonry (i.e. the bed joints and the head joints directions) also as principal axes of damage.

More recently, Pelà et al. [158, 159] proposed an orthotropic damage model for the analysis of masonry structures, in which the orthotropic behavior is simulated through the concept of mapped tensors from the anisotropic field to an auxiliary workspace. The model affords the simulation of orthotropic induced damage, while also accounting for unilateral effects, thanks to a stress tensor split into tensile and compressive contributions. The damage model has also been combined with a crack-tracking technique [160] to reproduce the propagation of localized cracks in the FE problem.

Although the described direct continuum anisotropic approaches (Figure 12) represent scientifically sound solutions, their application on real case study has been limited by the fact that their computational effort and the number of material properties to be mechanically characterized is substantially higher than isotropic approaches.

Additionally, other solutions adopt an homogeneous FE model of the structure, but, instead of a proper continuum, they use alternative solutions to describe

the nonlinear behavior of masonry. For example, Reyes et al. [161] proposed a numerical procedure for fracture of brickwork masonry based on the strong discontinuity approach, accounting for the anisotropy of the material.

Other approaches, based on FE limit analysis, conceive the homogeneous structural-scale model made of rigid or deformable elements, placing nonlinear interfaces in between the elements, where plastic dissipation can occur. Dealing with historic full-scale buildings, FE limit analysis approaches have been successfully applied [162, 32] by using averaged mechanical properties, without using a rigorous homogenization procedure.

Finally, other approaches based on systems of springs [163, 164] can be fully characterized through a suitable calibration of linear and nonlinear spring properties.

These latter approaches (FE limit analysis and spring-based approaches) can be considered borderline in the context of continuum models (as they have interfaces between elements or spring systems instead of a proper continuum). However, given that they eventually behave as a continuum (where all the deformabilities and nonlinearities are lumped in the interfaces/springs) and the structure is effectively discretized by means of a continuum mesh, their classification in this category could be considered legitimate.

2.6.2 *Homogenization procedures & multi-scale approaches*

The constitutive law of the homogeneous structural-scale model which tries to represent masonry can be deduced from homogenization processes, typically based on RVEs. The definition of a proper RVE is essential, as it should be statistically representative of the material-scale heterogeneity under study, embodying the characteristic material heterogeneities. To this aim, several RVEs geometries have been proposed, to account for different periodic and non-periodic patterns of masonry (Figure 14).

Given the mechanical complexity of masonry, in terms, for example, of anisotropy, a very wide family of continuum approaches rely on homogenization procedures and multi-scale approaches [170]. Basically, three main families of approaches could be distinguished (Figure 15):

(i) *A priori homogenization approaches* (Figure 15(a)), which typically rely into two steps: in the first step, (*a priori*) RVE-based homogenization is performed to deduce the mechanical properties of the structural-scale material; the second step relies into the introduction in the structural-scale model of the homogenized mechanical properties.

(ii) *Step-by-step multi-scale approaches* (Figure 15(b)), in which the overall behavior at the structural scale is step-by-step determined by solving a boundary value problem (BVP) on the RVE for each integration point of the structural-scale model. In this way, an estimation of the expected average response to be used as constitutive relations in the structural-scale model is step-by-step
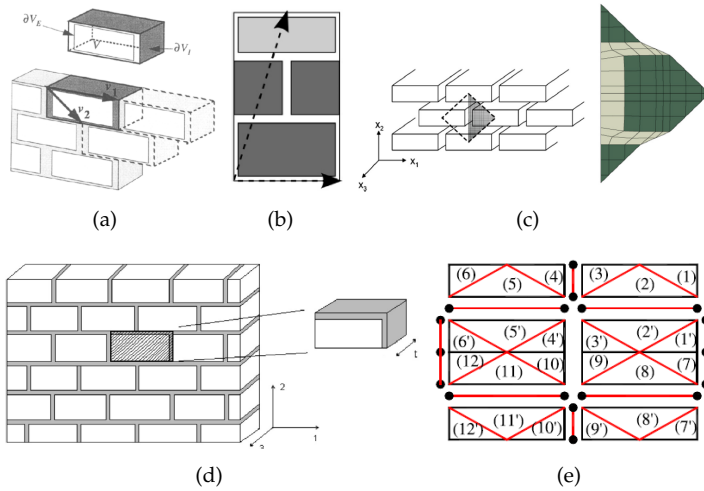
Figure 14: Examples of RVEs adopted for the derivation of homogenized masonry mechanical properties [165, 166, 167, 168, 169].

obtained. In these approaches, the heterogeneity of masonry is not directly accounted for in the structural-scale model, being explicitly accounted for into the material-scale RVE.

(iii) *Adaptive multi-scale approaches* (Figure 15(c)), in which the material-scale model is adaptively inserted and resolved on the structural-scale model, thus establishing a strong coupling between the two scales.

2.6.2.1   *A priori homogenization approaches*

Although *a priori* homogenization approaches typically consists of two steps (i.e. in the first step the mechanical properties are deduced through an homogenization process, and in the second step homogenized properties are introduced in the structural scale model), most of the solutions provided in the literature focused on the first step, while only few approaches dealt with both steps.

The deduction of homogenized constitutive laws for the analysis of heterogeneous quasi-brittle materials, such as masonry, can be based on closed-form (analytical), quasi-analytical, and numerical methods.

A pioneering contribution on the mathematical description of the macroscopic behavior of brick masonry has been given in [174]. Successively, Anthoine [165] rigorously derived the in-plane elastic characteristics of masonry through homogenization theory. Briccoli Bati et al. [175] applied a material-scale model for the determination of the overall linear elastic mechanical properties of a simple texture of brick masonry. In the framework of the Cosserat continuum models, Masiani & Trovalusci [176] studied the case of 2D periodic rigid block assemblies joined

(a)

(b)

(c)
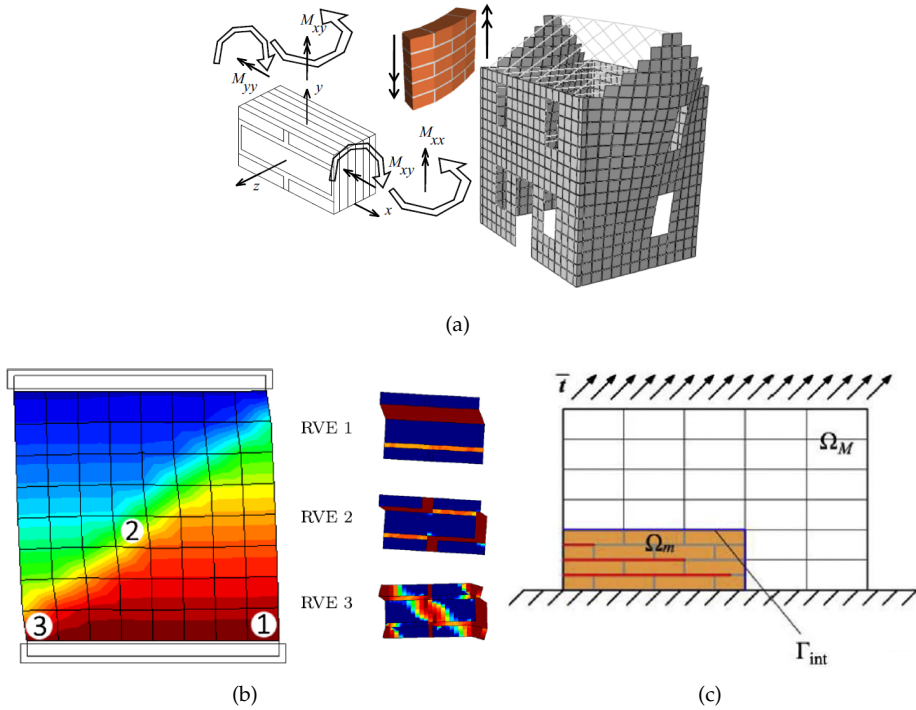
Figure 15: Homogenization procedures and multi-scale approaches: (a) *a priori* homogenization [171], (b) step-by-step multi-scale [172], and (c) adaptive multi-scale [173] approaches.

by linear elastic mortar joints, deducing the structural-scale model characterization of the equivalent medium by equating the virtual stress power of the coarse model with the virtual power of the internal actions of the discrete fine model. An extension to the 3D case has been analyzed in [177]. Further approaches for the derivation of homogenized elastic properties of masonry can be found in [178, 179, 180, 181, 182, 167].

Other approaches, beyond the definition of elastic properties, attempted to derive masonry strength domains (both in-plane and out-of-plane) [183]. For example, in [184], a structural-scale strength criterion for in-plane masonry response is derived through a continuum model. Zucchini & Lourenço [185, 186] derived both elastic moduli and failure surfaces through a linear and nonlinear homogenization procedures. Wei & Hao [187] develop a continuum damage model for masonry accounting for the strain rate effect, using a homogenization theory implemented in a numerical algorithm. Stefanou et al. [168] provided a straightforward methodology for the estimation in closed-form of the overall strength domain of an in-plane loaded masonry wall by accounting for the failure of its bricks.

Most of the existing models for masonry concerned periodic material-scale textures. Cecchi & Sab [188] analyzed non-periodic masonries, typical of historic buildings, by means of a perturbation approach, while Cavalagli et al. [166, 189] used a random media material-scale approach.

Moreover, several approaches for the derivation of the homogenized failure surfaces for masonry have been based on FE limit analysis [190, 191, 192, 169, 193, 194]. For example, in [190] a simple material scale model for the homogenized limit analysis of in-plane loaded masonry has been proposed. In particular, a linear optimization problem is derived on the RVE in order to recover the homogenized failure surface of the brickwork, under plane stress conditions. One of the main benefits of these approaches relies on the fact that, once homogenized the masonry properties in terms of elastic moduli and strength domain (so, they are *a priori* defined), they can be directly implemented in structural-scale models (Figure 16), to solve real case studies [195, 196].

(a)   (b)
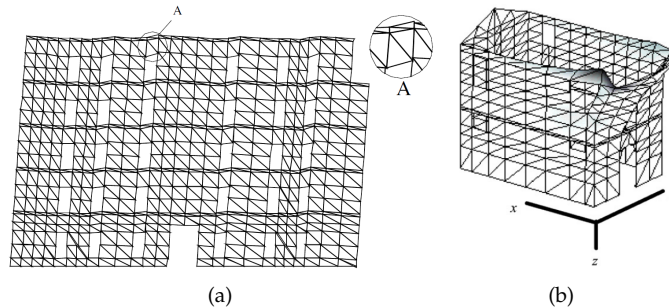
Figure 16: Examples of homogenized FE limit analysis approaches [195, 196].

The same benefit can be observed in RBSM approaches [197, 198, 199, 171], where the linear and nonlinear properties of the springs between rigid elements, which do not represent the actual masonry bond, can be *a priori* homogenized (Figure 17). Once determined the homogenized properties, they can be directly used for structural applications [171].

(a)   (b)
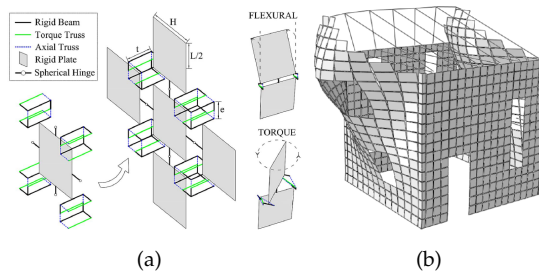
Figure 17: Examples of homogenized RBSM approaches [199, 171].

2.6.2.2 *Step-by-step multi-scale approaches*

Plenty of step-by-step multi-scale approaches can be found in the scientific literature, which may differ in terms of:

- Continuum type adopted in the structural-scale model (Cauchy continuum, Cosserat continuum, etc);

- Type of homogenization procedure (first or second order computational homogenizations, transformation field analysis (TFA), etc);

- Type of modeling of the RVE (i.e. modeling strategy adopted for the material-scale model, e.g. block-based models).

These approaches typically rely on step-by-step and point-by-point transitions between the structural-scale model and the material-scale model, and vice-versa. Multi-scale computational homogenization methods are traditionally implemented within the FEM framework and, so, also called FE^2 approaches. Most of these approaches are based on FE first-order homogenization schemes.

In this context, Cauchy continuum models have been classically adopted in structural-scale models, which are recovered applying periodic homogenization techniques for the simulation of in-plane behavior of masonry structures (Figure 15(b)).

A pioneering computational homogenization method has been proposed by Papa [200], where a unilateral damage model for masonry based on a homogenization procedure has been developed, and by Luciano & Sacco [201, 202], where a damage model for periodic masonry has been developed from a material-scale heterogeneity analysis. Around that time, Gambarotta & Lagomarsino [203] considered an equivalent stratified medium made up of mortar joints and brick units layers, adopting the damage constitutive laws both for the bricks and the mortar joints developed in [58]. Successively, a continuum framework has been developed for modeling of inelastic behavior of structural masonry in [204]. This formulation incorporated the anisotropic material characteristics and addressed both stages of the deformation process, i.e. those associated with homogeneous as well as localized deformation mode. Calderini & Lagormarsino [205] obtained homogenized in-plane constitutive equations, in terms of mean-stress and mean-strain. Different in-plane damage mechanisms have been considered, being the damage process governed by evolution laws based on an energetic approach and on a non-associated Coulomb friction law. Later, Zucchini & Lourenço [206] proposed an improved material-scale model for masonry homogenization in the non-linear domain, incorporating suitably chosen deformation mechanisms coupled with damage and plasticity models.

Sacco [207] proposed a multi-scale procedure based on a micromechanical analysis of the damaging process of the mortar material, assuming linear elastic blocks. In this case, a nonlinear homogenization procedure based on TFA has been proposed, making use of the superposition of the effects and the FE method. An improvement of this approach has been developed by Marfia & Sacco [208],

where an extension of the TFA-based homogenization procedure to the case of nonuniform eigenstrain, as well as the use of nonlinear behavior of blocks in the material-scale model has been implemented.

In first-order computational homogenization schemes, where the formulation relies on the first gradient of the kinematics field, two main limitations could arise.

The first limitation is linked to the principle of separation of scales, which enforces the assumption of uniformity upon the structural-scale fields attributed to each RVE. Indeed, this assumption is not totally effective in structural-scale parts where high deformation gradients are present in the relative RVE.

The second limitation derives from the cohesive (quasi-brittle) response of masonry, i.e. due to the fact that softening effects arise in the stress–strain relationships. Being the characteristic lengths of the structural- and material-scales non-intrinsically accounted for in classical Cauchy continuum models, mesh-sensitivity issues tend to arise when material softening behavior appears. In order to overcome such a drawback, nonlocal approaches, higher-order continuum models, as well as regularization processes can be adopted to guarantee problem objectivity.

A simple way to overcome localization problems consists in following a regularization process, for example, in terms of fracture energy. A classical first order computational homogenization together with a regularization procedure based on the fracture energy of the material-scale model has been proposed in [172]. In this approach, a generalized geometrical characteristic length takes into account the size of the structural-scale element as well as the size of the RVE, ensuring objectivity of the dissipated energy at the structural-scale.

Massart et al. [209] proposed an enhanced multi-scale model using nonlocal implicit gradient isotropic damage models for both the constituents, describing the damage preferential orientations and employing at the macroscopic scale an embedded band model.

A second-order computational homogenization of periodic masonry has been proposed by Bacigalupo & Gambarotta [210, 211]. This computational procedure has been derived assuming an appropriate representation of the material-scale displacement field as the superposition of a local structural-scale displacement field and an unknown material-scale fluctuation field accounting for the effects of the heterogeneities.

Other approaches have been based on the adoption of Cosserat continuum models at the structural-scale. Generally, this allowed to account for a internal length of the material and to overcome localization problems [212]. Salerno & de Felice [213] investigated on the accuracy of various identification schemes for Cauchy and Cosserat continua, showing that micro-polar continuum better reproduces the discrete solutions, in the case of non-periodic deformation states, due to its capability to take scale effects into account. Alternatively, Casolo [214] considered isotropic linear elastic models both for the brick and the mortar and used a computational approach to identify the homogenized elastic tensor of the equivalent Cosserat medium. In addition, Addessi et al. [215] developed a structural-

scale Cosserat continuum, which automatically accounts for the absolute size of the masonry components, derived by a rational homogenization procedure based on TFA. Another homogenization method for the Cosserat continuum has been presented by De Bellis & Addessi [216]. Finally, Addessi & Sacco [217] developed a nonlinear constitutive law for the material-scale model, which includes damage, friction, crushing and unilateral contact effects for the mortar joints. The nonlinear homogenization has been performed employing the TFA technique, properly extended to the structural-scale Cosserat continuum.

Although the multi-scale approaches mentioned earlier where focused on the in-plane response of masonry walls, also the out-of-plane analysis of masonry structures is an interesting issue, especially from a earthquake engineering point of view. To this aim, Mercatoris & Massart [218] presented a multi-scale framework for the failure of periodic quasi-brittle thin planar shells, using a shear-enhanced element with the Reissner- Mindlin description and employing it for the failure of out-of-plane loaded masonry walls. Furthermore, a computational homogenization approach for the analysis of general heterogeneous thick shell structures, with special focus on periodic brick-masonry walls has been proposed in [219].

A very efficient multilevel approach has been developed by Brasile et al. [220, 221]. Although this approach could be considered borderline in a multi-scale framework (being rather a multilevel approach), the strategy proposed in [220, 221] is based on an iterative scheme which uses two different (local and global) masonry models simultaneously. The former is a fine block-based model and describes the nonlinear mechanical response including damage evolution and friction toughness phenomena. The latter is a linearized FE approximation of the previous model, defined at the rough scale of the wall and used to accelerate the iteration. The proposed iterative scheme proved to be efficient and robust for in-plane nonlinear analysis of masonry façades.

2.6.2.3 *Adaptive multi-scale approaches*

A second multi-scale strategy consists in the use of the so-called adaptive multi-scale methods [222, 223, 173, 224] (Figure 15(c)). In these approaches, a first-order homogenized model initially represents the masonry response until a threshold criterion is reached. For instance, such a criterion could be able to account for the onset of damage propagation. After reaching the threshold, the area of interest is replaced by an heterogeneous material-scale description able to represent the high localized deformation without the mesh-dependency of the first-order theory.

2.7 GEOMETRY-BASED MODELS

In geometry-based models, the structure is modeled as a rigid body. The geometry of the structure represents the main (or even the only) input of these modeling strategies. These approaches typically investigate the structural equilibrium

and/or collapse through limit analysis-based solutions (Figure 18), which can be based on either static or kinematic theorems. Although typically based on limit analysis and on the Heyman's rigid no-tension model [39], these approaches have been formulated following several innovative solutions.
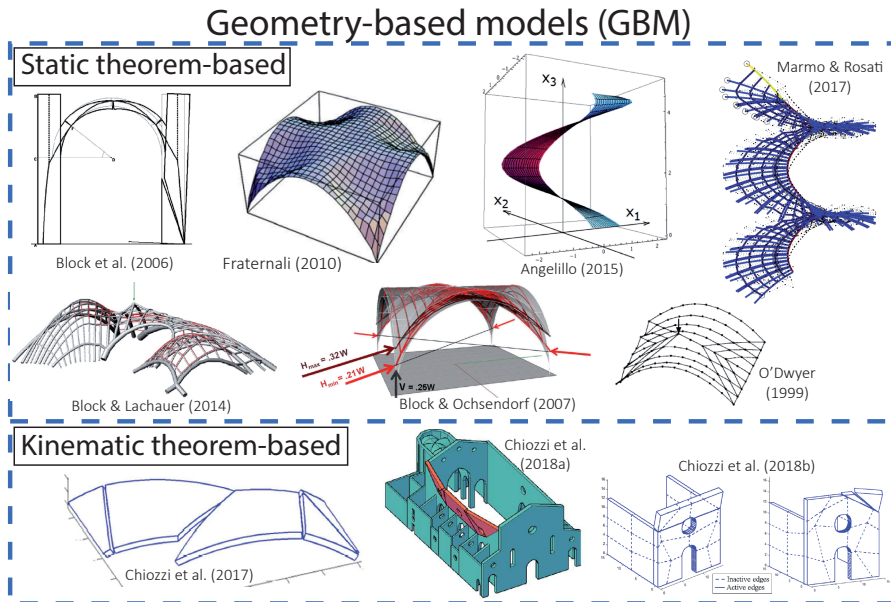
Figure 18: Examples of geometry-based models.

2.7.1 *Static theorem-based approaches*

As shown by Heyman in [39], applications of the static theorem of limit analysis on real masonry structures were possible by simple graphic statics [39, 41]. Particularly, static theorem-based approaches (Figure 18) appear specially suitable for the investigation of the equilibrium states in masonry arches, vaults and domes (i.e. masonry vaulted structures). In general, these approaches can provide the range of possible equilibrium states of the vaulted structure, bounded between two extreme equilibrium conditions.

A first computational development for the equilibrium analysis of masonry vaults has been proposed by O'Dwyer [225], where, after the decomposition of the vault into an optimized system of arches in equilibrium, a procedure for the application of the static theorem to vaults and domes has been presented. Another computational approach, called funicular model, for the assessment of masonry structures based on the well-known analogy between the equilibrium of arches and that of hanging strings has been presented in [226]. Further, a computational tool for the real-time limit analysis of 2D vaulted masonry structures has been presented by Block et al. [227].

An innovative approach for the equilibrium analysis of vaulted masonry structures, called thrust network analysis (TNA), has been proposed by Block & Ochsendorf [228]. The TNA method, based on a duality between geometry and in-plane forces in networks, finds possible funicular solutions under gravitational loading within a defined envelope, generating compression-only vaulted surfaces and networks. In this way, the range of possible equilibrium states of the vault, bounded by a minimum and maximum thrust, can be obtained. A nonlinear extension of TNA has been presented in [229] for the application on Gothic masonry vaults, while in [230] TNA is extended with the use of structural matrix analysis and efficient optimization strategies. Finally, an extension of TNA with joints consideration has been provided in [231].

Another interesting thrust network approach has been developed by Fraternali [232], where the equilibrium problem of unreinforced masonry vaults is investigated through polyhedral stress functions. The masonry vault is conceived as a no-tension membrane carrying a discrete network of compressive singular stresses, through a non-conforming variational approximation of the continuous problem. The geometry of the thrust surface and the associated stress field are determined by means of a predictor–corrector procedure based on polyhedral approximations of the thrust surface and membrane stress potential. Another approach which considers masonry vaulted structures as unilateral membrane has been proposed by Angelillo et al. [233] and by Angelillo [234], where the discrete network of singular stresses has been defined basing on the Airy's stress formulation [235].

Finally, a reformulation of the original version of the TNA [228] by discarding the dual grid and focusing only on the primal grid, thus significantly enhancing the computational performances, has been proposed by Marmo & Rosati [236]. In [236], TNA is also extended by including horizontal forces in the analysis as well as holes or free edges in the vault. A further application on masonry helical staircases has been presented in [237].

In summary, static theorem-based approaches appear particularly attractive for the assessment of the statical safety of masonry vaulted structures. Indeed, if compression-only networks can be found within the boundaries of a vault, then the vault will stand in compression. Moreover, if the solution lie within the middle third of the section, any tension (and, therefore, any hinges) will be present in the section. This easy and powerful concept for understanding the stability and proximity to collapse of such structures has been formerly expressed by Heyman [39]. However, only few of the above-mentioned approaches can account for horizontal actions (such as seismic actions [236]), and no one could account for the interaction with the bearing structures (e.g. bearing walls), whose deformations could induce damage and equilibrium changes in the vaulted structure, as evidenced in [238] for earthquake actions.

2.7.2   *Kinematic theorem-based approaches*

Kinematic theorem-based limit analysis approaches have been widely used in the last decades for the fast and effective assessment of existing masonry buildings. Giuffrè [239] proposed a kinematic limit analysis approach for studying the seismic vulnerability of masonry buildings based on their decomposition into rigid blocks, following failure mechanisms actually observed in existing masonry buildings in Italy. Given the simplicity and effectiveness of the approach proposed by Giuffrè, it has been adopted in the Italian code [240, 24, 241, 242]. Figure 19 shows few examples of collapse mechanisms to be accounted for in the seismic assessment of masonry churches through kinematic limit analysis, from [24]. Kinematic linear and nonlinear (in which the displacement capacity of the structure until collapse is also evaluated) are commonly used in the professional practice for the safety assessment of existing masonry buildings [241].
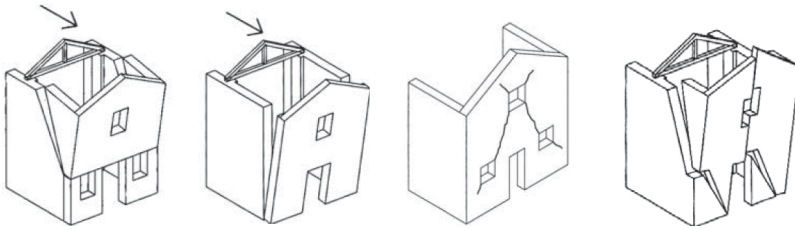
Figure 19: Examples of collapse mechanisms to be accounted for in the seismic assessment of masonry churches through kinematic limit analysis [24].

Basically, in all these cases, the collapse mechanisms to be analyzed are *a priori* determined, on the basis of recurring failure mechanisms actually observed. However, in the context of static theorem-based approaches, the collapse multiplier evaluated in this way is not necessarily the lower one, given, for instance, peculiar features of the geometry of the structure.

To this aim, more advanced computational static theorem-based approaches have been developed to precisely evaluate the collapse multiplier and the collapse mechanism of masonry structures (Figure 18). Milani [243] developed a simple discontinuous upper bound limit analysis approach with sequential linear programming mesh adaptation to analyze the actual failure mechanisms of masonry double curvature structures. Very recently, Chiozzi et al. [244] proposed a genetic algorithm for the limit analysis of masonry vaults based on an upper bound formulation. Given a masonry vault geometry, that can be represented by a non-uniform rational B-spline (NURBS) parametric surface, and a NURBS mesh of the given surface, each element of the mesh is a NURBS surface itself and can be idealized as a rigid body. The initial mesh is adjusted by means of a genetic algorithm in order to enforce that element edges accurately represent the actual failure mechanism. This approach has also been validated for the out-of-plane collapse behavior of masonry walls [245]. Finally, an automatic upper bound adap-

tive limit analysis program for masonry churches, called UB-ALMANAC, has been proposed in [28]. A NURBS mesh is directly prepared within a CAD environment based on the 3D geometrical model of the whole church. Limit analysis is then performed automatically under the desired horizontal loads distribution, using the kinematic theorem of limit analysis with dissipation allowed only along interfaces and progressive adaptation of the mesh through a genetic algorithm, leading to a quick estimation of the first activating failure mechanism and the most vulnerable part of the church.

Although these approaches cannot provide the displacement capacity of a masonry structures, they are very powerful for the fast and effective evaluation of the main vulnerabilities of a masonry building.

2.8   MACROELEMENT MODELS

In macroelement models (Figure 20), the structure is idealized into panel-scale structural components with a phenomenological or mechanical-based nonlinear response. Typically, two main structural components may be identified: piers and spandrels.

These approaches are mainly focused on the analysis of the global seismic response of masonry buildings. Indeed, macroelement models are generally based on the assumption that any activation of local failure mode, mainly associated with the out-of-plane response of masonry walls, is prevented [246]. In this framework, the global seismic response is, therefore, strictly related either to the in-plane capacity of walls or to the load transfer due to the presence of diaphragms. In these approaches, global analyses (incremental-iterative static and/or dynamic) are typically conducted on 3D models, to account for load transfer between the bearing walls due to an horizontal action.

In these modeling approaches, the structural components (piers and spandrels) need to be *a priori* identified, on the basis of damage observations on real buildings. Indeed, earthquake-damage observations showed that cracks and damages are usually concentrated in piers and spandrels. Piers are the vertical resisting elements which carry either vertical or horizontal loads. Conversely, spandrels are the horizontal parts of the structure between two vertically aligned openings, which couple the response of contiguous piers when horizontally loaded. Although the identification of masonry piers and spandrels [247, 248, 249, 250, 251, 252, 253, 254, 255] may result easy and rather trivial in case of masonry façades with regularly distributed openings (e.g. for regular ordinary masonry structures, see Figure 1(a)), it becomes more complex in case of irregularly arranged openings, being substantially impossible for very complex geometries (e.g. for historic monumental masonry structures, see Figure 1(b)).

Macroelement models are the most widely diffused modeling strategies particularly for the seismic assessment of masonry structures, substantially the only one used by practitioners. Indeed, their very limited computational effort (also in
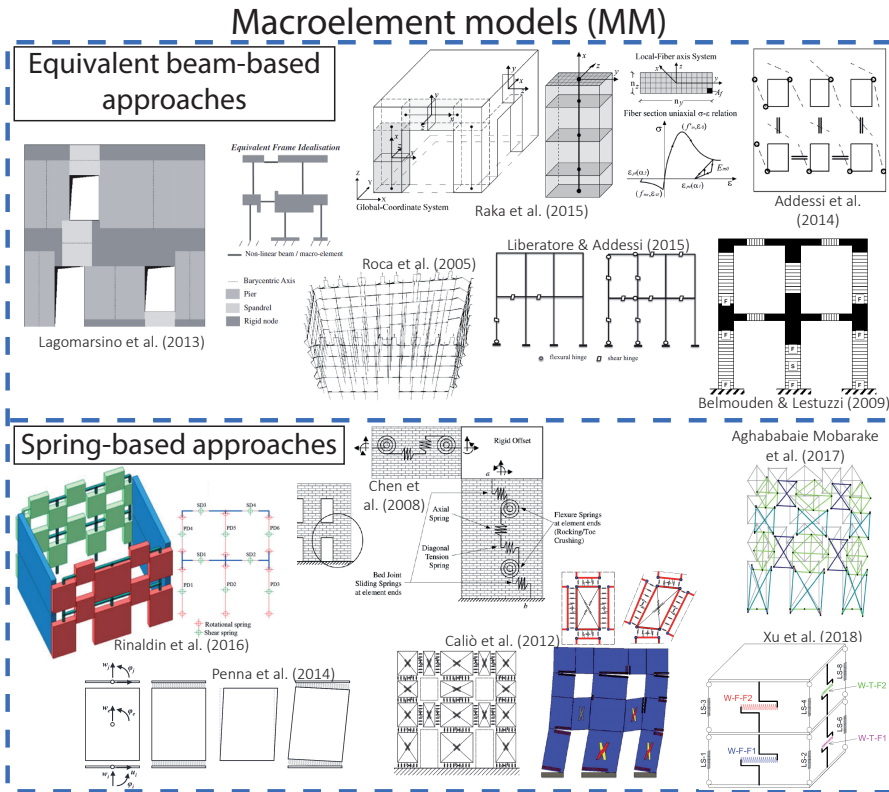
Figure 20: Examples of macroelement models.

case of 3D structures), coupled with the easy and quick definition of the model and mechanical properties, leaded their widespread dissemination.

However, being the macroelement models one of the most simplified approaches to analyze masonry structures (Figure 2), they present, together with their manageable computational effort, also some drawbacks. In particular, they usually assume that any activation of local (out-of-plane) failure mode is prevented. This decoupling assumption, although local failure modes can be separately assessed through kinematic limit analysis (see Section 2.7.2), could lead to conventional estimate of the seismic capacity, as in reality out-of-plane and in-plane damages can simultaneously arise [49]. Additionally, macroelement models cannot meticulously account for structural details, such as the toothing between orthogonal walls. Finally, the *a priori* idealization of the structure in piers and spandrels could lead to the definition of a mechanical system that could be far from the actual one, particularly for the case of very irregular opening layouts. Therefore, a certain level of expertise is anyway requested to the analyst.

Although most of macroelement models are equivalent beam-based [256], several spring-based approaches have also been recently developed. Either equiv-

alent beam-based or spring-based approaches (Figure 20) are reviewed in the following.

2.8.1   *Equivalent beam-based approaches*

The idealization of masonry panels as nonlinear beams represent the most common assumption in the so-called "equivalent frame models". A pioneering equivalent beam-based model has been proposed by Tomaževič [257]. The so-called POR method [257] was based on crude mechanical assumptions, i.e. in-plane damage for horizontally loaded masonry façades was only due to shear forces in the piers, while both spandrels and nodal regions were considered rigid and fully resistant. This simple mechanical description, based on simplified elasto-plastic relationships to describe beam nonlinearity, provided sufficient reliability only in the case of buildings with weak piers and strong spandrels. Successively enhancements were presented in [250], implementing the flexibility and the limited strength of masonry spandrels.

Other more advanced equivalent beam-based models [258, 259, 260, 261, 262, 263, 264] proposed the idealization the masonry structure as an assemblage of pier and spandrel beam elements, linked by rigid links (Figure 20) which represent the nodes between piers and spandrels (i.e. zones in which seismic damage is rarely observable). These models rely on the phenomenological nonlinear elasto-plastic constitutive laws adopted for the beam elements.

Later, Grande et al. [265] proposed a simple beam FE for the nonlinear analysis of masonry structures, based on three parts: two rigid offsets, able to simulate the very stiff behavior of the masonry pier-lintel intersections, and a flexible central part. Furthermore, special shear interfaces were also introduced in the model to account for the shear failure. Another 2-node force-based beam FE has been formulated in [266], where the resultant stress components were exactly interpolated along the beam axis, performing analytical integration (without resorting to a fiber approach). The beam FE was composed of a central flexible element, characterized by a no-tension constitutive relationship, and a lumped nonlinear shear hinge. A further beam FE has been proposed in [267], where both flexural and shear plastic lumped hinges were inserted at the two nodes of the beam, following a classical elastic-plastic constitutive relationship. Finally, Liberatore & Addessi [268] developed a 2-node force-based beam FE consisting of a central linear elastic element, two flexural hinges and a shear link with elastic-perfectly plastic behavior, determined by a predictor–corrector method.

A 2D nonlinear beam with lumped plasticity that assumes a bi-linear relation with cut-off in strength (without hardening) and stiffness decay in the nonlinear phase has been proposed in [251], as implemented in the Tremuri software [269]. Being the latter particularly efficient for monotonic actions, more recently the formulation of this nonlinear beam has been refined by Cattari and Lagomarsino [270] through a piecewise-linear behavior. In particular, such refined constitutive law allows the description of the nonlinear response until very severe damage

levels (from 1 to 5), through progressive strength degradation in correspondence of assigned values of drift.

The model includes also an accurate description of the hysteretic response formulated through a phenomenological approach, to capture the differences among the various possible failure modes (flexural type, shear type or even hybrid) and the different response of piers and spandrels, which revealed particularly efficient in performing nonlinear dynamic analyses [271].

Finally, a very advanced equivalent beam-based macroelement has been recently proposed by Raka et al. [272] for the nonlinear static and dynamic analysis of masonry buildings. The beam formulation considered axial, bending, and shear deformations within the framework of the Timoshenko beam theory. In particular, a phenomenological cyclic law for the beam section, accounting for the shear panel response, has been coupled with a fiber-based model that accounts for the axial and bending responses. Although the model accuracy is strongly dependent on the fiber and shear constitutive laws adopted, the formulation proposed in [272] is general and versatile.

2.8.2 *Spring-based approaches*

Alternatively to the use of equivalent beam elements, several macroelement models have been formulated by implementing nonlinear springs (Figure 20), within a fictitious frame, to approximate the in-plane nonlinear response of masonry walls and façades.

A pioneering application of a spring-based macroelement model has been presented in [273], adapting a model with nonlinear shear springs in series with rotational springs originally developed, in the 1980s, for the in-plane analysis of reinforced concrete walls. The proposed formulation for the analysis of masonry structures included an axial spring, three shear springs, and two rotational springs to simulate the axial, bed joint sliding, diagonal tension, and rocking/toe crushing failure modes experimentally observed on masonry pier tests.

In [274] and [275] a two-node element capable to represent the in-plane cyclic behavior of a whole masonry panels has been proposed aimed to describe both the shear behavior and the coupled axial-flexural one at the two nodes thanks to a bed of spring and two additional internal degree of freedom. In particular, the shear stress-strain cyclic relation has been derived by the macroscopic integration of the continuum model developed in [203]. Some aspects of this original formulation were further improved by Penna et al. [276] including a nonlinear degrading model for rocking damage, which permits to keep into account the effect of limited compressive strength. The latter model has also been implemented in the Tremuri software [251].

An interesting advance in the context of spring-based macroelement models has been developed by Caliò et al. [277], where piers and spandrels where idealized through equivalent discrete elements made of nonlinear springs to simulate the in-plane nonlinear response of masonry walls. The basic panel element is

represented by an articulated quadrilateral constituted by four rigid edges connected by four hinges and two diagonal nonlinear springs. Each side of the panel can interact with other panels by means of a discrete distribution of nonlinear springs. The reliability of the proposed approach has been evaluated by means of nonlinear incremental-iterative static analyses performed on masonry structures. In [277] (and also in [278] for infilled frame structures), such a modeling approach has been used to directly represent piers and spandrels through basic panel elements. Nevertheless, given the versatility of the approach, such a modeling strategy has been used in [163, 164, 279] to simulate the masonry material response (and, so, not only the structural components response), see Section 2.6.1.

Another spring-based approach has been presented in [280], where each structural component has been described through multi-spring nonlinear elements connected by rigid links. In particular, nonlinear springs were placed at the two ends of the piers and spandrels for describing the flexural behavior and in the middle for representing the response in shear. The other parts were constituted of rigid links. Specific hysteretic rules for the degradation of stiffness and strength were also used for modeling the structural response under cyclic loading.

Aghababaie Mobarake et al. [281] proposed a basic panel element made-up of six sub-elements including upper and lower rigid beams and right, left (bilateral) and X-bracing nonlinear trusses, with four nonlinear zero-length sub-elements between the upper and lower beams and truss sub-elements. Each pier, spandrel and node between them is idealized by using a single proposed basic panel element. The approach proposed in [281] provided a rather simple and efficient platform for nonlinear static and dynamic analyses by considering the in-plane behavior of masonry panels.

Finally, a very recent and simplified solution has been presented by Xu et al. [282], where the masonry façade is considered as an integral unit, rather than composed of independent piers and spandrels. According to the strategy proposed in [282], the masonry façade is modeled by means of two vertical springs and a horizontal nonlinear spring that governs the wall shear response. The hysteretic behavior is governed by a group of control parameters, that depend on the distribution of openings and/or confining elements as well as on the dimensions, material properties and boundary conditions of the façade. The extremely simplified modeling strategy proposed in [282] could represent a complementary approach for the analysis of masonry structures subjected to horizontal cyclic loadings.

2.9   CONCLUSIONS

In this chapter, a comprehensive review of the existing modeling strategies for masonry structures, as well as a classification of these strategies, has been presented. The classification of modeling strategies for masonry structures consisted of four categories (Figure 2): block-based models, continuum models, geometry-based models, and macroelement models. Although a fully coherent collocation

of all the modeling approaches was substantially impossible due to the peculiar features of each solution proposed, this classification attempted to put in order the wide scientific production on this field.

From the comprehensive review of modeling strategies for masonry structures carried out in this chapter, the following conclusions can be drawn:

- Block-based models could represent the most accurate strategy to analyze the mechanical response of masonry structures. Several applications showed the potentialities of BBM to investigate the structural behavior of large-scale structures (specifically for contact-based approaches), with irregular and complex geometries as well. However, although the area of application of BBM appears theoretically large, their high computational demand strictly limits their employment to very important case studies and academic works. Anyway, they could be adopted to gain in-depth insights on specific features of the mechanics of masonry structures, and to provide reference solutions for more simplified approaches (e.g. MM).

- Continuum models represent widely used solutions for the structural analysis of masonry buildings. Concerning direct approaches, isotropic smeared crack and plastic-damage constitutive laws have been widely used for the structural assessment of historic monumental structures. Indeed, these approaches often represent the only suitable strategy to deal with such complex structures. However, the results obtained should be carefully interpreted, as they could sensibly overestimate, for example, the ultimate displacement capacity. Although no-tension continuum approaches seem to fail in a proper mechanical analysis of masonry structures, other simplified approaches, such as homogenized FE limit analysis and homogenized discrete approaches, appear particularly suitable for the structural assessment of full-scale masonry structures, even though the difficulties in the homogenization processes. Concerning multi-scale approaches, although very smart solutions have been proposed, they present some limitations. In particular, most of them have been tested only on 2D panel-scale masonry structures, with very few exceptions (see for example [220, 221]). Eventually, the so called FE^2 methods appears computational demanding. Indeed, although theoretically more efficient than BBM, the fact that their are usually implemented in homemade codes sensibly limits their efficiency and optimization. So far, no example of 3D computational homogenization method exists, being all the approaches developed in the last decades limited to 2D problems. Furthermore, being these approaches based on the mechanical response of the periodic RVE, the possibility of accurately represent specific structural details appears rather limited.

- Geometry-based models, although typically based on limit analysis solutions, can provide very useful outcomes. On the one hand, static theorem-based computational approaches represent effective solutions (substantially the only ones) for the investigation of the equilibrium states (and, there-

fore, the safety) in masonry vaulted structures. On the other hand, static theorem-based computational approaches appear especially suitable to predict the collapse mechanism (and the collapse multiplier) in complex masonry structures. These results, although non-comprehensive, represent a fundamental information in the mechanical analysis of masonry structures.

- Macroelement models mostly represent the only modeling strategy manageable by practitioners. Nevertheless, their reliability should be further improved by accounting for structural details (e.g. toothing between orthogonal walls) and the interaction between out-of-plane and in-plane damages. Anyway, MM are limited to the seismic assessment of ordinary masonry structures.

In summary, although significant advances have been made in the context of modeling strategies for masonry structures, each computational solution shows specific limitations and a restricted area of application. Therefore, the choice of the most suitable modeling strategy should be formulated depending on the features and the complexity of the structure under investigation, the output required, the data available, and the expertise level.

Finally, the use of 3D models, which can represent the 3D features of a masonry structure, appears particularly indicated for the seismic assessment of masonry buildings to account for the geometric irregularities and the structural details which usually characterize ordinary and monumental buildings.

MESH GENERATION PROCEDURES FOR HISTORIC STRUCTURES

In this chapter, two mesh generation procedures are proposed to transform 3D point clouds into 3D solid FE models of historic monumental buildings. The first procedure, called CLOUD2FEM, consists in the slicing and subsequent stacking of the geometry. The second procedure, called watertight meshing, considers the structure as a watertight surface and eventually fills the volume.

3.1 INTRODUCTION

Historic structures are characterized by an enormous complexity in terms of geometry, material properties, loads and boundary conditions (see Section 2.2). In most cases, direct continuum-based methods have been used to model these structures [46], see Section 2.6.

However, the numerical modeling of historic monumental buildings is still a challenging task for contemporary civil engineers. One of the main reasons for this is that, due to the complex geometry of such historic structures, it is unavoidable to resort to a fully 3D modeling that is often performed using the computer-aided design (CAD).

In general, CAD-based modeling is an expensive and complex process, often manually carried out by the user. This inevitably leads to the introduction of geometric simplifications (*defeaturing*) or interpretations.

In order to reduce the time that the user has to spend to reproduce the complex geometry of these structures, a precious support can be supplied by automatic advanced survey techniques such as terrestrial laser scanner (TLS) [283] and terrestrial photogrammetry [284], which can generate 3D detailed point clouds in a rapid way. Although the TLS is still today an expensive survey technique, in comparison with closed range photogrammetry systems [285], its usage is showing a high growth coupled with a continuous technological development. In particular, in the field of architectural heritage several TLS and photogrammetric applications have been performed: from simple documentation [286] to monitoring the condition of historic buildings, and also in order to support restoration works or structural checks [287]. An example is reported in [288], where a detailed geometric survey of a Portuguese castle is conducted by means of the laser scanning

technique, allowing for a precise characterization of dimensions and disposition of the masonry blocks used for the FE discretization. Another example is shown in [289], where the significant deformation of a Spanish church has been surveyed by means of TLS: the 3D structural model has been created in a CAD environment using the results of the laser scanner survey. Thereby, the current deformation of the church has been directly considered in the structural analyses.

Several studies tried to transform 3D points clouds in FE models [290], but in most cases the output was partial or dramatically simplified. For instance, in [291] an example of FE analysis of a historic theater is performed using laser scanning data limited to the inner surfaces of the building. Massive structures, such as masonry bridges can also be investigated by summing the laser scanner survey information to those obtained by ground penetrating radar and as a result generate a fine picture of the external and internal features [292]. Here, the cloud simplification lies on the sampling of some points that are useful to reconstruct the geometry by means of regular shapes. Other interesting contributions are proposed in [293, 294], where an attempt to precisely capture the geometry of the building through the automatic reconstruction of its boundary is presented. Moreover, in [295] a point-based voxelization method to automatically transform point cloud data into solid models for computational modeling is developed. The method constructs a triangular irregular network (TIN) mesh by means of a voxel grid bounding the cloud region. The resulting model captures the 3D features of the survey, but does not capture the whole structure, since it is designed for façades only.

Furthermore, a method for the direct transfer of high accuracy TLS-based 3D models to a FE structural analysis software, subsequently employed to interpret and verify structural health of the historic building, has been recently presented in [296]. Additionally, Fortunato et al. [145] developed a CAD-based model of a historic structure starting from very dense outlines obtained by point cloud slices. Subsequently, the analysis has been developed in a nonlinear framework, in which the behavior of the structure is investigated under seismic loads.

One of the most frequent problems when dealing with complex historic buildings is the impossibility to generate "watertight surfaces" from the point cloud of the surveyed object. Thereby, it is not possible to directly transform the TIN mesh surfaces into solid geometry and consequently into a FE mesh, as done, for instance, for human organs and agricultural objects in [297] and for Michelangelo's David in [298].

In this chapter, two mesh generation procedures to transform 3D point clouds into 3D solid FE models of historic monumental buildings are proposed. Firstly, a semi-automatic procedure, called CLOUD2FEM, to transform 3D point clouds of complex objects into a 3D FE model is presented in Section 3.2. The procedure is then applied on a real case study (a medieval masonry fortress damaged by an earthquake) and validated. Secondly, a simplified and rapid procedure for the automatic transformation of point clouds (surveyed on historic structures) to 3D FE meshes, passing from the concept of watertight mesh, is proposed in Section

3.3 through the application on a medieval ruined masonry tower. The accuracy of the geometry of the mesh generated appears suitable for structural purposes.

3.2 CLOUD2FEM

In this section, a semi-automatic procedure to transform 3D point clouds of complex objects to 3D FE models (CLOUD2FEM) is presented and validated. In summary, the surveyed point cloud is firstly processed by standard operations, i.e. reduction of points' density and generation of the TIN mesh. Then, the TIN mesh is broken down in 2D sub-domains by slicing it perpendicularly to the vertical direction with a certain step. The boundary polygons, which enclose the outer and inner points of each slice, are computed by means of concave hull algorithms, generating filled regions. Afterwards, each slice is transformed into a digital image composed of pixel with a certain resolution. As the digitalization is performed of a fixed region of space, the slices are stackable and the subsequent stacking operation generates voxels. Finally, each voxel is converted into an 8-node hexahedral FE and, hence, the structure is completely discretized as a unique continuum composed by evenly spaced hexahedral elements.

3.2.1 *Proposed procedure*

Given an accurate description of a complex geometry, the CLOUD2FEM procedure allows the reconstruction of the original 3D geometry by means of a particular discretization.

In order to apply the procedure, some preliminary (common) operations may be required to improve the reconstruction quality and to reduce the error propagation due to the registration of large and complex point clouds. The point clouds can rarely be directly transformed into a complete 3D model without user intervention: the complex shape of the geometry, the irregularly distributed spatial points and the missing faces are critical aspects that usually prevent the automation of the process.

3.2.1.1 *CLOUD2FEM conceptual work-flow*

The CLOUD2FEM procedure is synthesized in the flowchart of Figure 21. The input data consists of generic point clouds, merged into a single point data file for the whole building surveyed. The work-flow begins with a 3D analysis divided into sequential steps. Most of the operations here described are completely automated (highlighted in green in the flowchart) using different algorithms. At the end of this first part, the building is described with a dataset of slices, each one containing bi-dimensional points. These are subsequently analyzed individually in a 2D environment , and this phase includes some semi-automatic or manual analysis (highlighted in orange in the flowchart). All data are georeferenced using a unique local or global reference system. Therefore, final datasets are stackable.

Each pixel grid, obtained from the corresponding slice, contributes to the creation of the voxel model.
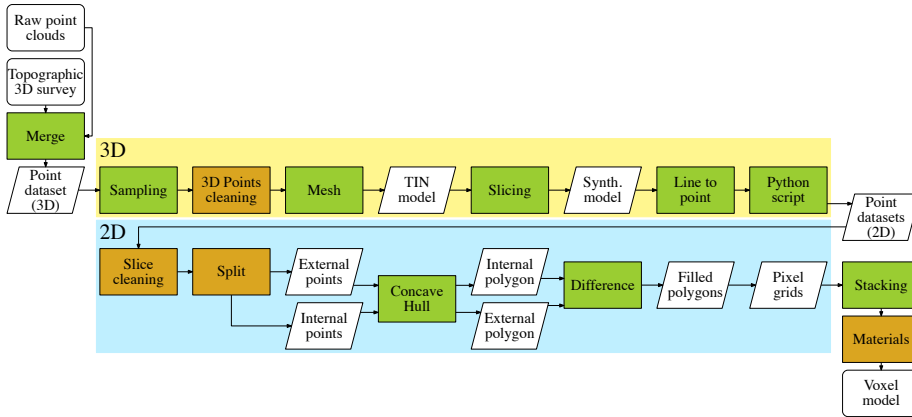
Figure 21: Flowchart for the CLOUD2FEM procedure: completely automated procedures (green) and semi-automated or manual procedures (orange).

3.2.1.2 *Slice generation from the point cloud*

Point cloud slicing is a common procedure to extract sections and details from large point cloud databases. CAD-based procedures are often used to transform sliced points into line-based models using automated procedures based on segmentation or using a manual extraction of profiles, e.g. see [283] for the processing of building façades. Upon this condition, the point cloud is conceived as a stacking layer sequence of planar points. In Figure 22, a simple geometry is illustrated and referenced to the Cartesian system, where the axis Z is the principal direction of the stacking sequence (Figure 22(c)). The structure is subdivided by subsequent section planes Π_j^z, each one characterized by an incremental z-coordinate of Δz. Then, all of the points within the range $[z_j - \Delta z/2, z_j + \Delta z/2]$ are projected to the mid-plane Π_j^z (see Figure 22(d)).

Therefore, it is possible to reduce a 3D problem to a 2D problem. By means of a parsing algorithm, which walks through the dataset and separates points belonging to each slice, it is possible to generate a number of 2D layers describing the whole structure when they are stacked together. This model is composed from slices containing only points with variable (x, y) coordinates and a constant z_j coordinate. The distance between two adjacent slices has to be chosen according to the desired final resolution of the FE model.

It is possible to operate on each slice independently with effective techniques with a linear work-flow using software packages for the management of spatially-referenced data, e.g. geographic information systems (GIS). The pattern of points located on the Π_j^z plane is generated from the points belonging to each section
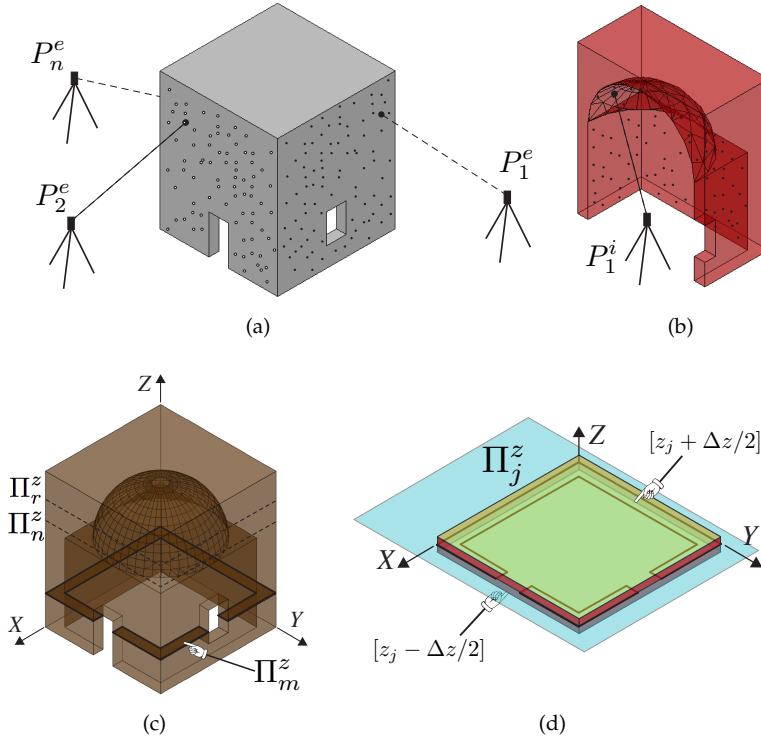
Figure 22: Visualization of the stacking layer sequence concept: (a) point cloud survey of external façades, (b) point cloud survey of internal surfaces, (c) illustration of the m-th slice, and (d) Π_j^z layer.

of Δz thickness. A sequence of points at a constant interval and high density is placed along the lines contained in each slice. A boundary polygon that encloses the points can be computed using a concave or convex hull algorithm [299].

In the case of a building, the slices contain two principal profiles. The first is made by connecting the points that belong to the external point cloud (consider, for instance, the survey of the external façade of a building, see Figure 22(a)) The second is made by connecting the points that belong to the internal point cloud (consider, for instance, the survey of the internal rooms of a building, see Figure 22(b)).

The first result in a filled geometry (external) which envelops the whole building. This might also be composed of several islands that represent the outside face of the building walls.

Similarly, the second produces a boundary polygon (internal) that is computed selecting only the points acquired in the internal rooms. It is important to emphasize that also this polygon, in the same way as the external one, is created using a concave hull algorithm [300], enveloping the point selection from the outside.

Additionally, this polygon may also be composed of several islands representing the various rooms of the building.

Once the two polygons with filled geometry are created, one external and one internal, a filled polygon is obtained by subtracting the second from the first for each slice of the building, describing the entire structure.

3.2.1.3 *FE model generation from slices*

Once created the slices, a discretization procedure is introduced to set up the desired FE model. Firstly, discretization is performed on the 2D sections, and, then, they are used to build the 3D discretized model. By using the computed tomography (CT) approach [301], each slice is idealized as a digital image, with a certain resolution, composed of picture elements (pixels), so the stacking of these slices generates the volume elements (voxels). This procedure allows the reconstruction of the original 3D geometry by stacking all of the slices, obtaining a complete volumetric representation of the object by acquiring a contiguous set of slices.

The original polygon is then described by a $N \times M$ pixel matrix corresponding to a grid of pixels with a particular resolution. With reference to Figures 22(c) and 23, the pixel value will be, for instance in an 8-bit grayscale, 255 for the filled area and zero for empty spaces. This transformation is performed automatically for each slice with a fixed region preserving the output resolution. Therefore, all of the grids are aligned, and the voxel model is generated by stacking them in the original order, following their coordinates. It is worth noting that the voxels are not only placed along the internal and external profiles as proposed by other techniques [295, 293, 294].

(a)   (b)   (c)
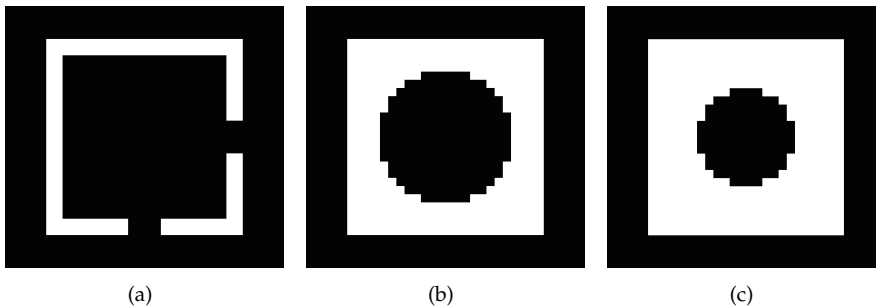
Figure 23: Two dimensional images obtained by slicing the structure illustrated in Figure 22: m, n and r represent three generic slices located at the z_m, z_n and z_r coordinates respectively. (a) Π_m^z, (b) Π_n^z, and (c) Π_r^z.

Voxels, as represented in Figure 24(a), define a particular grid structure that possesses the following features:

- Π_j^z planes are chosen with the normal along Z that is the building construction direction: features, layers and openings are conceived by a stacking of elements (i.e. bricks) along the Z direction;

- Δz is chosen according to the building complexity along the Z direction;

- Δx and Δy are chosen according to the in-plane complexity and are totally independent of Δz;

- The stacking procedure is here proposed as a linear stacking of contiguous slices, but can be, in general, considered as interpolated along the Z direction (i.e. considering more slices at a time);

- The resulting discretized volume does not need any particular further adjustment "to fill" the structure.

(a)   (b)
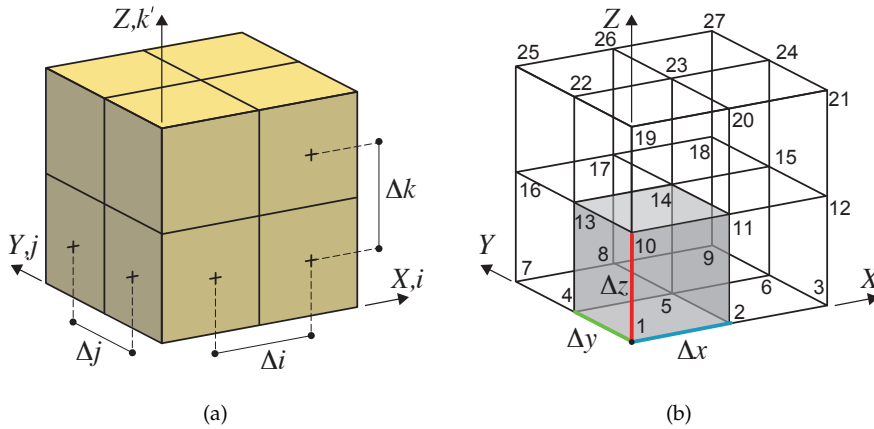
Figure 24: Voxel representation and FE transformation: {i, j, k} and {X, Y, Z} are the indexes of the voxels' 3D matrix and the global coordinates of the structure, respectively. The coordinate k' means $k' = R - k$, where R is the third size (along Z) of the voxels' 3D matrix ($N \times M \times R$). (a) Voxel indexes, and (b) hexahedral elements.

The resulting dataset is simple and easy to use with the FE technique: each voxel is automatically transformed into an 8-node hexahedral FE. By using a common space-partitioning data structure (KD-TREE), the scheme represented in Figure 24(a) is transformed into a FE structure (Figure 24(b)) by simply generating the connectivity structure of each element.

In theory, this operation can be performed for each voxel value (in this case, zero or 255) or only for a certain value of the voxel, i.e. only those with a value equal to 255. Therefore, it is possible to easily describe a database of multiple properties of objects by setting multiple values for the voxel. For instance, if a particular voxel value corresponding to a particular material is assumed, it is

therefore possible to describe, in addition to the geometry, also multiple mechanical properties.

With these features, the resulting discretized geometry already contains all of the information to be used within the FE model, including the mechanical properties associated with the material features. The proposed method guarantees, with a simple procedure, the construction of a fine discretized geometry and, then, an automatic generation of a reliable FE solid model. Dealing directly with the definition of FE nodal coordinates and with the FE connectivity matrix, the proposed method is generally customized to work with any commercial FE software. This rational organization is certainly a key novelty introduced by the method.

Figure 25 illustrates the FE mesh obtained by applying the CLOUD2FEM procedure to the structure represented in Figure 22. As can be noticed, as long as the surface is regular and parallel to the axis directions, the resulting mesh precisely matches the original geometry (Figure 25(a)), but when the surface is irregular (curved) or not planar to an axis direction, the resulting FE mesh is a jagged representation of the original geometry (Figure 25(b)). Despite this fact, it is always possible to improve the mesh accuracy using a smoothing method to reduce the faceting, see Figure 25(c). Concisely, these methods are linear low-pass filters that remove high curvatures variations (jag) and have to be chosen in order to not produce shrinkage [302].

(a)   (b)   (c)
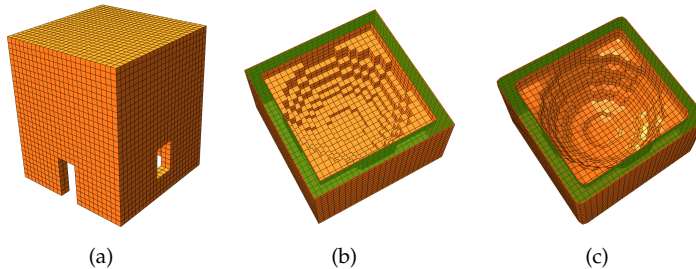
Figure 25: FE mesh obtained by applying the procedure to the structure represented in Figure 22. (a) External restitution, (b) internal restitution, and (c) smoothed internal restitution.

3.2.2 *Application to a medieval castle: The San Felice sul Panaro fortress, Italy*

In order to show the capabilities of the proposed mesh generation procedure (CLOUD2FEM), an application to a real case study, i.e. the San Felice sul Panaro fortress, is presented and discussed. Particularly, a brief description of the case study is given in the following.

The San Felice sul Panaro fortress (Figure 26(a)) is a monumental historic masonry building located near the city of Modena, in San Felice sul Panaro (Italy). The monument is a typical example of fortified medieval architecture, composed by a massive quadrilateral plan with an inner yard and five towers (Figure 26(b)).

Four towers are located at the corners, while another one is placed on the north fortress façade. The S-E tower is called *Mastio* because of its dominant dimensions compared to the rest of the building (Figure 26(a)).

(a)   (b)
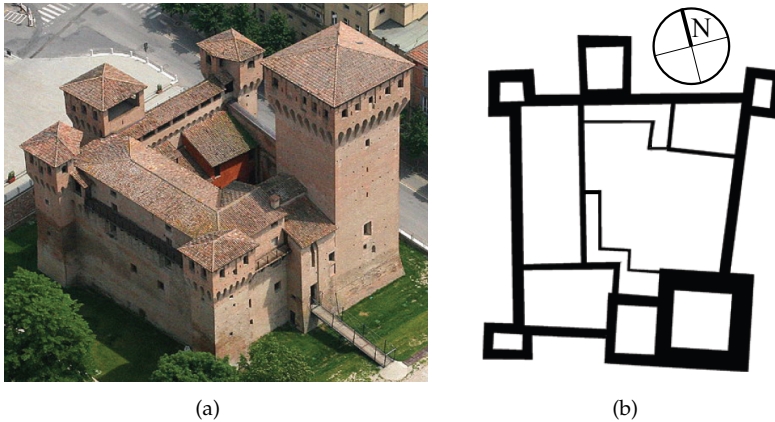
Figure 26: San Felice sul Panaro fortress: (a) photo and (b) schematic plan.

The San Felice sul Panaro fortress exhibited a complex historical evolution during the centuries. The main construction stages of the fortress historical evolution can be summarized as follows:

– lower parts of Mastio and North Tower and curtain walls: XIV century;

– upper parts of Mastio and North Tower and other towers: XV century;

– roofings and internal structures: from XVI to XVIII centuries;

– modern interventions (such as concrete curbs on minor towers and Mastio's trunk reinforcement): XX century.

3.2.2.1 *Emilia earthquake damage*

In 2012, the San Felice sul Panaro fortress was hit by the Emilia earthquake with two magnitude peaks of $M_W = 5.86$ (May 20th) and $M_W = 5.66$ (May 29th) [303]. The epicenters of the first (May 20th) and the second (May 29th) main shocks were located at about ten and five kilometers far from the fortress, respectively. After such a seismic sequence, the collapse of the four minor towers' roofs was observed and cracks of different relevance appeared on all the fortress structural elements extensively, see Figure 27. In [304], an accurate description of the monument damage mechanisms is reported.

(a)

(b)

Figure 27: San Felice sul Panaro fortress after Emilia earthquake (2012): (a) South front, and (b) North front.

After first-aid structural interventions aimed to preserve the building were performed, the municipality of San Felice sul Panaro commissioned a fine survey of all the external and internal surfaces of the damaged building by using TLS (Figure 28) in order to acquire a snapshot of the post-earthquake condition of the structure and to measure its complex geometry.

The survey was performed by ABACUS s.a.s., using a FARO Focus 3D X 330 laser scanner and a total station Trimble S6. The survey has become more complex after the earthquake, because of the presence of debris in some interior rooms. Numerous targets were then placed, for precise identification of correlation points between scans, for both the exterior and the interior of the fortress.

A closed polygonal topographic network was prepared, to detect the position of each target using the total station. This network has been properly calculated and compensated. Subsequently, 163 point clouds have been acquired by different scanning positions using the laser scanner. These scans were aligned to the topographic network through correlation with the reference targets, resulting in millimetric precision. Finally, the aforementioned clouds were merged into a unique cloud containing more than 40 million points (Figure 28(a)), which as been then used to generate a global TIN mesh (Figure 28(b)).

(a)   (b)
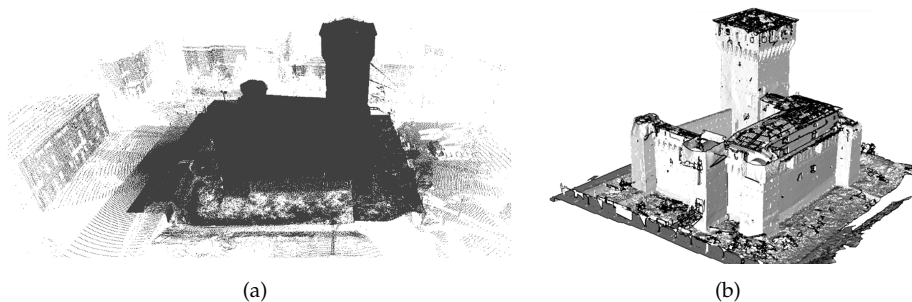
Figure 28: TLS survey: (a) point cloud, and (b) TIN mesh.

3.2.3 *Generation and validation of the Mastio FE model*

To preliminary assess the capability of the CLOUD2FEM procedure, attention is initially focused on the generation and validation of the Mastio FE model [29].

As shown in Figure 29, the tower is composed of six layers of different kinds: cross-vaults, wood slabs with old and remodeled structures. Each level is then characterized by irregular dimensions and thickness. By inspecting the south front illustrated in Figure 29(a), it is shown how the seismic shock hit and damaged the tower by producing a lateral and torsional oscillation and residual displacements on the actual configuration. Openings are placed irregularly on

the structure and also have irregular shapes and sections (Figure 29(c) and Figure 29(d)). Summing up, the structure is anything but regular.

(a)	(b)	(c)	(d)
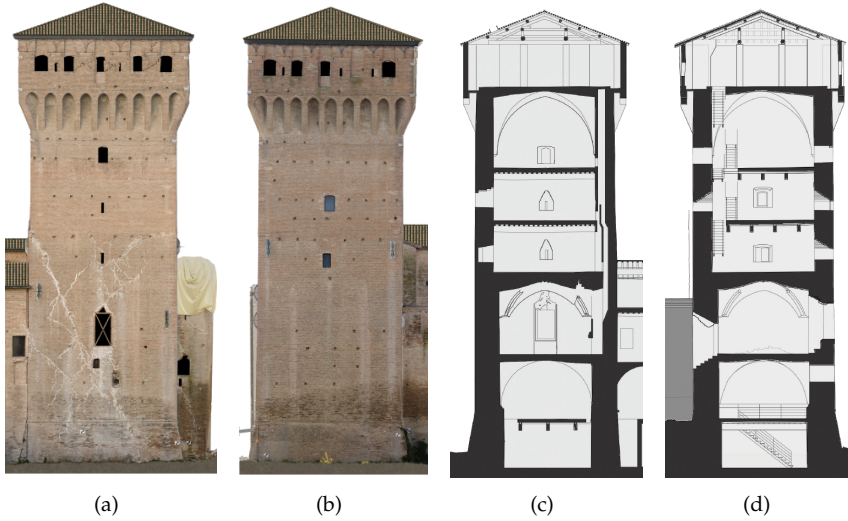
Figure 29: Mastio of the San Felice sul Panaro fortress: (a) South front, (b) east front, (c) E-W section, and (d) S-N section.

3.2.3.1 *Generation of the Mastio FE model*

In order to simplify this initial point cloud, a new dataset has been generated with a point sampling obtained through a Poisson-disk distribution (sampling procedure in Figure 21). The result was a new point cloud reduced to 3.2 million points, with a regular spatial sampling of 0.05 m, suitable for further analysis.

The next operation was to clean the point cloud (3D point cleaning in Figure 21), mainly removing all neighbor points not belonging to the building of interest. In fact, other surrounding buildings were acquired during the initial scan, in order to align all of the different point clouds. These buildings were removed from the point cloud, reducing it further down to 1.9 million points.

From the point cloud, a subset of 0.8 million points related to the Mastio has been extracted and analyzed, see Figure 30(a). As represented in Figure 30(b), the survey finely describes every single feature of the structure. The point cloud has a very heterogeneous density, primarily related to the distance between the single scan positions and the object acquired. Figure 31(a) represents the points that are located within the range $[z_j - \Delta z/2, z_j + \Delta z/2]$, at a given z_j coordinate. In Figure 31(a), the lower left corner is magnified to show the original point cloud density.

The special conditions of the building must be considered. Regarding the exterior part of the model, there were problems with the roofs that were partially
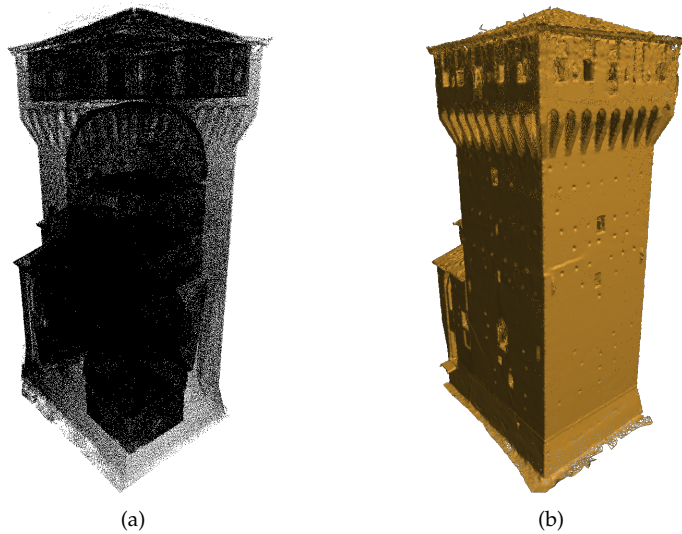
Figure 30: 3D models for Mastio tower: (a) points, and (b) TIN mesh.

collapsed, and these were covered with large plastic tarpaulins in order to avoid water infiltration. Furthermore, in the surroundings and in the internal courtyard of the building, there were piles of rubble and debris. All of these elements hide the actual geometry of the building from the laser scanner point of view. In fact, in the 3D point cloud, these elements are acquired and then intrinsically fused with the proper model of the building, and there is no automatic procedure to perform a full cleaning in advance.

The point cloud is a 3D model. However, it is necessary to build a model that consists of continuous surfaces in order to define the exterior and interior shell of the structure (mesh and polygonal model in Figure 21), through TIN
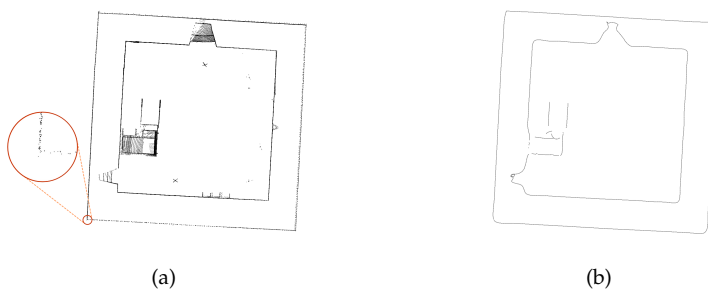
Figure 31: First part of the slicing work-flow (3D data): the magnified portion shows the uneven density of the raw data. (a) Points within the Δz increment, and (b) final processed slice of points.

mesh or NURBS surfaces. After having obtained the shell of the structure, it is possible to define the volume of the structure to be filled with voxels following the other steps, which will be listed later. In order to create a volume model, the structure would need to be filled with more voxels, having to solve non-trivial problems for areas in shadow with respect to scan positions. In correspondence to these positions, the data are missing. Therefore, holes remain in the model they cannot be filled. This issue is overcame by analyzing the model slice by slice. In this study, the polygonal model has been realized using the TIN mesh (Figure 30(b)). Considering the points (x, y, z) in space, the conjunction between them is realized with lines forming adjacent triangles in order to represent the object with a continuous surface.

The mesh consists of a total of 4.8 million triangles. This model describes all of the surfaces surveyed with the laser scanner, but it cannot be considered a correct closed model from the topological point of view, consider for instance the roof surface in Figure 30.

During the laser scanner acquisition, there was furniture in different rooms, as well as rubble and debris in some areas. Each disturbing element increases the complexity of the building, as illustrated in Figure 31.

By inspecting every single slice in a GIS software, it appears very easy to find and properly clean every slice from points that do not belong to the building, even though they have been inevitably acquired during the scanning. However, by creating a concave hull that envelopes the internal points from the outside, the presence of internal debris or any furniture located inside the room is irrelevant, because each new shape is based on the peripheral points. This operation is fundamental to obtain a closed shape for each slice, directly using the geometry provided from the previous step, without any smoothing.

This part of the procedure is semi-automatic. Some manual intervention appears essential at this stage for an accurate separation between internal points and external points. This is especially true with data from complex buildings, such as the one analyzed. Anyway, the proposed work-flow aims at minimizing manual intervention in terms of time in order to maximize the efficiency of the procedure itself.

Based on the Mastio geometry properties, a fine description of the tower is obtained by slicing the tower height with a $\Delta z = 0.2$ m, which corresponds, more or less, to three layers of bricks and two layers of mortar. On the other hand, the resolution of each slice is set to have $\Delta x = \Delta y = 0.115$ m, which corresponds to the short dimension of the brick (half-brick).

The resulting stacking sequence is composed of 153 horizontal slices, where each one is represented by a $N \times M$ grid of 116×107 pixels. Figures 31 and 32 illustrate the i-slice representative of a generic section.

The structure has been entirely described by using five different materials, whose mechanical properties are set according to [242], see Table 1. Figure 33 shows the representation of a generic section where the user can visualize and set the material properties based on his knowledge, which might have been acquired

(a) (b) (c)
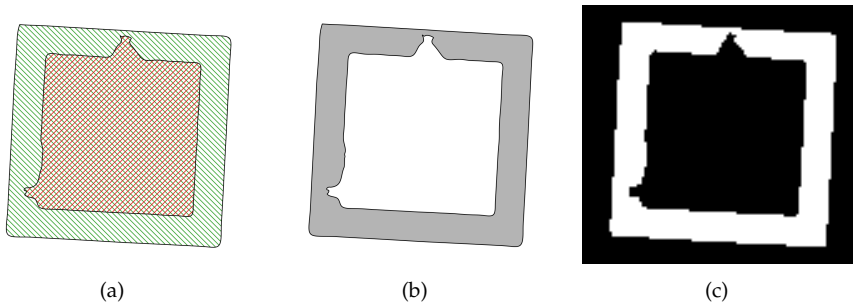
Figure 32: Second part of the slicing work-flow (2D data). (a) Internal (red), external (green), (b) filled slice, (c) bitmap: 116×107 pixels.

Table 1: Mechanical characterization of the materials by color.

Material	Color (0–255)	Elastic Modulus (MPa)	Poisson's Coefficient (-)	Density (kg/m^3)
Masonry	255	1500	0.20	1800
Reinf. Masonry	150	1900	0.20	1800
Terrain	125	–	–	–
Timber	100	8000	0.37	415
Air	0	–	–	–

from direct inspection or available images. The resulting 3D matrix is visualized by plotting its pattern by means of RGB colors in Figure 34.

Voxels are plotted by transforming row and column indexes to a unitary coordinate. Then, the generation of the 8-node hexahedral element-based FE model is done according to the instructions given in Figure 24 by associating their coordinates respectively to the Δx, Δy, Δz volume. It is important to notice that the 3D matrix contains volumes for any arbitrary index (i, j, k) combination, i.e. values are also assigned to empty spaces (surrounding air, terrain, etc). The user can choose, according to the FE model purposes, to filter out some of the values. For instance, here, the voxels corresponding to the air and terrain properties are excluded by not being processed during the mesh generation procedure. The final mesh is then characterized by 745,668 nodes and 661,105 elements, see Figure 35(a).

3.2.3.2 *Structural analyses and validation*

The FE model generated through the proposed procedure is used within a structural analysis framework. In order to assess the accuracy of the proposed model, a linear natural frequency analysis (eigenvalue analysis) is performed.
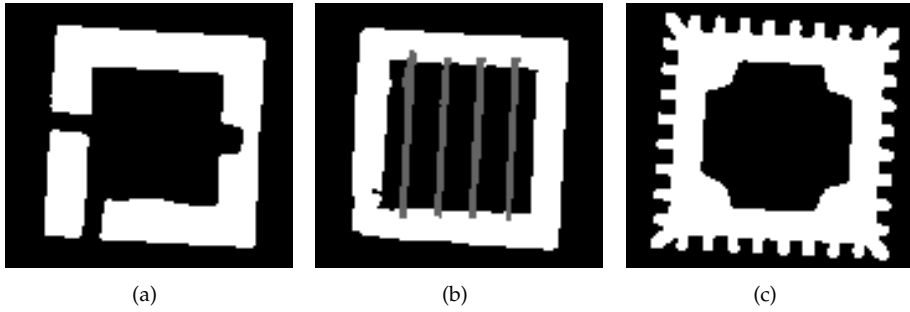
Figure 33: Examples of bitmap slices: (a) 42nd slice, (b) 84th slice, and (c) 128th slice.
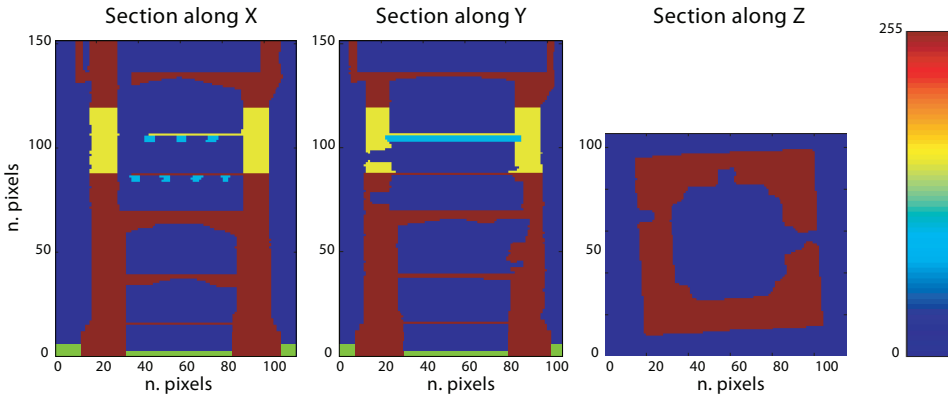
Figure 34: Visualization of the 3D material matrix: voxels possess unitary dimension. Five materials (colors) are used to represent the structure according to the mechanical characterization given in Table 1.

In particular, a comparison is performed using a very accurate FE model obtained through a precise CAD approach based on the same laser scanner dataset, see Figure 35(b). The CAD-based model consists of tetrahedral four-node elements, counting 54,340 nodes and 215,938 elements.

The linear natural frequency analysis is a common tool for the characterization of the structural dynamic behavior and also used for historic masonry structures. The natural frequencies and the natural modal shapes of vibration, which are the characteristics of the structure, are given by the solution of the eigenvalue problem $\mathbf{K}\Phi = \lambda\mathbf{M}\Phi$, where $\mathbf{M}$ is the mass matrix, $\mathbf{K}$ is the stiffness matrix, λ is an eigenvalue and Φ is its relative natural modal shape of vibration (eigenvector). The eigenvalue problem does not fix the absolute amplitude of the vector Φ, but only its shape.

It is evident that both $\mathbf{M}$ and $\mathbf{K}$ are highly conditioned by the correct representation of the geometry and by the accurate mass and stiffness distribution along
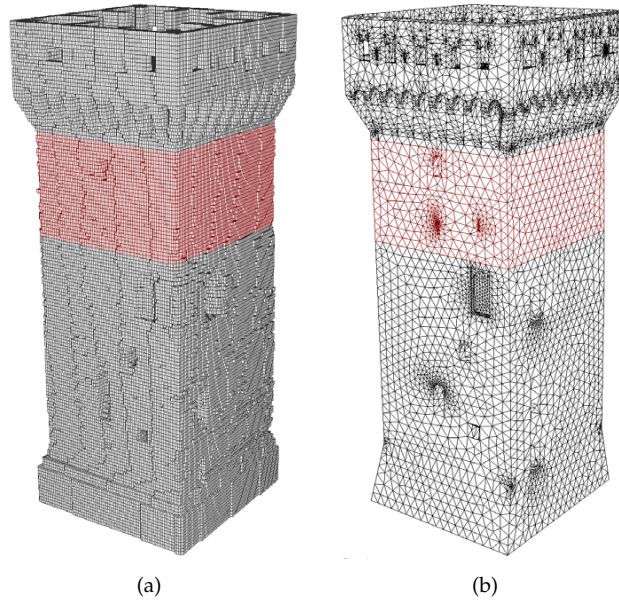
Figure 35: FE discretization comparison, colors are set according to the material properties: gray and red colors are used to illustrate the masonry and the reinforced masonry elements, respectively. (a) CLOUD2FEM discretization, and (b) CAD-based discretization.

the structure. Table 2 summarizes the computed mass and the overall dimensions for both models. By inspecting Table 2, it is clear that the application of the proposed technique produces a FE model that describes the main features of the building geometry and its mass distribution.

Table 2: Mass, overall dimensions and center of mass height.

Model	Mass	Max Dimensions	h_g
	(tons)	$\{L \times B \times H\}$ (m)	(m)
CAD	3055.78	$9.97 \times 9.97 \times 30.64$	13.67
Voxel	3032.11	$9.90 \times 9.80 \times 30.60$	14.07

Table 3 collects the obtained results in terms of computed frequencies and computed errors. It appears that, for the first six modes, the computed error is always less than 4%, and it is less than 0.1% for the fundamental modes (Mode 1 and Mode 2). Figure 36 illustrates the first modal shape, where colors are associated with the magnitude of the computed amplitude (normalized). Concerning the overall response, modal shapes are in good agreement, see Table 2.

This description obviously introduces a higher number of degrees of freedom (dof): the voxel model counts 2,237,004 dofs, whereas the CAD-based model enu-

Table 3: Mastio natural frequencies. Comparison between the voxel-based model and the CAD-based model.

Mode	Voxel fr. (Hz)	CAD fr. (Hz)	Error (%)	Mode descr.
1	1.9131	1.9137	0.031%	1st bend. mode (E-W)
2	1.9276	1.9289	0.067%	1st bend. mode (N-S)
3	4.5437	4.4253	2.675%	tors. mode
4	7.0804	7.3518	3.692%	2nd bend. mode (E-W)
5	7.1654	7.3665	2.730%	2nd bend. mode (N-S)
6	8.1623	8.0055	1.959%	axial mode

merates 163,020 dofs. Despite the larger number of dof, the proposed procedure allows to transform the user time into computational time. Moreover, a more effective FE model prone to optimizing the computational cost, preserving the accuracy, might be obtained by coarsening the resolution of the voxels. The voxel discretization introduces a simplified description of the geometry and leads to a fine FE model able to precisely capture the geometry features and the corresponding mass properties. The mechanical properties are defined by a punctual characterization, which leads to a very accurate description of the structure, since each voxel can be automatically associated with a particular property definition, whereas for the CAD-based model each material or property needs a partition of the whole solid model.

3.2.3.3 *Mesh optimization*

Here, an optimization of the Mastio FE model depicted in Figure 35(a) is proposed. In particular, a coarser model, characterized by a vertical slicing step equal to 0.25 m with also a slice resolution of 0.25 m, is developed through the CLOUD2FEM procedure.

The coarser mesh is then characterized by a considerable reduction of dofs (443,076). More precisely, it counts 147,692 nodes and 118,554 elements. A comparison of the two voxel-based meshes is shown in Figure 37. By inspecting Figure 37 and Table 4, appears clear that the two models are equivalent from a structural point of view.

Table 4: Mass, overall dimensions and center of mass height.

Model	Mass (tons)	Max Dimensions {L $\times$ B $\times$ H} (m)	h_g (m)
Voxel	3032.11	9.90 $\times$ 9.80 $\times$ 30.60	14.07
Voxel coarser	3081.99	10.00 $\times$ 10.00 $\times$ 30.50	13.89
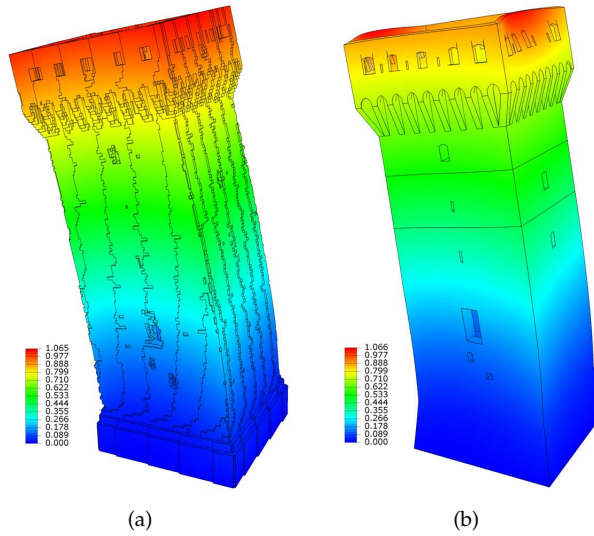
Figure 36: Mode 1: bending modal shape. Displacements magnitude. (a) Voxel frequency = 1.9131 Hz, and (b) CAD frequency = 1.9137 Hz.

However, to assess the accuracy of the coarser model, a natural frequency analysis is carried out. Table 5 collects the results obtained in terms of computed frequencies and computed errors. It appears that the computed error is always

Table 5: Mastio natural frequencies. Comparison between two resolutions of voxel-based models.

Mode	Voxel fr. (Hz)	Voxel coarser fr. (Hz)	Error (%)	Mode descr.
1	1.9131	1.8635	2.592%	1st bend. mode (E-W)
2	1.9276	1.8705	2.962%	1st bend. mode (N-S)
3	4.5437	4.4004	3.154%	tors. mode
4	7.0804	6.6999	5.374%	2nd bend. mode (E-W)
5	7.1654	6.7792	5.390%	2nd bend. mode (N-S)
6	8.1623	7.8249	4.133%	axial mode

less than 5.5% for the first six modes. Figure 38 illustrates the modal shapes 2 and 5 of the voxel model (Figure 38(a) and Figure 38(c), respectively) and of the voxel coarser model (Figure 38(b) and Figure 38(d), respectively). Consequently, the coarser model appears structurally equivalent to the reference one [305]. In this way, it can be utilized to carry out advanced numerical analyses with a reasonable computational cost.
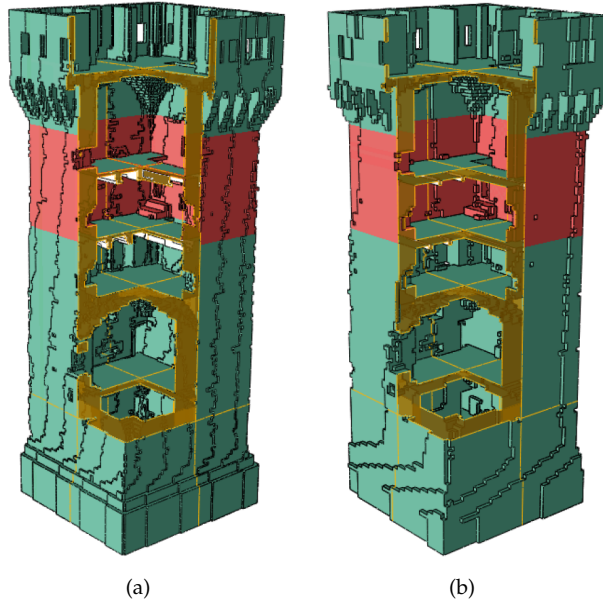
Figure 37: FE mesh discretizations: (a) voxel discretization, and (b) voxel coarser discretization.

3.2.4 *Generation and validation of the whole fortress FE model*

In order to extensively test the CLOUD2FEM procedure and to show its capabilities and reliability, an application to the whole San Felice sul Panaro fortress has been carried out [30].

3.2.4.1 *Generation of the whole fortress FE model*

Following the work-flow in Figure 21, 121 digital slices of the whole fortress have been generated from the point cloud and, then, stacked. A vertical gap $\Delta z = 0.25$ m coupled with a bi-dimensional resolution in the horizontal plane of 0.25 cm $\times 0.25$ m has been chosen, as suggested in Section 3.2.3.3. Indeed, the resolution $0.25 \times 0.25 \times 25$ m was found to be the best compromise between results accuracy and computational effort.

Although this mesh size does not accurately reproduce every small architectural detail, it guarantees a good accuracy in terms of global structural response. Figure 39 shows some examples of digitalized slices of the fortress and a sketch of their stacking sequence.

The resulting mesh, depicted in Figure 40, is characterized by 409,300 hexaedral FEs (each one $0.25 \times 0.25 \times 0.25$ m) and 1,512,444 dofs. Four different materials have been used, whose mechanical properties have been set according to [242] and are collected in Table 6. In Figure 40, the Mastio's trunk top part is depicted
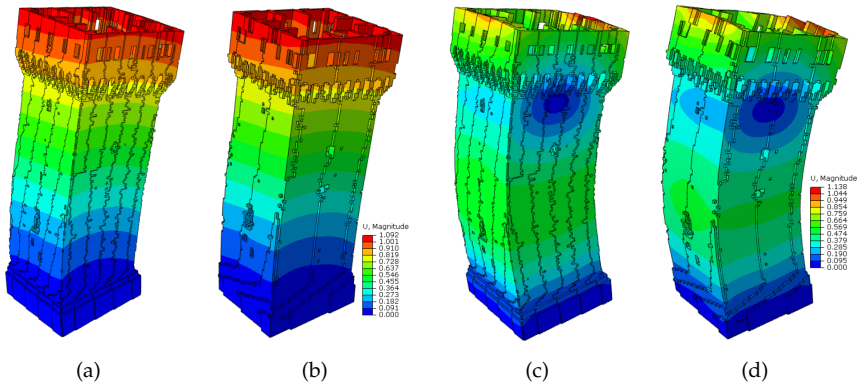
Figure 38: Comparison of modal shapes: (a) mode 2 voxel mesh (1.9276 Hz), (b) mode 2 voxel coarser mesh (1.8705 Hz), (c) mode 5 voxel mesh (7.1654 Hz), and (d) mode 5 voxel coarser mesh (6.7792 Hz).

m-th slice   n-th slice   r-th slice
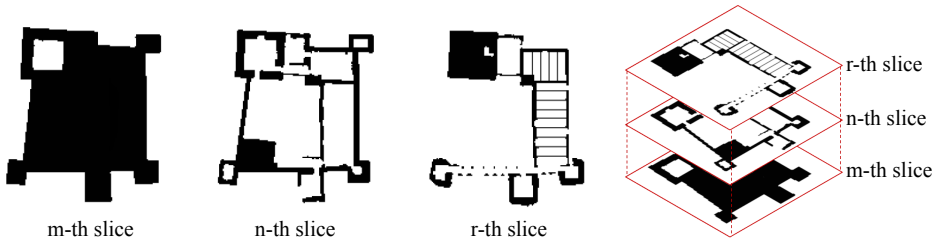
Figure 39: Examples of digitalized slices of the fortress and their stacking.

with a different color because it is composed by reinforced masonry due to the presence of steel tie-rods added in the 90s.

Modeling the floors and vaults has always been a very significant issue when dealing with numerical models of masonry structures. Following the proposed strategy, floors and vaults are automatically meshed through a jagged representation of the original geometry. Anyway, it is always possible to improve the mesh accuracy using a smoothing method to reduce the faceting, as presented in [305]. Nevertheless, in order to assess the global behavior of a historic structure, the geometrical accuracy of the raw mesh can be considered satisfactory even if vaults are present, as in the current case (Figure 40).

In the past, the fortress was surrounded by a moat. Therefore, the ground level is located at two different altitudes: inner ground level, located at 0.00 m (assumed as origin of the reference system), and outer ground level, located at −3.50 m. The boundary conditions account for this difference: all the nodes located at the moat level have clamped boundary conditions applied, whereas the elements located into the courtyard have been modeled through an elastic material to take into account the presence of the terrain. For all of the following

Table 6: Materials mechanical properties [242].

ID	Material	Young's modulus [MPa]	Shear modulus [MPa]	Density [kg/m^3]
1	Masonry	1500	625	1800
2	Reinf. masonry	1900	792	1800
3	Timber	8000	2918	415
4	Terrain	935	316	1200

analyses, these boundary conditions have been considered. Moreover, roofing structures have been modeled as concentrated mass.

3.2.4.2 *Structural analyses and validation*

In this section, few preliminary structural analyses are conducted to verify the usability of the model.

It should be pointed out that historic buildings are often composed of several adjacent structures built in different eras. Their structural response is, therefore, influenced by the interaction of adjacent parts. To account for this interaction and aiming at obtaining the simplest FE model, in this study such interaction is simply modeled by modifying the material properties of the connection zone. The introduced structural connections are shown (in red) in Figure 40. Indeed, connections between adjacent structures are here simply inserted by manipulating the 3D voxels-based matrix, or, equivalently, a layer of 3D FE between adjacent structures.

Since historic monumental buildings are characterized by great dimensions, the 3D domains associated to the connections are in most cases negligible in comparison to the global volume. Moreover, masonry buildings are characterized in the majority of cases by orthogonal walls, resulting in a mesh grid which is well oriented and with evenly spaced nodes. Therefore, the identification and selection of the layer of elements associated to the connection is rather easy. However, in the uncommon case of diagonal connections, or when walls are not parallel to the digitalization directions, a local re-meshing can be used to model the connections.

In general, the mechanical behavior of connections varies from a compression stress state (closing of connections) to a tensile stress state (opening of connections), given the unilateral response of masonry. Plausibly, in compression stress states the connections tend to have the same mechanical behavior of the surrounding material. Conversely, in a tensile stress state the connections behavior is largely affected by the quality of the masonry toothing between adjacent structures. In the following, three connection levels are distinguished: high quality connections (*Fully connected*), absence of toothing between structures (*Not connected*), and an intermediate level (*Partially connected*). Assuming, for simplicity, that the connections have an isotropic behavior, the simplified mechanical characterization of the three connection levels is sketched in Table 7.
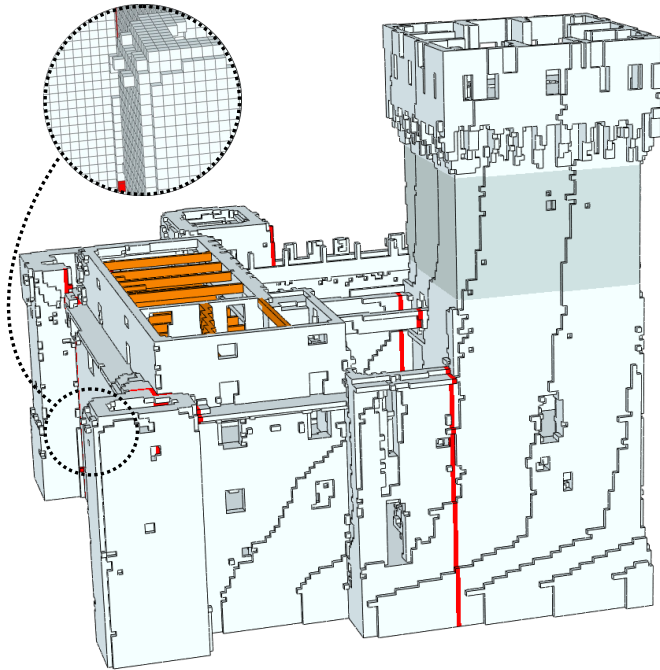
Figure 40: San Felice sul Panaro fortress FE mesh. Structural connections are highlighted in red. The magnified portion shows the mesh discretization.

A numerical assessment of the effect of connections characterization on the dynamic behavior of the fortress has been conducted by means of natural frequencies analyses. In particular, two different connections configurations have been considered: *Fully connected* and *Not connected* (e.g. without any toothing) adjacent structures.

Due to its nonlinear character, the pounding between adjacent structures cannot be contemplated in these linear analyses. Indeed, in a *Not connected* configuration adjacent structures behave as isolated and independent structures.

The influence of connections on the dynamic behavior has been assessed by comparing results between the two connections configurations in terms of natural frequencies and modal shapes. In particular, results of the first nine natural frequencies of the fortress are reported in Table 8 for the two connections configurations. As it can be noted, the structural effect of connections on the dynamic behavior of the fortress remains rather limited, with a percentage variation of the natural frequencies under the 16%.

Figure 41 shows the comparison between the modal shapes of mode 2 (Mastio's bending mode) for the *Fully connected* and *Not connected* configurations. As it can be observed, this modal shape does not essentially change between the two cases.

Table 7: Connections simplified mechanical characterization: E_{con} and G_{con} are the Young's modulus and shear modulus of the connection, respectively, while E_m and G_m are the Young's modulus and shear modulus of the masonry, respectively.

Closing of connection		
E_{con}	$= E_m$	
G_{con}	$= G_m$	*Fully connected*
	$= G_m/\gamma_{Gc}$ with $\gamma_{Gc} \geqslant 1$	*Partially and Not connected*
Opening of connection		
E_{con}	$= E_m$	*Fully connected*
	$= E_m/\gamma_{Et}$ with $\gamma_{Et} \geqslant 1$	*Partially connected*
	$\ll E_m$	*Not connected*
G_{con}	$= G_m$	*Fully connected*
	$= G_m/\gamma_{Gt}$ with $\gamma_{Gt} \geqslant 1$	*Partially connected*
	$\ll G_m$	*Not connected*

Conversely, Figure 42 shows the comparison between the modal shapes of mode 3. The modal shape's change is significant: in the *Not connected* configuration also the East curtain wall is activated.

Similarly, in the comparison between the modal shapes of mode 6 (Mastio's torsional mode), depicted in Figure 43, it is clear the modal shape's change concerning the North tower.

In this study, preliminary linear static analyses have been also utilized to test the usability of the numerical model generated through the CLOUD2FEM procedure.

For the sake of brevity, the attention is focused on the preliminary structural response of the Mastio and its interaction with adjacent structural elements. For simplicity, horizontal forces proportional to the Mastio's first bending modal shape in E-W direction (mode 2, Figure 41), with a maximum horizontal acceleration equal to 0.3g, have been applied together with vertical dead loads.

After the analysis of the masonry toothing between Mastio and its adjacent structures, considering also the fortress historical evolution, three different connections levels have been assumed along the connection zones between Mastio and its adjacent structures, as reported in Figure 44. With reference to Figure 44, the portion A has been supposed as *Partially connected* with reduction factors (see Table 7) $\gamma_{Et} = \gamma_{Gt} = 1.6$ due to its quite good masonry toothing, the portion B as

Table 8: Results of the first nine natural frequencies of the fortress and relative variation for the two connections configuration.

Mode	Fully connected freq. [Hz]	Not connected freq. [Hz]	% Var.
1	2.2231	1.9809	-10.895
2	2.4278	2.0500	-15.561
3	4.0917	3.8555	-5.773
4	4.4717	3.8857	-13.105
5	4.8790	4.2838	-12.199
6	4.9832	4.5906	-7.878
7	6.8285	6.3173	-7.486
8	7.3270	6.9297	-5.422
9	8.1807	7.9072	-3.343

(a)   (b)
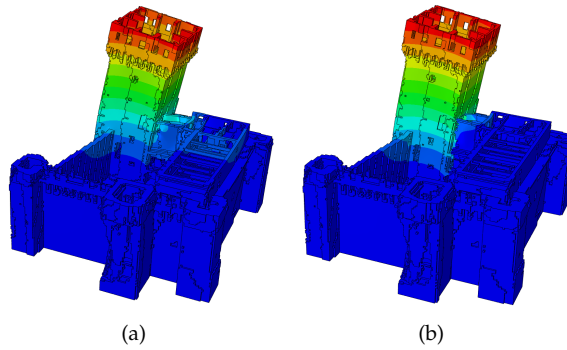
Figure 41: Mode 2: (a) *Fully connected* configuration (2.4278 Hz), and (b) *Not connected* configuration (2.0500 Hz).

Partially connected characterized by a poor toothing quality with $\gamma_{Et} = \gamma_{Gt} = 10$, and the portion C *Not connected* since the absence of toothing between the parts is clear. Finally, for simplicity, it has been assumed $\gamma_{Gc} = 1$ for all the portions.

The results of the linear static analysis for a West directed force are depicted in Figure 45 for the South front and in Figure 46 for the North front. As it can be easily realized, in this case the connections tend to be in compression and, hence, these results refer to the condition of connections closing. In particular, concerning the South front, the stress states in terms of normal vertical stress component and in-plane tangential stress component are depicted in Figures 45(a) and 45(b), respectively. As it can be noticed, the recovered stress fields are well represented over the structural domain and are not influenced by the jagged representation of the geometry.

(a)   (b)
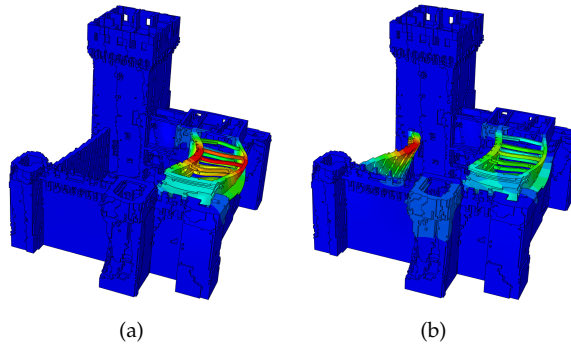
Figure 42: Mode 3: (a) *Fully connected* configuration (4.0917 Hz), and (b) *Not connected* configuration (3.8555 Hz).

(a)   (b)
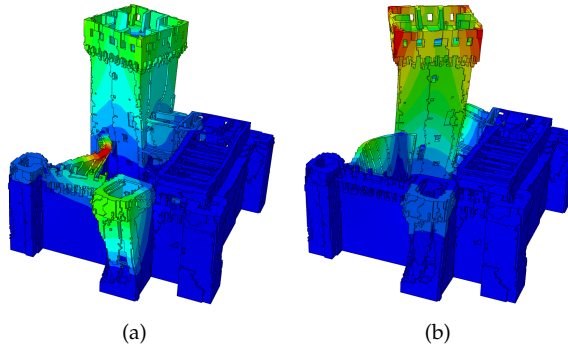
Figure 43: Mode 6: (a) *Fully connected* configuration (4.9832 Hz), and (b) *Not connected* configuration (4.5906 Hz).

Moving to the Mastio's North front, Figure 46 shows the comparison between the stress state (reported in Figure 46(a) in terms of maximum principal stress) and the crack pattern which is characterized by a curved crack, highlighted by a dotted line in Figure 46(a) and by arrows in Figure 46(b). As it can be noted, they are in good agreement: the emphasized crack is almost perpendicular to the grater maximum principal stress' spatial vectors.

The results of the linear static analysis for an East directed force are shown in Figure 47 for the South front and in Figure 48 for the North front. As it can be easily argued, in this case there is an opening of connections since the joint between the Mastio and its adjacent structure is in a tensile stress state. Similarly to the previous case, a comparison between linear static analysis results is proposed in terms of maximum principal stress and the crack pattern suffered by the structure. Regarding the South front, the stress state is shown in Figure 47(a) and the crack pattern in Figure 47(b).
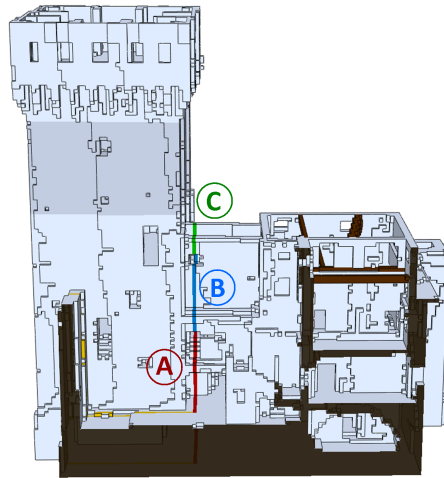
Figure 44: San Felice sul Panaro fortress FE mesh. Detail of Mastio's connections.

Segments $\overline{AB}$, $\overline{CD}$, $\overline{EF}$ and $\overline{GH}$ shown in Figure 47(a) correspond to the major cracks of the Mastio's South front indicated by arrows in Figure 47(b). As it can be noted, the maximum principal stresses are almost perpendicular to the highlighted segments (Figure 47(a)). In this sense, it can be stated that the stress state and the crack pattern shown in Figure 47 are in good agreement. Moreover, it can be noticed that prolonging these segments they all run into point O. Thereby, an hypothetic point between O and O' can be considered as the center of rotation for a plausible overturning mechanism.

Concerning the Mastio's North front, the linear static analysis results relative to a East directed force are shown in Figure 48. In particular, the distribution of the maximum principal stresses is shown in Figure 48(a) and the crack pattern in Figure 48(b). Also in this case there is a good agreement between the maximum principal stresses distribution and the cracks suffered by the Mastio's trunk.

As already mentioned, one of the features of the proposed modeling strategy is its ability to give a fine geometrical representation of the whole building, including the secondary structural elements. Among these, Figure 49 focuses the attention on the stiffening walls located in the Mastio's top. In particular, Figures 49(a) and 49(b) show the maps of the vertical stress component due to a horizontal East directed and West directed force, respectively, and Figures 49(c) and 49(d) show the crack pattern. Inspecting Figures 49(a) and 49(b) reveals the presence of compression and tensile stress peaks at the base of the E-W directed stiffening walls. This is in good agreement with the crack pattern suffered by these stiffening walls (Figure 49(c)), where a sub-horizontal crack is clearly evident (Figure 49(d)).

In summary, the FE model generated through the CLOUD2FEM procedure appeared rather employable in the framework of numerical analysis, and it seems suitable to be used in more advanced nonlinear analyses to assess, for instance,
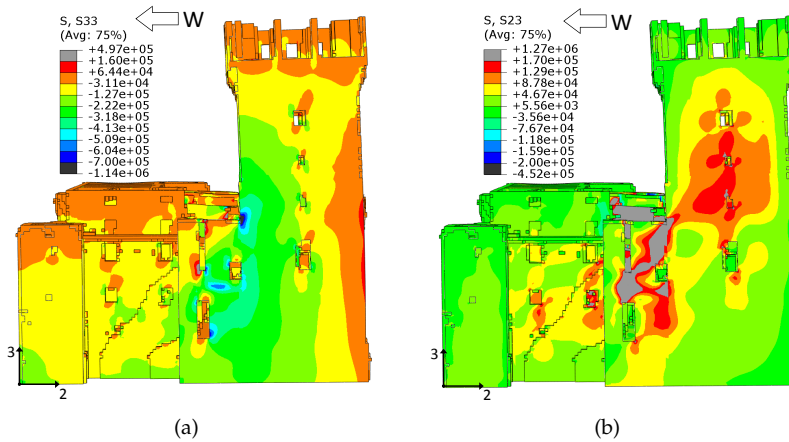
Figure 45: Linear static analysis results relative to a West directed force, South front: (a) vertical stress (Pa), and (b) tangential stress (Pa).

the seismic response of historic structures. The favorable application on the San Felice sul Panaro fortress, which embodies all the typical complexities of historic monumental buildings, represented a positive outcome of the proposed mesh generation procedure. The FE model of the fortress in its post-quake condition has been adopted by Bassoli et al. [306] for the ambient vibration-based FE model updating of an earthquake-damaged masonry tower (i.e. the Mastio of the San Felice sul Panaro fortress), investigating the mechanical properties of the tower and the level of connections with the rest of the fortress in the current damaged state. In [306], to fully characterize the actual behavior of the tower in operational condition, mesh elements corresponding to the damaged masonry have been identified and different material properties have been assigned to them. This allowed to account for the effect of damage and cracks, which appeared essential in the calibration process. Further applications of the FE model presented here are shown in Chapter 4.

(a)   (b)
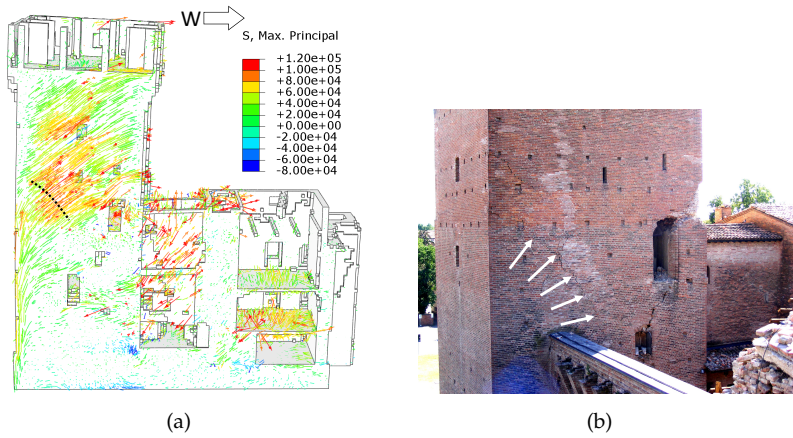
Figure 46: Comparison between linear static analysis results relative to a West directed force and the crack pattern suffered by the structure during the Emilia earthquake, North front: (a) maximum principal stress (Pa), and (b) crack pattern.

(a)   (b)
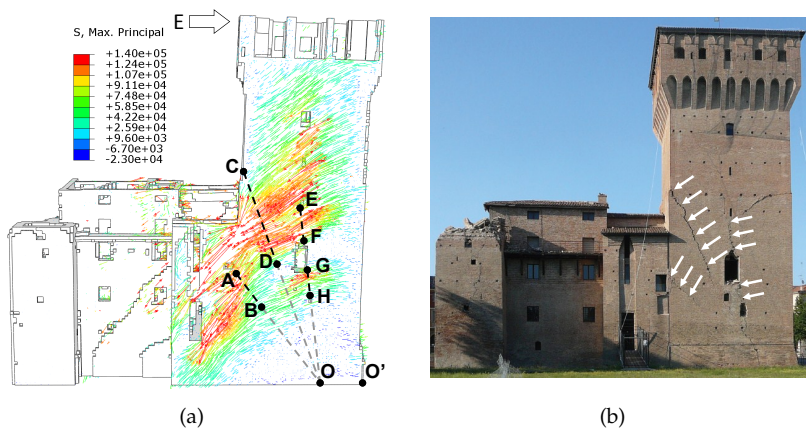
Figure 47: Comparison between linear static analysis results relative to a East directed force and the crack pattern suffered by the structure during the Emilia earthquake, South front. Segments $\overline{AB}$, $\overline{CD}$, $\overline{EF}$ and $\overline{GH}$ correspond to the major cracks. (a) Maximum principal stress (Pa), and (b) crack pattern.

(a)

(b)
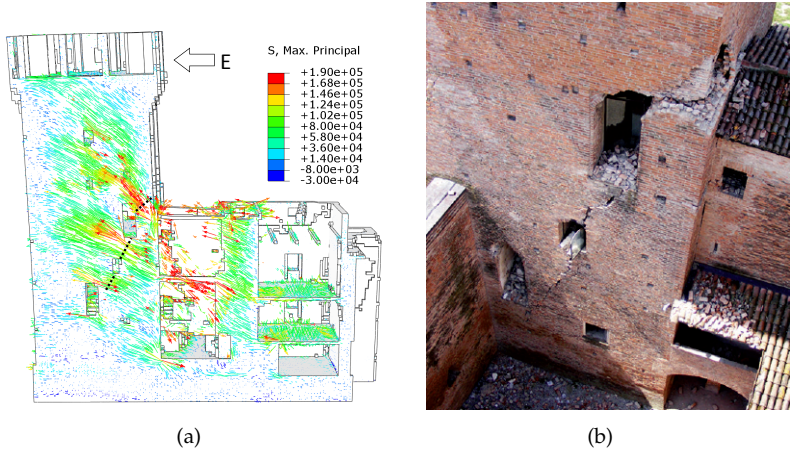
Figure 48: Comparison between linear static analysis results relative to a East directed force and the crack pattern suffered by the structure during the Emilia earthquake, North front: (a) maximum principal stress (Pa), and (b) crack pattern.

(a)

(b)

(c)

(d)
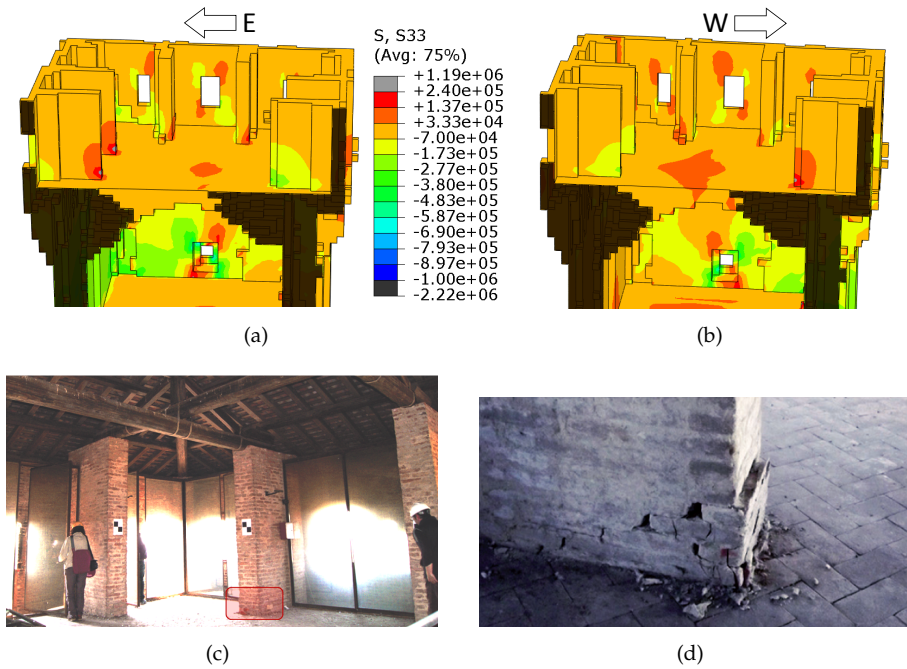
Figure 49: Comparison between numerical results and the crack pattern on Mastio's top stiffening walls. (a) East horizontal force: vertical stress (Pa). (b) West horizontal force: vertical stress (Pa). (c) Mastio's top. (d) Particular of the crack pattern related to the red highlighted square in Figure 49(c).

3.3 WATERTIGHT MESHING

In this section, a simple approach for processing point clouds (surveyed on historic structures) is proposed for their automatic transformation to 3D FE meshes, following the concept of watertight mesh. Watertight means that the mesh on all the surfaces is complete, so that the volume is fully enclosed. This approach appears appealing for historic ruined structures, which are generally characterized by the absence of inner spaces, furniture, doors and window frames etc. The proposed mesh generation approach treats historic structures similar to 3D objects such as stone sculptures, building ornamental components etc and follows an akin concept of digital reproduction of 3D objects from 3D scanning to 3D printing. However, in this instance, instead of using the mesh to perform 3D printing, its usage is aimed for structural analysis purposes (i.e. FE mesh made of 3D solid elements).

The proposed procedure requires a point cloud of the historic structure under study. The point cloud could be the output of either terrestrial laser scanning or close-range photogrammetry. These survey techniques generate dense clouds of 3D points, generally characterized by several millions of points for full-scale buildings.

Often, a few preliminary and standardized operations on the point cloud dataset may be required to facilitate the subsequent operations. Firstly, a specific algorithm [46] is used to populate a new dataset of points with a sampling generated according to a Poisson-disk distribution. The resulting reduced point cloud is characterized by a regular spatial sampling, which can be chosen depending on the level of detail desired for the case at hand. Millimetric details are generally negligible to analyze the structural behavior of historic constructions. Moreover, the point cloud has to be cleaned mainly by removing all neighbor points, which are not relevant to the structure. Although this operation is manual, it is easy to implement and substantially fast.

Afterward, a TIN mesh is generated based on the point cloud (in the condition after sampling and cleaning). The TIN mesh is created by linking triplets of nodes to form non-overlapped triangles. Ideally, if every portion of the object's surface is meticulously surveyed, this mesh could be already watertight. However, this never occurs for large-scale and complex structures since their surfaces are continuous with the terrain. Furthermore, few parts of the object's surface are commonly missing, due to access difficulties during the survey.

Since the aim is to obtain a watertight mesh, further processing of the data is necessary. Thus, the Poisson surface reconstruction [307] can be adopted. Poisson surface reconstruction is a well-known computer graphics technique for creating watertight surfaces from oriented point samples acquired with 3D range scanners. This algorithm expresses surface reconstruction as the solution of a Poisson equation. Therefore, Poisson reconstruction considers all the data at once, creating very smooth surfaces that robustly approximate noisy data [307], suffering, however, from a tendency to over-smooth the data. All these operations are basi-

cally common and standardized, and they can be conducted by means of any 3D mesh processing software.

Once the watertight mesh has been obtained, it can be directly exploited for setting up the 3D FE mesh. The main aim is to generate a final mesh that will be robust when used for FE calculations. Although an adaptive (skin) mesh could be used in areas where more detail is desired, it is even more important to have a final (solid) mesh with appropriate topology. To this aim, three alternative operations are suggested herein.

In the first case, the triangles which constitute the watertight mesh are directly transformed into FE triangles. Then, the triangles are transformed into solid 4-nodes tetrahedral FEs filling the whole volume by means of automatic advancing front methods which are already implemented in most commercial software packages (see for example the one implemented in Abaqus [308]). This operation is fully automatic, and therefore, extremely fast. In addition, it does not introduce any further geometric approximation. Nevertheless, being the watertight mesh not conceived for FE analysis, this approach could lead to excessively distorted FEs and, therefore, it could fail. In most cases, few local manual refinements could overcome this drawback, but sometimes the simple regularization of the metrics on the surface (watertight mesh) cannot lead to a good (undistorted) solid mesh. This aspect mainly depends on the mesh generation software that can or cannot employ robust mesh generation procedures.

In the second case, the volume defined by the watertight mesh is filled by voxels, using well-known and established voxelization algorithms (see for instance [309]). The outcome strictly relies on the adopted voxel dimension, which can be chosen depending on the case at hand. In this case, the voxel model is nothing more than a 3D matrix in which the value 1 refers to the structure and the value 0 represents voids, as well as the information of the voxel dimensions. Therefore, their transformation to 8-nodes hexahedral FEs is a simple, common and standardized operation, see Section 3.2. The voxel dimension should represent a good compromise between geometric accuracy and computational effort of FE analyses. Given a watertight mesh, its voxelization is always possible and the generation of the FE mesh is guaranteed. Therefore, although the voxelized model is generally rougher than the one obtained through direct transformation of the watertight mesh, the voxelization of the domain represents a robust and always guaranteed approach for the FE mesh generation.

In the latter case, the watertight mesh is processed by means of a retopology algorithm (see for example [310]) to generate a coarser representation of the surface [311]. This kind of algorithms are able to re-mesh a surface into a triangular mesh, with a certain resolution chosen by the user, using unified local smoothing operators that optimize both the edge orientations and vertex positions in the output mesh [310]. Then, the triangles are transformed into solid 4-nodes tetrahedral FEs. Therefore, the problem dimensions, as well as the number of solid FEs, are broken down thanks to the reduction of the triangles of the watertight mesh. This operation produces a further approximation of the surface depending on the resolution of the triangles chosen.

In a case where the surveyed structure presents several inner spaces (e.g. rooms) and the presence of furniture, doors and windows, i.e. the TIN mesh cannot become watertight anyway, other semi-automatic mesh generation approaches (e.g. the CLOUD2FEM procedure, Section 3.2) can be employed. Indeed, although the CLOUD2FEM procedure is more laborious than the proposed one, being not completely automatic, it always guarantees the mesh generation of the 3D geometry. In Figure 50, a general flowchart for the FE mesh generation from point clouds of historic buildings is shown.
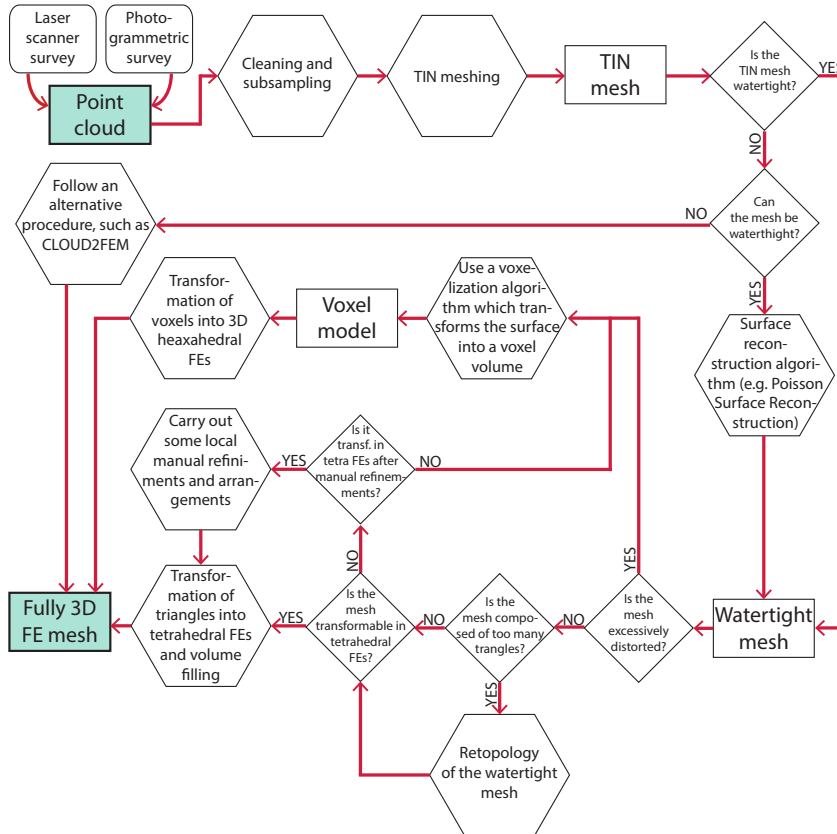
Figure 50: Exploiting point clouds of historic constructions for structural purposes: A general flowchart for FE mesh generation.

3.3.1 *Application to a ruined leaning tower: The SW tower of Caerphilly castle, UK*

The watertight meshing procedure just proposed is applied to a significant case study, which represents a geometrically irregular historic structure, to show the

procedure potentialities: the SW ruined leaning tower of Caerphilly castle, UK (Figure 51).

Caerphilly castle is a medieval fortification in Caerphilly, South Wales, UK. The castle was constructed by Gilbert de Clare in the 13th century [312] and it is the second largest in the UK. The tower has been in a ruined and leaning condition for several centuries [312, 313].

(a)

(b)

(c)

(d)
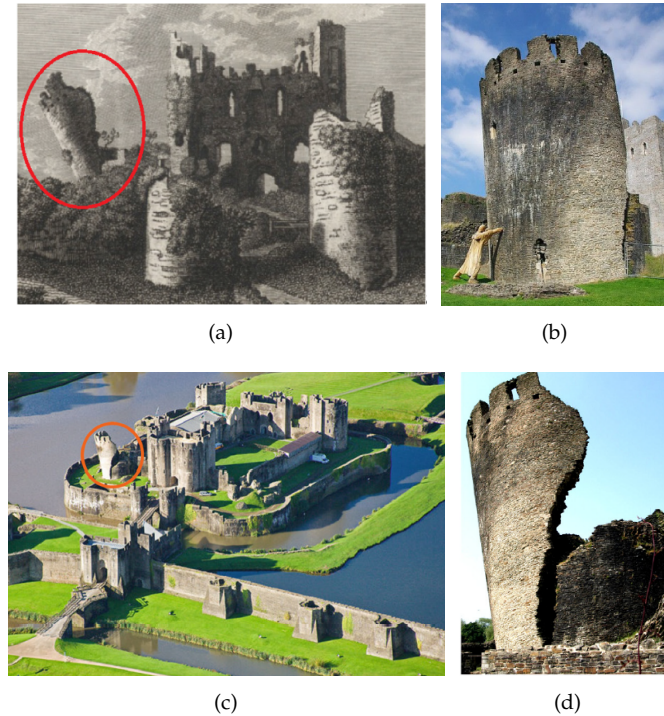
Figure 51: Southwest tower of Caerphilly castle. (a) Historic drawing. (b), (c), (d) Photos of the leaning tower in its actual condition.

The tower is approximately 17 m tall. It used to have a circular ground plant of approximately 9 m in diameter. Today, the inclination of the tower is approximately 10 degrees. For the sake of comparison, the campanile of Pisa is 55.86 m tall and leans at an angle of 5.5 degrees. The southwest tower is made of stone masonry with a fully irregular texture. No information is available about masonry material properties, soil stratigraphy and foundations. However, medieval fortified structures were generally characterized by particularly shallow foundations. According to Renn [312], the deterioration subsequent leaning of the tower was probably the result of subsidence caused by de-watering in the 18th century, as there is no evidence of deliberate destruction having been ordered.

In 2014, a detailed survey of the southwest tower commissioned to document its health condition [313]. A total of 27 scans were surveyed using a FARO focus

3D X130 terrestrial laser scanner. The inclinometer, altimeter, compass, clear contour and clear sky were also activated and far distance deactivated. A series of scans have been taken from points on the ground around the base of the tower. During the scanning, challenges were mainly due to scaffolded areas around the tower and the presence of tourists. The complexity of the geometry also proved challenging in the placement of targets. Twelve spherical targets used to locate the scans.

3.3.2   *Generation of the case study FE model*

Here, the FE mesh generation of the SW tower of Caerphilly castle is shown. Figure 52 presents the main outcomes of the mesh generation operations conducted on the case study. Figure 52(a) shows the initial point cloud and Figures 52(b),52(c) show the TIN mesh. As it can be observed, several portions of the structure surface are lacking due to the aforementioned drawbacks in the surveying operations. However, the main geometric features of the structure were successfully collected. The Poisson surface reconstruction has been conducted on the case study data set. Figures 52(d),52(e) show the resulting watertight mesh consisting of triangles, where it is superimposed on the TIN mesh of the previous step. As can be noted, the watertight mesh reasonably approximates the original TIN mesh. The level of approximation introduced in the geometry in this circumstance appears to be included, in the authors' opinion, within the engineering tolerance.

   On the one hand, the FE model of the case study obtained through voxelization is shown in Figure 52(f), where the value 0.175 m has been adopted as voxel dimension. On the other hand, Figure 52(g) shows the solid FE model obtained through the direct transformation. In this case, no excessive distortion arose. Therefore, this latter model has been herein preferred over the voxelized model since it does not introduce further geometric approximations, as voxelization does. The mesh consists of 28,738 nodes and 145,893 4-nodes tetrahedral FEs. In Figure 52(h), all the nodes of the bottom part of the mesh have been projected to a horizontal plane to allow the easy setup of the boundary conditions in the model. Finally, the solid mesh (Figure 52(i)) obtained through retopology [310] (with an average size of the side of the triangles equal to 60cm) consists of 5,639 nodes and 27,114 tetrahedral FEs. As can be noted, the mesh is characterized by a largely reduced number of solid FEs. Nevertheless, it is still suitable for structural purposes.

   The application of the generated mesh (Figure 52) for the stability analysis of leaning historic masonry structures is shown in Chapter 5.
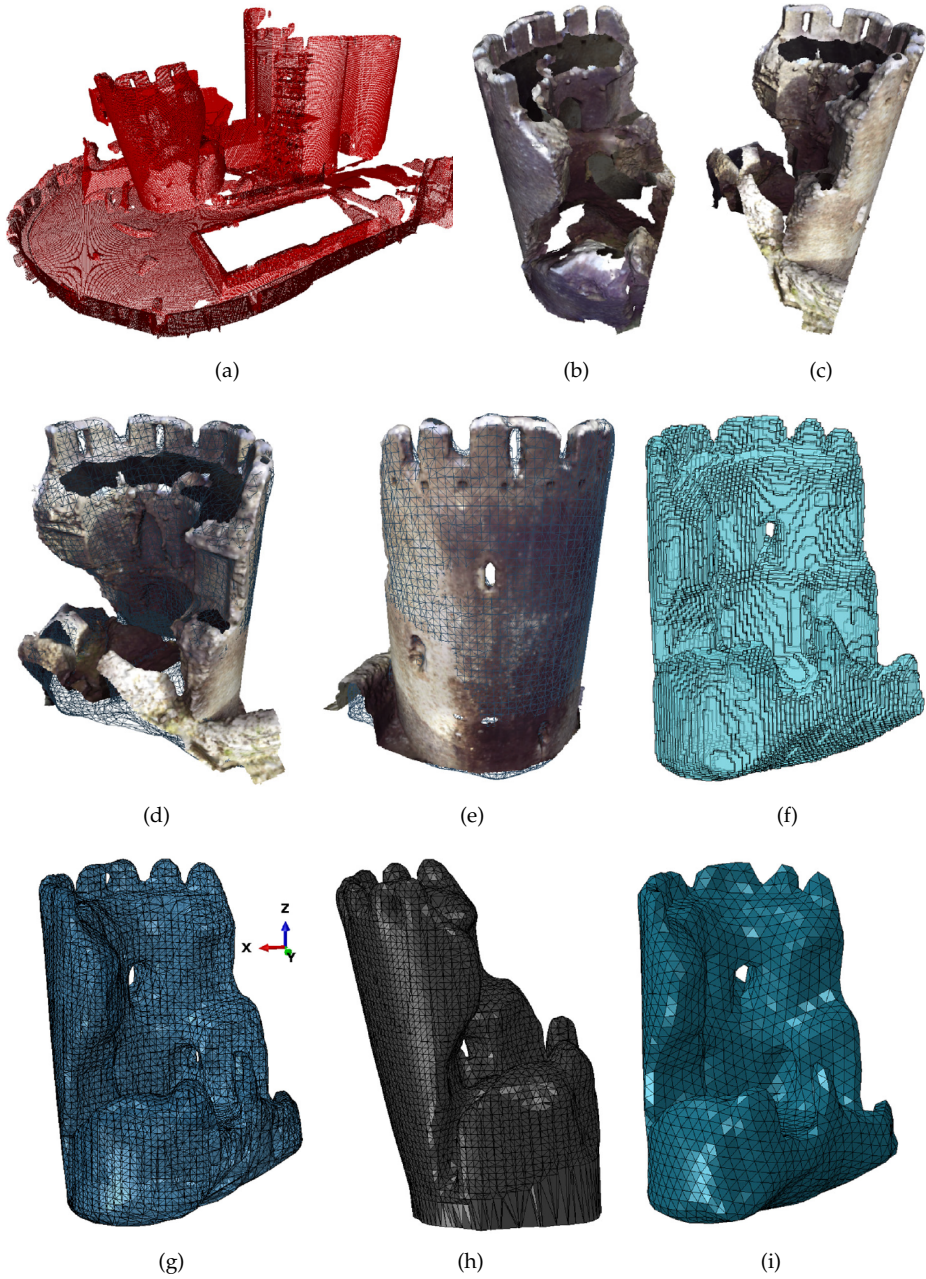
Figure 52: Points cloud manipulation and mesh generation. (a) Rough points cloud. (b),(c) Tower's TIN mesh. (d),(e) Superposition of TIN mesh and watertight mesh. (f) Example of voxelization of the domain. (g) Transformation of the watertight mesh into a tetrahedral mesh. (h) Solid FE mesh with base nodes projected on a common plane. (i) Solid mesh obtained through retopology.

3.4 CONCLUSIONS

In this chapter, two mesh generation procedures (CLOUD2FEM and watertight meshing) have been proposed to transform 3D point clouds into 3D solid FE models of historic monumental buildings.

The CLOUD2FEM procedure generates solid FE meshes through a slicing of the initial point cloud and the subsequent stacking of the geometry. The resulting mesh contains all of the information to be used within the FE method, including the mechanical properties associated with the material features, guaranteeing the automatic generation of a reliable FE model. An increase of the level of automation in the mesh generation process is observed and a large reduction in the required time in comparison to CAD-based modeling procedures is achieved. The validation of the strategy has been performed on the San Felice sul Panaro fortress, which embodies all the typical complexities of monumental historic buildings.

The watertight meshing procedure considers the structure as a watertight surface and eventually fills the volume. Although not always applicable to historic buildings, e.g. in case of inner spaces, rooms, furniture, doors, windows, etc., this procedure represents a very fast solution for the direct and fully automatic mesh generation of a geometrically irregular masonry building.

AN ANALYSIS PROCEDURE FOR SEISMICALLY INTERACTING STRUCTURES

The damage occurred due to past earthquakes highlighted that the seismic behavior of historic masonry structures characterized by an aggregation of units with an own seismic behavior (e.g. palaces, fortresses, castles, etc.) is strongly affected by their dynamic interaction. At present, no codified and operational tools are available to perform the seismic assessment of such mutually interacting structures. This chapter introduces a numerical procedure based on the use of nonlinear static analyses to fill this gap. The proposed procedure firstly requires the execution of a modal analysis on a 3D finite element model of the whole structure to define the modes which involve the dynamic response of each unit and their modal shapes. The latter are then fitted to define the load patterns to be applied on each unit through pushover analyses. The pushover curves obtained for each unit are then converted into capacity curves to finalize the seismic assessment. The effectiveness of the proposed procedure is shown through an application to a medieval fortress significantly damaged by the 2012 Emilia earthquake (Italy). The results achieved are promising and support the possible extension of the procedure to other typologies of complex historic structures composed by various interacting units.

4.1 INTRODUCTION

This chapter deals with the seismic assessment of mutually interacting historic masonry structures carried out through nonlinear static analyses. This kind of structures is characterized by a seismic behavior which is ruled by the structural response of the many interacting units forming the whole building. This interaction can be relevant especially if the units are characterized by various architectural features that lead to different dynamic properties, stiffness and strength of the units. Such typology includes a huge number of examples: a bell tower incorporated in a church, monumental palaces which are often the result of subsequent additions of structural units, and fortified constructions (as fortresses and castles), which are usually formed by towers connected through curtain walls (Figure 53).

Although the activation of local mechanisms is significant (e.g. mainly interesting out-standing portions such as battlements), the assessment of the global response is equally relevant. The chapter focuses the attention only to the latter, particularly referring to the case of fortresses.

(a)   (b)

Figure 53: Examples of two Emilian fortresses: (a) Vignola fortress, and (b) Castello Estense in Ferrara.

The vulnerability of fortresses was strongly highlighted by the 2012 Emilia earthquake [304]. In fact, such typology is particularly frequent in that area and offered several examples of severe damage, pointing out the complexity in interpreting their seismic behavior. A classification of the recurrent seismic damage mechanisms was originally proposed in [304], based on observed damage and typical configurations. In particular, the main observed mechanisms were: (i) damage mechanisms due to the interaction between the towers and the fortress' curtain walls; (ii) damage mechanisms involving the main body of the towers; (iii) damage mechanisms involving the upper parts of the towers; (iv) damage mechanisms at the level of the roofs. Starting from the proposal of [304] for the Emilia fortresses, further damage mechanisms were then added in [314], corroborated by the damage collected for a large number of cases hit by other past Italian earthquakes.

The seismic assessment of such complex structures poses several critical issues. The first problem deals with the definition of the best modeling choice to be adopted that has to balance the need of a reasonable computational effort with that of guaranteeing a reliable assessment capable to catch the interaction effects. The second problem is instead connected to the lack of tools and standardized procedures to perform the seismic analysis and verification of such complex masonry structures. While Standards [242] are more oriented to ordinary buildings, Recommendations addressed to monumental assets (i.e. [24]) in general state a series of general principles and indications for possible methodologies of analysis, without however prescribing operational tools or indicating specific models and standardized procedures.

In this context, this study aims to overcome the aforementioned lack of operational tools by proposing a procedure for the seismic assessment of mutually interacting masonry structures based on the use of nonlinear static analyses. The required steps of the procedure are explained in Section 4.2. The procedure is then applied to a case-study, i.e. the San Felice sul Panaro fortress already presented in Section 3.2.2. It is worth to note that the procedure uses a 3D FE solid

model of the entire structure (Section 4.3). Therefore, in the whole model the dynamic interactions among the different units of the entire asset are explicitly accounted for. Furthermore, the use of efficient numerical algorithms keeps bearable the computational effort (Section 4.4). The comparison between the occurred damage and the one predicted - in terms of crack pattern and ductility demand obtained by the analyses - allowed to validate the procedure (Section 4.5).

4.2 SEISMIC ASSESSMENT THROUGH NONLINEAR STATIC ANALYSES

4.2.1 *Modeling issues*

The seismic assessment of complex monumental assets can be pursued by following two different approaches that affect also the choice in the modeling strategies: (i) the decomposition of the whole asset into different units (e.g. on the basis of historical and constructive features) by performing separate verifications, or (ii) the realization of a unique global model of the entire asset, performing the pushover analyses and, consequentially, make the verification through the capacity curve representative of the overall global seismic behavior. In principle, both alternatives can be considered reliable and have to be chosen depending on the specific features of the examined asset, on its complexity (that can make feasible only few alternatives) and on its expected structural behavior. However, they both present pros and cons.

Regarding the first approach, the difficulties are mainly related to the need of defining a "border" for the asset and for each unit and consequentially the "equivalent" boundary conditions for each modeled unit. Then, obviously, the analysis of the monument decomposed in independent units is not able to consider the possible interaction effects between the different parts, unless in an approximate and conventional way. Conversely, the second approach implicitly considers these interactions, although affected by computational effort complications induced by the modeling of the whole structure.

Even both alternatives can be pursued, the second one is considered the most reliable for the fortresses which this study focuses on. In fact, this kind of structures are characterized by an aggregation of adjacent units (e.g. towers, curtain wall, buildings, etc.), which interact due to mutual boundary conditions. The effects of adjacent buildings on the seismic behavior of a masonry tower have been discussed in [141], where the seismic behavior of a tower has been found to be considerably influenced by the presence of adjacent buildings. Particularly, in [141] it has been shown that the results obtained by numerical models which accounted for the adjacent parts were in good agreement with the damaged condition of an actual non-isolated tower that suffered an earthquake. However, the definition of equivalent boundary conditions to simulate the adjacent parts appears non-trivial and generally excessively approximated for this kind of structures. Therefore, the application of conventional boundary conditions on each unit of the structure

appears inadequate and a comprehensive model of the whole structure is more appropriate to investigate its seismic behavior.

Historic monumental structures are usually characterized by huge dimensions and complex and irregular geometries. These features contribute in making the numerical modeling a challenging task. The use of 3D solid continuum models allows to keep limited the computational effort, see Chapter 2.

The 3D solid geometry of these structures is usually developed in a CAD environment, which is generally an expensive and complex process with inevitable geometrical simplifications. However, recent mesh generation procedures allow to semi-automatically transform 3D point clouds, e.g. surveyed through TLS, into solid numerical models, see Chapter 3.

4.2.2 *Issues on analysis' methods*

Once defined the most suitable numerical model, a further critical issue deals with the procedure for the analysis and verification, which is not manageable *a priori*. At present, Standards and Recommendations [242, 24] do not suggest a well-established procedure for the assessment of such complex structures. Linear analyses or methods based on the local verification of stress states can produce very conventional assessments since the redistribution effects are very significant. Furthermore, linear analyses need the adoption of a behavior factor which would be completely conventional for non-standard typologies as the one examined, being the values recommended in codes only calibrated for ordinary new buildings.

Thus, the use of nonlinear procedures appears essential to obtain more reliable results. In this framework, the options are two: nonlinear dynamic analyses (NLDA) and nonlinear static analyses (NLSA) based on the pushover framework.

NLDA are the most advanced analysis method today available. However, this procedure is not only computationally demanding, but it also presents some drawbacks. Only few numerical models allow to run time history analyses especially for masonry structures, due to the complexity of defining cyclic constitutive models and viscous damping models, see Chapter 2. Moreover, the computational effort required in so complex models is not usually feasible even with very powerful computers. Finally, but not secondary, the interpretation of the huge amount of information of the NLDA results is not straightforward aiming at carrying out a performance-based assessment [47].

For these reasons, the use of NLSA is considered an effective tool [47] and it represents the most widespread method to study the global response of existing buildings, as well.

The main assumption of pushover-based methods is that the structure vibrates predominantly in a single mode. For this reason, NLSA is usually based on the application of a unique force distribution (for example proportional to masses or proportional to masses per height). Then, most Standards propose to apply at least two different load patterns (LP) or a combination of force distributions to approximately consider the evolution of inertial forces which depends on the

progressive degradation of the structure. However, the use of a single LP on the whole model risks to be too conventional in a pushover analysis framework. Indeed, it could fail in activating the nonlinear behavior of all the units in the aggregate. For example, when the most vulnerable units of the structure exhibit a nonlinear behavior, the others can almost remain in the elastic field. Furthermore, this assumption may not be fulfilled, especially in high-rise buildings, where higher modes effects may be important along their height [315]. However, both in low-rise buildings (like the majority of ordinary masonry structures) and in more complex structures (like the monumental ones) higher modes effects may be significant, due to the presence of in-plan irregularities (which induce torsional effects) or flexible diaphragms (then, the first mode does not activate all the walls). Other strategies in the field of NLSA as the multimodal or adaptive approaches have been mostly developed for other structural types (reinforced concrete and steel buildings) and their application to masonry is still under investigation even for simple structures [316, 317].

The second problem is connected to the availability of robust criteria to define proper performance levels on the pushover curve in case of complex masonry buildings. In the case of other typologies, e.g. RC buildings, the structural elements are usually modeled without a post-peak strength degradation and the seismic verification is developed through local safety checks. This procedure is not suitable for unreinforced masonry buildings, since their structural elements often present a significant strength degradation that needs an analysis involving the building in its entirety.

Finally, in order to evaluate the seismic demand corresponding to the attainment of the different performance levels, the NLSA needs a procedure to compare the capacity with a response spectrum. To this aim, firstly, the pushover curve representative of the behavior of the multi-degree of freedom (MDOF) system has to be transformed into the capacity curve of the equivalent single-degree of freedom (SDOF) one and, then, a procedure to properly reduce the elastic spectrum has to be adopted. Concerning the latter issue, several methods are proposed in literature and Standards (as the coefficient method in [318], the N2 method in [319], the capacity spectrum method (CSM) in [320]). Recent works highlighted how, among them, in case of structures characterized by a short period as the masonry structures the N2 Method risks to produce assessment not conservative [321]. Therefore, in Section 4.5 of this chapter the adoption of the CSM has been favored.

4.2.3   *Adopted procedure*

In order to face the aforementioned issues and to provide a first contribution to overcome the lack of operational tools identified in literature, this study proposes a procedure for the seismic assessment of irregular complex structures together with a first application to the case of fortresses. The procedure follows five steps:

1. Generation of a FE model of the whole aggregation of units aimed at explicitly capturing the mutual interaction effects;

2. Execution of a modal analysis to define the modes involving the dynamic response of all the units and their modal shapes;

3. Fitting of the modal shapes to define the LP distribution to be applied to each unit that may vary in plan and height;

4. Execution of a series of pushover analyses (for each unit) by applying to the whole numerical model the force distribution obtained from the modal shapes identified in point 3, which generally involves only one unit;

5. Conversion of the pushover curve of each unit in the capacity curve representative of the equivalent SDOF system and then finalization of the seismic verification.

Figure 54 sketches the proposed procedure, applied to the San Felice sul Panaro fortress (Section 3.2.2), which is the structure analyzed in this chapter.

It has to be pointed out that the subdivision in the various units presupposes the analyst's interpretation of the global modal configurations. However, the few practical guidelines listed below can help in the definition of the different units:

- for the standardized building typology object of this study (fortified buildings, e.g. castles, fortresses, and citadels), the post-earthquake damage systematically highlighted their propensity to exhibit an independent dynamic behavior of the towers, which are affected by the dynamic interactions with the adjacent structural bodies [314, 304]. This dynamic behavior is mainly due to: i) the architectural transformations occurred over the centuries which led to the actual structural configuration, mostly formed by towers connected through massive defensive walls; ii) the different dynamic properties, stiffness and strength which characterize the different units, thus determining these significant dynamic interactions. In this case, the experience from the damage observed after past earthquake can primarily address the analyst in the identification of the units;

- more in general, when there is no evidence of the dynamic behavior by the post-earthquake damage or for other building typologies (such as aggregates, monumental palaces or bell towers incorporated in a church) which are not characterized by recurring and standardized architectural configurations, identifying the various units can be not so trivial. However, also in these cases, a deepen preliminary analysis on the historical transformations faced over the-centuries and the analysis of their peculiar constructive features (also through in-situ investigations) can help the analyst to identify the various units and outline the most reliable hypotheses on their mutual interaction.
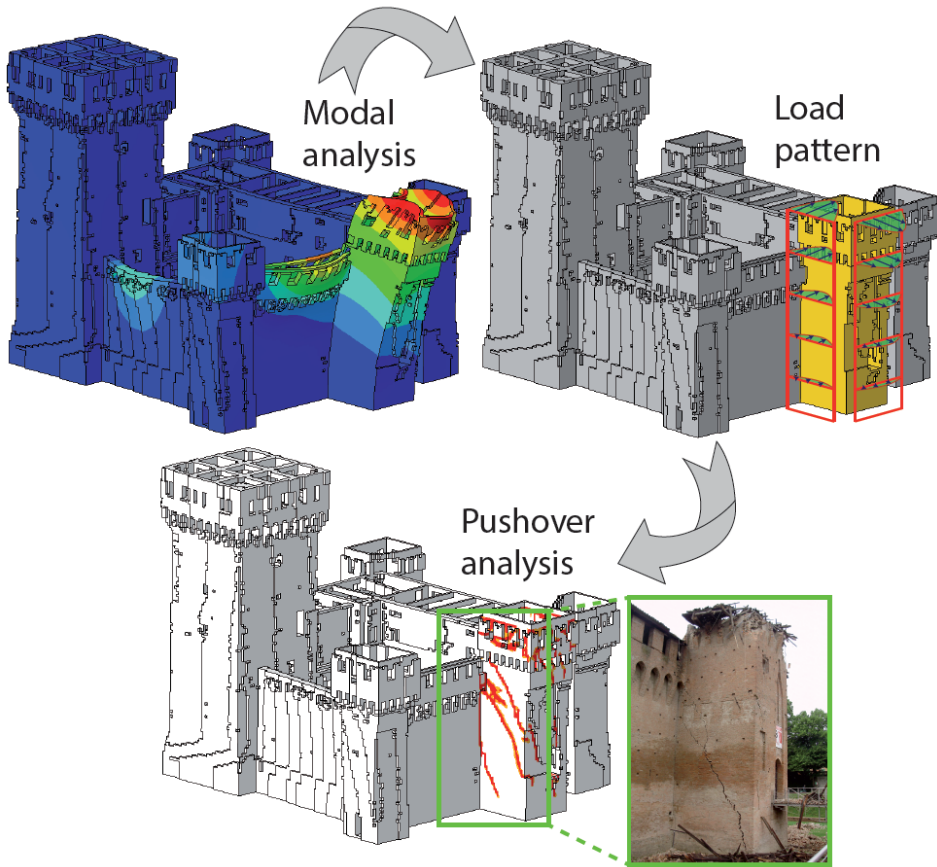
Figure 54: Sketch of the proposed procedure.

4.3 NUMERICAL MODELING OF THE CASE STUDY

The procedure has been then applied to the medieval fortress in San Felice sul Panaro (Section 3.2.2), significantly damaged by the 2012 Emilia earthquake. The finite element model of the fortress in San Felice sul Panaro has been developed by means of a non-standard mesh generation procedure called CLOUD2FEM, as showed in Section 3.2.4. In this section, the FE mesh generation of the case study is briefly revisited to account for the before-quake condition of the structure. Furthermore, the description of the adopted constitutive law for masonry, as well as the verification of the consistency of its mechanical parameters, are reported. Finally, the load pattern implementation and the analysis algorithm adopted are discussed.

4.3.1 *FE mesh generation*

As anticipated in Chapter 3, the municipality of San Felice sul Panaro commissioned a laser scanner survey of the fortress to acquire a detailed snapshot of its condition in the aftermath of the 2012 Emilia earthquake, see Section 3.2.2.2.

Although the survey and, hence, the generated model were based on the after-quake condition of the structure, it was possible to include the collapsed portions of the fortress in the FE model to obtain its before-quake condition. Indeed, by processing the 2D slices in a voxel framework, the lacking parts of the structure have been geometrically modeled with reference to a before-quake documentation (drawings, plans and photos). Figure 55 shows two examples of processed slices in which the geometry of the minor towers' crowning (collapsed due to the seismic events) has been recreated with a reasonably good approximation. Such an operation was facilitated by the peculiar mesh regularity, which helped the user in the geometrical reconstruction.
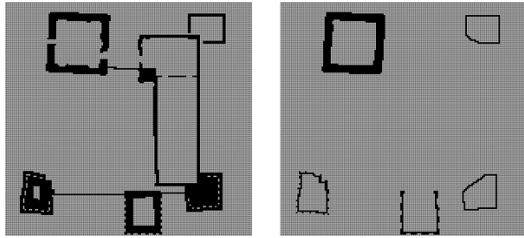
Figure 55: Example of processed slices to include the collapsed parts of the structure in the model.

Figure 56 shows the obtained 3D FE model of the fortress. The whole model counts 526,985 nodes and 424,096 eight-node hexahedral elements. As can be noted from the magnified portion, the adopted discretization is quite fine aiming at investigating the fortress global structural behavior. Indeed, all the structural elements of the fortress present at least 2-3 hexahedral elements along the walls' thickness. Exception is made for the minor towers crowing's walls, where in some portions only one element along the thickness is present. However, following the aforementioned scope, this condition can be tolerated.

Aiming at assessing the behavior under horizontal loading of masonry buildings, timber decks and masonry vaults have been found to significantly influence the overall response of a structure [47]. On the one hand, due to the well-known difficulties in modeling such horizontal elements, equivalent diaphragms can be used to model them. On the other hand, the utilized mesh generation approach automatically generates jagged 3D geometries of such elements. Such approximations, once again, can be considered satisfactory aiming at investigating the global structural response.

The effectiveness of the model generated is also shown in [306], where the model, in the after-quake condition, has been updated with ambient vibration
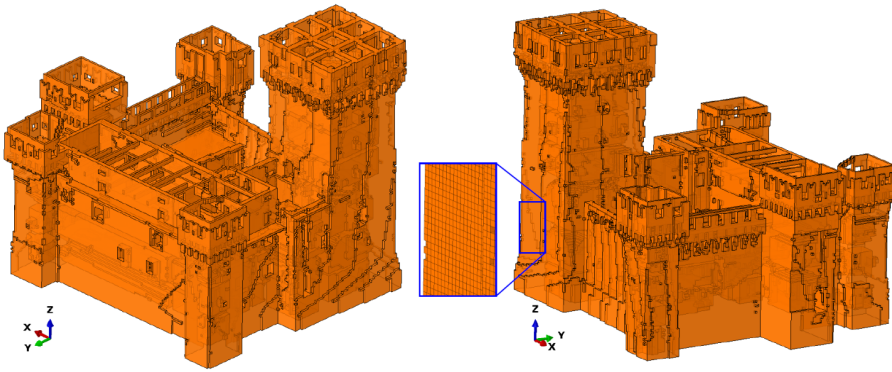
Figure 56: 3D finite element model of the fortress. The magnified portion shows the adopted discretization.

data measured on the Mastio. Indeed, the capability of adequately reproduce the first five natural frequencies and modal shapes of the Mastio showed the reliability of the FE model.

The fortress under study is a very complex building composed by several materials. For simplicity, four different material properties have been identified and implemented in the FE model (i.e. masonry, timber, reinforced concrete and terrain). Particularly, the last three materials have been assumed linear elastic, for simplicity. Conversely, the nonlinear behavior of masonry is described in the following, adopting a continuum model. It has to be noticed that, in order to do not alter the linear dynamic response of the structure (e.g. in terms of participating masses), the terrain, which is present in the courtyard of the building (with a level at approximately 3.50 m higher than the external one), has been considered with a very small density.

The model is assumed on a fix base. Indeed, although for massive structures as the fortresses the soil-structure interaction could be significant [322, 323], this assumption is considered reliable for the San Felice sul Panaro case study, since the soil underneath the fortress has not a poor quality and no damage caused by soil-structure interaction problems has been highlighted on the structure.

4.3.2 *Constitutive model for masonry*

In this study, the isotropic plastic-damage constitutive model developed by Lee and Fenves [136] for quasi-brittle materials is adopted for masonry. In the following, the main features and parameters involved in the model are recalled. For the reader's convenience, a summary of the model equations, accounting for the role of the parameters involved, is given in the Appendix A.

Two independent scalar damage variables are supposed. Particularly, one scalar damage variable for the compressive behavior ($0 \leqslant d_c < 1$) and one for the tensile behavior ($0 \leqslant d_t < 1$) are employed. According to the concepts of ef-

fective stress and strain decomposition, the stress-strain relations under uniaxial compression, σ_c, and tension, σ_t, are:

$$\sigma_c = (1 - d_c) E_0 (\varepsilon_c - \varepsilon_c^p), \quad \sigma_t = (1 - d_t) E_0 (\varepsilon_t - \varepsilon_t^p), \tag{1}$$

where E_0 is the initial Young's modulus of the material, ε_c and ε_t are the uniaxial compressive and tensile strains, and ε_c^p and ε_t^p are the uniaxial compressive and tensile plastic strains (Figure 57). In particular, the curves shown in Figure 57 denote the main input data required by the model.
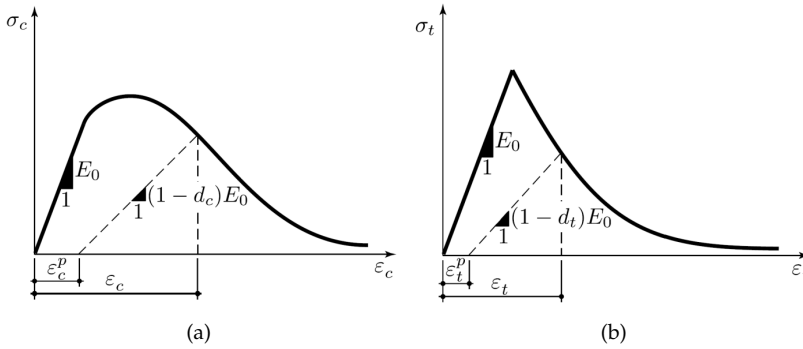
Figure 57: Plastic-damage constitutive law for masonry: (a) compressive and (b) tensile uniaxial stress-strain relationships.

The constitutive model is formulated in the context of non-associated plasticity [136]. Therefore, the plastic potential is characterized by the dilatancy angle ψ, generally assumed equal to $10°$ for masonry [324], and by a smoothing parameter ϵ usually assumed equal to 0.1 [325]. A multiple-hardening Drucker-Prager type surface is assumed as yield surface. This surface is specified by the ratio f_{b0}/f_{c0} between the biaxial f_{b0} and uniaxial f_{c0} initial compressive strengths and a constant ρ, which represents the ratio of the second stress invariant on the tensile meridian to that on the compressive meridian at initial yield. The values $f_{b0}/f_{c0} = 1.16$ and $\rho = 2/3$ are typically adopted for masonry [325].

Reference to the Italian code [242, 241] has been made to set the mechanical properties of the material (clay brick and lime mortar masonry). The value 1500 MPa has been adopted as Young's modulus of masonry.

The adopted compressive and tensile uniaxial stress-strain relationships are shown in Figure 58, leading to an indirect definition of the fracture energies in tension and compression, see the Appendix A. Particularly, the values 2.40 MPa and 0.12 MPa have been assumed as uniaxial compressive and tensile strengths, respectively [242, 241].

The evolution of the scalar damage variables d_t and d_c, as function of the uniaxial strains, has been kept substantially proportional to the decay of the uniaxial stresses (Figure 58), as adopted in several numerical campaigns of masonry
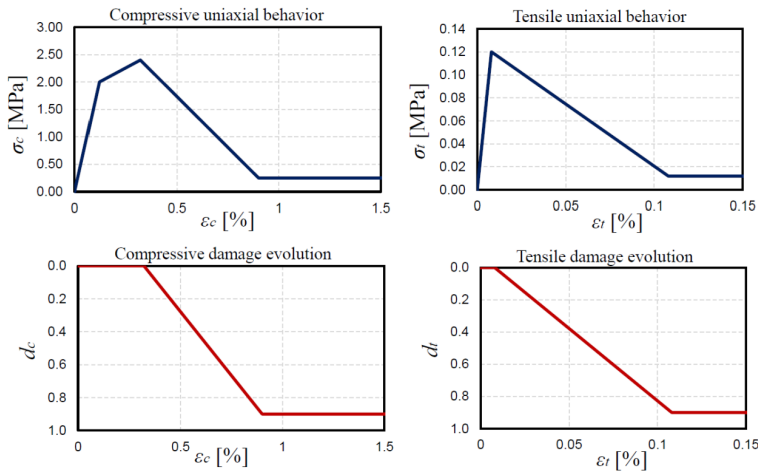
Figure 58: Uniaxial behavior and damage evolution for the compressive and tensile regimes.

structures [325, 141]. Although stress states in fortified masonry structures are usually far from compressive failures in static conditions, when these structures are pushed horizontally their compressive stresses significantly increase. Therefore, compressive softening is herein accounted for.

A summary of the adopted mechanical parameters is collected in Table 9. The

Table 9: Masonry mechanical parameters. E is the Young's modulus, ν is the Poisson's ratio, w is the material density and VP is the viscosity parameter used in the analysis.

E [MPa]	ν	w [kg/m3]	ϵ [\]	ψ [\]	f_{b0}/f_{c0} [\]	ρ [\]	VP [\]
1500	0.2	1800	0.1	$10°$	1.16	2/3	0.002

effectiveness of the constitutive model employed for masonry and of the mechanical parameters assumed with respect to the consequent strength predictions at the scale of masonry panels is shown in the following section.

4.3.3 Mechanical parameters consistency

The definition of reliable mechanical properties for existing masonry structures is a challenging task. This is even more complex when dealing with historic structures, where in situ destructive tests are limited or often forbidden. Therefore, reference to literature or codes material properties is usually undertaken. In particular, [241] provides mechanical properties for several representative masonry typologies which can be found on the Italian territory. However, such parameters (e.g. shear strength) are referred to the scale of masonry panels rather than the scale of the material, as contemplated instead in continuum FE formulations.

Thereby, the evaluation of the consistency of the adopted mechanical parameters with consolidated panel-scale strength criteria appears of primary importance.

To this aim, a simple benchmark of a masonry panel (Figure 59) has been modeled. The numerical outcomes obtained on the benchmark have been compared with well-known shear-strength criteria, as the ones contemplated in the Italian code [242, 24].
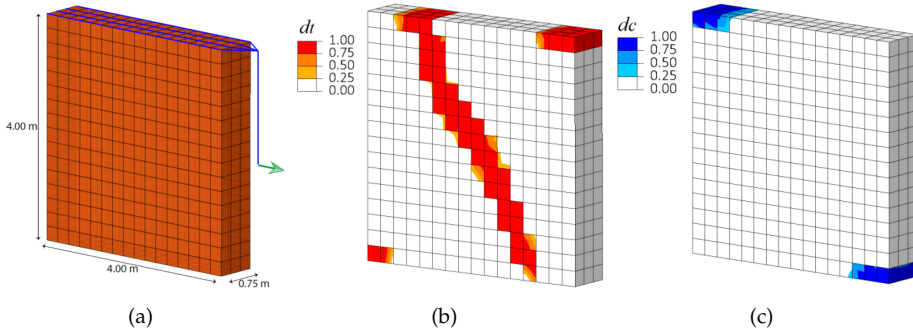
Figure 59: Benchmark used for the verification of the mechanical parameters: (a) 3D mesh, examples of (b) tensile and (c) compressive damage contour plots at failure ($\sigma/f_m = 0.43$).

Figure 59(a) shows the mesh used and its geometrical dimensions. Blue line elements in Figure 59(a) represent rigid links. The implemented mesh corresponds to the discretization adopted in the fortress model. The masonry panel has been subjected to vertical compressive normal stress coupled with shear stress. Several simulations have been carried out with different values of the vertical normal stress in order to simulate the whole strength domain of the panel. Typical tensile and compressive damage contour plots at failure are shown in Figure 59(b) and Figure 59(c), respectively.

Numerical findings, in terms of ultimate shear, have been compared with two well-known shear strength domains, which are contemplated in the Italian code [242, 241, 24], see Figure 60. In particular, the Turnsek-Cacovic [326] criterion with the modification then introduced in [327], see (2), and the criterion based on the failure due to combined compressive and bending stress, see (3), have been considered:

$$V_u = \frac{1.5\tau_0 Bt}{b} \sqrt{1 + \frac{\sigma}{1.5\tau_0}} \tag{2}$$

$$V_u = \frac{\sigma B^2 t}{2} \left(1 - \frac{\sigma}{0.85 f_m}\right) \frac{1}{B/2} \tag{3}$$

where V_u is the ultimate shear, τ_0 is the masonry shear strength without vertical normal stresses (the value 0.08 MPa has been assumed according to [242] for clay
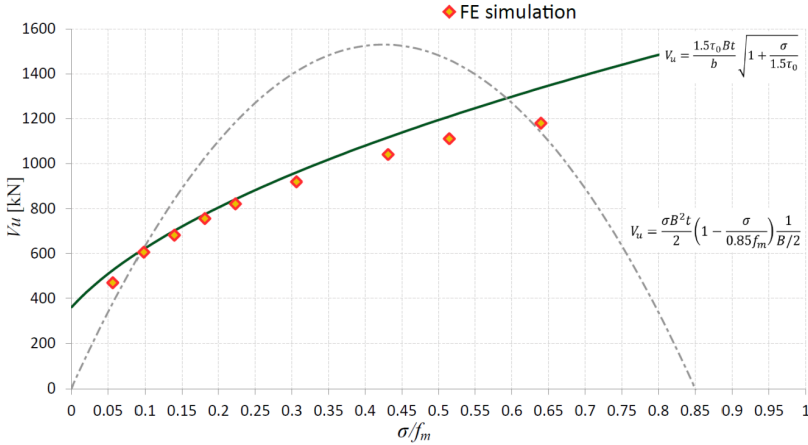
Figure 60: Ultimate shear comparison between strength domains for masonry panels and the results of FE simulations.

brick masonry with weak mortar and quite regular texture), B is the length of the panel, t is the thickness of the panel, σ is the average normal vertical stress and b is a corrective coefficient assumed equal 1. As can be noted in Figure 60, a good agreement between the FE results and the Turnsek-Cacovic shear-strength criterion can be observed. It has to be pointed out that the criterion defined in (3) is based on the conservative hypotheses of no-tension material and stress-block behavior in compression. Therefore, the slight overestimation of the numerical results with respect to (3) for very low or very high compressive stress appears reasonable and expected.

Generally, constitutive models which show softening behavior and stiffness degradation suffer from convergence issues in implicit analysis programs. A common stratagem to overcome some of these difficulties consists in using a viscoplastic regularization of the constitutive law, which leads the consistent tangent stiffness of the softening material to become positive for suitably small-time increments.

The adopted isotropic damage-plasticity model is regularized using viscoplasticity, i.e. eventually permitting stresses to be outside of the yield surface. The regularization is governed by the viscosity parameter (VP), which represents the relaxation time of the viscoplastic system. A small value of the VP, compared to the characteristic time increment, usually helps to improve the convergence of the model in the softening regime, without compromising results.

To evaluate the sensitivity of the numerical results to the VP value, a preliminary sensitivity analysis was performed on the FE model of the SW tower, which was extracted from the whole model. The LP defined in Section 4.4 for the SW tower was considered in the analyses. The results of the sensitivity analysis, in terms of pushover curves and tensile damage contour plots, are shown in Figure 61, whereas the times required by the numerical analyses are collected in Table 10.

Furthermore, the influence of the mesh size is shown in Figure 61, where a finer mesh, generated by subdividing each 8-node hexahedral element into four FEs the with orthogonal vertical planes (in order to preserve the same geometrical features), is considered.
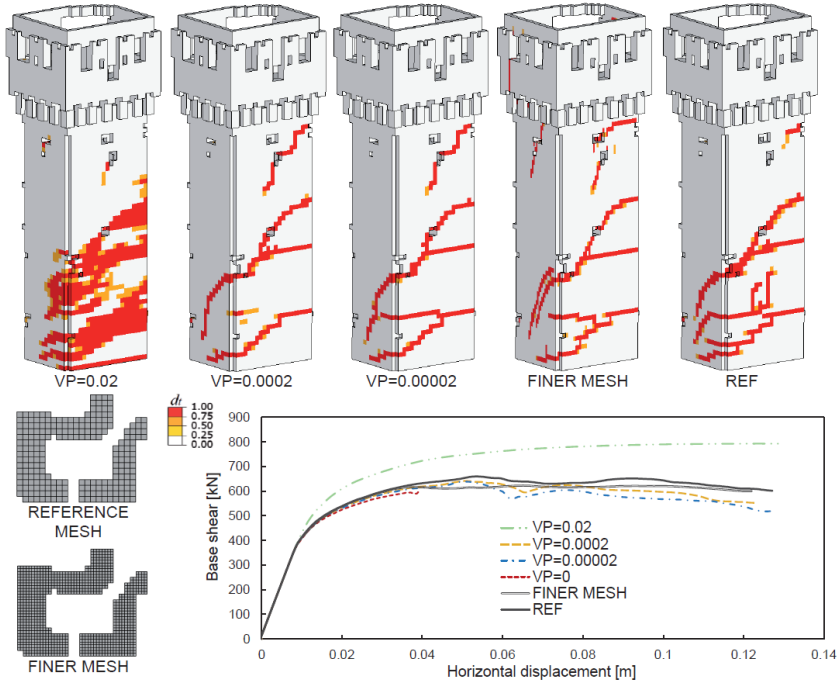
Figure 61: Sensitivity analysis on viscosity parameter and mesh size. The tensile damage contour plots are referred to a top horizontal displacement equal to 0.08 m.

By inspecting Figure 61 and Table 10, the REF analysis (VP=0.002) appears the best compromise between results accuracy and computational effort. This value, indeed, is used in all the computations herein presented. Although faster (Table 10,), greater VP values, e.g. 0.02, lead to a considerable overestimation of the shear force (Figure 61) together with a more spread distribution of the tensile damage, which makes the cracking pattern sensibly unrealistic (Figure 61). Conversely, localized cracks (usually defined by a single row of solid FEs) and similar cracking patterns are recorded for analyses with VP equal to 0.002 and smaller values. These analyses are also characterized by similar pushover curves, i.e. by small differences in the maximum shear force registered, which, in the Authors opinion, are included in between the constitutive law approximations. Analyses with VP values lower than 0.002 are, however, characterized by a sensibly higher computational demand. Emblematic is the case with VP equal to zero, i.e. no viscoplastic regularization is adopted. Indeed, in this case, although in the first part of the response the pushover curve appears quite close to the REF one, divergence

Table 10: Times required by the numerical analyses. [x] on a commercial laptop equipped with a processor Intel®Core™ i7-6500U CPU @ 2.50GHz and 16GB RAM.

Analysis	VP	Time required[x]
REF	0.002	00:41:05
FINER MESH	0.002	11:28:44
VP=0	0	Diverged
VP=0.00002	0.00002	04:38:13
VP=0.0002	0.0002	03:09:56
VP=0.02	0.02	00:27:12

is prematurely achieved. Finally, no particular influence of the mesh size on the pushover curve and on the cracking pattern is recorded.

4.3.4 *Load application and analysis procedure*

The FE model depicted in Figure 56 has been imported into the software Abaqus Standard [308], which has been used to perform the pushover analyses. The Italian Tier-1 cluster (GALILEO), devoted to scientific computing on the basis of national and European proposals (recently introduced in CINECA), has been exploited to conduct the simulations. Particularly, an 8-nodes supercomputer (RAM 128 GB per node) with two 8-cores Intel Haswell (2.40 GHz per node) has been utilized. Each pushover analysis lasted for 24 hours.

A two-step analysis approach has been implemented. Firstly, gravitational loads are applied to the structure. Secondly, non-uniform-distributed element-based horizontal loads have been applied through user-defined subroutines, following the LPs defined from the modal analysis.

To compute the solution up to the collapse of the structure (also in case of softening), a quasi-static direct-integration dynamic analysis algorithm has been adopted [308]. This algorithm allows to analyze quasi-static responses in which inertia effects are essentially introduced to regularize unstable behaviors. The Authors experienced a better performance of this algorithm, specifically in the softening regime, with respect to more common arc length procedures. Geometric non-linearity has been considered in the analyses to account for large-displacement effects.

4.4 APPLICATION OF THE PROPOSED PROCEDURE

As highlighted by the interpretation of the surveyed damage pattern [304], the San Felice sul Panaro fortress (Section 3.2.2) is composed of an aggregation of units (towers, curtain walls and recently added buildings) which exhibited an own behavior although strongly influenced by their mutual interaction. In the

following sections, the steps of the procedure are hereinafter illustrated referring to the units identified in Figure 62.

1. North (N) tower
2. North-West (N-W-) tower
3. South-West (S-W) tower
4. Mastio
5. North-Est (N-E) tower
6. West unit
7. North wall
8. Construction named "Casa Matta"
9. East wall
10. Entry unit
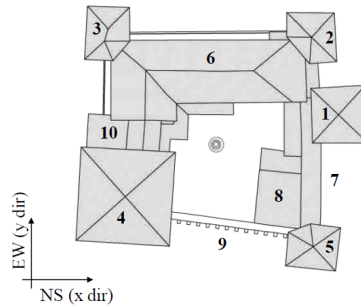
Figure 62: Identification of the main units in the San Felice sul Panaro fortress.

4.4.1   *Definition of the load patterns*

Once realized the 3D model of the whole structure, the procedure requires to perform a modal analysis to define the modes involving the dynamic response of all the units and their modal shapes.

To this aim, the identification of the main units of the structure (see Figure 62 for the case under study) is firstly required. Then, a modal analysis is performed (Figure 63) and each unit mass participant factor e^* (computed with reference to the mass of the unit under investigation) is evaluated (Table 11). Thereby, the modes which activate a significant mass with respect to each examined unit are so considered to define the load patterns. Therefore, rather than considering the modes with a significant participant mass with respect to the global structure, the ones which activate a significant mass with respect to each examined unit are here evidently preferred. Table 11 presents in particular: the units under investigation (use Figure 62 for the ID number); the selected mode/modes for each unit, together with the main direction/directions in which the mode is activated; the analyses' directions; and the mass participant factor e^* (computed with reference to the mass of the unit under investigation).

For each unit, only the modes involving its dynamic response have been considered and, for each mode, the so obtained modal shapes have been fitted with exponential, polynomial and linear functions, which vary in plan and height.

Table 12 collects the main dynamic parameters of the first twelve modes in terms of period T and participant mass in the x and y directions (M_x and M_y, respectively). Furthermore, the main units activated by each mode are identified (the identification number of units refers to Figure 62). It is worth noting that the modes of the Mastio (1 and 2 in Table 12) are coherent with the ones ob-
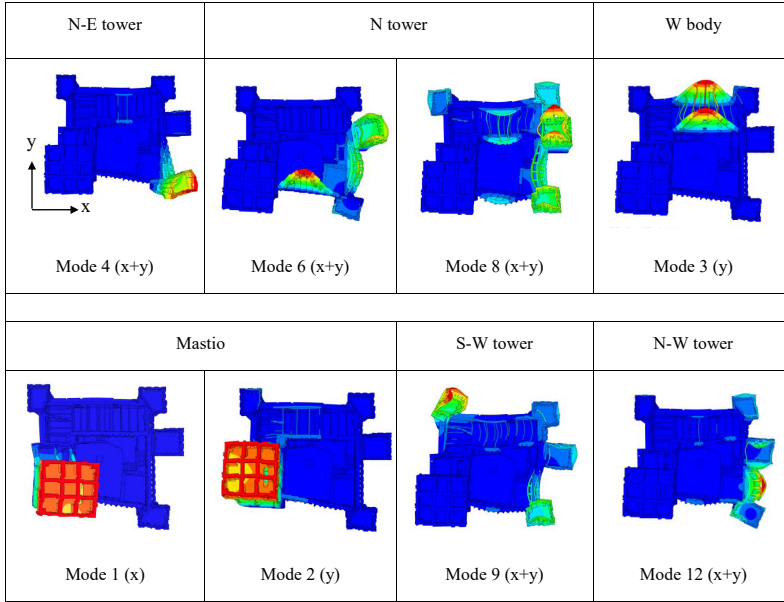
Figure 63: Modal shapes of the selected modes for each examined unit.

tained from the dynamic identification [39], performed on the Mastio after the earthquake.

Figure 64 shows the modal shape in plan and a sketch with the 3D LPs applied in the pushover analyses for some units of the fortress. Figure 65 collects the functions fitted from the modal shapes, showing the selected mode with its main direction (the axes are indicated in Figure 62), the functions fitted from the maximum and minimum modal displacements assumed for the force distribution in the nonlinear pushover analyses (where z is the vertical axis), and the function and a sketch of the LP applied in plan. As one can see from the table, three kinds of LPs have been applied in plan (constant, parabolic and linear trapezoidal), with a vertical outline which varies in height.

As it is possible to see from Figure 64 and from Figure 65, the applied distribution varies only in height while it remains constant in plan for some units (such as the Mastio), whereas for other units (such as the West unit), it varies both in height and in plan.

More specifically, Figure 65 collects: the kind of LP applied in plan (distinguishing between constant, parabolic and linear trapezoidal); the examined unit (Mastio, W unit, N-E tower, S-W tower, N-W tower, N tower); the selected modes with its main direction/directions; and the expressions of the functions used for the LP, fitted from the selected modal shapes. It has to be pointed out that for those modes characterized by significant displacements both in the x and y directions (i.e. modes 4, 6, 8, 9 and 12), the pushover analyses have been performed by simultaneously applying the x and y component of the LP.

Table 11: Values of the participant mass fractions e^* obtained for each unit.

Unit	Modes (direction)	Analysis	e^*
Mastio (n. 4)	2 (y)	W	0.486
	1 (x)	S	0.554
	2 (y)	E	0.559
	1 (x)	N	0.511
N tower (n. 1)	6 (x+y)	E+S	0.529
	6 (x+y)	W+N	0.498
	8 (x+y)	E+N	0.471
	8 (x+y)	W+S	0.521
SW tower (n. 3)	9 (x+y)	W+N	0.543
NE tower (n. 5)	4 (x+y)	W+N	0.618
W unit (n. 6)	3 (y)	E	0.174
	3 (y)	W	0.326
NW tower (n. 2)	12 (x+y)	E+N	0.555

Table 12: Dynamic parameters of the first twelve modes.

Mode	1	2	3	4	5	6
T [s]	0.470	0.431	0.284	0.251	0.227	0.216
M_x [%]	32.4	0.9	0	6.1	0.3	3.9
M_y [%]	0.9	34	8.1	1	6.8	2.6
Involved units	4	4	6	5	4-5-9	1

Mode	7	8	9	10	11	12
T [s]	0.209	0.199	0.186	0.182	0.166	0.162
M_x [%]	0	16.4	4.4	0	4.5	1.5
M_y [%]	0	7.8	8.2	0.5	3.8	6.8
Involved units	1-7-9	1	3	1-3-5-7	2-3-6	2
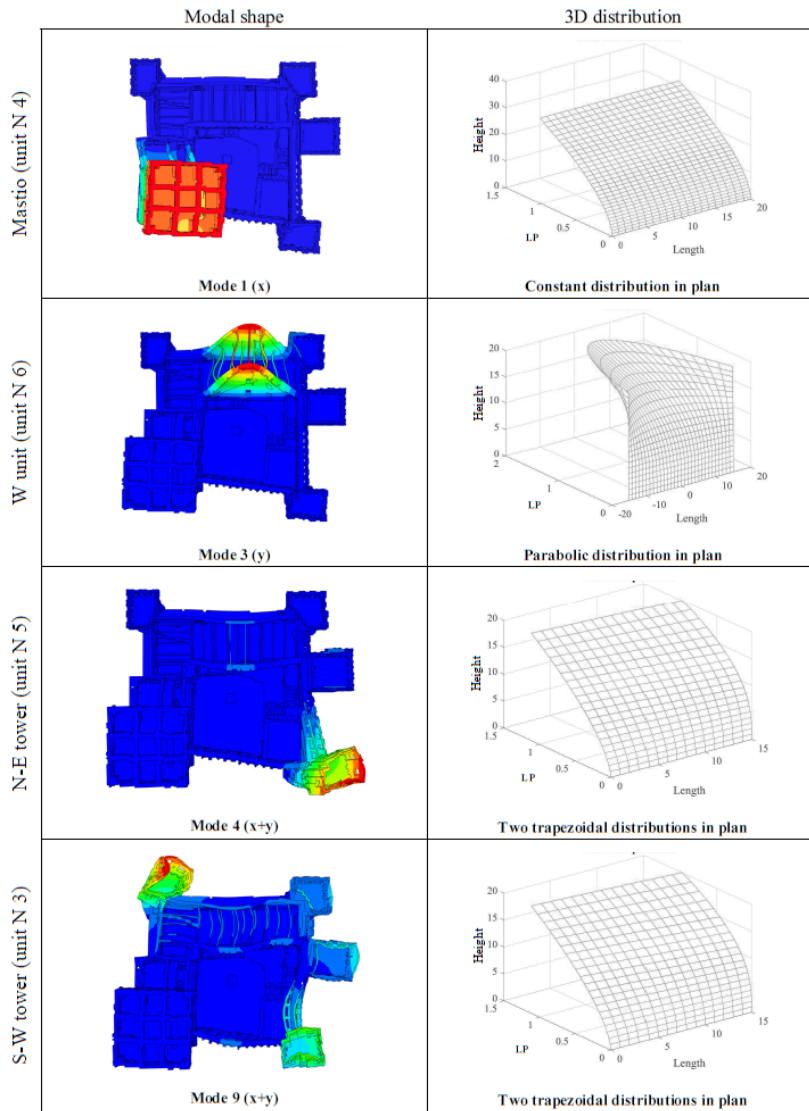
Figure 64: Identification of the main units in the San Felice sul Panaro fortress.
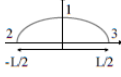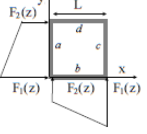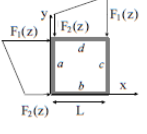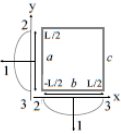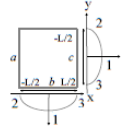
LP	Unit	Mode (dir.)	Function		
			Max	Min	Plan
Constant	Mastio	1 (x dir)	$F(z) = 0.0021 \cdot z^{1.78}$	$F(z) = 0.0021z^{1.78}$	-
		2 (y dir)	$F(z) = 0.0021 \cdot z^{1.77}$	$F(z) = 0.0021z^{1.77}$	-
Parabolic	W unit	3 (y dir)	$F_1(z) = 4e^{-05} \cdot z^{3.54}$	$F_2(z) = 8e^{-05} \cdot z^{1.63}$	$F(x,z) = F_1(z) - \left[\left(\frac{4x^2}{L^2}\right) \cdot (F_1(z) - F_2(z))\right]$
Linear trapezoidal on a and b	N-E tower	4 (x dir)	$F_1(z) = 0.0095 \cdot z^{1.59}$	$F_2(z) = 0.0003 \cdot z^{2.70}$	$F(x,z) = F_1(z) + \left(\frac{F_1(z) - F_2(z)}{L}\right)x$
		4 (y dir)	$F_1(z) = 0.01 \cdot z^{1.33}$	$F_2(z) = 5e^{-7} \cdot e^{0.70z}$	
	S-W tower	9 (x dir)	$F_1(z) = 0.0124 \cdot z^{1.50}$	$F_2(z) = 0.0002 \cdot z^{2.72}$	
		9 (y dir)	$F_1(z) = 0.01 \cdot z^{1.47}$	$F_2(z) = 0.0002 \cdot z^{2.56}$	
Linear trapezoidal on a and d	N-W tower	12 (x dir)	$F_1(z) = 0.0073z^{1.555}$	$F_2(z) = 0.0035e^{0.27z}$	$F(x,z) = F_1(z) + \left(\frac{F_1(z) - F_2(z)}{L}\right)x$
		12 (y dir)	$F_1(z) = 0.0078z^{1.649}$	$F_2(z) = 0.0008z^{2.317}$	
Parabolic on a and b	N tower	6 (x dir)	$F_1(z) = 0.004 \cdot z^{1.76}$	$F_2(z) = 3e^{-5} \cdot z^{3.17}$	$F(x,z) = F_1(z) - \left(\frac{4x^2}{L^2} \cdot (F_1(z) - F_2(z))\right)$
		6 (y dir)	$F_1(z) = 0.0063 \cdot z^{1.66}$	$F_2(z) = 0.0003 \cdot z^{2.42}$	
Parabolic on b and c		8 (-x dir)	$F_1(z) = 0.0079e^{0.26z}$	$F_2(z) = 0.0005z^{2.45}$	$F(x,z) = F_1(z) - \left(\frac{4x^2}{L^2} \cdot (F_1(z) - F_2(z))\right)$
		8 (y dir)	$F_1(z) = 0.0084e^{0.25z}$	$F_2(z) = 0.0007z^{2.15}$	

Figure 65: Functions of the LPs applied to the different units of the fortress.

4.4.2 *Nonlinear static analyses results*

Once evaluated the LPs (Figure 65), the procedure has been firstly applied to the Mastio to verify its effectiveness. The results have been compared with those obtained by applying a unique load proportional to the height to the whole fortress; the latter is consistent with that usually proposed in codes [242]. The results were compared in terms of damage pattern (Figure 66), pushover curves (Figure 67(a)) and capacity curves (Figure 67(b)) showing a quite good agreement.

(a)   (b)
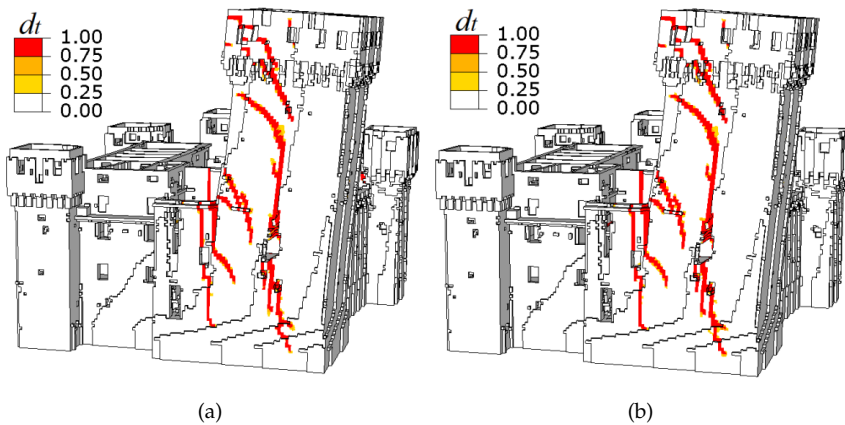
Figure 66: Comparison in terms of damage pattern obtained applying a unique LP: (a) to the whole fortress, and (b) only to the Mastio.

(a)   (b)
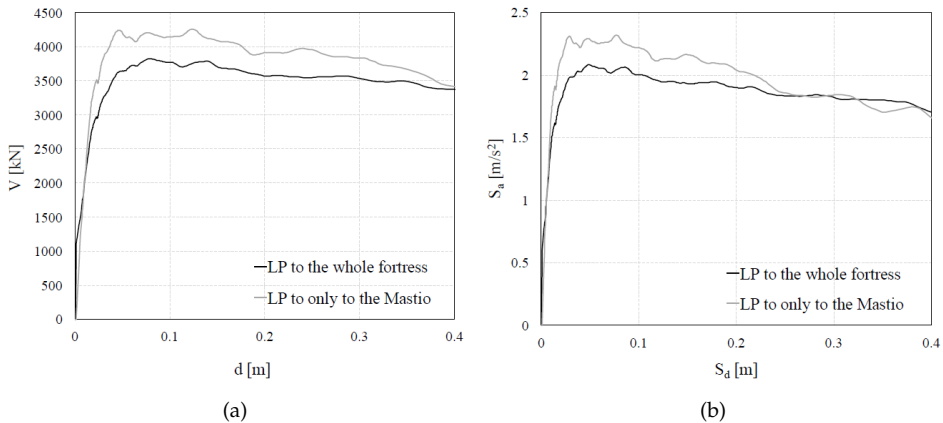
Figure 67: Comparison in terms of (a) pushover curves and (b) capacity curves obtained applying a unique LP to the whole fortress (curves in black) and only to the Mastio (curves in gray).

However, by applying a unique LP to the whole fortress, only the nonlinear response of the Mastio (which is the first unit to be damaged) is activated (Figure 66), while the response of the other minor towers is substantially still linear elastic. This is highlighted from the simulated damage pattern in Figure 66(a) obtained by applying the force distribution to the whole fortress, where it is evident that the main damage is concentrated in the Mastio, while the other towers and the adjacent unit are interested only by a very light damage.

Furthermore, in Figure 67 the curves are rather akin in terms of stiffness and they differ of less than 10% in terms of maximum strength. The base shear is evaluated at the base of the Mastio for both analyses, for the sake of comparison. Then, it is possible to observe that, when the LPs are applied to the whole fortress (black curves in Figure 67), the softening effect is less pronounced.

Nonlinear static analyses have been then carried out in both the directions +/- X and +/- Y, as indicated in Figure 62. From the results, the following data have been extracted:

i the global shear at the base of the whole fortress, expressed as function of the average displacement at the top level of each unit;

ii the displacements of several nodes evenly placed along the height of each unit at the beginning of the response, thus representative of an elastic phase. These values allowed calculating the participation coefficient and the participation mass necessary to transform the pushover curves into the capacity curves of the equivalent SDOF system.

Starting from these data, the pushover curves $(V - d)$ of each unit have been obtained and then converted into the corresponding capacity curve $(V^* - d^*)$, following the general principles of [319], adopted in [242] as well, and based on the evaluation of the participation coefficient Γ and the mass M^* of each unit (see Eq. (4)), where ϕ_i is the ith component of the eigenvector representative of the first modal shape and m_i is the correspondent modal mass). Hence, the capacity curve was obtained by dividing the displacement d by $\Gamma(d^* = d/\Gamma)$ and the base shear by the product $\Gamma M^*(V^* = V/(\Gamma M^*))$, where Γ and M^* were related to the unit under investigation.

$$\Gamma = \frac{\sum m_i \phi_i}{\sum m_i \phi_i^2} = \frac{\sum m_i \phi_i}{\sum m_i \phi_i^2} \tag{4}$$

4.5 VALIDATION OF THE PROPOSED PROCEDURE

This section presents the results of the application of the proposed procedure to the examined case study, in terms of comparison between the seismic demand and the system capacity. In particular, in this case, the seismic demand came from the records of the SAN0 station from the ITACA network, which was very near to the Fortress. Two seismic shocks of comparable entity occurred in May 2012. However, no near-field records of the first shock were available. Hence, in the

examined case, the actual records that hit the monument on the 29th May 2012 was considered as seismic action.

Figure 68 shows (a) the localization of the SAN0 station with respect to the Fortress, and (b) the comparison (in terms of acceleration-displacement response spectra) of the two components North-South (NS) and East-West (EW) of the actual record of the 29th May 2012.

<table>
</table>

(a)   (b)
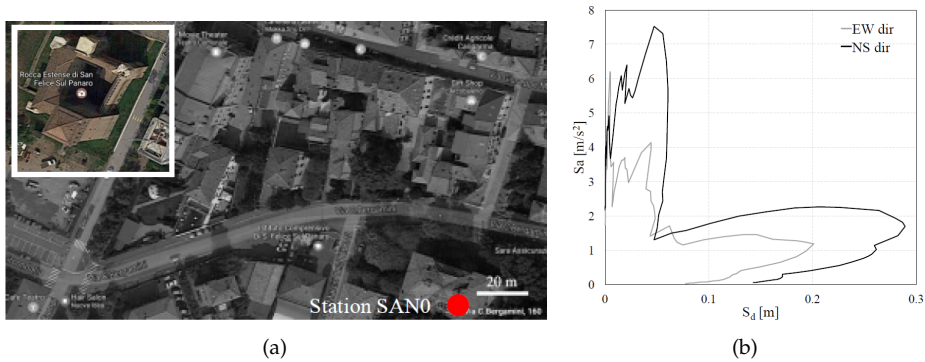
Figure 68: (a) Localization of the SAN0 station. (b) Comparison in terms of acceleration-displacement response spectra between the NS and the EW components of the actual 29th May 2012 seismic event (from SAN0 station - ITACA network).

The results were interpreted in terms of expected ductility demand μ_{PP}, representative of the ductility reached by the different units during the 2012 earthquake. This parameter has been assumed as reference to estimate the entity of the damage level attained together with its qualitative comparison with the actual one occurred. Indeed, it is expected that the units with higher values of ductility demand would correspond to the ones characterized by a more significant damage (in terms of spread and gravity of the cracks).

4.5.1 *Assessment of the expected seismic demand*

The first step to evaluate the ductility demand was the estimation of the seismic demand d_{PP} expected from the 2012 earthquake. This latter was evaluated by applying CSM [320], since recent studies proved that other methods of verification proposed in literature and in Standards (as the N2 method [319]) cannot considered equally reliable for masonry structures, such as the examined one [47].

The CSM is based on the use of overdamped reduced spectra, computed using a reduction coefficient (ξ) aimed to conventionally take into account the progressive nonlinear response trough the concept of hysteretic damping for ductility values higher than 1. In the examined case, the overdamped response spectrum has been

evaluated on the basis of the well-known reduction law, adopted in [242] as well:

$$\xi = \xi_{el} + \xi_{max}\left(1 - \frac{1}{\mu^{\beta}}\right) \tag{5}$$

where ξ_{el} is the elastic damping (assumed equal to 5%); ξ_{max} is the maximum hysteretic damping (assumed equal to 20%); μ is the ductility computed starting from the displacement associated to the considered limit state, calculated once converted the capacity curve in the equivalent bi-linear; β is a coefficient herein assumed equal to 0.6. The latter value is compatible with the ones traditionally assumed for masonry structures [328]. It is worth noting that the evaluation of the bi-linear curve from the capacity curve is not strictly necessary to apply the CSM but only to evaluate the ductility μ.

Therefore, once evaluated the capacity curve for each unit, the expected seismic demand d_{PP} was evaluated as the spectral displacement obtained comparing the capacity curve with the overdamped response spectrum generated from the actual records of May 2012.

Figure 69 shows, by way of example in the case of the Mastio, the comparison between the capacity curve of the system (in black) and the actual overdamped spectrum (through the continuous grey). In this case, the response spectrum is the one obtained considering the EW component of the record (grey dotted line in the figure), properly overdamped as above described, that is starting from a period corresponding to ductility values higher than 1.
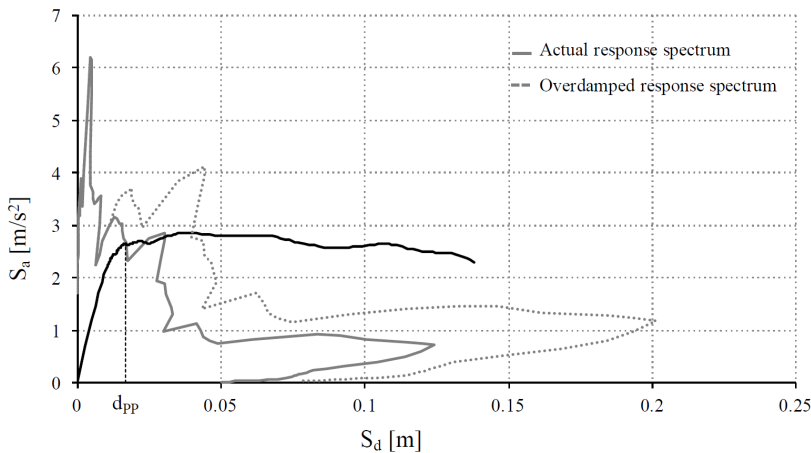
Figure 69: Comparison between the capacity curve of the system and the actual over-damped spectrum (EW component of the record) for the estimation of the expected seismic demand.

Although the use of a real response spectrum can be conventional in the application of the CSM (due to its irregular shape), is has been considered more

representative with the aim of validation being more representative to the real event that hit the structure.

It has to be pointed out that, in the CSM method framework, the seismic assessment has been developed:

i in the X and Y directions for the units where the LP applied in the pushover analyses pushed the unit in those directions one at a time;

ii with respect to the resultant axis of the two forces' distributions applied simultaneously along the orthogonal axes X and Y. In this case, the values of shear and displacement obtained from each pushover have been projected with respect to the above-mentioned axes.

4.5.2 *Definition of the ductility demand and comparison with the actual damage*

Once evaluated the demand displacement d_{PP}, it was necessary to estimate a conventional yielding point d_y to convert the d_{PP} into the expected ductility demand to provide an estimate of the comparison with the actual damage level occurred. To this aim, a bi-linear curve was defined according to the principles proposed for masonry structures by [34] and assuming an initial stiffness which was representative of the actual one of each unit. Then, the actual ductility demand μ_{PP} is computed as $\mu_{PP} = \frac{d_{PP}}{d_y}$.

Table 13 presents a summary of the results obtained for all the units (identified by the numbers of Figure 62), in terms of:

i period which defines the initial elastic branch of the bi-linear curve (T*);

ii value of the calculated ductility demand μ_{PP}, obtained alternatively comparing the capacity curve of each unit with the overdamped response spectrum obtained from the NS or EW component of the actual record.

Moreover, an empirical Damage level graduated according to the EMS98 scale [329] has been assigned to each unit, distinguishing between the one occurred in the main body of the unit (D) and the one interesting the tower top parts ($\overline{D}$). In particular, concerning the assignment of D, the criteria summarized in Table 14 have been adopted, while for the top parts ($\overline{D}$) the damage level has been assigned depending on the seriousness and extent of the damage interesting towers corbels, battlements and roofs. The qualitative correspondence between the obtained ductility level μ_{PP} and the empirical damage level assigned has been assumed as further factor for assessing the reliability of numerical analysis performed. In fact, values of μ_{PP} higher than 1 indicated the structural response progressed in the nonlinear field and increasing values should be associated to more significant and spread damage.

Figure 70 indicates, on the fortress plan, the damage levels (D [329] and $\overline{D}$) associated to each unit and the maximum ductility demands obtained from the procedure. The number in red identifies the different units (as in Figure 62).

Table 13: Results of the proposed procedure validation.

Unit	N	Dir.	T*[s]	μ_{PP}[-] (NS rec.)	μ_{PP}[-] (EW rec.)
Mastio	4	W	0.379	3.373	1.192
		S	0.471	3.229	2.397
		E	0.466	3.306	2.484
		N	0.419	3.383	1.417
North tower	1	E+S	0.120	0.768	0.831
		W+N	0.176	1.312	1.309
		E+N	0.219	1.409	1.159
		W+S	0.0844	1.548	1.172
S-W tower	3	W+N	0.182	1.046	1.048
N-E tower	5	W+N	0.306	4.911	0.957
N-W tower	2	E+N	0.127	1.088	0.674
West unit	6	W	0.518	4.207	3.843
		E	0.509	3.590	3.253

As one can see from Figure 70, it is clear that referring to the damage in the top parts ($\overline{D}$), damage mechanisms due to the interactions with the roof are present in almost all towers (sometimes the roofs even collapsed). Instead, the damage interesting the tower main body is more differentiated. In particular, from the observation of the post-earthquake damage (confirmed also by the damage pattern numerically simulated), it appears that two different situations occurred:

i the damage occurs first in the top parts; hence, the forces in the pushover are not able to further increase and the tower main body is not damaged, remaining almost in the elastic phase. This for example happened in N-W and S-W towers (respectively, units 2 and 3 in Figure 62);

Table 14: Criteria for the definition of the damage level D [329] expressed in Figure 70.

Damage Level	Observed damage
D2	Visible cracks. However, the structure preserves its structural functionality but is close to the attainment of its maximum shear strength
D3	Significant and spread cracks. The structure has reached the maximum resistance to horizontal actions and present permanent deformations
D4	Partial local collapse, due to the in-plane behavior of the units
D5	The unit is near to the collapse
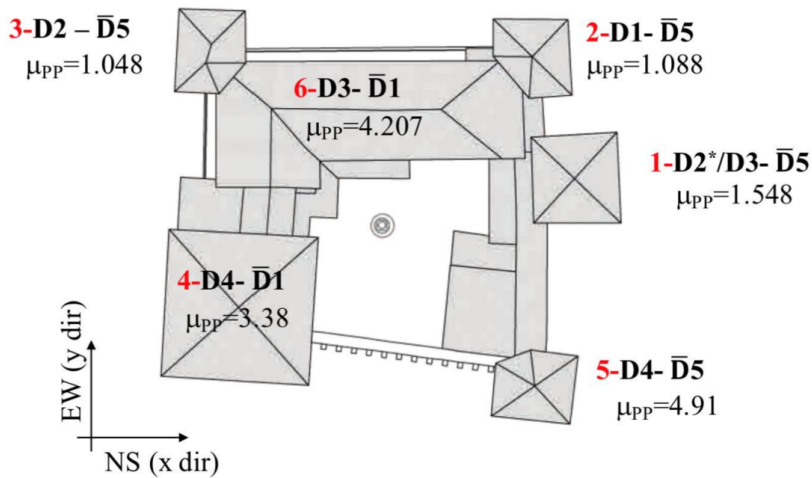
Figure 70: Damage levels associated to the tower main bodies (D) and top parts ($\overline{D}$) and maximum obtained ductility demands, identified on the fortress plan.

ii the damage occurs first in the tower main body and then it spreads across the top parts. This latter happened in the Mastio, the N-E tower and the N tower (units 4, 5 and 1 respectively in Figure 62).

Interpreting the results in light of these two possible occurred situations, one can observe that there is a good correspondence between the level of damage and the highest value of maximum expected ductility demand μ_{PP}. In fact, the first condition is associated to a minor level of ductility (N-W and S-W towers reach a maximum ductility level equal to 1.088 and 1.048, respectively), whereas the second one corresponds to higher level of expected ductility. This latter is for example the case of the North tower (with a maximum ductility level in the most punitive direction equal to 1.548), of the N-E tower (with a maximum ductility equal to 4.911) and of the Mastio (with maximum ductility level in the most punitive direction equal to 3.383).

Furthermore, the comparison with the actual damage occurred after the 2012 earthquake highlighted a very good correspondence with the one numerically simulated. Hence, the obtained results confirmed the proposed procedure reliability. Figure 71 and Figure 72 show the damage contour plots in terms of tensile damage (d_t), extracted at the maximum expected ductility demand (performance points), for some units of the fortress. For the sake of comparison, photos of the actual crack pattern experienced by the structure due to the 2012 Emilia earthquake are reported as well. A very good agreement between the simulated crack pattern and the actual one is observed in terms of both damage level and crack location.
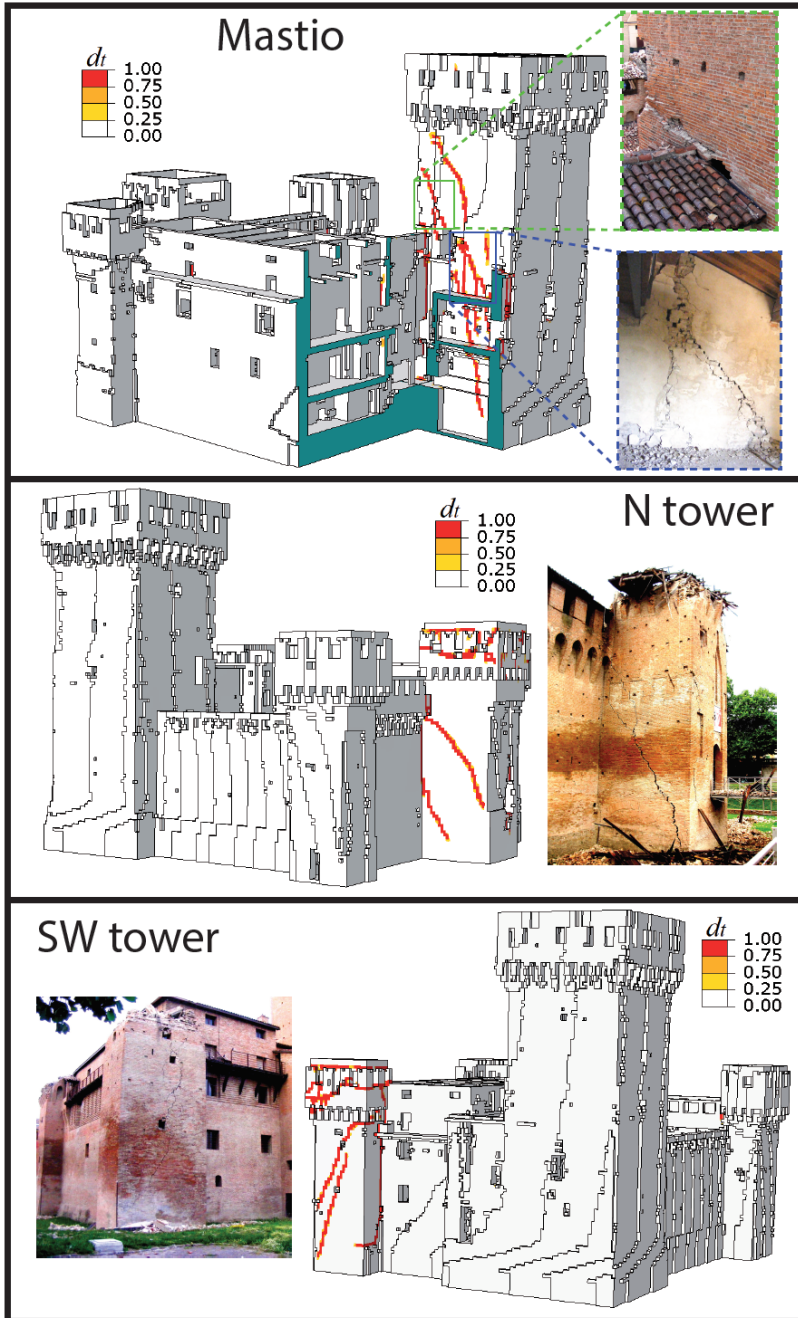
Figure 71: Comparison between the actual damage pattern and the simulated one for some units of the fortress at the performance point: Mastio (S dir.), N tower (W+S dir.) and SW tower (W+N dir.).
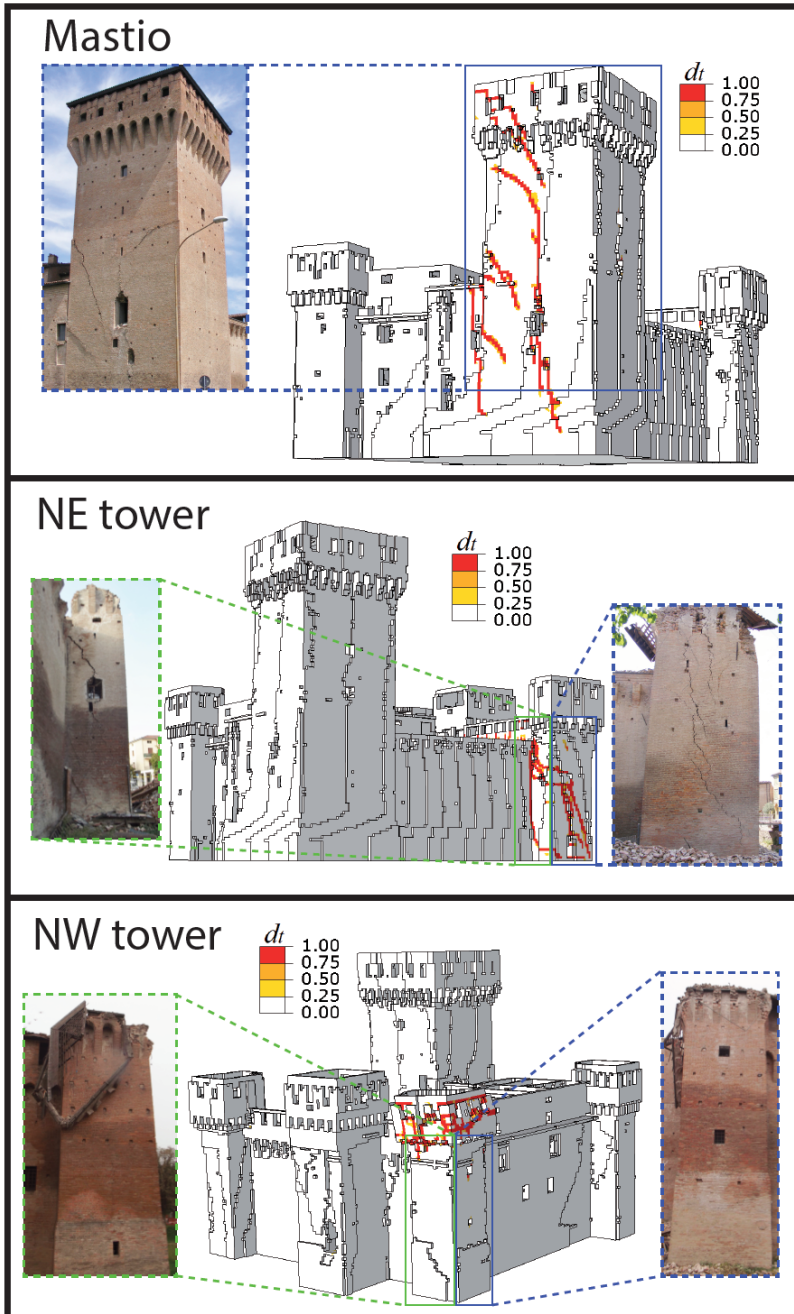
Figure 72: Comparison between the actual damage pattern and the simulated one for some units of the fortress at the performance point: Mastio (E dir.), NE tower (W+N dir.) and NW tower (E+N dir.).

4.6   CONCLUSIONS

The seismic assessment of interacting structural units in complex historic masonry constructions is a very difficult task, not manageable *a priori* through well-defined procedures of analysis and verification. As a first attempt to provide operative tools, this study proposed a procedure for the seismic assessment of such complex structures.

The procedure requires: a numerical model of the entire aggregation of units, in order to explicitly consider the interaction effects among these latter; the execution of a modal analysis to define the modes involving the dynamic response of each unit and their modal shapes; the execution of a series of pushover analyses (one for each unit) by applying time by time the load pattern fitted according to the identified modal shapes; the conversion of the pushover curve of each unit into the corresponding capacity curve of the equivalent SDOF system, in order to perform the seismic verification.

The procedure has been then applied to a case-study, the medieval fortress in San Felice sul Panaro, significantly damaged by the 2012 Emilia earthquake. The results are good in terms of comparison between the damage experienced by the structure and the one predicted (evaluated computing a ductility demand required by the actual seismic event), showing the potential of the proposed procedure. Given such promising results, the application of the procedure could be extended in the future to other kinds of complex monumental structure (e.g. palaces in aggregate).

AN ANALYSIS PROCEDURE FOR LEANING STRUCTURES

This chapter introduces an automatic, powerful and easy to use procedure for undertaking stability analyses of leaning historic masonry structures, based on an upper bound FE limit analysis (FELA) approach. The procedure proposed here consists of a two-step FELA that reduces drastically optimization variables assuming only active few elements inside a restricted processing zone. To generalize the Heyman's intuition to complex real geometries, the use of a 3D upper bound FELA with a recursive kernel of variables reduction becomes necessary for a precise evaluation of the limit inclination that makes the structure collapse under gravity loads. This outcome permits to estimate the structural health condition of a historic structure by comparing the critical inclination angle against the actual one. To demonstrate the effectiveness of the automated procedure, the southwest leaning tower of the Caerphilly castle (Wales, UK) is investigated and failure mechanisms with collapse inclination angles are evaluated through FELA. The proposed procedure presents a high degree of automation at each operational level and, hence, could be effectively used to assess the stability of historic structures at a national scale and provide useful information to asset owners to classify the structural health condition of leaning historic masonry structures in their care.

5.1   INTRODUCTION

Leaning historic masonry structures are fascinating to observe. Perhaps the most famous examples include the Pisa [1, 330] and the Ghirlandina towers [331]. The reason why historic masonry structures lean is a complex area of study and have stimulated the interest of the scientific community for over a century [332]. Due to their narrow foundations, tall and slender historic masonry structures such as towers, whose height is much greater than their width, are generally more prone to lean. Two major reasons why masonry towers tilt are: (a) lack of foundation strength; and (b) lack of foundation stiffness aggravated by progressive soil creep phenomena [332]. Several advanced soil-structure interaction models have been developed to study these phenomena [332]. However, such models require the setting of a numerous amount of mechanical parameters; most of them correlated with in-depth in-situ soil tests. Furthermore, they do not allow for a rapid check on the structural condition of the structure.

Heyman [333] was probably the first to study analytically the safety of leaning towers by assuming masonry as a rigid material unable to withstand tensile

stresses. Such simplification allowed deriving a quite simple differential equation describing the crack curve delimiting the failure mechanism and providing very useful hints on the limit inclination angle associated with the collapse of the structure. However, the hypothesis of rectangular full or thin-walled sections and the absence of any irregularity along the height represent a remarkable limitation of the approach, since in practice it is not realistic. Vertical walls of towers vary considerably in thickness and they often present irregular openings [1]. Furthermore, historic towers, or other height-prevalent historic structures (e.g. walls in churches, curtain-defensive walls etc.), frequently stand in a ruined condition, and have been subjected to unforeseen load events (e.g. bombing, successive demolitions, sabotages, raids etc.) over the centuries [334]. Often, such structures suffered alternations and today, only a few portions of the original structure remain standing. Consequently, the geometry of these structures is generally extremely complex and irregular (see for instance [335]). Their complex geometries suggest to consider advanced methods of analysis where the actual 3D geometry of the structure is accounted for in the calculations [336].

One of the first challenging tasks that appears when dealing with the numerical modeling of this kind of structures lasts in acquiring their 3D geometric features. The use of automated surveying techniques, such as terrestrial laser scanning and close-range photogrammetry which produce dense point clouds, appears particularly suitable for obtaining the geometry and the mesh of historic structures, as pointed out in Chapter 3.

Once the mesh is available (see Chapter 3), it can be used within several computational tools for the structural analysis of historic masonry buildings, see Chapter 2.

Another issue is how to determine the maximum inclination angle that leads to the collapse of a tower due to the loss of stability under the application of gravity loads. Concerning a no-tension material with rectangular cross section, Heyman [333] was able to analytically determine the collapse inclination angle and the corresponding crack pattern shape. Unfortunately, an analytical approach for real irregular geometries is hardly applicable, and an automatic procedure is needed.

To deal with such key issue, and following the Heyman's work [333], the use of a two-step 3D upper bound FELA on the mesh of the actual geometry is conducted and the critical condition (i.e. maximum inclination capacity) of a leaning historic masonry structure is evaluated.

The procedure is indeed an upper bound limit analysis with FE discretization obtained by means of tetrahedron rigid elements and rigid-perfectly plastic interfaces exhibiting frictional behavior and very low cohesion (i.e. mimicking a quasi no-tension material with friction).

Considering that FE meshes obtained, for instance, from the watertight meshing procedure (Section 3.3) would be constituted by hundreds of thousands of elements and interfaces, the limit analysis problems derived would be characterized by millions of variables, i.e. in practice impossible to solve even with super-computers.

An alternative to parallelization is proposed here, which is essentially a master-slave approach conceived with the aim of reducing drastically the total number of optimization variables. The procedure is based on the hypothesis that the tower collapses for the plasticization of few elements located in a limited processing zone, which is a-priori established in the first step. Elements with centroids inside the processing zone are assumed potentially active. The rest of the mesh is excluded from computations and it is treated as a single rigid body characterized by six degrees of freedom (i.e. three centroid velocities and three rotation rates). The solution of the linear programming problem found in the first step provides a more accurate estimation of the potential interfaces undergoing plasticization.

In the second step, the processing zone is further reduced to those elements whose interfaces exhibit meaningful inelastic deformation rates plus few contiguous ones, to further drop-down the optimization variables. Conversely, the failure surface linearization on the active interfaces is refined to obtain more accurate estimates of the collapse multiplier. The master-slave kernel is then coupled with a sequential linear programming algorithm to deal with the linearization of the normalization condition equation, which results nonlinear due to the assumption of the inclination angle at failure as collapse multiplier.

The outcome obtained with the limit analysis permits to practically estimate the structural health condition of a leaning historic structure, e.g. by comparing the maximum critical inclination angle against the actual one. Since the computational approach proposed herein presents a high degree of automation at each operational level, its usage could be addressed to the stability analysis of historic structures at a national scale. In particular, this approach could be beneficial for asset managers, which want to classify the structural condition of leaning historic assets in their care and devise action plans for their survival.

In this research, the southwest leaning ruined masonry tower of the Caerphilly castle (Section 3.3.1) is employed as a case study to demonstrate the effectiveness of the proposed approach.

5.2   LIMIT ANALYSIS OF LEANING STRUCTURES

The stability assessment of 3D masonry structures having complex geometry by means of limit analysis can be performed with 4-nodes rigid infinitely resistant tetrahedrons and triangular interfaces where plastic dissipation can occur. The utilization of interfaces has proved to be effective for cohesive frictional materials [337, 338, 190, 195], even if yield lines are fixed and re-meshing would be required. However, the utilization of rigid elements reduces to a great extent the optimization variables, which is desired in case of complex geometries. The following formulation permits the flow rule to be violated in the discontinuities preserving, nevertheless, the upper bound property of the solution. The discontinuity occurs at the common edge between two adjacent tetrahedrons. To be kinematically admissible, the normal and tangential velocity jumps across the discontinuity must satisfy the flow rule.

5.2.1 *Finite element limit analysis 3D model*

The kinematic variables of a tetrahedron E are the three centroid velocities (u_x^E, u_y^E, u_z^E) and the three rotation rates (Φ_x^E, Φ_y^E, Φ_z^E) around the centroid (Figure 73). Jump of velocities $[\mathbf{U}(P)]$ at a point $P = (x_P, y_P, z_P)$ on an interface I between two adjoining elements M and N are evaluated as follows:

$$\left[\mathbf{U}_P^M - \mathbf{U}_P^N\right] = \mathbf{U}_G^M - \mathbf{U}_G^N + \mathbf{R}^M\left(P - G^M\right) - \mathbf{R}^N\left(P - G^N\right) \tag{6}$$

$$\mathbf{U}_P^E = \begin{bmatrix} u_x \\ u_y \\ u_z \end{bmatrix} = \begin{bmatrix} u_x^E \\ u_y^E \\ u_z^E \end{bmatrix} + \begin{bmatrix} 0 & -\Phi_y^E & \Phi_z^E \\ \Phi_y^E & 0 & -\Phi_x^E \\ -\Phi_z^E & \Phi_x^E & 0 \end{bmatrix} \begin{bmatrix} x_P - x_G \\ y_P - y_G \\ z_P - z_G \end{bmatrix} = \\ = \mathbf{U}_G^E + \mathbf{R}^E\left(P - G\right) \tag{7}$$

$[\mathbf{U}(P)]$ must be written in the local coordinate system of the interface $\mathbf{r}_1^I - \mathbf{r}_2^I - \mathbf{s}^I$ as $\Delta \mathbf{U}(P) = \begin{bmatrix} \Delta r_1 & \Delta r_2 & \Delta s \end{bmatrix}^T = \mathbf{R}^I [\mathbf{U}(P)]$, where Δr_1, Δr_2 and Δs are the velocity jumps (two tangential and mutually orthogonal and one perpendicular to the interface, see Figure 73) in the local coordinate system and $\mathbf{R}^I$ is the rotation matrix of the local frame of reference with respect to the global one.
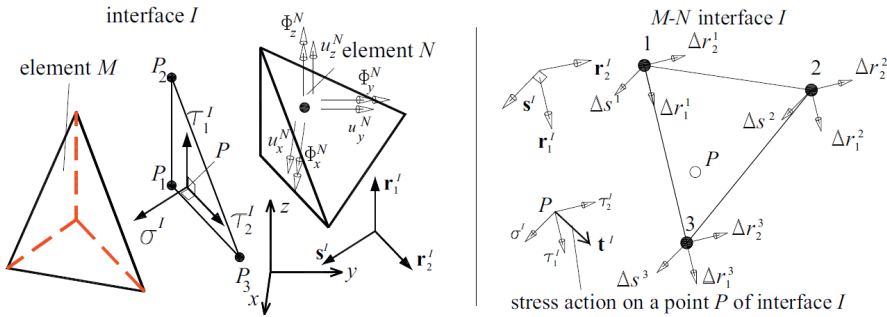
Figure 73: Interface I between two adjoining elements M and N, stress acting on the interface and local frame of reference (left); jump of velocities of nodes of the same interface in the local frame of reference (right).

Let's $\mathbf{t}^{I^T} = \begin{bmatrix} \tau_1^I & \tau_2^I & \sigma_s^I \end{bmatrix}$ denotes the stress vector with normal and tangential components acting along local axes $\mathbf{r}_1^I(\tau_1^I)$, $\mathbf{r}_2^I(\tau_2^I)$ and $\mathbf{s}^I(\sigma_s^I)$, see Figure 73.

On the interface I of the area Ω connecting nodes 1-2-3 (Figure 73), assuming for the masonry material a linearized strength domain in the local coordinate system constituted by m^I planes (q^I plane of equation $A_{r_1}^{q^I}\tau_1^I + A_s^{q^I}\sigma_s^I + A_{r_2}^{q^I}\tau_2^I =$

$C_I^{q^I}$ $1 \leqslant q^I \leqslant m^I$), see Figure 74, and introducing fields of plastic multipliers at the interface (one for each linearization plane), it can be easily shown that power dissipated is the following:

$$P^I = \frac{\Omega}{3} \sum_{q^I}^{m^I} \left(\dot{\lambda}_{q^I}^{I,1} + \dot{\lambda}_{q^I}^{I,2} + \dot{\lambda}_{q^I}^{I,3} \right) C_I^{q^I} \tag{8}$$

where $\dot{\lambda}_{q^I}^{I,j}$ is the q^I plastic multiplier of node j.

Associated flow rule constraints are imposed again on interface nodes in the following form:

$$\Delta \mathbf{U} \left(P_j \right) = \sum_{q^I}^{m^I} \dot{\lambda}_{q^I}^{I,j} \left[\begin{array}{ccc} A_{r_1}^{q^I} & A_{r_2}^{q^I} & A_{\sigma_s^I} \end{array} \right]^T \tag{9}$$

The external power dissipated can be written as $P^{ex} = \left(\mathbf{P}_0^T + \lambda \mathbf{P}_1^T \right) \mathbf{v}$, where $\mathbf{P}_0$ is the vector of permanent loads, λ is the load multiplier for the structure examined, $\mathbf{P}_1$ is the vector of variable loads and $\mathbf{v}$ is the vector of assembled centroid elements velocities. As the amplitude of the failure mechanism is arbitrary, the additional classic normalization condition $\mathbf{P}_1^T \mathbf{v} = 1$ is also added, reducing thus the external power to linearity.

Formally, the linear programming problem obtained is classic, and relies into the constrained minimization of the total internal power dissipated minus the power dissipated by external loads which do not depend by λ:

$$\begin{cases} \min \left\{ \mathbf{P}_I^{in,ass} \dot{\boldsymbol{\lambda}}^{I,assT} - \mathbf{P}_0^T \mathbf{v} \right\} \\ \text{such that} \begin{cases} \mathbf{A}^{eq} \mathbf{U} = \mathbf{b}^{eq} \\ \dot{\boldsymbol{\lambda}}^{I,ass} \geqslant 0 \end{cases} \end{cases} \tag{10}$$

where $\mathbf{U}$ is the vector of global unknowns which collects the vector of elements centroids velocities ($\mathbf{v}$) and rotations ($\boldsymbol{\Phi}$) of masonry elements and the vector of assembled interface plastic multiplier rates ($\dot{\boldsymbol{\lambda}}^{I,ass}$). $\dot{\boldsymbol{\lambda}}^{I,ass}$ is the vector of assembled plastic multipliers of the interfaces. Also, $\mathbf{A}^{eq}$ and $\mathbf{b}^{eq}$ are the overall constraints matrix and vector and collect normalization condition, velocity boundary conditions and plasticity normality rules on interfaces.

5.2.2 *Master-Slave optimization procedure*

Aiming at reducing the numerous amount of optimization variables involved in the limit analysis computations, a master-slave approach is herein proposed. Indeed, considering that the FE model studied (Figure 52(h)) is constituted by 145,893 elements and approximately 170,000 interfaces and assuming rigid elements (i.e. those with six degrees of freedom to determine) and interfaces obeying a rough linearization of the Mohr-Coulomb failure criterion with tension cut-off with only 5 plastic multipliers (at least in the first step, as it will be explained later on), the limit analysis problem derived would be characterized by slightly less than 2 million variables. This is certainly a linear programming problem which requires the utilization of either super-computers or parallelization, with considerably long computational times or out-of-memory issues to tackle. In order to circumvent such problems and reduce the huge computational effort required, the two-step procedure shown in Figure 74 adopted. Substantially, a rough approximation of the Mohr-Coulomb failure surface with tension cut-off is utilized in Step 1 to reduce the computational burden. This approximation is constituted by only 5 planes. Step 1 is used to roughly identify the active failure mechanism and to proceed to Step 2 using a new active zone band, closer to the actual one. In Step 2, a more refined discretization of the failure domain is utilized to determine with higher accuracy the active failure surfaces inside each interface.
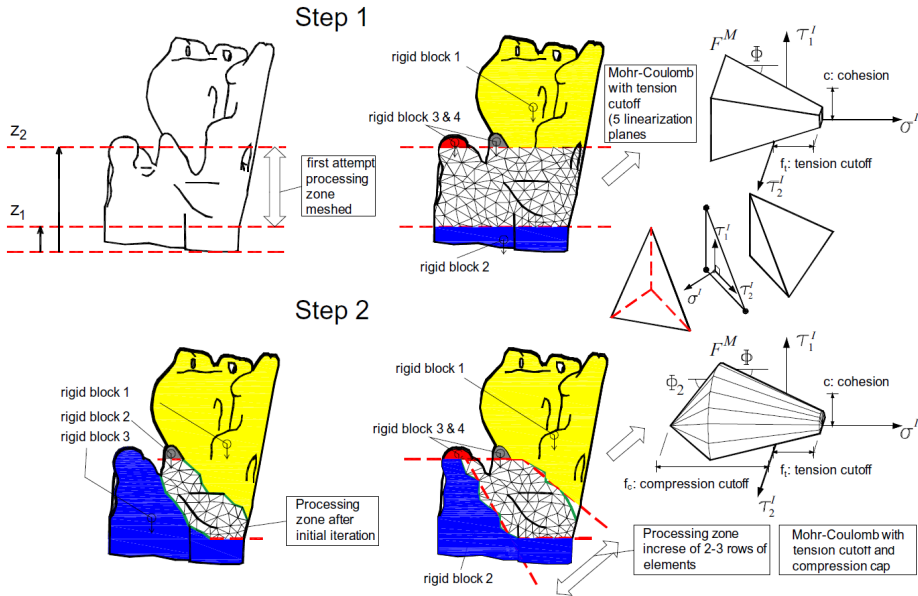

Figure 74: Two-step master-slave approach adopted.

In the Step 1, a processing zone is a-priori established, assuming only active interfaces between two distances z_1 and z_2 from the ground. All elements with

centroids inside such region are assumed potentially active and any interface involving at least one of such elements is also considered active. Regions outside the interval z_1-z_2 are assumed to behave kinematically as a rigid block, fully characterized by the knowledge of the position of the centroid and six degrees of freedom (3 rotations around the centroid and 3 velocities of the centroid). All interfaces outside the established processing zone are indeed not active and contiguous elements cannot separate in any manner. Being rigid elements, they are therefore constrained to move as part of the same rigid body. Therefore, the slave region is treated as the assemblage of few single rigid elements with complex geometry, so the finite element nodes on the edges between the meshed region and the rigid bodies are the slave nodes being dependent on the degrees of freedom expressed at the centroids of the rigid bodies.

Although this assumption is arbitrary, the user generally knows in advance the nature of the expected failure mechanism. For the problem under investigation, a failure mechanism characterized by a shear-flexural hinge located near the base is expected. The exclusion of the mesh on the upper part does not preclude in any manner a correct estimation of failure loads and collapse mechanisms. In Step 1, there is also no need to refine the linearization of the failure surface assumed for the interfaces, because the aim is only to identify possible sub-regions of active interfaces. In this manner, the obtained linear programming problem contains a reasonable total number of optimization unknowns. The width of the active region can be properly tuned to obtain problems that are computationally more sustainable for the available computers.

Once the exact regions of active interfaces are known (from the solution of the linear programming problem in Step 1), the processing zone is again reduced in Step 2 to further drop-down the optimization variables. Generally, authors experienced that such new processing zone found in Step 1 should be slightly enlarged including 2 or 3 rows of neighbouring inactive elements with the aim of compensating potential inaccuracies of the procedure due to, for example, the rough discretization adopted for the failure surfaces of the interfaces in Step 1. The strong reduction of the active interfaces in Step 2 allows for a refinement of the linearization of the interfaces failure surfaces, with the possible inclusion of a compression cut-off, although this is not essential for such kind of problems.

In Step 1, computations are performed assuming 129,872 slave elements, 4 master regions of rigid blocks and a total number of active elements equal to 16,021, as depicted in Figure 75 (active elements are indicated in orange in the picture). Such a choice leads to tackle a linear programming problem constituted by about 14,000 interfaces and around 160,000 optimization variables. As it will be discussed later on in this chapter, the evaluation of the ultimate inclination can be assimilated to the study at collapse of the same structure resting on a tilting plane. Such problem becomes nonlinear, due to the presence of a few nonlinearities.

A sequential linear programming (SLP) strategy is therefore adopted, linearizing the nonlinear constraints and repeating a sequence of few linear programming iterations, typically 4-5. On a work station equipped with 32 in-parallel processors and CPLEX solver [339], Step 1 within the SLP procedure is solved
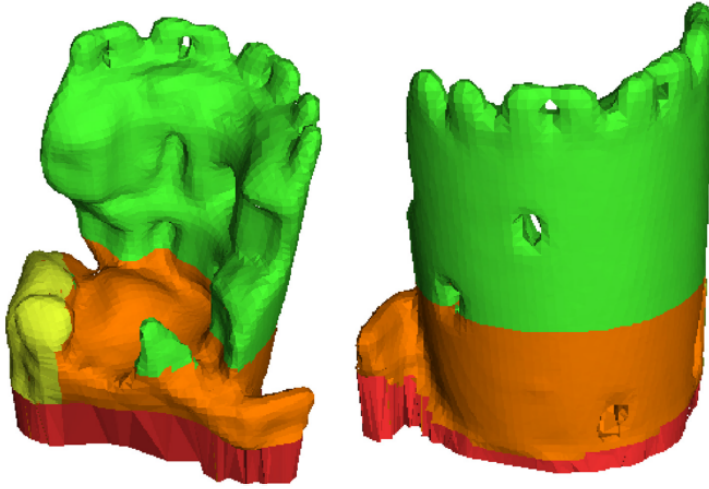
Figure 75: Two-step master-slave approach. Slave elements: 129,872, Master regions: 4, To-
tal #elements: 16,021.

in less than 3 hours. The rough identification of the processing zone reduces fur-
ther the number of active elements to about 4,000, with less than 5,000 active
interfaces. Assuming a quite refined linearization of the failure surface for the
interfaces with 25 planes, the total number of optimization variables involved is
roughly 150,000, comparable with those utilized in Step 1 and hence, with similar
processing times needed.

5.2.3   *Limit analysis on a tilting plane*

The limit inclination angle of a masonry structure (i.e. the angle which leads the
collapse of the structure under gravity loads only) can be computed within a
mathematical programming FE procedure. This is a particular type of limit state
problem, where the collapse of a structure resting on a tilting plane is determined
by progressively increasing the inclination of the base plane from the horizontal
direction (i.e. by increasing the angle ϑ, see Figure 76) up to collapse. In this
framework, the collapse multiplier adopted is ϑ, i.e. the limit inclination angle of
the tilting base.

External loads (due exclusively to gravity) are the components of the gravity
load which act perpendicular and tangential to the tilting base. The progressive
rotation of the tilting plane results into a decrease of the vertical load and an
increase of the horizontal one, according to the decomposition of the gravity
loads W into the horizontal component $(W\sin\vartheta)$ and the vertical component
$(W\cos\vartheta)$ respectively, Figure 76.

If the inclination angle of the tilting plane ϑ is assumed to play the role of the
collapse multiplier in the limit analysis problem (10), it is worth noting that there
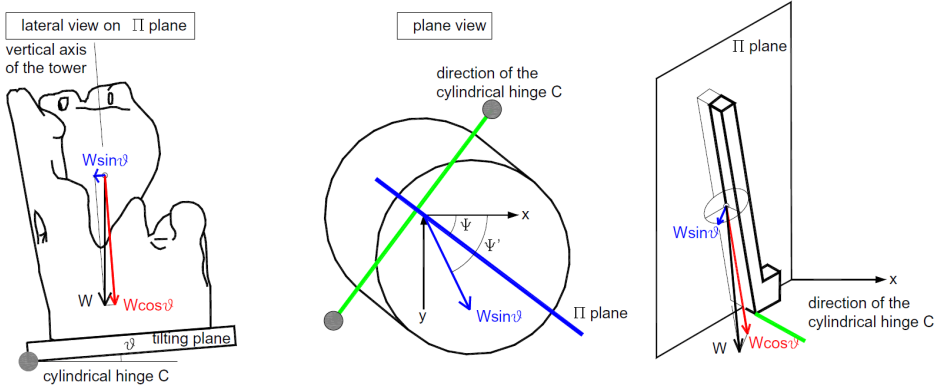
Figure 76: Limit analysis strategy for evaluating the collapse inclination of a 3D structure.

is no way to deal with it using linear programming routines, because the normalization condition becomes nonlinear. Obviously, the external power dissipated (which contains only loads dependent upon the collapse multiplier) is nonlinear. In limit analysis, loads are applied contemporaneously and a snapshot of the situation is provided at failure via the solution of a constrained minimization problem.

In such a particular case, $P^{ex} = \left(\mathbf{P}_0^{\mathsf{T}} + \vartheta \frac{\mathbf{P}_1^{\mathsf{T}}(\vartheta)}{\vartheta} \right) \mathbf{v}$, where again $\mathbf{P}_0$ stands for the vector of loads not dependent on ϑ, $\mathbf{P}_1^{\mathsf{T}}$ is the vector of all loads dependent on ϑ and $\mathbf{v}$ is the vector of assembled velocities at the centroid of the elements. The normalization condition is obviously $\frac{\mathbf{P}_1^{\mathsf{T}}(\vartheta)}{\vartheta} \mathbf{v} = 1$, which is clearly a nonlinear function.

Such nonlinearity has the consequence that the obtained mathematical programming problem is nonlinear. Almost identical to (10), such nonlinear programming problem (where the nonlinear normalization condition is put in evidence) can be written as follows:

$$
\begin{cases}
\min \left\{ \mathbf{P}_{\mathrm{I}}^{in,ass} \dot{\boldsymbol{\lambda}}^{\mathrm{I},ass\mathsf{T}} - \mathbf{P}_0^{\mathsf{T}} \mathbf{v} \right\} \\
\text{such that} \begin{cases}
\mathbf{A}^{eq} \mathbf{U} = \mathbf{b}^{eq} \\
\frac{\mathbf{P}_1^{\mathsf{T}}(\vartheta)}{\vartheta} \mathbf{v} - 1 = 0 \\
\dot{\boldsymbol{\lambda}}^{\mathrm{I},ass} \geqslant 0
\end{cases}
\end{cases}
\tag{11}
$$

The nonlinear programming problem (11) can be solved by means of two distinct possible approaches: a) using a standard nonlinear programming (NLP) routines, and b) implementing a sequential linear programming SLP procedure, linearizing the nonlinear normalization condition. This last approach is preferred

here, and it is worth mentioning that the linearization of the nonlinear equation can be written as follows:

$$\left(\frac{\mathbf{P}_1^\mathsf{T}(\vartheta_0)}{\vartheta_0}\mathbf{v}_0 - 1\right) + \left.\frac{\frac{d\mathbf{P}_1^\mathsf{T}(\vartheta)}{d\vartheta}\vartheta\mathbf{v} - \mathbf{P}_1^\mathsf{T}(\vartheta)\mathbf{v}}{\vartheta^2}\right|_{\substack{\vartheta = \vartheta_0 \\ \mathbf{v} = \mathbf{v}_0}} \qquad \vartheta = 0 \qquad (12)$$

where subscript 0 indicates the solution of the previous iteration. The starting point selected at the beginning of the SLP procedure when linearizing Equation (12) coincides with an inclination angle of the tilting plane equal to $\vartheta = 0$. Therefore, the limit inclination angle of the structure is evaluated as the sum of the limit inclination angle of the tilting plane ϑ and of the actual inclination of the structure. As a matter of fact, the evaluation of the actual inclination of the structure is not an easy task, because it depends on the in-plane direction along which the inclination is evaluated.

For the case study at hand, plotting the in-plane position of nodes belonging to two horizontal planes as shown in Figure 77, and assuming that the vertical distance between the two planes is known, it is possible to estimate easily the out-of-plane inclination of the tower along the different in-plane directions considered. Such inclination, as it will be explained later on in this chapter, varies

| Axonometric view | Planar view |
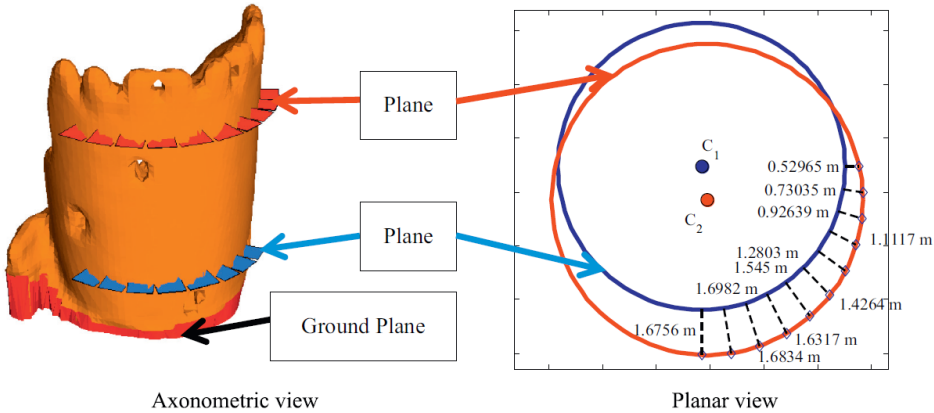
Figure 77: Evaluation of the actual inclination of the structure along different in-plane directions.

typically between about 10° to about 2°, passing from a direction almost parallel to y to the horizontal direction, respectively. Authors experienced that the SLP approach converges very quickly, with stabilization of the collapse inclination angle of the tilting plane after few iterations (3-5).

A final issue to tackle is the choice of the in-plan direction of the horizontal load, namely the angle Ψ' shown in Figure 76. In general, the angle Ψ' cannot coincide with Ψ, the angle identifying the direction of plane Π (the angle 90°- Ψ

identifies on the other hand the direction of the cylindrical hinge around which the tower rotates during the collapse under self-weight).

Authors experienced that it is necessary to scan angles Ψ' within the range -10°-100° to obtain in output angles Ψ between 0° and 90°. Then, the identification of the Ψ associated with the minimum of the collapse inclination of the tower can be obtained by a simple spline interpolation of the different angles Ψ obtained by limit analysis computations.

5.3 RESULTS AND DISCUSSION

Limit analyses are performed on the actual 3D geometry of the structure (Figure 52(h)) which is derived from the laser scanning survey. The material of the tower, or more precisely all interfaces between adjoining tetrahedrons, was assumed to obey a Mohr-Coulomb criterion with tension cut-off, with mechanical properties approximating reasonably a continuum almost unable to withstand tensile stresses. In particular, considering that the tower is severally deteriorated and in agreement with consolidated literature [162], cohesion c and tensile strength f_t were kept constant through the tower and equal to 0.02 MPa. The assumption of small but non-zero values of cohesion and tensile strength improves the numerical stability of the linear programming solver and at the same time does not drastically increase failure multipliers. In such problems, indeed, almost all the stabilizing contribution is provided by gravity loads and internal dissipation turns out to play a negligible role on the increase of the collapse multiplier.

Stability problems, such as the leaning historic masonry structures, are governed by geometry. Mechanical properties of the masonry tower were not available. Material properties assumed based on authors experience and from codes of practice. Thus, the friction angle ϕ of masonry has been set equal to 25°, a value very similar to that assumed in the Italian code for the evaluation of the ultimate base-sliding shear for piers. Such value of the friction angle allows avoiding the formation of failure mechanisms due to sliding of macro-parts, which are unlike in such kind of limit analysis problems. The choice to remove the cap in compression (see Figure 74) has been made for a twofold reason: first of all, to limit as close as possible the optimization variables and second because the collapse of a tower after having reached the limit inclination angle occurs without evidence of crushing near the compressed toe.

According to the two-step master-slave procedure proposed in the previous Sections, in Step 1 a rough linearization with 5 planes (and hence 5 plastic multipliers is adopted), whereas in Step 2 a piecewise linear approximation with 25 planes (24 for the pure Mohr-Coulomb strength domain, 6 per quadrant and 1 for the tension cut-off) is assumed. The SLP procedure is here utilized to deal with the nonlinearity presented in such special limit analysis problem.

The resultant limit inclination angles of the structure so obtained varying the direction of the tilting plane are depicted in Figure 78 and compared with its actual inclination (thick black line), computed as shown in Figure 77. The col-

lapse mechanism of the structure for a horizontal direction corresponding to the smallest limit inclination ($\Psi = 60°$) is highlighted in Figure 79.
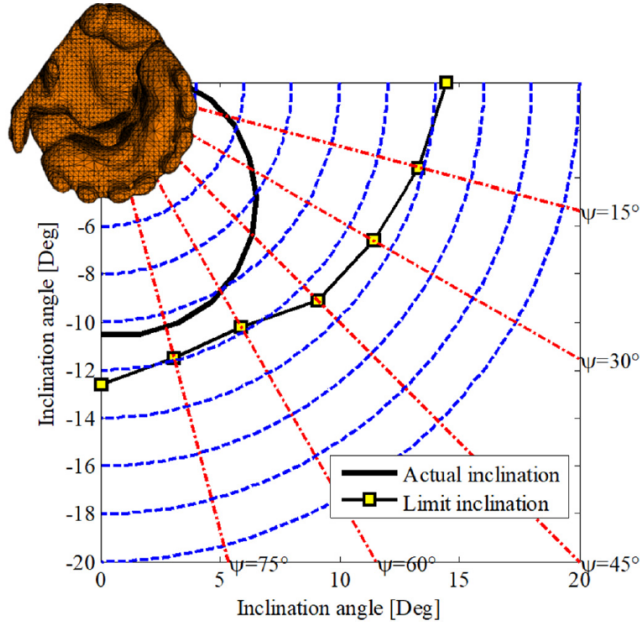
Figure 78: Comparison between actual inclination and limit inclination of the structure for several horizontal directions of the rocking direction.

From a careful analysis of the numerical results obtained, the following considerations can be drawn:

1. The tower is at present in a state not far from its collapse state. In particular, for a direction of the rocking plane Π roughly within the range: $60° \leqslant \Psi \leqslant 75°$, an additional inclination of 1.5° would lead to the collapse of the structure, see Figure 78. Considering the recent wetting-drying cycles which the structure has been subjected to, a careful analysis of the most suitable interventions to preclude rocking failure would be needed.

2. Crack pattern found by means of the limit analysis simulation corresponding to $\Psi = 60°$ (Figure 79) shows the clear formation of a cylindrical rotational hinge near the base. The plasticization band is relatively narrow and tends to follow the geometric irregularities of the structure near the base, passing through the weakest transversal sections. The definition of a cylindrical hinge is therefore in principle not proper, because of both the finite thickness of the band and the not straight configuration of the plasticization zone.
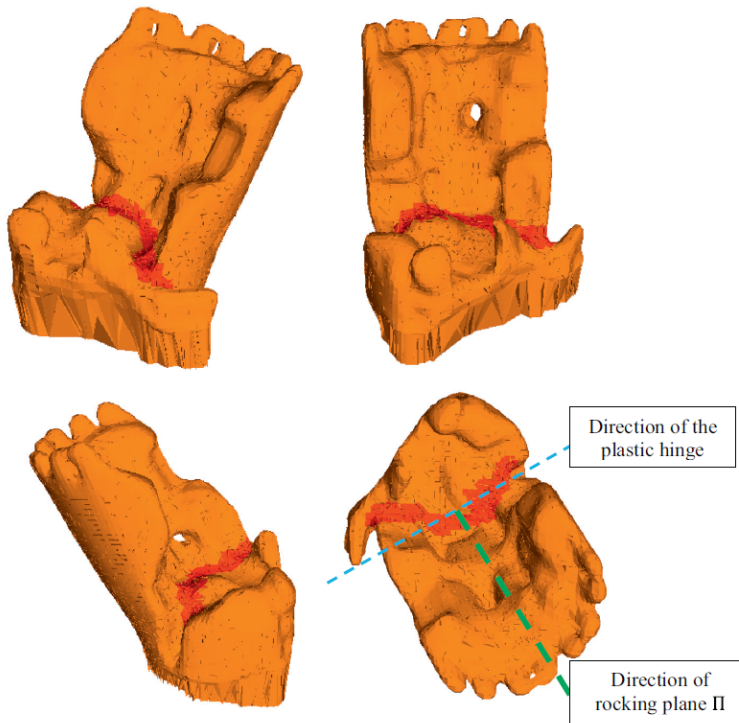
Figure 79: Collapse mechanism (with indication of the plastic processing zones) in the horizontal direction corresponding to the smallest limit inclination (Ψ=60°).

3. The concentration of all the plastic flow near the base, in agreement with intuition, indirectly confirms that the master-slave approach proposed is fully consistent with the real behavior.

4. Once the exact shape of the crack at the base is known, the failure mechanism is clearly identified and hand calculations (or assisted by a CAD program) can be performed to evaluate the position of the center of gravity of the macro-part subjected to rocking. In this way, the estimation of the collapse inclination angle is very straightforward and provides a further validation of the procedure proposed, as well as a ready to use instrument by common practitioners involved in the safety assessment of leaning historic masonry structures.

5.3.1 Verification of the procedure: Enlarged active volume and single-step analysis

Additional limit analyses have been conducted to show the reliability of the assumption of rigid bodies (master-slave approach) by employing different sizes of the processing zones (Step 1), in order to check the convergence of the limit analysis solution (see Mesh #1 and Mesh #2 in Figure 80).
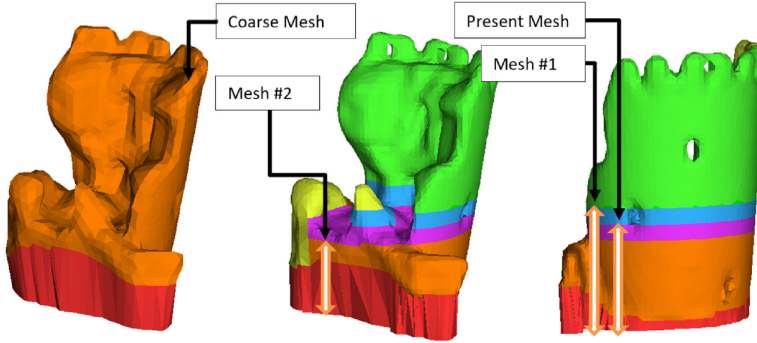
Figure 80: Different sizes of the processing zones (Step 1) tested to check the convergence of the limit analysis solution (middle and right) and coarse mesh (left) utilized to solve the LP problem (single-step approach). Present Mesh refers to the processing zone depicted in Figure 75.

Particularly, Mesh #1 is characterized by an enlargement of the processing zone, with respect to the one employed in the previous sections (Present Mesh in Figure 80), which represents the largest active volume employable for the computers at disposal. Conversely, Mesh #2 (Figure 80) represents a restriction of the previous processing zone, which also excludes interfaces where plastic dissipation occurred in the Present Mesh (Figure 79). In addition, the mesh obtained through retopology (Coarse Mesh in Figure 80) has been utilized to solve the LP problem in the framework of a single-step analysis, i.e. without master-slave approach.

Figure 81 shows the comparison among collapse inclinations of the structure at several horizontal directions of the rocking direction, with different meshes/processing zones tested. Furthermore, Figure 82 shows the comparison between the collapse deformed shapes of the coarse mesh (top) and Mesh #1 (bottom) in the horizontal direction $\Psi=60°$. For the sake of brevity, the failure mechanism of Mesh #2, which is completely different from the others (characterized by a sub-horizontal crack surface), is not reported.

As can be noted in Figure 81, a very good agreement is achieved in terms of collapse inclinations between Mesh #1 and the Present Mesh. Conversely, Mesh #2 radically overestimates the collapse inclinations of the structure. Indeed, the excessive restriction of the active volume, i.e. the exclusion of interfaces where plastic dissipation occurs, is responsible for the increase of the load carrying capacity of the structure, as well as a different failure mechanism. Moreover, the collapse inclinations evaluated through the Coarse Mesh (single-step analysis), although slightly overestimated due to the coarser mesh adopted, are in a reasonable agreement with the ones obtained with Mesh #1 and the Present Mesh, confirming the reliability of the two-step approach proposed.

Additionally, the failure mechanisms collected in Figure 82 further validate the one obtained with the Present Mesh (Figure 79). Indeed, they substantially show the same failure mechanism with plastic dissipation essentially in the same
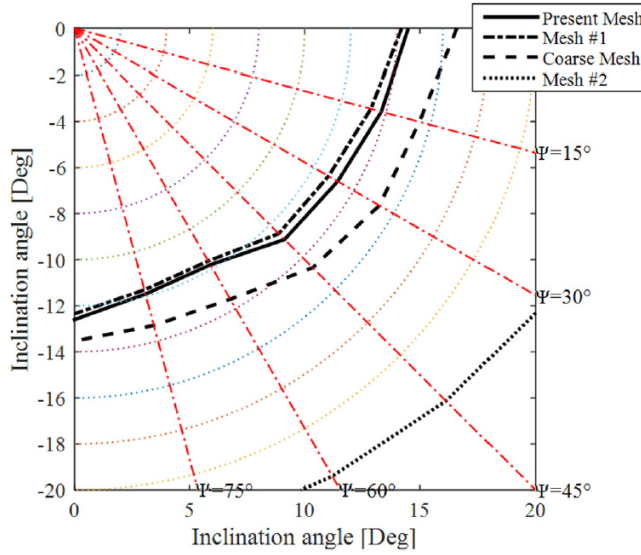
Figure 81: Comparison among collapse inclinations of the structure at several horizontal directions of the rocking direction and with the different meshes/processing zones tested.

zones (compare Figure 82 with Figure 79), although the failure mechanism obtained with the Coarse Mesh (Figure 82, top) is computed through a single-step approach (fully active volume). Therefore, this outcome further confirms the effectiveness of the master-slave approach proposed and the choice of the processing zone adopted for the Present Mesh (Figure 75).

Finally, Table 15 collects the computational times required to solve the limit analysis problems. The following considerations can be drawn:

1. The time needed to solve the problem with the Present Mesh is around 18 hours, considerably less than the time needed by Mesh #1. Therefore, the Present Mesh, which is more accurate than the Coarse mesh (Figure 80), appears a suitable compromise to speed up computations with a precise geometric and mechanical approximation of the real situation.

2. Step 2 requires generally more time to be performed, because of the utilization of several planes to approximate interfaces failure surface. Mesh #2 requires the same time for Step 1 and Step 2 because of the too restricted processing zone in Step 1, which does not allow to find a plausible failure mechanism.
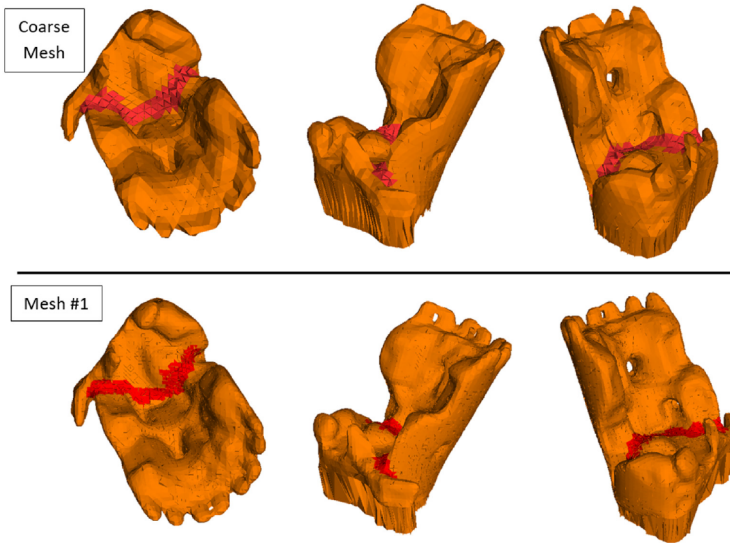
Figure 82: Comparison between collapse deformed shapes (with indication of the plastic processing zones) for the coarse mesh (top) and Mesh #1 (bottom), in the horizontal direction corresponding to the smallest limit inclination (Ψ=60°).

5.3.2   *Verification of the procedure: Nonlinear finite element analysis*

A further verification of the proposed structural analysis approach is achieved by means of the comparison with the results of a nonlinear finite element tilting plane incremental analysis. In this analysis, the isotropic plastic-damage model adopted in Chapter 4 and described in Chapter A is used for masonry.

Reference to the Italian code has been made to set the mechanical properties of the material (cluttered stone masonry), which are collected in Table 16. In particular, the general mechanical parameters for quasi-brittle materials have been kept the same of Chapter 4. Furthermore, the tensile strength has been kept equal to the value used in the FELA, whereas the evolution of the scalar damage variables d_t and d_c has been kept substantially proportional to the decay of the uniaxial stresses, as adopted in several numerical campaigns [141] (Table 16).

Dead load is initially applied to the structure through an incremental procedure, considering clamped boundary conditions at the base. Then, a pattern of imposed displacements, which simulates a tilting plane, is incrementally applied at the base of the structure. Abaqus Standard [308] has been used to conduct the simulation. Geometric nonlinearity has been considered to account for large-displacement effects, which, in this case, are expected to play a fundamental role.

Figure 83 shows the tensile damage (d_t) contour plot obtained with a nonlinear finite element tilting plane incremental analysis. In particular, Figure 83 refers to the condition in which the base inclination of the tower equals the limit inclina-

Table 15: Times required to solve the limit analysis problems. [a] CPLEX solver on a work station equipped with 64bit 2x16GB DDR4 RAM (16 slots). Computations are referred to the evaluation of the collapse inclination for 7 tilting directions. Computations include also pre-processing phases, such as identification of the interfaces and assemblage of the equality and inequality constraints.

	Solution of the LA problem[a] hh:mm:ss	
	Step 1	Step 2
Present Mesh	06:12:44	12:01:05
Mesh 1	15:48:09	33:19:52
Mesh 2	03:31:28	03:27:02
Coarse Mesh (single-step analysis)	21:25:13	

tion computed through FELA, in the horizontal direction with the smallest limit inclination ($\Psi = 60°$).
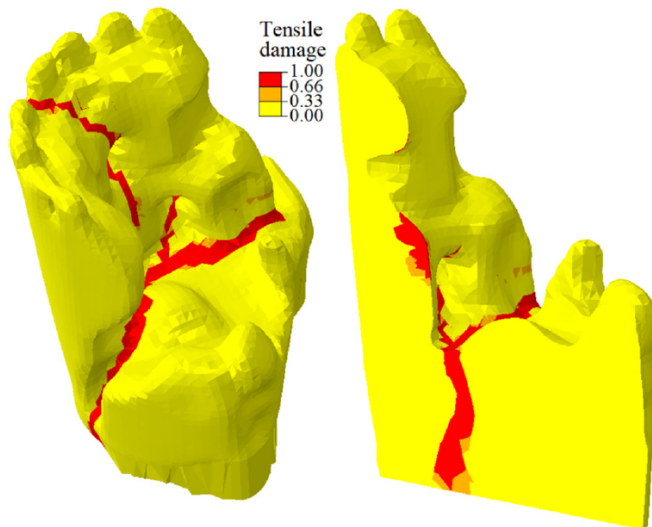
Figure 83: Tensile damage contour plot obtained with a nonlinear finite element tilting plane analysis, in the condition of a base inclination of the tower equal to the limit inclination computed through FELA, in the horizontal direction with the smallest limit inclination ($\Psi = 60°$).

As can be noted, the crack pattern in Figure 83 is in good agreement with the collapse mechanism observed with FELA (Figure 79 and Figure 82). Indeed, all of the failure mechanisms are governed by the overturning of the highest part of the tower with a detachment from the remaining part, which pseudo-horizontally runs from one side of the tower to the opposite one. Although the crack pattern in Figure 83 also shows a pseudo-vertical crack along the central part of the tower's trunk, it does not cross the thickness of the wall (Figure 83). Therefore, such crack

Table 16: Mechanical properties adopted for masonry in the FELA and in the continuum plastic-damage models. E is the Young's modulus, ν is the Poisson's ratio, and w is the density.

FELA model

Tensile strength f_t [MPa]	Cohesion c [MPa]	Friction angle ϕ
0.02	0.02	$25°$

Continuum plastic-damage model

E [MPa]	ν	w [kg/m3]	ϵ [\]	ψ [\]	f_{b0}/f_{c0} [\]	ρ [\]
870	0.15	1900	0.1	$10°$	1.16	2/3

Tensile uniaxial behavior				Compressive uniaxial behavior		
Stress [MPa]	Inel. strain	d_t [\]		Stress [MPa]	Inel. strain	d_c [\]
0.02	0	0		1.0	0	0
0.001	0.0001	0.95		1.1	0.001	0
				0.05	0.007	0.95

does not appear essential in the main failure mechanism of the tower. Rather, this vertical crack develops after the formation of the horizontal main fissure, being the result of large-displacement effects.

Finally, it should be pointed out that the evaluation of the limit inclination angle by means of the standard nonlinear finite element tilting plane analysis herein adopted is non-trivial and, in facts, requires specific interpretation of the results. Therefore, further studies on this topic are needed. Consequently, the proposed FELA approach appears more robust than standard nonlinear FE methods, being able to directly compute the limit inclination angle of a masonry structure.

5.4   CONCLUSIONS

In this chapter, the use of an actual geometry-based mesh in a multi-step upper bound limit analysis with automatic variables reduction, has been proposed for the stability analysis of leaning historic masonry structures.

Following the Heyman's intuition, the use of 3D FELA on a mesh of the actual geometry is implemented to evaluate the critical condition (i.e. maximum inclination capacity) of a leaning historic masonry structure. In this way, the structural health condition of a historic structure is evaluated by comparing the maximum critical inclination angle against the current one. A recursive identification of the processing zone has been proposed, excluding from computations all those elements which do not undergo plastic deformation. The automatic procedure adjusts iteratively the processing zone, progressively restricting the analysis to the few elements interested by the failure mechanism and considering the other portions outside the processing zone as rigid blocks. Also, a sequential linear

programming kernel has been adopted to linearize the normalization condition, which becomes nonlinear if the inclination angle at failure is considered as collapse multiplier.

To demonstrate the effectiveness of the automated procedure, the SW leaning ruined tower of the Caerphilly castle has been employed as a case study. It emerged that the tower in its actual condition is not far from its collapse. Indeed, an additional inclination of the structure by 1.5° appears to be critical. In this limit condition, the collapse mechanism of the structure has been found in agreement with intuition, i.e. it consists in the overturning of the main leaning part of the structure. The results have been further validated by means of the comparison with the outcomes of single-step analyses (fully active volume) and nonlinear FE analyses.

The procedure proposed herein is characterized by a high degree of automation at each operational level. Such approach could be effectively utilized to assess the stability of historic structures at a national scale and provide useful information to engineers and managers to classify the structural health condition of historic assets in their care.

Although the procedure proposed represents a novel solution for evaluating the stability of extant masonry structures, it could be enriched with an adaptive mesh enhancement in the framework of a multi-step strategy.

DAMAGING BLOCK-BASED MODELING

In this chapter, a damaging block-based model is proposed for the numerical analysis of the mechanical response of masonry structures. Two main versions of this model are proposed. In the first case, the model is characterized by textured units, consisting of one brick and few mortar layers, represented by 3D solid FEs obeying to plastic-damage constitutive laws in tension and compression. Textured units are assembled by means of zero-thickness rigid-cohesive-frictional interfaces, based on the contact penalty method. Experimental-numerical comparisons are provided for the in-plane and out-of-plane behavior of masonry panels. In the second case, solid 3D FEs governed by a plastic-damage constitutive law in tension and compression are used to model the blocks (in this case without mortar layers), while a cohesive-frictional contact-based formulation is developed to simulate their cyclic interaction. The use of tests on small-scale specimens to calibrate the mechanical properties of the numerical model is presented and discussed. The tests belong to a comprehensive experimental campaign performed on calcium silicate brick masonry. The calibrated models are used to simulate in-plane and out-of-plane cyclic tests on masonry walls made of the same material, as well as a quasi-static cyclic pushover test on a full-scale terraced masonry house. Finally, the effects of differential settlements on historic masonry barrel vaults are investigated through the second version of the model proposed. Firstly, the numerical model is used to simulate an experimental campaign on a scaled pointed barrel vault (representative of a typology of late-medieval barrel vaults in Scotland) under non-uniform differential settlement. Then, further analyses are carried out to gain insight on the effects of several plausible uniform and non-uniform settlement patterns on representative historic barrel vaults.

6.1 INTRODUCTION

In the context of block-based models, the development of a novel model whose mechanical setting could be exclusively based on small-scale specimen tests of masonry components (i.e. mortar and brick) and small masonry assemblages, without using spread mechanical properties, such as the masonry compressive strength, was considered. Furthermore, the idea of developing a 3D solid model able to account for, at the same time, the in-plane and out-of-plane response of masonry elements (since, in practice, they can be coupled) was also contemplated.

To pursue this goal, a novel numerical approach to model masonry is conceived (Section 6.2). In particular, a 3D detailed block-based model for the in-plane and

out-of-plane numerical analysis of masonry structures is proposed in this chapter. In this modeling approach, textured units consisting of one brick and few mortar layers are explicitly modeled using 3D solid FEs obeying to plastic-damage constitutive laws conceived in the framework of nonassociated plasticity. Particularly, two plastic-damage models with distinct parameters are assumed for brick and for mortar, both in tension and compression regimes. This permits to represent the brick and mortar behavior when cracking and/or crushing occur.

Textured units are assembled, accounting for any actual 3D through-thickness arrangement of masonry, by means of zero-thickness rigid-cohesive-frictional interfaces based on the contact penalty method. In the pre-failure contact behavior, all the significant linear elastic deformability of the system is addressed to the 3D brick and mortar FEs, being negligible the contact deformations. The interfaces are characterized by a Mohr-Coulomb failure surface with tension cut-off. The post-failure contact behavior is defined by an exponential coupled cohesive behavior in tension and a cohesive-frictional behavior in shear, accounting for the brick-mortar bond failure both in tension and shear.

The coupling of contact-based rigid-cohesive interfaces with 3D nonlinear-damaging textured units (which explicitly account for the mortar layers) to model masonry appears a novelty in the scientific literature. This novel modeling approach can, in fact, be fully characterized by the properties obtained on small-scale specimen tests on brick and mortar (stiffness, compressive and tensile responses) and on small masonry assemblages (tensile and shear responses of the mortar-brick bond).

To reach this goal, this chapter introduces an contact-based constitutive behavior, obtained by an ad-hoc modification of the standard surface-based contact behavior implemented in Abaqus [308]. Contextually, an ad-hoc automatic subroutine (UFIELD, see Abaqus [308]) is implemented to reproduce a Mohr-Coulomb failure surface with tension cut-off.

The contact behavior appears consistent with experimental outcomes on small-scale masonry specimens. Experimental-numerical comparisons are provided for the in-plane and out-of-plane behavior of masonry panels. The direct characterization of all the model mechanical properties from small-scale tests on brick, mortar and brick-mortar bond and their clear mechanical meaning constitute an appealing quality of the model proposed.

Moreover, this model is further extended to analyze the cyclic response of full-scale masonry structures (Section 6.3). Aiming to obtain a model with an affordable computational effort for full-scale structures and to facilitate the definition of the contact cyclic mechanical response, this second version of the modeling strategy consists of expanded blocks, so without an explicit 3D definition of the mortar layers. Solid 3D finite elements governed by a plastic-damage constitutive law in tension and compression are used to model the blocks and a cohesive-frictional contact-based formulation is developed to simulate their interaction, accounting for the sliding and the separation of the blocks also in the cyclic regime. The capability of explicitly representing structural details (e.g. running bonds) and any in-plane and through-thickness texture of masonry, which appears essential

to study the response of masonry structures, is guaranteed by the block-based modeling approach.

A strategy for the comprehensive mechanical characterization of the mechanical properties of the numerical model from small-scale experiments is also discussed. In particular, an experimental campaign on calcium silicate masonry small-scale specimens is used to calibrate the mechanical properties of the model. These mechanical properties are used to simulate in-plane and out-of-plane cyclic tests on masonry walls made of the same material, as well as a cyclic pushover test on a full-scale terraced masonry house. The efficiency of the contact-based formulation and the potentialities and the accuracy of the model herein proposed are discussed.

Finally, the effects of differential settlements on historic masonry barrel vaults are investigated (Section 6.4) through the second version of the block-based model proposed. Firstly, the numerical model is used to simulate an experimental campaign of a scaled pointed barrel vault (representative of a typology of late-medieval barrel vaults in Scotland). The numerical results validate the experiments in terms of crack pattern and transverse-longitudinal deformation profiles. This makes possible further analyses to gain an insight on the effects of several plausible uniform and non-uniform settlement patterns on a representative historic barrel vault. Various settlement patterns are simulated investigating the complex failure mode of the vault.

6.2   DETAILED BLOCK-BASED MODELING OF MASONRY

In the modeling approach herein proposed, the brick-mortar bond failures (Figures 5(a),5(b) are accounted for by brick-mortar contact cohesive behavior, whereas the combined mechanisms involving also brick and mortar (Figures 5(c),5(d),5(d)) are accounted for by the nonlinear behavior of brick and mortar FEs. Therefore, brick and mortar crushing and cracking, although characterized by a complex evolution of micro-cracks, are represented by the inelastic behavior of brick and mortar FEs [11].

Textured units composed of 3D solid FEs (Figure 84) with brick properties (red elements in Figure 84) and mortar properties (grey elements in Figure 84) are conceived and they are assembled by means of zero-thickness contact interfaces (green surfaces in Figure 84). For single leaf masonry panels, the textured unit concerns one brick as well as one head joint and one bed joint (Figure 84). Brick and mortar FEs are characterized by distinct nonlinear plastic-damaging behavior, both in tension and compression regimes.

Each mortar layer is continuously linked to a brick and separated by contact from other bricks. This reduces considerably the number of contact definitions (instead of considering all the two interfaces of a mortar layer), and therefore the computational cost of the model, without compromising the model accuracy. Indeed, the fact that a brick-mortar bond failure occurs in the upper or lower bond of a mortar layer does not affect the mechanical response of masonry.
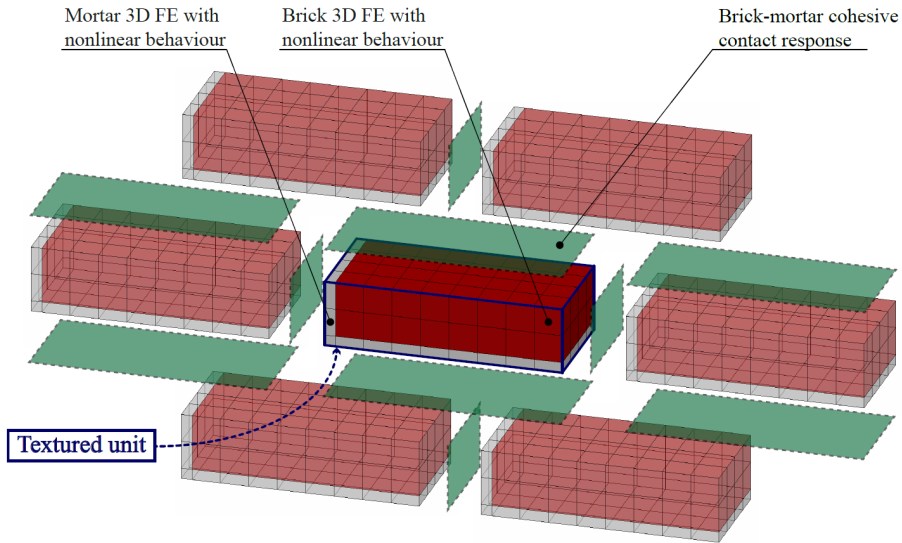
Figure 84: Detailed micro-modeling approach. An example of textured unit mesh is given in the picture.

Contact penalty method is enforced in the zero-thickness interfaces between the textured units. Traditional point-against-surface contact method is considered [340]. The penalty stiffness is assumed to keep insignificant the penetration of the elements and to guarantee good convergence rates of simulations (compared, for example, with Lagrange multipliers methods [340]). In this study, penalty stiffness is assumed to be equal to 500 times the representative stiffness of underlying elements. In the pre-failure of interfaces, all the significant deformability of the system is addressed to the 3D FE part.

Dilatancy plays an important role in the mechanical behavior of masonry [324], although it is still currently object of investigation and debate [106, 341], and its characterization is complex as it is influenced by several mechanical factors (e.g. materials micro-structure, geometrical imperfections, etc). Experimental characterizations of dilatancy by van der Pluijm [324] show that the dilatancy ratio is significantly influenced by the type of interface failure. Particularly, the magnitude of dilatancy turns out to be substantially higher when the crack crosses mortar (and/or units), compared to the dilatancy measured when detachment of the brick-mortar interfaces occurs (bond failure), which is considerably smaller.

In the modeling approach herein proposed, contact behavior is conceived without a dilatant behavior, whereas dilatancy is considered in the 3D nonlinear FEs in the framework of nonassociated plasticity [136]. This approach, although simplified, appears to be consistent with the experimental outcomes, i.e. significant dilatant behavior only occurs when mortar (and/or units) undergoes failure.

The main idea at the base of the setting of the parameters is that the contact properties are based on brick-mortar bond tests (tensile failure and shear sliding),

whereas the properties of the mortar and brick FEs are based on tests on the single components. Although the experimental data available makes non-trivial the separation of the two problems, this assumption, in the Authors opinion, appears reasonable and leads to a rationally easy setting of the parameters.

6.2.1 *Brick-mortar contact behavior*

In the normal direction, the contact stress σ is computed by means of the linear relationship:

$$\sigma = k^n_{penalty} u \, , \tag{13}$$

where $k^n_{penalty}$ is the penalty stiffness in normal direction and u is the normal displacement. Through the contact penalty method, this relation is assumed to be valid also for tensile stresses until the contact tensile strength f_t is reached, see Figure 85(a). As can be noted in Figure 85(a), penetration can occur between elements. However, although no procedures to remove penetration have been implemented, by using quite high penalty stiffnesses (i.e. equal to 500 times the stiffness of the underlying elements) the penetration between elements has been found negligible. Furthermore, the penalty stiffness adopted has been found a good compromise between convergence and accuracy (i.e. negligible penetration).

In the shear direction, the tangential slip δ is linearly related to the interface shear stress with the relation:

$$\tau = k^s_{penalty} \delta, \tag{14}$$

where $k^s_{penalty}$ is the penalty stiffness in shear. This relation is valid until the shear stress equals the shear strength f_s, see Figure 85(b). The contact shear strength f_s is assumed to be dependent on the contact stress:

$$f_s(\sigma) = -\tan\phi \; \sigma + c, \tag{15}$$

where c is the cohesion and $\tan\phi$ is the initial friction of the shear response.

Contact failure occurs, i.e. the process of degradation begins, when the contact stresses at a point satisfy a failure criterion. Particularly, failure is supposed when the maximum contact stress ratio intersects a Mohr-Coulomb failure surface with tension cut-off. This simple criterion can be expressed as:

$$\max \left\{ \frac{\langle \sigma \rangle}{f_t}, \frac{\tau}{f_s(\sigma)} \right\} = 1 \, , \tag{16}$$

where the symbol $\langle x \rangle = (|x| + x)/2$ denotes the Macaulay bracket function. The Macaulay brackets are used to signify that a purely compressive stress state does not induce contact failure. A sketch of the failure surface adopted for the contact behavior is shown in Figure 86. Once contact failure is reached, cohesive contact behavior in tension and cohesive-frictional contact behavior in shear is activated.
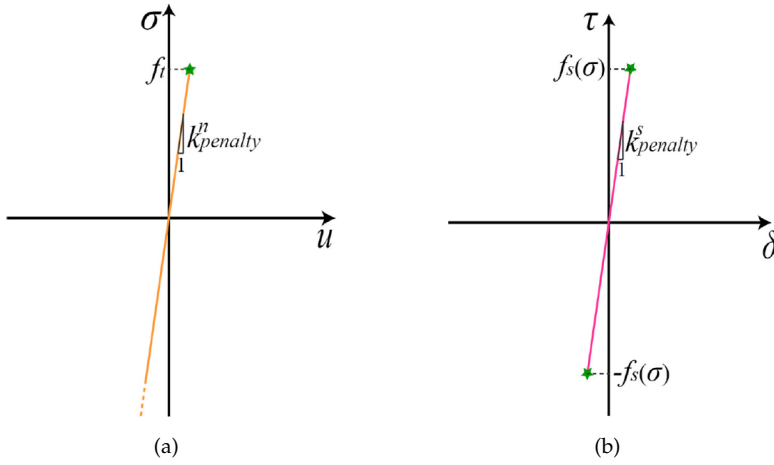
Figure 85: Contact pre-failure behavior: a) normal behavior and b) shear behavior.

After reaching tensile strength f_t, contact cohesive behavior is activated in normal direction and the stress σ decreases with an increasing separation u, while at $u = u_k$ stress ends to be transmitted, see Figure 87(a). The stress follows the relationship:

$$\sigma = \begin{cases} (1-Q)\,f_t, & u < u_k \\ 0, & u \geqslant u_k \end{cases}, \tag{17}$$

where Q is an exponential scaling function defined as:

$$Q = \frac{1 - e^{-\zeta \frac{u_{MAX}}{u_k}}}{1 - e^{-\zeta}}, \tag{18}$$

being ζ a non-dimensional brittleness parameter and u_{MAX} the maximum separation ever experienced by the contact point. The cohesive behavior is only activated for tension, whereas for pure compression stress states no failure is considered at the contact level (see Figure 86).

Concerning the shear behavior, when the shear stress τ reaches the shear strength $f_s(\sigma)$, a simplified cohesive-frictional behavior is activated, and the contacting surfaces start sliding. After failure the shear stress is composed of a cohesive term $(1-H)\,f_s(\sigma)$ and a frictional one $H\mu \langle -\sigma \rangle$ (Figure 87(b)), according to the relationship:

$$\tau = \begin{cases} (1-H)\,f_s(\sigma) + H\mu \langle -\sigma \rangle, & \delta < \delta_k \\ \mu \langle -\sigma \rangle, & \delta \geqslant \delta_k \end{cases}, \tag{19}$$
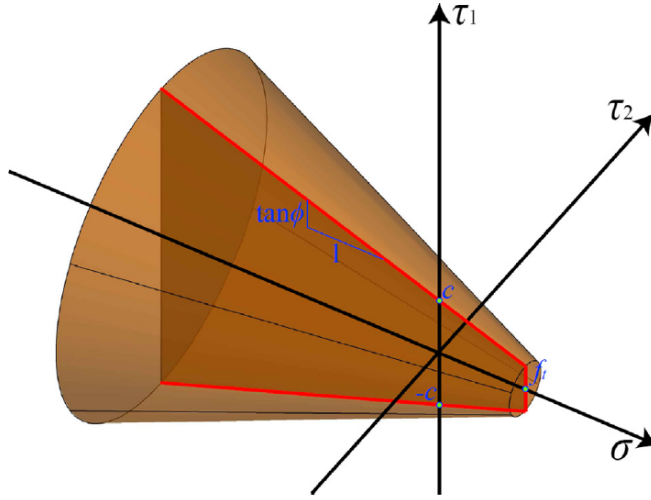
Figure 86: Contact failure surface: Morh-Coulomb surface with tension cut-off (τ_1 and τ_2 are the shear stress components along two orthogonal directions in the plane of the interface).

where δ_k is the ultimate slip of the cohesive behavior, μ is the frictional coefficient and H is an exponential scaling function defined as:

$$H = \frac{1 - e^{-\xi \frac{\delta_{MAX}}{\delta_k}}}{1 - e^{-\xi}}, \tag{20}$$

being ξ a non-dimensional brittleness parameter and δ_{MAX} the maximum slip ever experienced by the contact point.
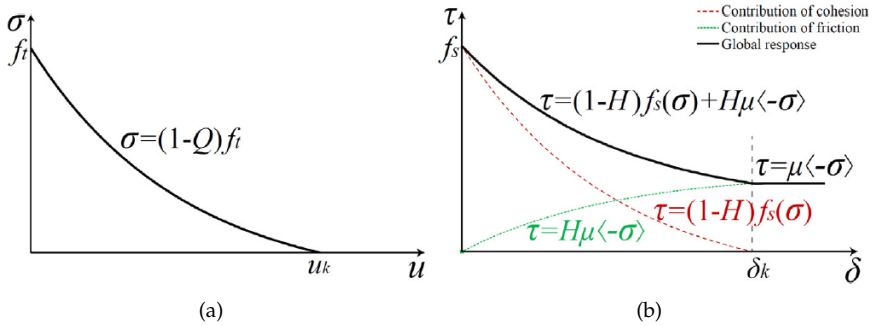
Figure 87: Post-failure contact behavior: (a) tensile response and (b) shear response.

It has to be pointed out that the two variables Q and H are forced to assume the same value at any step of the analysis (Q = H). This means that the damage evolution of Mode I and Mode II are fully coupled. Therefore, the degradation

of cohesion in tension degrades the cohesion in shear and vice versa. Although this adoption can be considered approximated, it is, however, more realistic than considering independent the two phenomena. In particular, the two variables Q and H can increase from 0 to 1 only. Indeed, the degradation of the cohesion is an irreversible process. Once the maximum degradation has been reached, the cohesive contribution to the tensile and shear stresses is zero, and the only contribution to the shear stresses is from the frictional term.

The interface behavior is based on large displacements. In particular, the finite-sliding tracking approach implemented in Abaqus [308], which allows for arbitrary separation, sliding, and rotation of the surfaces, is adopted.

6.2.1.1 *Comparison between experimental and numerical results for small-scale masonry specimens*

Experimental tests conducted by van der Pluijm in [324, 342] on small-scale masonry specimens, composed of two bricks jointed together by a mortar joint, were used as reference to compare with numerical outcomes and to tune the brittleness parameters ζ and ξ. As in [324, 342] the tensile and shear failures were only observed in the brick-mortar interfaces, linear elastic behavior for brick and mortar has been assumed. The mechanical properties adopted in the numerical simulations are collected in Table 17. Figure 88 shows the comparison between experimental and numerical results for small scale masonry specimens subjected to tension (Figure 88(a)) and shear (Figure 88(b)).

Table 17: Mechanical properties for small-scale masonry specimens.

Mortar properties		Contact properties			
E [MPa]	2970	Tensile behavior		Shear behavior	
ν [\]	0.15	f_t [MPa]	0.28	$\tan\phi$ [\]	1.01
		u_k [mm]	0.20	c [MPa]	0.87
Brick properties		ζ [\]	4.38	δ_k [mm]	0.4
E [MPa]	16700			ξ [\]	1.1
ν [\]	0.15			μ [\]	0.73

The tensile properties of the interface are assumed to be consistent with the fracture energy of the brick-mortar interface in tension (Mode I), which in [342] is equal to $G_I^{int} = 12.0\text{N/m}$. Indeed, once the tensile strength f_t and the displacement u_k are fixed, which can be defined directly from the experimental envelope (Figure 88(a)), the brittleness parameter ζ is chosen so that the area under the curve in Figure 87(a) equals G_I^{int}.

Analogously, the shear properties of the interface are assumed to be consistent with the Mode II-fracture energy of the brick-mortar interface, which, in [324], follows the relation $G_{II}^{int} = 130\sigma + 58\text{N/m}$ (with σ in MPa). In this case, $\tan\phi$,
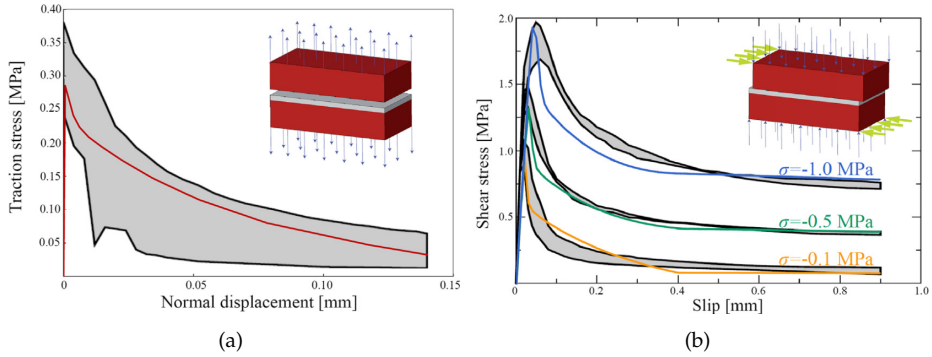
Figure 88: Comparison between experimental and numerical results for small-scale masonry specimens: (a) tensile behavior (experimental envelope (grey area) and numerical response (red line)) and (b) shear behavior (experimental envelopes (grey areas) and numerical responses (blue, green and orange lines) for three different levels of initial compression: 0.1, 0.5 and 1.0 MPa).

c, δ_k, and μ are defined directly from the experimental outcomes [324], whereas the brittleness parameter ξ is chosen to be the best approximation of G_{II}^{int} for the three experimental curves in Figure 87(b).

Finally, as can be observed in Figure 88, the tensile (Figure 88(a)) and shear (Figure 88(b)) contact behaviors here proposed appear in good agreement with the experimental results obtained in [324, 342]. It has to be pointed out that the shear stiffness which can be read in Figure 88(b) is given by the deformability of the 3D FEs (in this case mainly to the mortar FEs) and not by the deformability of the interfaces, which can be considered rigid-cohesive.

6.2.2 *Brick and mortar nonlinear behavior*

Tensile and compressive plastic-damage nonlinear behavior is assumed for brick and mortar, based on the plastic-damage model developed by Lee and Fenves [136] for quasi-brittle materials. For the reader's convenience, a summary of the model equations, accounting for the role of the parameters involved, is given in the Appendix A. The general parameters for quasi-brittle materials [343] adopted in the model are shown in Table 18, in agreement with those chosen in Chapter 4.

Table 18: General parameters for quasi-brittle materials.

ϵ [\]	ψ [\]	f_{b0}/f_{c0} [\]	ρ [\]	VP [\]
0.1	$10°$	1.16	2/3	0.002

6.2.3   *Numerical results*

Experimental-numerical comparisons for the in-plane and out-of-plane behaviors of masonry panels are here provided to show the effectiveness and the accuracy of the model proposed. The detailed micro-model herein proposed has been implemented in Abaqus Standard [308]. Geometric nonlinearity is considered in all the analyses to account for large-displacement effects.

Experimental tests conducted by Vermeltfoort and Raijmakers [344] and by Chee Liang [345] are considered for the in-plane and out-of-plane response of masonry panels, respectively. Mechanical properties utilized for the in-plane and out-of-plane benchmarks are collected in Table 19. When more than one value is given in the same cell of the table, the first value refers to the in-plane benchmark, whereas the second one refers to the out-of-plane benchmark. In general, the tensile response of masonry joints is defined in terms of the tensile strength and fracture energy in tension (Mode I), whereas the shear response of masonry joints is defined in terms of friction, cohesion, residual friction and Mode II-fracture energy. It appears clear that u_k and ζ will be derived from the value of fracture energy in tension (Mode I), whereas δ_k and ξ will be derived from the value of Mode II-fracture energy. To this aim, the brittleness parameters ζ and ξ have been kept equal to the ones of Section 6.2.1.1, and the values u_k and δ_k have been chosen so that the fracture energy values were satisfied. Reference to [346] has been made to define the uniaxial inelastic stress-strain relationships. The evolution of the degradation damage scalar variables d_t and d_c has been kept substantially proportional to the decay of the uniaxial stresses, as successfully experienced is several numerical campaigns [325, 141].

Concerning the in-plane benchmark, the mechanical properties for brick, mortar and brick–mortar interfaces employed in the analyses (Table 3) were reported in previous research [104, 53, 67]. In addition, the tensile strength of mortar has been assumed with reference to the results on mortar prisms obtained in the experimental campaign carried out in the TU Delft laboratories in 1991 [342].

Concerning the out-of-plane benchmark, the material parameters used for the interfaces elements (Table 19) are equivalent to the values used in [67] for the same wall. The elastic stiffness of brick and mortar were not investigated by Chee Liang [345]. Therefore, the Young's modulus of mortar has been assumed according to [346], whereas the Young's modulus of brick has been kept the same as that shown in [342], being the materials of the same type. The other properties are the same to the in-plane benchmark.

Table 19: Mechanical properties utilized for the in-plane and out-of-plane benchmarks. When more than one value is given in the same cell, the first value refers to the in-plane benchmark, whereas the second one refers to the out-of-plane benchmark.

Contact mechanical properties

Tensile behavior		Shear behavior	
f_t [MPa]	0.20, 0.12	$\tan\phi$ [\]	0.75, 0.58
u_k [mm]	0.36	c [MPa]	0.22
ζ [\]	4.38	δ_k [mm]	0.4
		ξ [\]	1.1
		μ [\]	0.75, 0.58

Mortar mechanical properties

E [MPa]	850, 2300
ν [\]	0.15

Tensile uniaxial behavior			Compressive uniaxial behavior		
Stress [MPa]	Inel. strain	d_t [\]	Stress [MPa]	Inel. strain	d_c [\]
1.5	0	0	7.8	0	0
0.1	0.002	0.95	8.2	0.002	0
			0.4	0.015	0.95

Brick mechanical properties

E [MPa]	16700
ν	0.15

Tensile uniaxial behavior			Compressive uniaxial behavior		
Stress [MPa]	Inel. strain	d_t [\]	Stress [MPa]	Inel. strain	d_c [\]
3.5	0	0	11.0	0	0
0.3	0.002	0.95	11.5	0.001	0
			0.6	0.007	0.95

6.2.3.1   *In-plane response*

Results obtained by Vermeltfoort and Raijmakers [344] in shear tests on single-leaf panels are here considered. The identical wall specimens, named J4D, J5D and J7D in [344], with a length (990 mm) to height (1000 mm) ratio of approximately 1 were considered (Figure 89). They are characterized by 18 brick layers of which 2 were fixed to steel beams so as to keep the top and bottom edges of the element straight during the test (green zones in Figure 89(a)). Each brick is 204 × 98 ×50 mm, whereas the bed and head mortar joints are 12.5 mm thick. Particularly, the masonry panels were initially preloaded with a vertical top pressure, Pv=0.3 MPa for J4D and J5D and Pv=2.12 MPa for J7D. Then a horizontal load was then applied in the plane of the walls at the top edge under displacement control up to collapse, see Figure 89(a).

During the tests, first, horizontal cracks appeared at the top and bottom of the walls. Then, cracks started to develop diagonally along the bed and head mortar joints and through the bricks, up to failure. The experimental response was characterized by a softening branch that started when diagonal cracks appeared in the center of the specimens.

The wall is modeled here using the detailed micro-modeling approach presented in the previous sections. The analyses followed the two-step boundary conditions depicted in Figure 89(a). The assembly of textured units employed in the numerical model is highlighted in Figure 89(b).
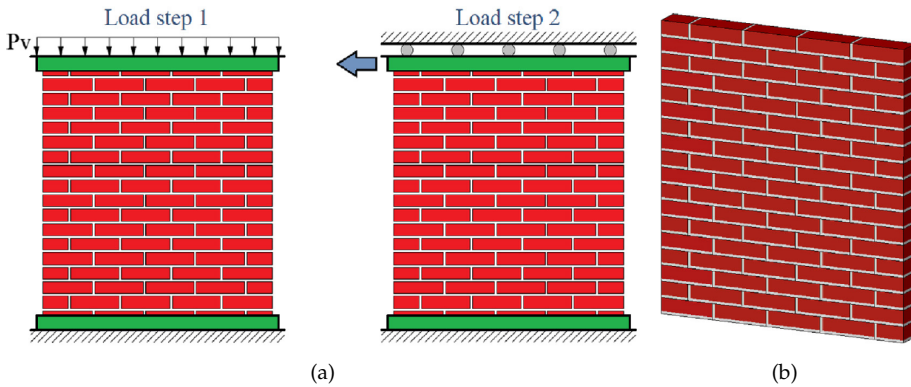
Figure 89: In-plane response of masonry wall panels [347]: (a) boundary conditions and (b) assembly of textured units employed in the numerical model.

Figure 90 provides experimental-numerical comparisons: the experimental load-displacement curves for J4D, J5D and J7D walls are compared with the numerical results carried out using a textured unit mesh composed of 20 hexahedral 8-nodes FEs. In this figure, the numerical predictions reported by Lourenço & Rots [53] and by Macorini & Izzuddin [67] are also shown. A good agreement between experimental and numerical results can be observed up to collapse, including initial stiffness, maximum capacity and the post-peak response of the panels. Also,

the predictions of the proposed modeling approach are generally close to those reported in [53, 67] for all the considered walls, with the current predictions of the post-peak response for wall J7D better than the one obtained in [53].
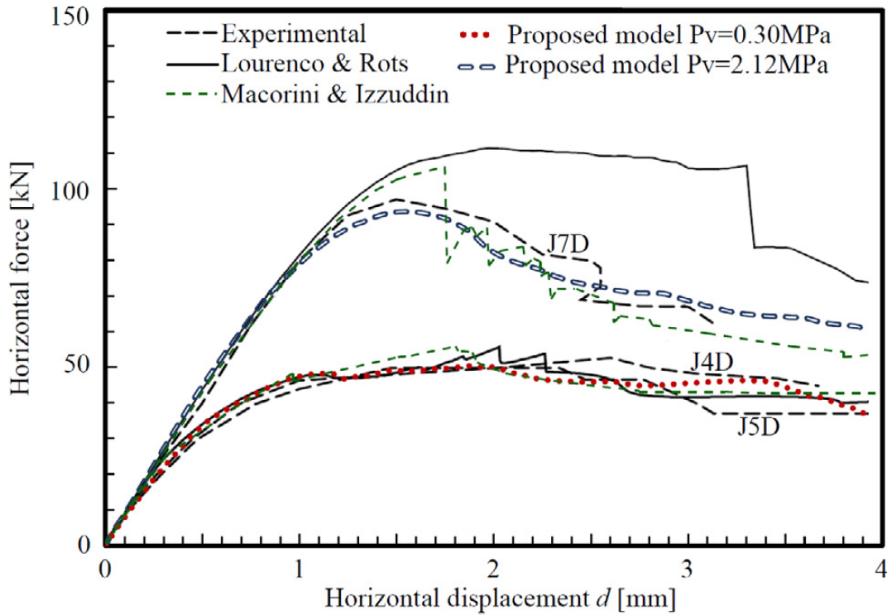
Figure 90: Experimental – numerical comparisons of the load – displacement curves for the masonry wall panels loaded in plane.

The discretization of the textured units is explicitly chosen by the user. The role of the mesh size is shown in Figure 91(a), in which the influence of mesh refinement on the load-displacement curves is collected. The results obtained using a textured unit mesh consisting of 20 hexahedral 8-nodes FEs (coarse mesh) and a textured unit mesh consisting of 108 hexahedral 8-nodes FEs (fine mesh) are compared. As can be noted, very small discrepancies emerged. Thereby, mesh dependency appears negligible, also thanks to the regularization of the fracture energy in the continuum plastic-damage model. This aspect is particularly appealing as the analyses with the coarse mesh presented a computational cost considerably smaller than the fine mesh.

Figure 91(b) shows the influence of the nonlinear behavior of textured units on the load-displacement curves. As can be noted, the fact of accounting for the cracking and crushing of textured units significantly affects the post-peak behavior (Figure 91(b)), whereas the hypothesis of linear elastic textured units slightly overestimates the peak load. Basically, it is expected that the differences in considering or not the nonlinear behavior of textured units would increase by increasing the vertical pressure as well as the interlocking of the masonry texture (e.g. for multi-leaf walls).
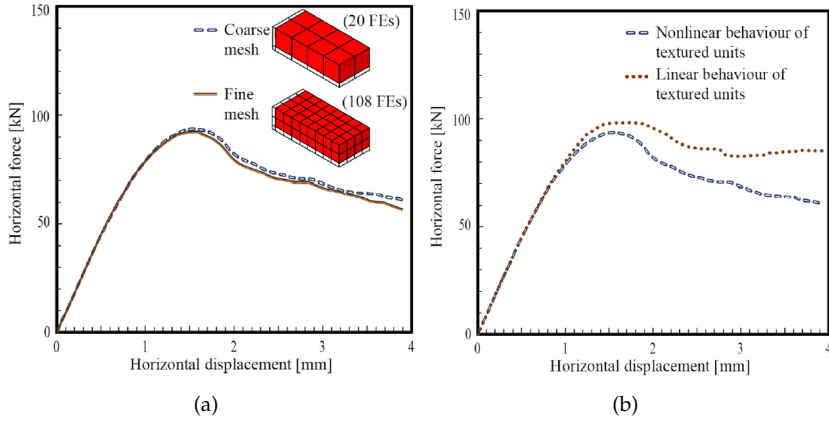
Figure 91: Load — displacement curves for Pv = 2.12 MPa: (a) investigation of the mesh dependency and (b) influence of the nonlinear behavior of the textured units.

Finally, Figure 92 shows the deformed shape and crack pattern in the masonry wall panel obtained from the numerical model, in terms of tensile damage contour plot (Figure 92(a)), compressive damage contour plot (Figure 92(b)), and interfaces which exhibited failure (Figure 92(c)). Also, numerical results are compared with the experimental crack pattern experienced in [344] (Figure 92(d)). As can be noted in Figure 92, these predictions are in good agreement with the actual crack pattern. Particularly, the interfaces which exhibited failure are placed along the panel diagonal. Furthermore, few textured units experienced tensile failure in the central part of this diagonal (Figure 92(a)), representing brick and mortar cracking. In addition, few textured units also showed crushing in the two extremities of the diagonal (Figure 92(a)). These features have also been experienced by the experimental tests [344], see for example Figure 92(d), confirming the good accuracy of the model proposed. Finally, these predictions are also in good agreement with the main crack paths and with the numerical results reported in [53, 67].
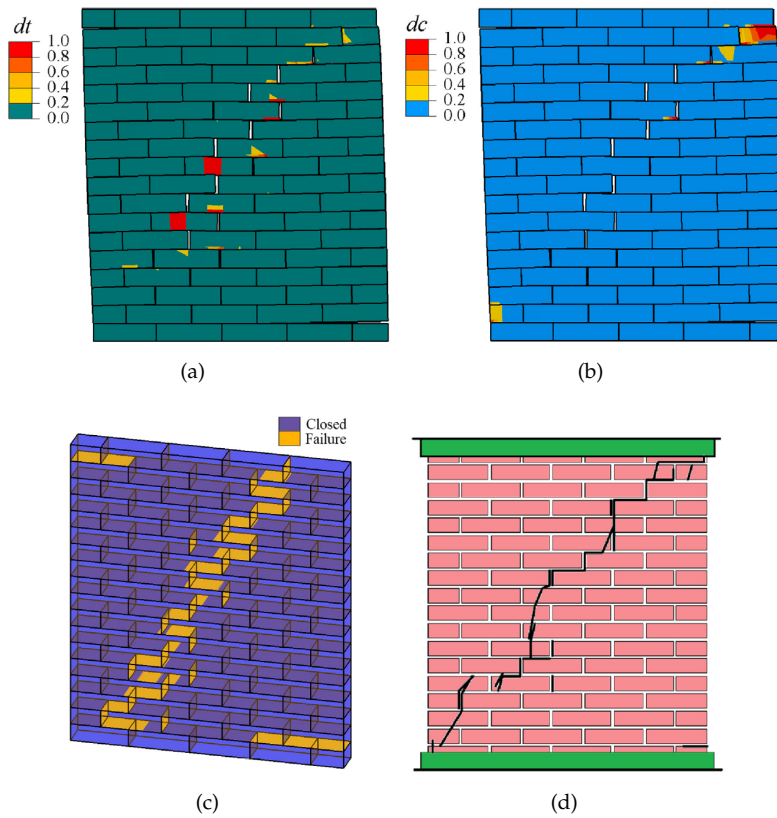
Figure 92: Comparison of the panel's crack pattern: (a) tensile damage contour plot, (b) compressive damage contour plot, (c) interfaces which exhibited failure and (d) experimental crack pattern for the specimen with Pv=2.12 MPa (J7D in [347]).

6.2.3.2   *Out-of-plane response*

Numerical analyses are also carried out to assess the effectiveness of the detailed block-based approach developed to investigate the out-of-plane behavior of masonry panels. Comparisons are carried out against the experiments performed by Chee Liang [345].

The out-of-plane behavior of a solid wall, simply supported along its four edges and subjected to bi-axial bending, is considered, and reference is made to experiments on two identical specimens: wall 8 and wall 12 in [345]. The single-leaf masonry wall panels were 1190mm high, 795mm wide and 53mm thick. The dimensions of the brick were $112 \times 53 \times 36$ mm and the thickness of the mortar joints were 10 mm. The two specimens were loaded up to collapse by applying a uniform out-of-plane pressure through an air-bag sandwiched between the wall and a stiff reacting frame. Another stiff steel frame was connected to the wall on the other side, so as to prevent out-of-plane displacements and provide fixed supports along the four edges. The crack pattern experienced by the two wall specimens [345] is shown in Figure 93.

(a)   (b)
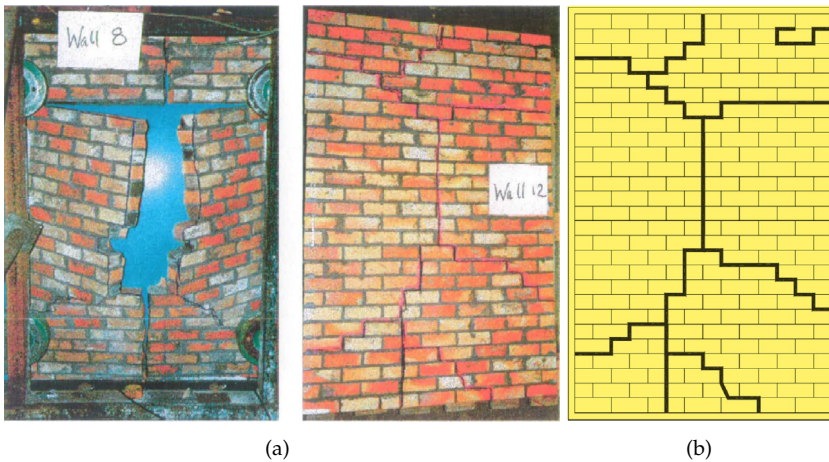
Figure 93: Experimental crack pattern: (a) photos of the failure of Wall 8 and Wall 12 from [348] and (b) sketch of the crack pattern of Wall 12.

To compute the solution up to the collapse of the panel (also in case of softening), a quasi-static direct-integration dynamic analysis procedure has been adopted [308]. This algorithm permits to study quasi-static responses in which inertia effects are introduced primarily to regularize unstable behaviors. The Authors experienced a better performance of this algorithm, specifically in the softening regime, with respect to more common arc length procedures.

Figure 94 provides the numerical-experimental comparisons in terms of lateral pressure-transversal displacement curves, where the textured unit mesh composed of 20 hexahedral 8-nodes FEs, shown in Figure 91(a), has been imple-

mented. Although the through-thickness discretization may play a certain role, especially in the out-of-plane analysis of multi-leaf walls [349], the utilization of two 8-nodes hexahedral FEs through-thickness appears sufficiently accurate for the case under study.
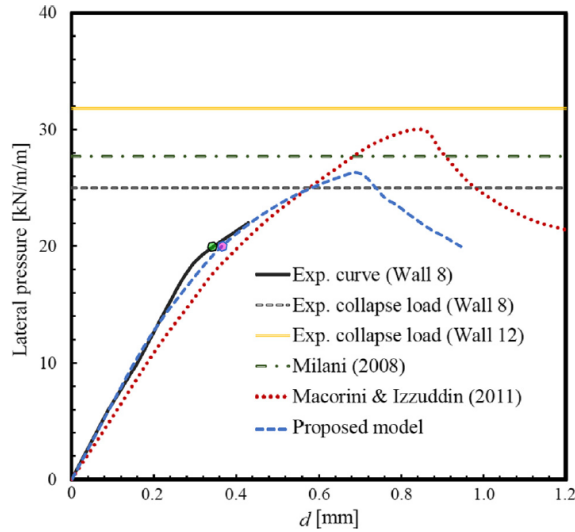
Figure 94: Comparison of the lateral pressure – out-of-plane displacement curves.

The experimental results reported in [345] consist of a partial load-displacement curve for wall 8 and the maximum capacity for the walls 8 and 12. Good agreement between the numerical and experimental results can be observed. The maximum lateral pressure obtained with the proposed model appears very close to the experimental capacity [345], to the collapse pressure determined in [116] through a 3D limit analysis approach and to the numerical curve obtained in [67]. Particularly, the curve obtained with the proposed approach very well fits the partial load-displacement curve for wall 8. Additionally, Figure 95 provides the comparison between the experimental and numerical out-of-plane deflections at the instant, shown in Figure 94 by means of a green point and a magenta point, with lateral pressure equal to 20 kN/m^2, i.e. at an instant slightly prior to failure. Here again, a good numerical-experimental agreement is achieved in terms of out-of-plane deflections.

Finally, Figure 96 shows the crack pattern obtained by means of the proposed model, in terms of deformed shape at collapse (Figure 96(a)), out-of-plane displacement contour plot (Figure 96(b)), tensile damage contour plot (Figure 96(c)) and compressive damage contour plot (Figure 96(d)). By comparing the numerical crack pattern of Figure 96 with the experimental one (Figure 93), it can be noted that the actual failure mechanism, although slightly different in the two walls, is qualitatively represented by the numerical model proposed. Particularly, the large vertical crack that runs in the middle of the panel crossing head mortar
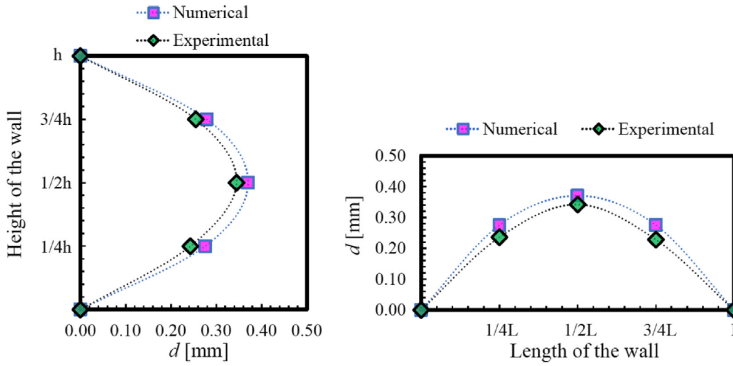
Figure 95: Comparison between experimental and numerical out-of-plane deflections when the lateral pressure is equal to 20 kN/m^2, see the green and magenta points in Figure 108.

joints and bricks as well as the diagonal cracks observed in the tests are well represented. Indeed, as can be noted in Figure 96(c), tensile damage is experienced in the central part of the textured units which are placed in the central vertical part of the wall, in agreement with the actual vertical cracks experienced by both walls (Figure 93) which alternatively crosses the bricks.

6.2.4 *Discussion of the results*

Summing up, although this model accounts for a very detailed description of masonry constituents and is characterized by a larger complexity with respect to existing numerical models, its computational demand appears reasonably acceptable. Indeed, as shown in Table 20, the computational time needed in the simulations are, after all, moderate. Even, the 3D detailed micro-model proposed appears faster than other more standard 2D micro-modeling approaches, see in [172] the time needed for the same in-plane benchmark, based on well-known interface elements [53]. Therefore, the contact-based formulation proposed appears preliminarily efficient.

Table 20: Times required to conduct the analyses. [b] utilizing a commercial laptop equipped with a processor Intel®Core[TM] i7-6500U CPU @ 2.50GHz and 16GB RAM.

Simulation	Time required[b] (hh:mm:ss)
In-plane coarse mesh (Pv=0.30MPa)	00:06:33
In-plane coarse mesh (Pv=2.12MPa)	00:07:18
In-plane fine mesh (Pv=2.12MPa)	00:23:20
Out-of-plane	00:09:11
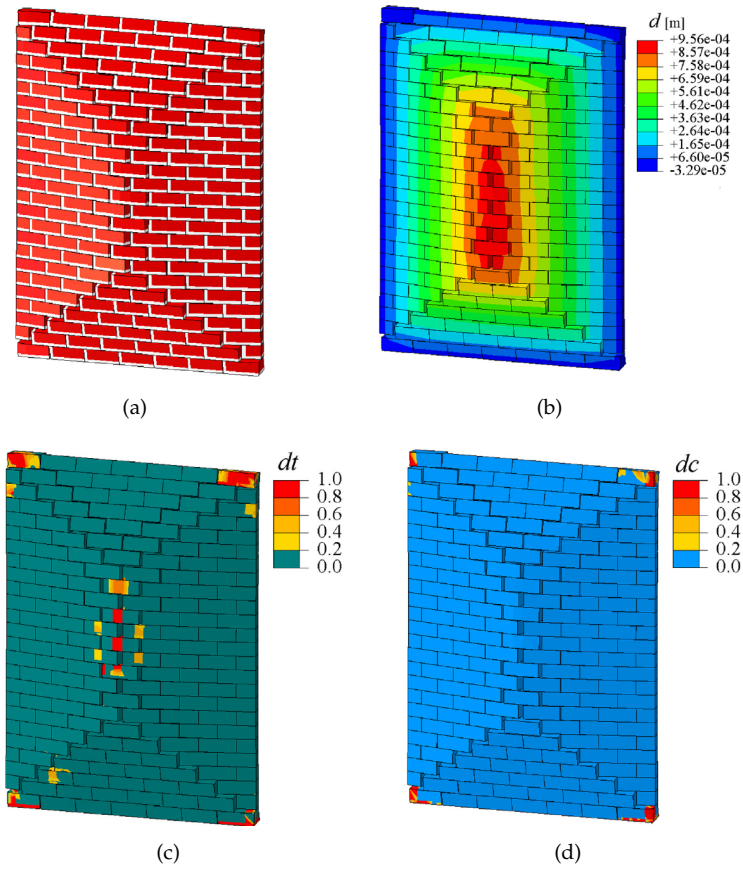
Figure 96: Crack pattern obtained from the proposed model: (a) deformed shape, (b) out-of-plane displacements contour plot and (c) tensile and (d) compressive damage contour plots at the end of the simulation.

6.3   CYCLIC RESPONSE OF FULL-SCALE MASONRY STRUCTURES

In this section, following an approach akin to the one proposed in Section 6.2 and aiming to extend it to the cyclic behavior, a damaging block-based model is developed for the numerical analysis of the cyclic behavior of full-scale masonry structures.

The interaction between adjacent blocks (which do not include any mortar layer in this version of the model) is formulated in a contact-based framework accounting for cohesion and friction, whereas the blocks follow a continuum plastic-damage constitutive law [136] both in tension and compression (Figure 97). As the mortar layers are not explicitly modeled, the use of expanded blocks is adopted (Figure 97), as commonly employed in block-based models [53, 67].
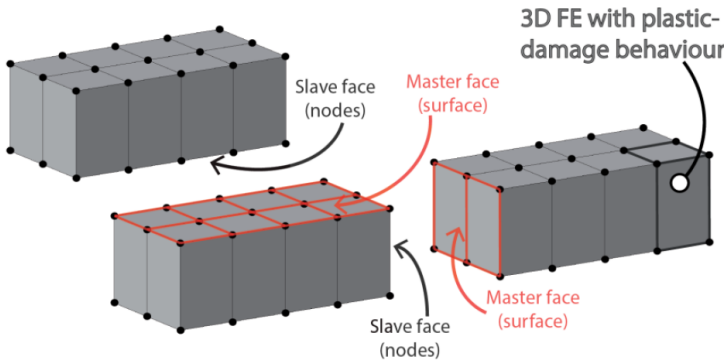
Figure 97: Node-against-surface contact approach adopted in the damaging block-based modeling.

The adopted contact formulation conceives contact pairs composed of one slave face and one master face (Figure 97), following the traditional node-against-surface approach [350]. In particular, the nodes of the slave face contact the surface of the master face (Figure 97). Therefore, contact is enforced at discrete points, which are the nodes of the slave face. After the assembly of the blocks, the contact pairs between adjacent blocks are defined by means of fully automatic contact detection algorithms [308]. A finite-sliding formulation, which allows for arbitrary separation, sliding, and rotation of the surfaces, is adopted [308]. The cohesive contact behavior is governed by an ad-hoc modification of the standard surface-based contact behavior available in Abaqus [308]. In this context, an ad-hoc automatic subroutine is implemented to reproduce a Mohr-Coulomb failure surface with tension cut-off.

The sliding between blocks is conceived without a dilatant behavior, whereas dilatancy is considered in the 3D nonlinear FEs used for the blocks, in the framework of nonassociated plasticity [308].

The formulation of the proposed model allows for a direct setting of the mechanical parameters from small-scale experimental tests on masonry specimens.

The main idea at the base of this setting is that the properties of the cohesive-frictional behavior between blocks are based on brick-mortar bond tests (tensile failure and shear sliding), whereas the properties of the block 3D FEs are based on tests on masonry wallets and on tests on single bricks.

In the following, the description of the contact mechanical behavior, the block nonlinear behavior, as well as the strategy suggested for the mechanical characterization of the model mechanical properties from small-scale tests on masonry are illustrated.

6.3.1 Cyclic contact behavior

In the normal direction, the contact stress σ is computed by means of a pressure-overclosure relationship in compression and a linear elastic relationship in tension:

$$\sigma = \begin{cases} \text{Pressure} - \text{overclosure relationship,} & u < 0 \\ K_{nn}u, & u \geqslant 0 \end{cases} \tag{21}$$

where K_{nn} is the cohesive stiffness in normal direction and u is the normal displacement (separation). The pressure-overclosure relationship represents the approach used to enforce the contact constraints. Several numerical strategies have been proposed to deal with the contact constraints [340]. The most common approaches are Lagrange multiplier methods and penalty methods. Lagrange multiplier methods introduce additional multipliers to enforce directly and exactly the contact constraint, whereas penalty methods avoid the need for additional variables by introducing an approximation of the constraint condition. In this study, the Lagrange multiplier approach implemented in Abaqus (hard contact) is adopted [308]. Relationship (21) is assumed to be valid for tensile stresses until the tensile strength f_t of the contact behavior is reached, whereas it is always valid in the compressive regime.

In the shear direction, the tangential slip δ is linearly related to the contact shear stress τ with the relation:

$$\tau = K_{ss}\delta, \tag{22}$$

where K_{ss} is the cohesive stiffness in shear. This relation is valid until the contact shear stress equals the shear strength f_s, see Equation (15).

Therefore, contact failure is supposed when the contact stresses at a point intersects a Mohr-Coulomb failure surface with tension cut-off, see Equation (16). A sketch of the failure surface adopted for the contact behavior is shown in Figure 86. Once contact failure is reached, cohesive behavior in tension and cohesive-frictional behavior in shear is activated.

The maximum value of the stress in the post-peak regime, in a contact point, is described in tension by the relationship:

$$\sigma = \begin{cases} (1-D)\,f_t, & u_0 < u < u_k \\ 0, & u \geqslant u_k \end{cases} , \tag{23}$$

and in shear by the relationship:

$$\tau = \begin{cases} (1-D)\, f_s\,(\sigma) + D\mu\,\langle -\sigma \rangle\,, & \delta_0 < \delta < \delta_k \\ \mu\,\langle -\sigma \rangle\,, & \delta \geqslant \delta_k \end{cases}, \qquad (24)$$

where the degradation scalar variable D is defined as:

$$D = \max \begin{cases} 1 - \dfrac{u_0}{u_{MAX}}\left(1 - \dfrac{1 - e^{-\zeta \frac{u_{MAX}-u_0}{u_k-u_0}}}{1 - e^{-\zeta}}\right) \\[4mm] 1 - \dfrac{\delta_0}{\delta_{MAX}}\left(1 - \dfrac{1 - e^{-\xi \frac{\delta_{MAX}-\delta_0}{\delta_k-\delta_0}}}{1 - e^{-\xi}}\right) \end{cases}, \qquad (25)$$

being μ the residual friction, u_0 and δ_0 the separation and the slip at the limit of the linear elastic behavior in tension and shear, respectively, u_{MAX} and δ_{MAX} the maximum separation and the maximum slip ever experienced by the contact point, respectively, u_k and δ_k the ultimate separation and the ultimate slip of the cohesive behavior, respectively, ζ and ξ non-dimensional brittleness parameters in tension and shear, respectively.
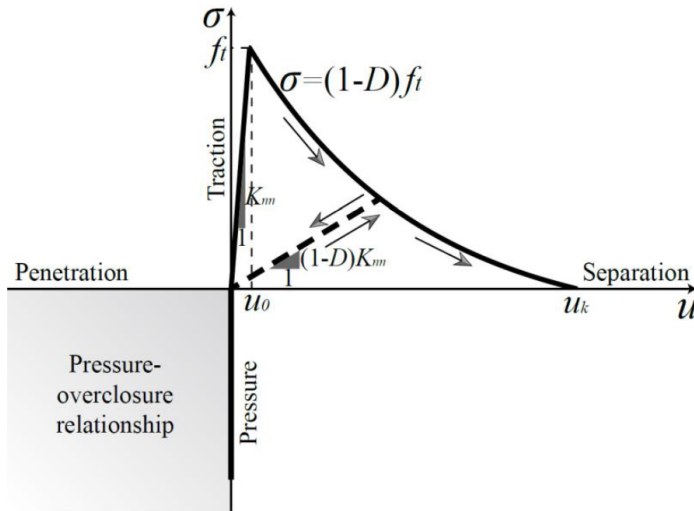

Figure 98: Contact normal cyclic behavior.
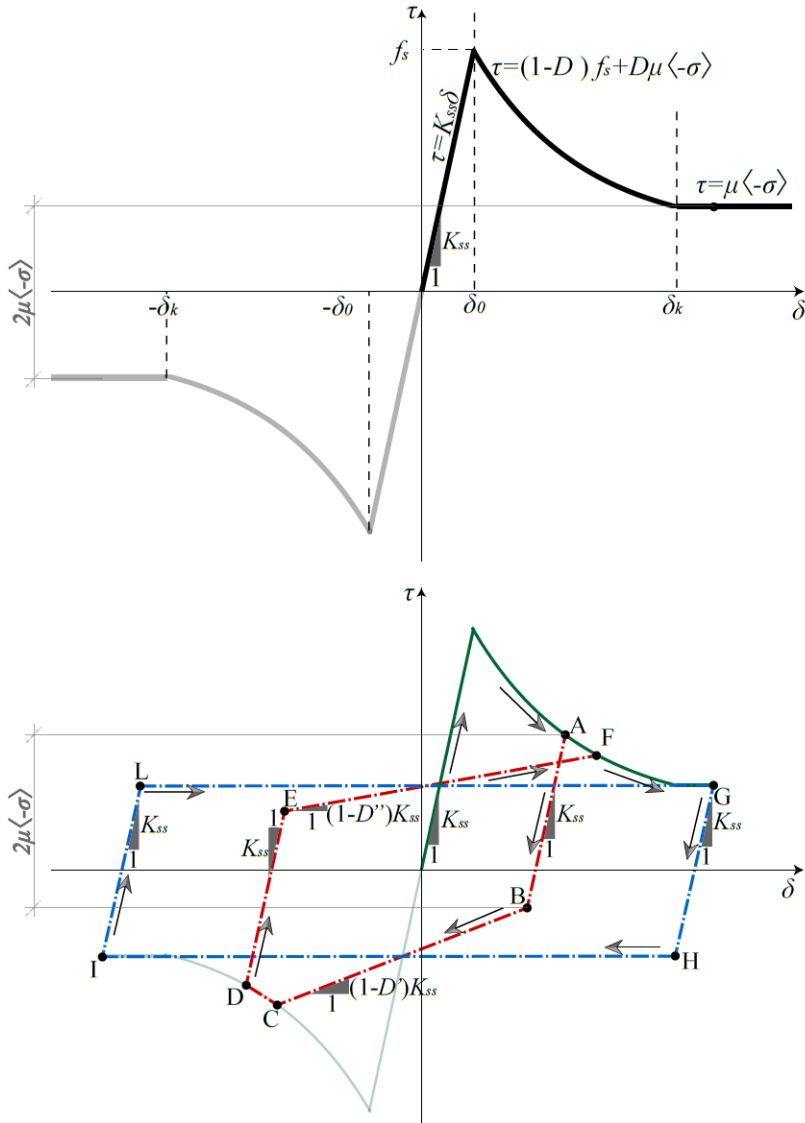
Figure 99: Contact shear cyclic behavior. Two unloading-reloading paths are indicated: ABCDEF in the shear softening stage, GHIL in the final shear friction stage. D′ and D″ are the values assumed by the degradation scalar damage variable D when reaching the point A and the point D, respectively

From equations (23), (24) and (25) it appears clear that the cohesive behavior in tension and shear is governed by the same degradation scalar variable D. Indeed, the damage evolution in tension and shear are fully coupled, i.e. the degradation of cohesion in tension degrades the cohesion in shear and vice versa.

Figures 98 and 99 show the contact normal and shear cyclic behavior, respectively. The monotonic behavior is depicted by means of black thick lines. Dealing with the tensile contact behavior (Figure 98), if a degraded contact point with $0 < D < 1$ undergoes unloading, the unloading path will be characterized by a linear branch with a degraded stiffness $(1-D)\,K_{nn}$ until the stress state reach compression. In the compression regime, the behavior is fully governed by the pressure-overclosure relationship adopted, which is completely independent by the state of degradation of the cohesion.

As can be noted in Figure 99, the contact shear cyclic behavior appears more complex than the normal one, as it is also governed by friction. If a degraded contact point $(0 < D < 1)$, e.g. point A in Figure 99, undergoes unloading, the unloading path will be characterized by a bi-linear branch. The first segment will be defined by the initial stiffness K_{ss} and by a stress drop equal to two times the maximum frictional contribution, i.e. $2\mu\langle-\sigma\rangle$. Therefore, the length of the first segment, e.g. AB in Figure 99, will be equal to $\overline{AB}=2\mu\langle-\sigma\rangle\sqrt{1+\frac{1}{K_{ss}^2}}$. The second segment, conversely, will be characterized by a degraded stiffness $(1-D)\,K_{ss}$ until the reaching of point C (Figure 99), which represents the specular point of A in Figure 99. From this point forward, the cohesive exponential behavior is re-established, and the contact point further degrades (for example, moving from point C to point D in Figure 99). If a fully degraded contact point (D = 1), e.g. point G in Figure 99, undergoes unloading, the unloading path will be characterized by a bi-linear branch, in which the first segment will be defined by the initial stiffness K_{ss} and by a stress drop equal $2\mu\langle-\sigma\rangle$, whereas the second segment will be characterized by an horizontal line, purely governed by friction.

The contact shear cyclic behavior proposed has been found to be consistent with the experimental results obtained by Atkinson et al. [351] on small-scale masonry samples, as well as with the numerical results found by Gambarotta & Lagomarsino [58], as shown in Figure 100.

6.3.2   *Block nonlinear behavior*

The isotropic plastic-damage nonlinear behavior based on the constitutive model developed by Lee and Fenves [136] for quasi-brittle materials is assumed for blocks. The general parameters adopted in the model for the block are shown in Table 18. For the reader's convenience, a summary of the model equations, accounting for the role of the parameters involved, is given in the Appendix A.
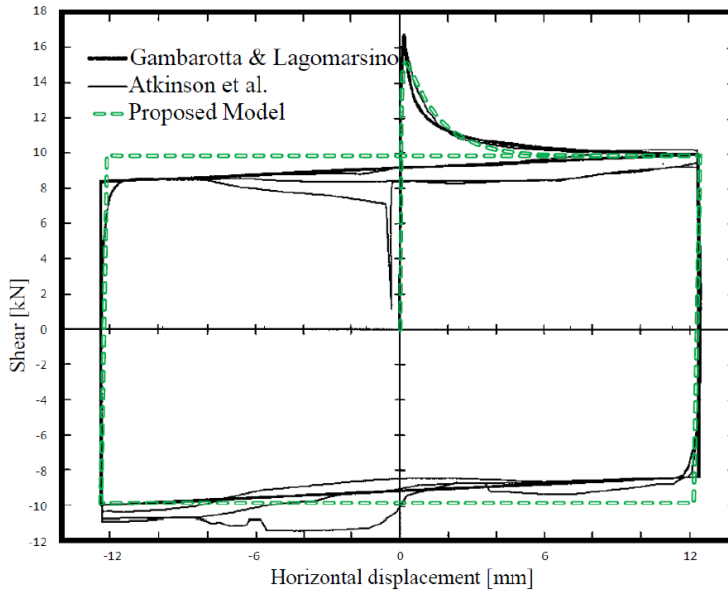
Figure 100: Cyclic shear behavior of masonry joints: Comparison between experimental tests (old bricks specimen in [351]) and numerical response.

6.3.3 Mechanical characterization of the model from small-scale experimental test

The proposed numerical model allows for a direct and easy setting of the mechanical parameters. The strategy that can be used for the mechanical characterization of the model based on monotonic small-scale experimental tests on masonry wallets and components is summarized in Figure 101. The main idea at the base of this setting is that the properties of the contact cohesive-frictional behavior between blocks are based on brick-mortar bond tests, whereas the properties of the block 3D FEs are based on tests on masonry wallets and blocks.

The contact shear behavior can be completely defined by shear tests on masonry triplets (Figure 101). The output of experimental tests on triplets (at least with 3 different levels of pre-compression) in terms of cohesion (c), initial friction (tanφ) and residual friction (μ) can be directly used as mechanical properties in the numerical model. Moreover, the ultimate slip of the cohesive behavior (δ_k) and the brittleness parameter ξ can be calibrated in order to better fit the post peak behavior of the tests, as well as to better approximate the Mode II fracture energy. Finally, the shear cohesive stiffness (K_{ss}) can be determined by fitting the initial linear branch of the shear-slip curve. Indeed, in the simulation of these tests, the deformability of the blocks plays a marginal role.

The contact normal characterization needs even less parameters (Figure 101). As a matter of fact, the compressive contact behavior does not need any parameter to be characterized. The tensile cohesive behavior can be characterized by bond
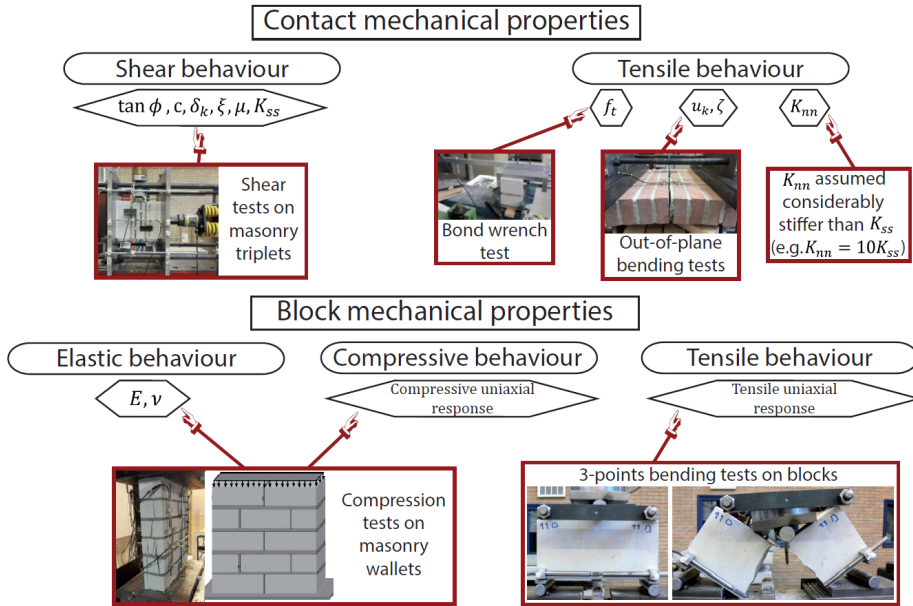
Figure 101: Strategy for the mechanical characterization of the model from small-scale experimental tests on masonry components and assemblages.

wrench tests, in terms of tensile strength (f_t), and out-of-plane bending tests which can be used to characterize the Mode I fracture energy and, also, can be used to verify the tensile strength measured by wrench tests. From the Mode I fracture energy, the ultimate separation of the cohesive behavior (u_k) and the brittleness parameter ζ can be calibrated. The cohesive stiffness in the tensile direction K_{nn} represents a further component of deformability in the normal direction, which acts only in the tensile regime. Although the Young's modulus of masonry in compression could be, in theory, different from the one in tension, no deep experimental investigation has been conducted on this topic. Therefore, the use of a stiff value of K_{nn}, considerably stiffer than K_{ss} (e.g. $K_{nn} = 10K_{ss}$), is suggested.

Dealing with the block mechanical properties, the continuum isotropic elastic properties as well as the compressive and tensile uniaxial nonlinear curves need to be characterized (Figure 101). As in the compressive regime the contact formulation does not account for any failure as well as any deformability, the compression tests on masonry wallets can be used to characterize the block elastic properties, in terms of Young's modulus E and Poisson's coefficient ν, as well as the compressive nonlinear behavior of the blocks. Therefore, the elastic and compressive responses of blocks is related to masonry properties. Conversely, the tensile nonlinear behavior of the blocks is deduced from tests on blocks (e.g. 3-points bending tests, see Figure 101), and, therefore, is related to a block property.

As one can note, the proposed numerical model shows, beyond the deformability of the continuum isotropic blocks, an additional deformability in the shear behavior due to the cohesive stiffness K_{ss} (considering negligible the deformability due to K_{nn}). Therefore, dealing with a masonry panel, the overall shear modulus G evaluated with the proposed model will be lower than the one predicted with an isotropic continuum model with the same parameters E and ν. Of course, masonry is not an isotropic material and the relationship between the three elastic constants is, in general, not valid. Indeed, by using the measured values of E and ν in a continuum model, the value of G will be, in general, overestimated. In addition, the values of E and G generally adopted in equivalent frame models [352] (see Section 2.8) for the simulation of masonry structures often lead to values of ν which have no mechanical meaning (even $\nu > 0.5$). Therefore, the use of an additional deformability in the shear behavior (governed by K_{ss}) allows the proposed model to overcome this limitation of continuum isotropic models. In particular, the authors experienced that the overall shear stiffness of masonry walls is generally gathered with a good accuracy by the proposed model utilizing the cohesive stiffness K_{ss} calibrated in triplet tests.

Finally, it has to be pointed out that the characterization of the mechanical parameters of the model can be fully described by monotonic tests on small-scale masonry specimens (and components), even if the model is suitable for cyclic simulations. This aspect constitutes a further appealing feature of the proposed model.

6.3.4 *Experimental campaign*

Extensive testing programs to characterize the behavior of masonry structures from a material to a structural level have been carried out at the laboratory of Delft University of Technology since 2014 [15]. At material level (small-scale tests), destructive laboratory tests were performed on both existing and replicated masonry specimens [353]. At structural level, several in-plane and out-of-plane tests on single piers have been performed [348]. Furthermore, the campaign comprehended also two quasi-static cyclic pushover tests on full-scale two-story high assembled structures [347]. All the tests considered have been conducted by using the same calcium silicate brick masonry.

6.3.4.1 *Small-scale tests*

Many small-scale tests on masonry samples (wallets, triplets, couplets) and on masonry components (brick and mortar) have been performed at the Stevin II laboratory at the Delft University of Technology [353, 354]. All the tests considered were performed on replicated calcium silicate brick masonry [354], made of $210 \times 71 \times 102$ mm bricks. Standardized monotonic destructive material tests for the characterization of masonry have been conducted and the experimental set-ups and results were collected in [354]. Particularly, compression tests on masonry wallets, brick and mortar specimens, bending tests on masonry wallets,

brick and mortar specimens, bond wrench tests on masonry couplets, and shear tests on masonry triplets have been performed.

6.3.4.2   *In-plane cyclic tests on masonry walls*

Seven 2.75 m high masonry walls made of calcium silicate brick masonry have been built and tested under in-plane cyclic loading. Two height/width aspect ratios (0.7 and 2.5) and two different configurations (i.e. cantilever and double clamped walls) were considered. In addition, different vertical pressure values have been initially applied to the walls. The used set-up provided a uniform vertical pressure and a horizontal imposed displacement on the top of the walls. A sketch of the set-up employed for the in-plane tests is shown in Figure 102(a). A quasi-static cyclic pushover test was performed on each wall in displacement control. Further details are collected in [348].

6.3.4.3   *Out-of-plane cyclic tests on masonry walls*

Four walls were also tested in the out-of-plane direction by applying a quasi-static cyclic loading using a system of airbags. Two different configurations (i.e. one-way and two-way spanning configurations) were considered. The tests were performed by employing a system of coupled airbags on both sides of the wall to apply a uniform pressure. The difference between the loads measured on both sides is the total out-of-plane load acting on the wall. A sketch of the set-up used in the tests (e.g. for the two-way spanning walls) is shown in Figure 102(b). The interested reader is referred to [348] for further details.
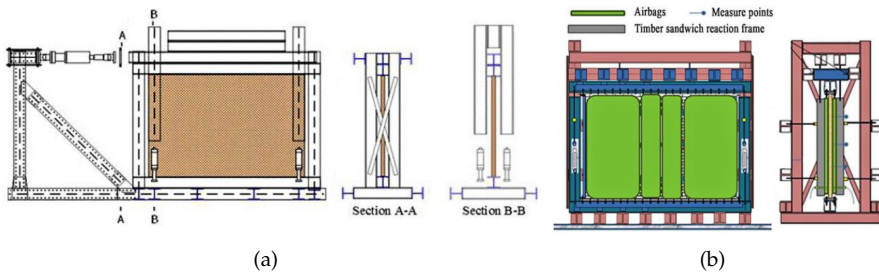
Figure 102: Sketch of the set-up used for the (a) in-plane and (b) out-of-plane tests on walls.

6.3.4.4   *Cyclic pushover test on a masonry full-scale terraced house*

The extensive experimental campaign conducted in Delft also included a terraced house typology, which was representative of the masonry constructions built in the Netherlands during the period 1960-1980. Two terraced houses (one made of calcium silicate bricks and the other of calcium silicate elements) were built

and tested through a quasi-static cyclic pushover loading [15]. In this study, reference to the calcium silicate brick masonry terraced house is made [347]. The construction is characterized by the presence of large daylight opening in the facades. Consequently, the load-bearing structure is composed of very slender piers and long transversal walls (Figure 103). The masonry bricks were laid using a stretcher bond and allowing for the interlocking of the bricks at the corners of the transversal walls and the piers (Figure 103). Each floor consisted of two separated prefabricated concrete slabs spanning between the load-bearing transversal walls. A braced steel tower was built to apply the cyclic horizontal loading to the house. A quasi-static cyclic pushover test was performed on the terraced house. The test was performed in displacement control with the additional condition of maintaining equal the forces applied at the two floor levels through four actuators (two per each floor). For the reader convenience, reference to [347] is made for further details.

Figure 103: Calcium silicate brick masonry terraced house: (a) sketch of the geometry and (b) photo.

6.3.5 *Mechanical properties calibration*

The mechanical characterization of the proposed damaging block-based model has been performed following the scheme depicted in Figure 101, thanks to the small-scale monotonic tests performed on calcium silicate brick masonry at the TU Delft [354] (briefly described in Section 6.3.4).

An example of calibration of the contact mechanical properties for the shear behavior is shown in Figure 104. The experimentally-determined values of cohesion

(c), initial friction (tanϕ), and residual friction (μ) have been directly implemented in the numerical model, whereas the ultimate slip of the cohesive behavior (δ_k) and the brittleness parameter ξ, have been calibrated to better fit the curves in Figure 104(b). In particular, the value of K_{ss} has been chosen to represent the average of the initial experimental branches.

(a)   (b)
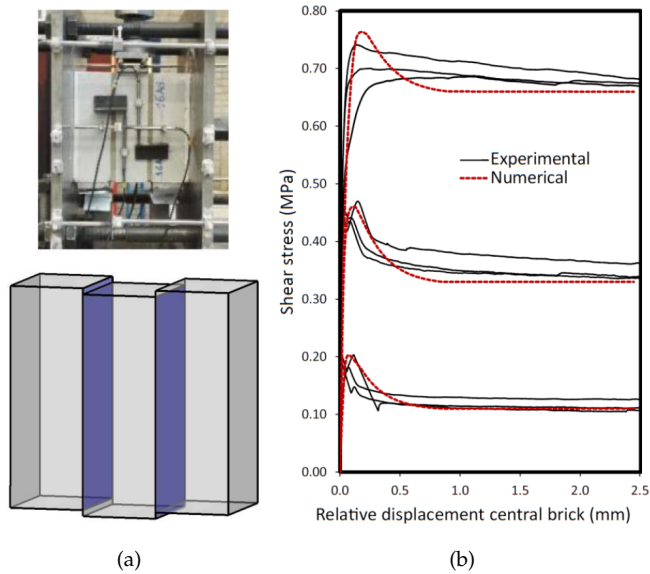
Figure 104: Shear tests on triplets: (a) experimental (top) and numerical (bottom) samples and (b) experimental-numerical shear stress – relative displacement of the central brick curves for three different level of pre-compression.

Figure 105 shows the mechanical characterization of the compressive nonlinear behavior of the blocks by means of compression tests on masonry wallets. The numerical model is not able to directly simulate the formation of vertical cracks through-thickness of the blocks (Figure 105(a)). However, the continuum damage formulation of the blocks allows to phenomenologically represent the peak and post-peak compressive behavior of masonry (Figure 105(b)) by showing a widespread distribution of compressive damage into the numerical model (Figure 105(c)).

The mechanical parameters calibrated from small-scale tests specimens and, then, used in the numerical simulation of panel-scale and full-scale structures are collected in Table 21. The tensile and compressive post-peak behavior of the blocks is described by means of a linear softening branch (Table 21), which characterize the brittleness of the material, leading to a value 0.41 N/mm of tensile fracture energy, and to a value 11.22 N/mm of compressive fracture energy, being the characteristic length related to the hexahedral finite elements (55 mm x 55 mm x 80 mm) used throughout this study, defined as specified in the Appendix, equal to 55 mm. The tensile and compressive scalar damage variables, which in
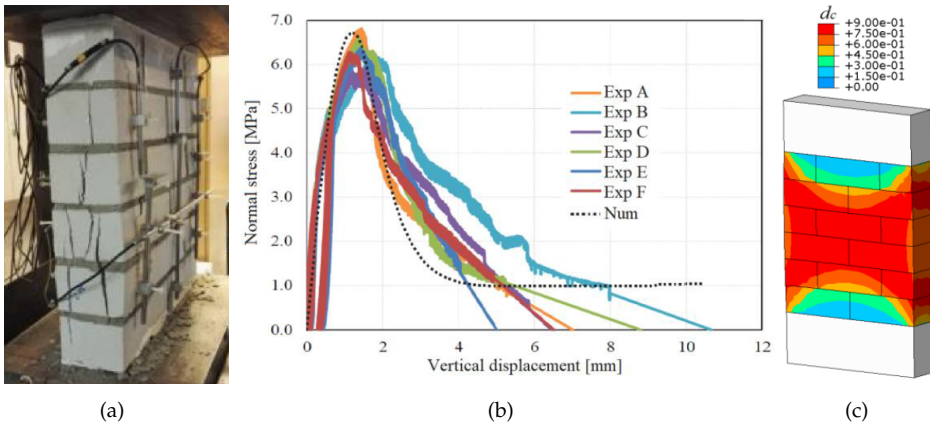
Figure 105: Compression tests on masonry wallets: (a) experimental failure, (b) experimental-numerical normal stress – vertical displacement curves, (c) and compressive damage contour plot.

theory can assume any value from 0 to 1, have been limited to 0.9 to increase the numerical convergence of the simulations (Table 21), as commonly carried out when using plastic-damage constitutive laws [325, 141]. For this reason, as well as the limitation of the softening regime to a residual value of stress (for the same purpose), the post-peak branch in Figure 105(b) is characterized by a (small) residual strength.

6.3.6 *Numerical results and discussion*

In this section, the results of the performed numerical simulations are critically compared with the experimental outcomes. In particular, two tests of in-plane cyclic loaded walls (with two height/width aspect ratios, i.e. 0.7 and 2.5), one two-way bending cyclic out-of-plane test of a wall, and one cyclic pushover test on a terraced masonry house have been simulated. For the sake of consistency, all the simulations have been conducted by using the mechanical properties collected in Table 21, and the discretization of the block shown in Figure 97.

A quasi-static direct-integration implicit dynamic analysis algorithm [308] has been adopted in the simulations. Geometric nonlinearity has been considered in the analyses to account for large-displacement effects.

6.3.6.1 *In-plane cyclic behavior of walls*

The cyclic in-plane tests COMP-2 (slender wall, height/width aspect 2.5) and COMP-6 (thick wall, height/width aspect 0.7) [348] have been considered and simulated. Both walls are characterized by a cantilever configuration. The walls have been modeled through the damaging block-based model herein presented,

Table 21: Mechanical parameters utilized in the numerical simulations.

Contact mechanical properties				
Tensile behavior			**Shear behavior**	
f_t [MPa]	0.12		$\tan\phi$ [\]	0.52
u_k [mm]	1.0		c [MPa]	0.11
ζ [\]	8		δ_k [mm]	1.0
K_{nn} [N/m^3]	$75\cdot10^9$		ξ [\]	4
			μ [\]	0.55
			K_{ss} [N/m^3]	$7.5\cdot10^9$

Block mechanical properties					
Young's modulus [MPa]	4800				
Poisson's ratio [\]	0.17				
Tensile uniaxial behavior			**Compressive uniaxial behavior**		
Stress [MPa]	Inel. strain	d_t [\]	Stress [MPa]	Inel. strain	d_c [\]
1.5	0	0	6.8	0	0
0.1	0.001	0.9	0.9	0.006	0.9

by considering a continuum quasi-rigid element on the top to prevent the warping of the wall, following the constraints of the experimental set-up.

The pseudo-time-history of the top displacement experimentally recorded has been applied to a top node of the model (in the center of the quasi-rigid element), and the pseudo-time-history of the resultant of the base shear has been measured.

Concerning the slender wall COMP-2 test, the comparison between experimental and numerical shear force against measured net displacement curves is shown in Figure 106, where the numerical monotonic response of the wall is collected as well. The experimental and numerical crack patterns are shown in Figure 107, where the numerical one is taken at the instant represented by the green circle in Figure 106. A good agreement between the results is observed, particularly for the prediction of the maximum shear load. In this regard, the cyclic and monotonic simulations presented practically the same maximum shear force. The experimental test showed a crack pattern characterized by the combination of rocking and sliding (Figure 107(a)) that gives a non-negligible energy dissipation (Figure 106). Although this aspect was not fully captured by the model, where almost-pure-rocking was recorded in the first cycles (Figure 106), dissipation occurred in the model for wider cycles due to masonry crushing (Figure 107(c)), see Figure 106.

Conversely, the thick wall COMP-6 (whose shear force against displacement curves are depicted in Figure 108, experimental and numerical crack patters in Figure 109, and compressive and tensile damage contour plots Figure 110) was
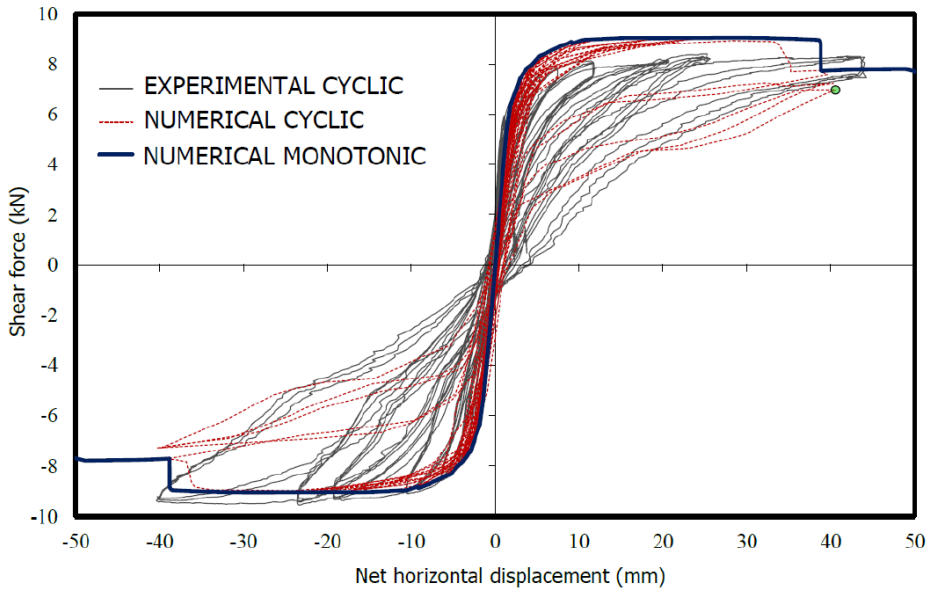
Figure 106: Shear force vs measured net displacement of the slender wall COMP-2: comparison between experimental and numerical (cyclic and monotonic) results.

mainly characterized by shear failure (Figure 109(a)). The hysteretic behavior of the wall has been excellently predicted by the model, in terms of maximum shear force (Figure 108), energy dissipation (Figure 108) and crack pattern (Figures 109(a)-109(b)). The deformed horizontal displacement contour plot of Figure 109(b) has been taken at the instant represented by the green circle in Figure 108. It is worth to note that, although taken at an almost-null top horizontal displacement (Figure 108), significant residual horizontal displacements are recorded at the two sides of the wall, which determine the formation of wide x-shaped shear cracks (Figure 109(b)).

Likewise, residual horizontal displacements have also been recorded during the experimental test. The numerical cyclic analysis diverged before the full-simulation of the experimental loading path (the non-simulated path has been reported in Figure 108 through a gray color), since two half-bricks at the base of the wall slid off as shown in Figure 109(b). It should be noted, anyhow, that the simulation of the considered test is extremely challenging given the co-existence of different failure mechanisms, and damage both along mortar joints (opening and sliding, Figure 109(b)) and in the bricks (crushing and splitting, Figure 110). Also in this case, the in-plane cyclic and monotonic simulations presented a very similar maximum shear force.

To evaluate the sensitivity of the model to the main mechanical properties, several monotonic analyses have been performed on the COMP-6 configuration and the results have been compared (Figure 111). In particular, the results of the
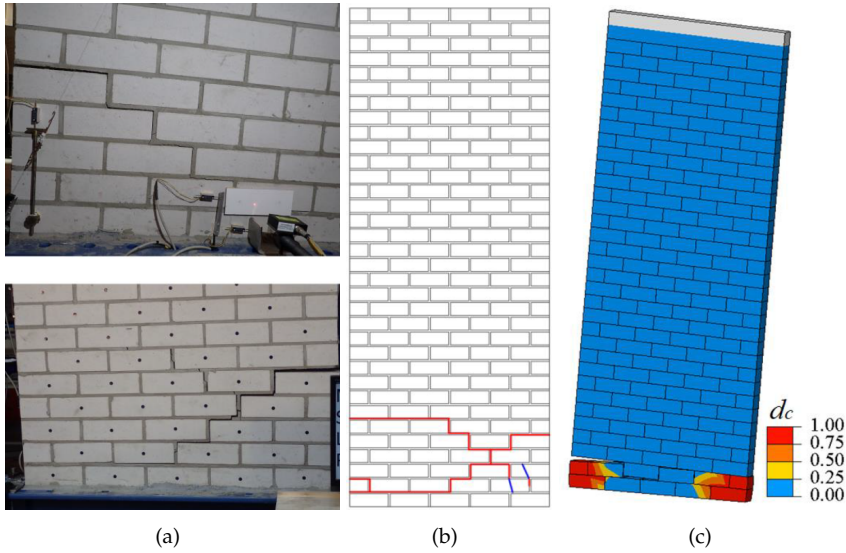
Figure 107: Slender wall (COMP-2) crack pattern: (a) photos of the cracked wall, (b) experimental crack pattern and (c) numerical compressive damage contour plot.

"Reference" analysis, conducted with the mechanical properties collected in Table 21, have been compared with the analyses "PAR_A" (characterised by doubled values of f_t and u_k), "PAR_B" (doubled values of c and δ_k), "PAR_C" (doubled values of $\tan\phi$ and μ), "PAR_D" (doubled values of f_c and G_f), and "PAR_E" (doubled values of all the aforementioned parameters), in terms of shear force against horizontal displacement curves and crack patterns (Figure 111).

The overall behavior of PAR_A and PAR_D appears akin to the Reference one, whereas PAR_B and PAR_C show a considerable greater maximum shear capacity. In particular, all the analyses showed a shear failure in the wall, exception made for PAR_B which initially showed a bending failure and, subsequently, a sudden shear failure just before a horizontal top displacement of 10 mm. This phenomenon is highlighted in the shear-displacement curve of Figure 111 by a significant drop of the PAR_B curve. Conversely, the response of PAR_E is completely different, characterized by a bending failure and with a considerably greater shear capacity. Therefore, a significant influence on the shear response of the wall of the contact shear cohesion c and δ_k, as well as contact frictional contributions $\tan\phi$ and μ is observed, as expected. A completely different parameters setting, e.g. PAR_E, gives also a completely different response of the wall, confirming the relevance of the use of correct material parameters.
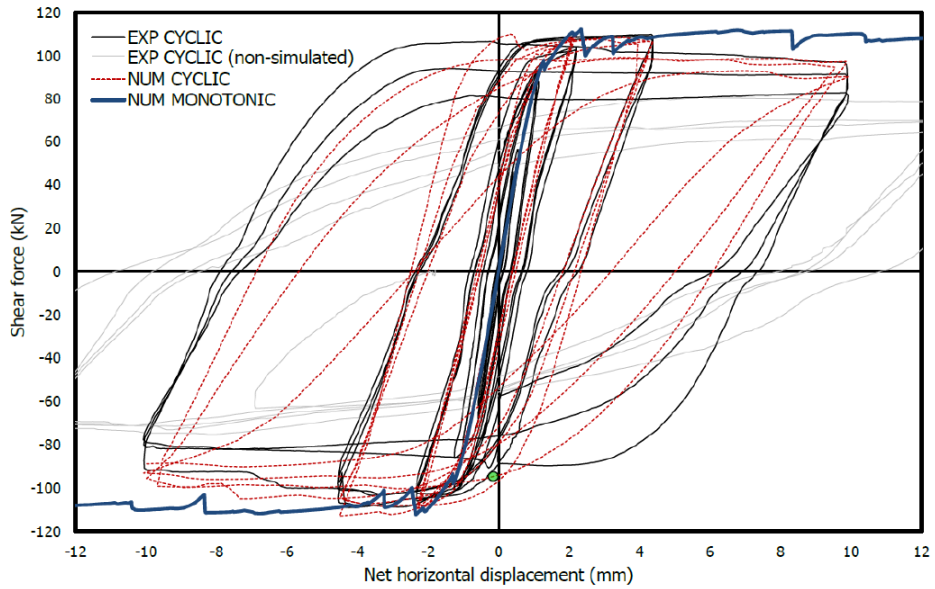
Figure 108: Shear force vs measured net displacement of the thick wall COMP-6: comparison between experimental and numerical (cyclic and monotonic) results.
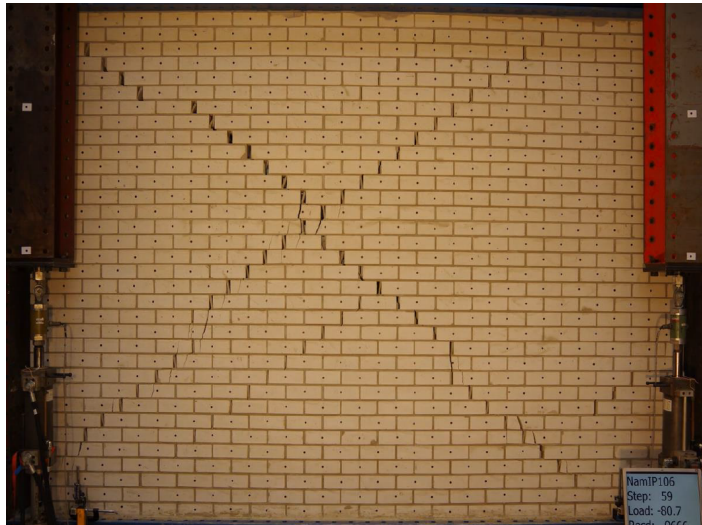
(a)
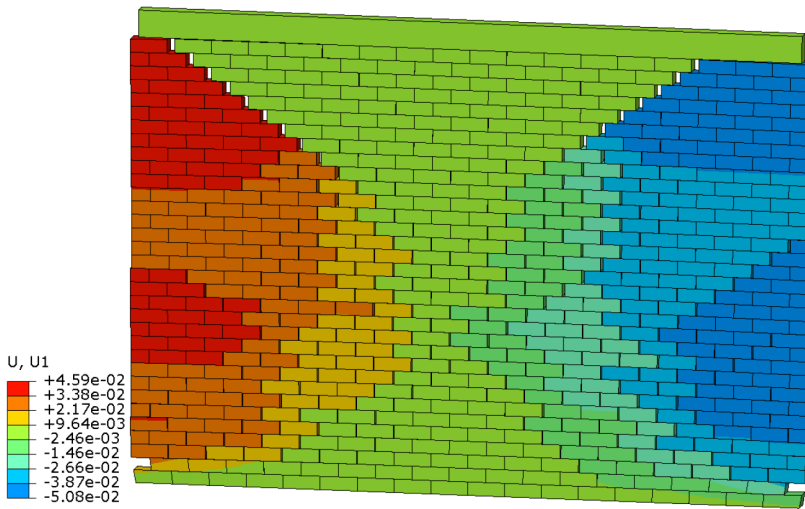
(b)

Figure 109: Thick wall (COMP-6) crack pattern comparison: (a) photo of the cracked wall and (b) deformed horizontal displacement contour plot in meters.
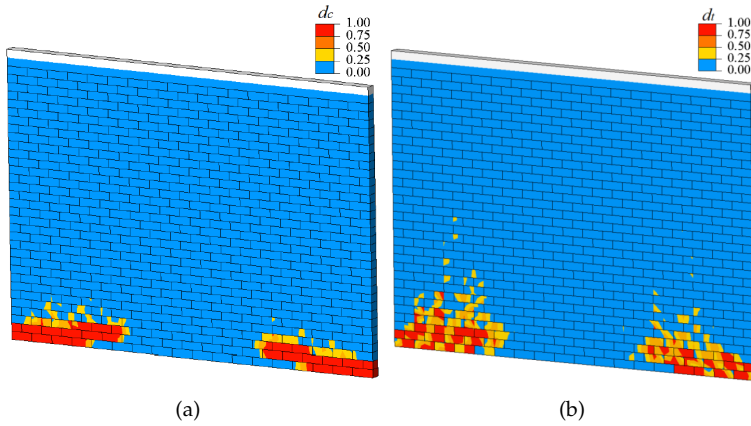
Figure 110: (a) Compressive and (b) tensile damage contour plots for the thick wall (COMP-6) at the end of the simulation.
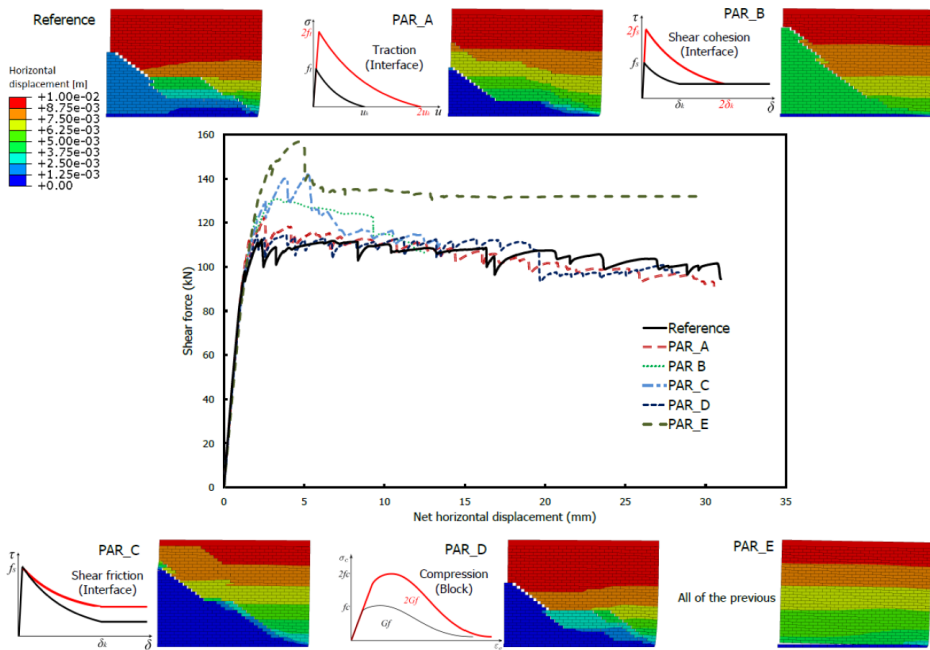
Figure 111: Sensibility analysis on the main mechanical parameters of the model. The horizontal displacement contour plots have been taken at a horizontal displacement of 10 mm.

6.3.6.2   *Out-of-plane cyclic behavior of walls*

The two-way spanning out-of-plane cyclic test COMP-11 conducted on a 3.874 × 2.765 × 0.102 m calcium silicate brick masonry wall has been considered and simulated. It has to be pointed out that the experimental set-up conceived for this test needed a considerable level of complexity in order to perform a cyclic out-of-plane test. Indeed, after the application of a vertical pressure (0.05 MPa) to the wall, a constant pressure was applied by the airbag on one side of the wall and a varying pressure by the airbag on the other side of the wall. The pressure in the airbag on the active side was adjusted to achieve the target deformation of a selected set-point; the pressure on the opposite side (passive side) remained constant during each test. Therefore, the set-up allowed for a displacement-controlled test.

To be able to reproduce numerically this complex loading protocol, a non-standard analysis procedure has been conceived and followed. Firstly, a uniform horizontal pressure is monotonically applied to one side of the wall and the equilibrium is investigated through the aforementioned quasi-static implicit dynamic algorithm. The solution is computed until a target displacement (the same considered in the experimental test). Then, a restart of the analysis is carried out: the previous analysis step is ended and a new step which consider a uniform horizontal pressure with an inverted sign is computed. In this way, the cyclic out-of-plane response of the wall is analysed.

The comparison between experimental and numerical lateral force against out-of-plane displacement curves for COMP-11 specimen is shown in Figure 112, where the numerical monotonic out-of-plane response is collected as well. The experimental and numerical crack patterns are shown in Figure 113, where the numerical one is taken at the instant represented by the green circle in Figure 112. A good agreement between the numerical and experimental outcomes is observed. The peak loads are well predicted by the numerical cyclic analysis for the first cycles. Then, the numerical model showed a greater degradation than the experimental test. The analysis has been stopped in correspondence of the green circle in Figure 112, as, notwithstanding the change in direction of the horizontal pressure, the wall was continuing to deform in the same direction, suggesting the collapse of the wall.

It has to be pointed out that, although the model carefully simulates the experimental set-up, the presence of the airbags in the two sides of the wall definitely increases the stability of the wall. In addition, unlike the in-plane benchmarks, a considerable difference between the cyclic and monotonic numerical responses is observed in terms of peak loads. Nevertheless, a sensible difference in peak loads is also observed in the experimental test between positive and negative responses [348], suggesting that the cyclic loading can influence the magnitude of the peak loads.

An excellent agreement is observed from the comparison of the crack patterns in Figure 113. The model appears able to well-represent the failure mode of the two-way spanning wall (Figure 113), characterized by diagonal cracking from the
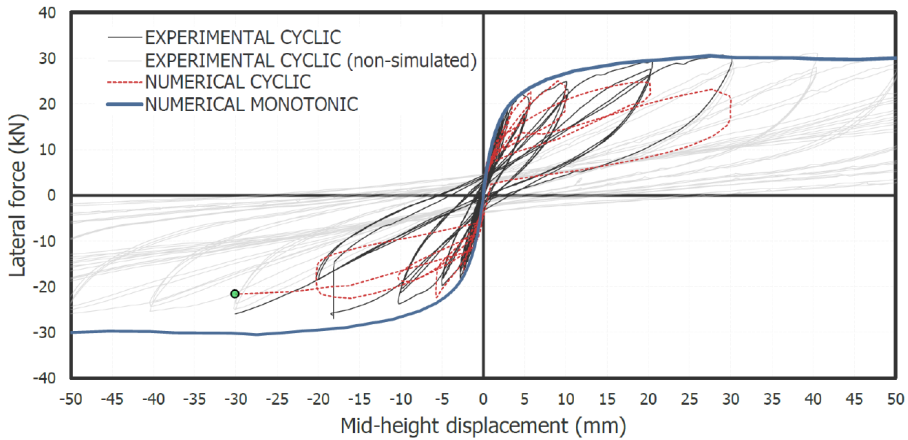
Figure 112: Experimental and numerical lateral force against out-of-plane displacement curves for COMP-11 specimen.

wall edges to the center of the panel, and horizontal cracks at the wall base, at an intermediate height, and at the top of the wall [348]. Indeed, most of the cracks are predicted with a very high accuracy.

6.3.6.3 *Cyclic behavior of a full-scale masonry structure*

The quasi-static cyclic pushover test conducted on the terraced masonry house shown in Figure 103 has been modeled and simulated. Numerical cyclic and monotonic analyses have been performed on a half-house model, given the symmetry of the structure and of the loading conditions. The numerical results in terms of base shear against horizontal displacement of the top floor have been collected and compared with the experimental ones in Figure 114. The "numerical cyclic actual" analysis (Figure 114) has been conducted by imposing the actual time-history of the horizontal displacement measured at the two floor levels. Differently, the "numerical cyclic reduced" analysis consisted of a reduced number of cycles. Particularly, a set of equal forces has been monotonically applied to the two floors of the structure until the top floor reached a target displacement and, then, the analysis has been stopped. Successively, a restart analysis has been performed by inverting the sign of the forces. This procedure has been repeated a certain number of times by increasing the magnitude of the top target displacement. Finally, also monotonic analyses have been performed in two directions. The crack pattern of the "numerical cyclic reduced" analysis are collected and compared with the experimental cracks in Figure 115, while the tensile and compressive damage contour plots at the end of the simulation are shown in Figure 116. The deformed shape and the tensile and compressive damage contour plots for the positive and negative "numerical monotonic" analyses are collected in Figure 117 and Figure 118, respectively.
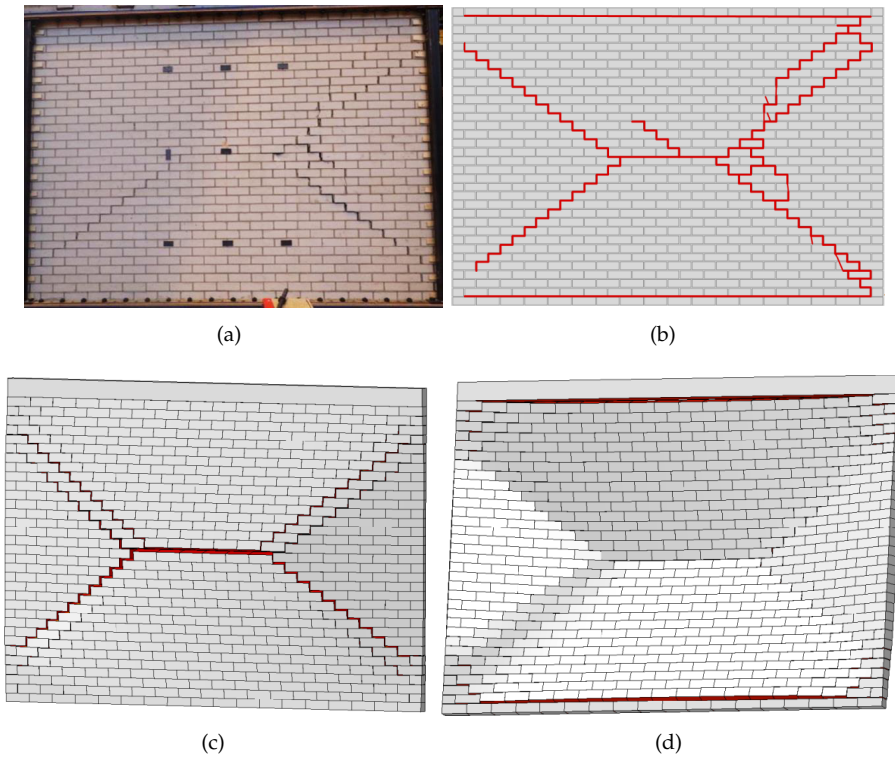
Figure 113: Out-of-plane benchmark crack pattern comparison. Specimen COMP-11 crack pattern after removing the airbags: (a) photo and (b) sketch. Numerical crack pattern: (c) front and (d) back views.

An overall positive correspondence between experimental and numerical curves can be observed in Figure 114. The "numerical cyclic actual" analysis is untimely stopped due to divergence in the solution of the continuum nonlinear equations in a single block. Differently, although ended for the same reason, the "numerical cyclic reduced" analysis was able to proceed further, until significant top displacements (e.g. ±60 mm). Anyhow, the prediction of the peak shear force for both cases is in good agreement with the experimental one (Figure 114). Interestingly, for the "numerical cyclic reduced" analysis a degradation of the shear force is observed in the positive direction for subsequent cycles, while no particular degradation is observed in the negative direction. This aspect appears particularly valuable as it is also an experimental trend (Figure 114), determined by the different width of the two piers of the house [347]. Furthermore, concerning the monotonic response of the model, in the positive direction the shear base is characterized by a peak load, followed by a significant softening until about +20 mm and, then, by a plateau, while in the negative direction, once reached the peak load, it remains practically constant. The differences in the peak load between
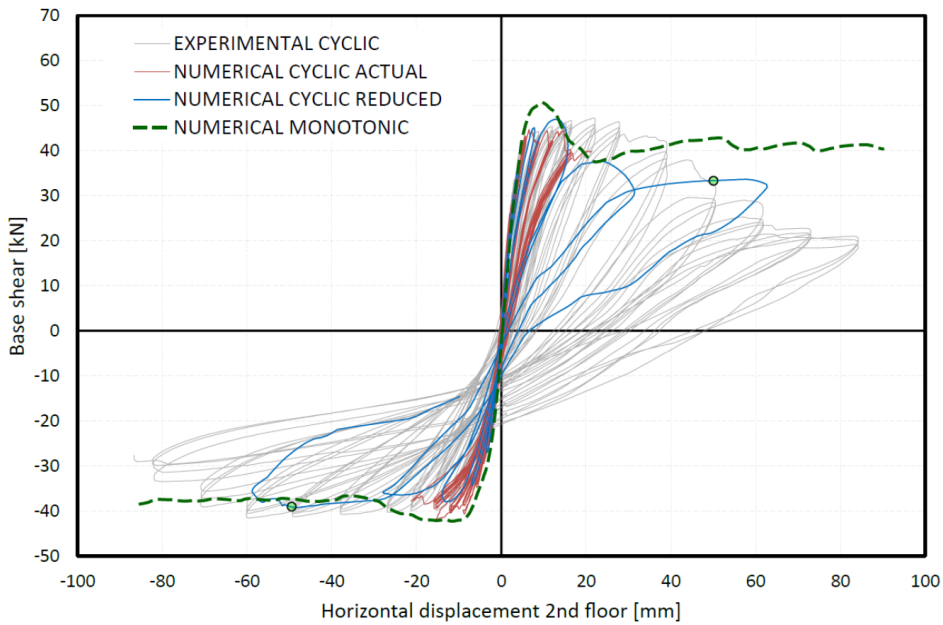
Figure 114: Terraced house base shear – horizontal displacement experimental-numerical comparison.

the numerical cyclic and monotonic responses are irrelevant for the negative direction, while they are significant in the positive direction, suggesting that the failure mechanism which occurs in the positive direction is influenced and degraded by a cyclic action, whereas the one which occurs in the negative direction appears independent from that.

The actual crack pattern experienced by the structure appears very complex and characterized by a combination of in-plane and out-of-plane failure mechanisms [347]. The comparison of the "numerical cyclic reduced" deformed shapes with the actual crack pattern shows the very good accuracy of the model which accounts for the main failures of the structure (Figure 115). Particularly, the shear-vertical crack experienced by the structure in the wider (left) pier (see Figure 115, top) is well-predicted by the model which shows a series of contact shear failures as well as a vertical distribution of tensile damage in the blocks (Figure 115, top), standing for a vertical crack which crosses the blocks as well (which is an experimental outcome too). Besides, the interaction of the piers with the transversal walls, due to the running bond texture, is fairly captured by the model. The different failure mechanism that develops in the piers for the two loading directions can be clearly observed also by comparing the deformed shapes of the model in the positive (+50 mm) and negative (−50 mm) directions (Figure 115 and Figure 116 for the cyclic analyses, and Figure 117 and Figure 118 for the monotonic analyses): while the wider (left) pier shows a shear-vertical failure in the lower level when loaded in a positive direction, it shows a completely different mechanism,

i.e. almost-pure rocking, when loaded in a negative direction. This also explains the different post-peak direction observed for the two loading directions. Again, the role of the transversal walls and their connection to the piers appears crucial in the structural response.

Finally, the cyclic evolution of the resultant of the vertical reaction for the walls of the structure depending on the horizontal displacement of the second floor is shown in Figure 119 for the "numerical cyclic reduced" analysis. This outcome allows to further investigate the cyclic response of the structure. Indeed, the cyclic redistribution of the vertical load between the transversal wall W1 (W2) and the pier P1 (P2), see Figure 119, appears particularly interesting, as, for instance, the first floor is connected in no way with the piers and it only stands on the transversal walls. Therefore, the load transfer passes through the corner, thanks to the toothing of the walls. In the negative direction, the vertical load is mainly borne by W1 and P2 (Figure 119). In particular, by increasing the top displacement in the negative direction, the vertical load is gradually transferred from W2 to P2 and at about –20 mm the vertical load is completely transferred and the wall W2 is completely unloaded. Conversely, in the positive direction the vertical load is mainly borne by W2 and P1 (Figure 119). If the load transfer between P2 and W2 follows a regular evolution, suggesting the activation of a pure rocking mechanism, the load transfer between P1 and W1 appears more complex in the positive direction, where the unloading path is different from the loading one (Figure 119). Once more, this aspect suggests a more complex failure mechanism in the positive direction.
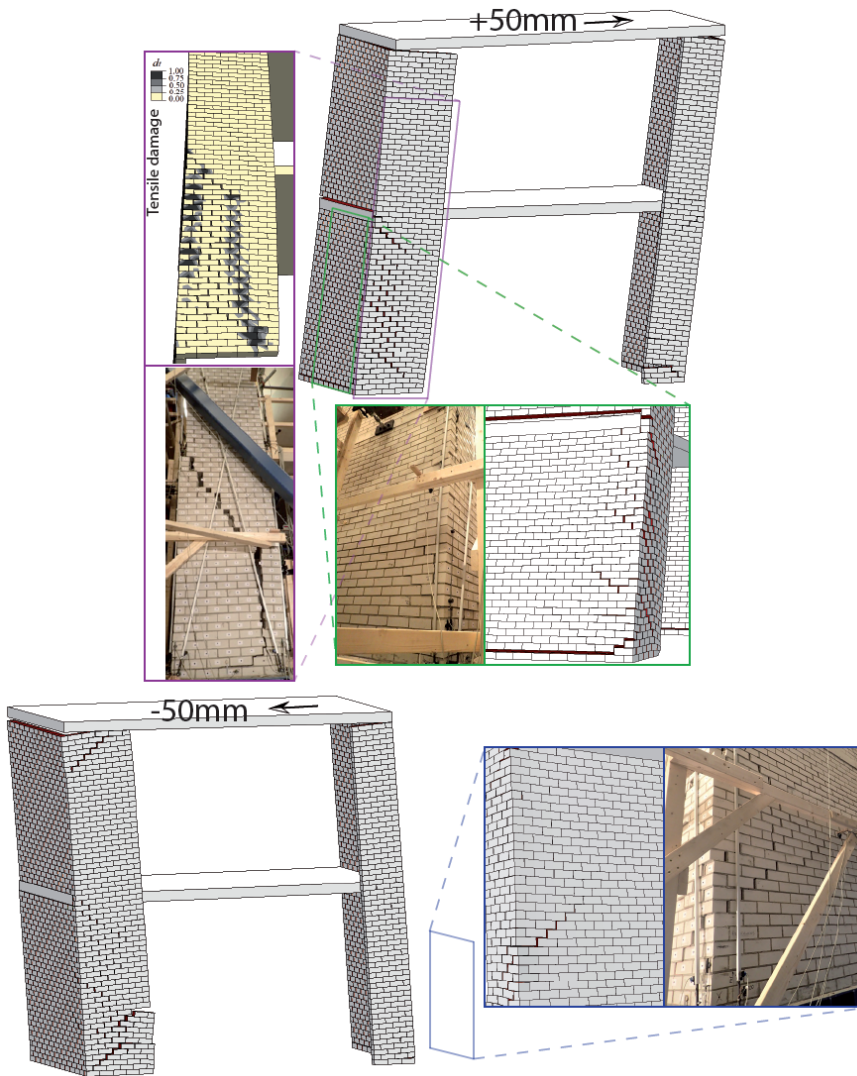
Figure 115: Numerical cyclic reduced analysis: deformed shapes and comparisons with the actual crack pattern. The numerical plots are taken in correspondence of the two green circles in Figure 114, for a top displacement ±50 mm, whereas the photos are taken during the last cycle of the experimental test.
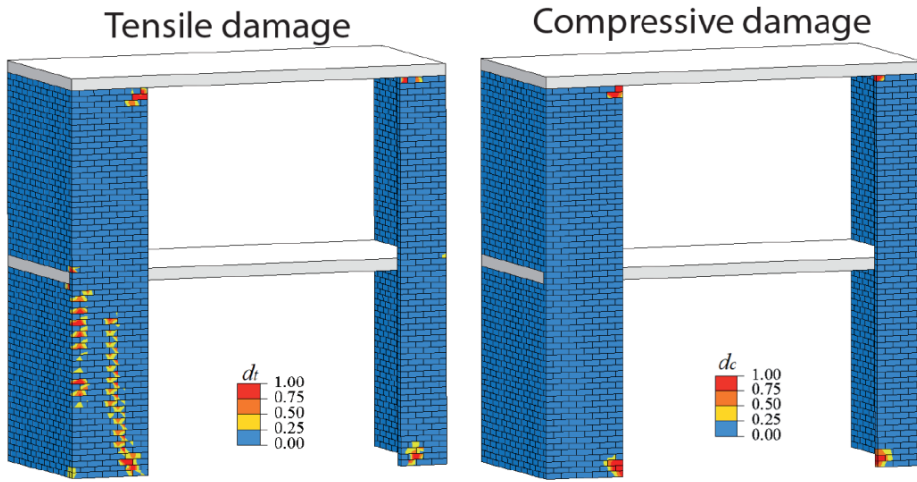
Figure 116: Numerical cyclic reduced analysis: tensile and compressive damage contour plots at the end of the simulation.
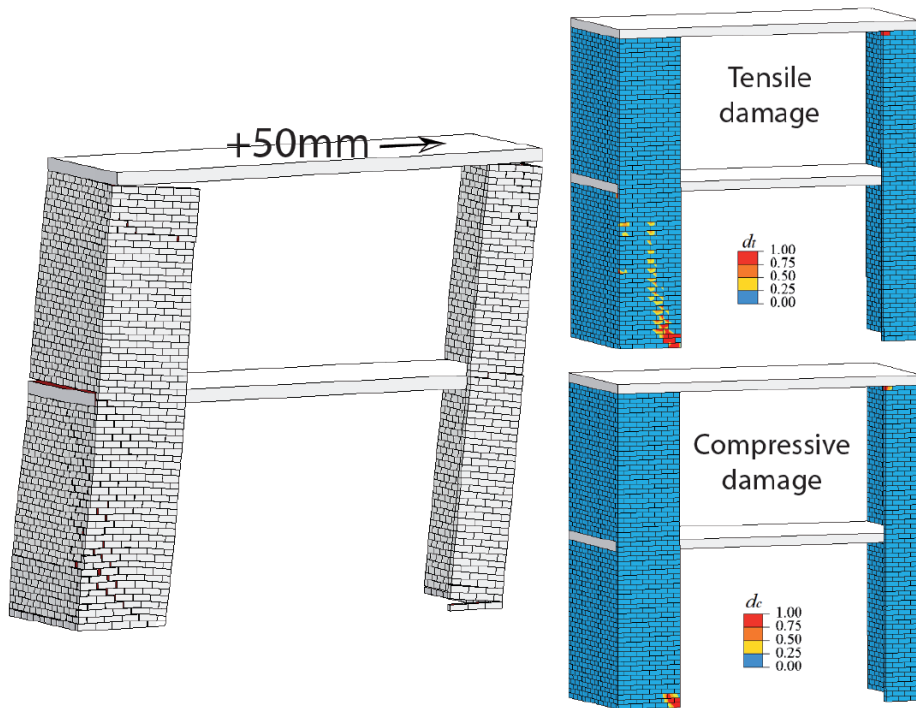
Figure 117: Numerical monotonic simulation in the positive direction: deformed shape at +50mm (left) and tensile and compressive damage variables contour plots.
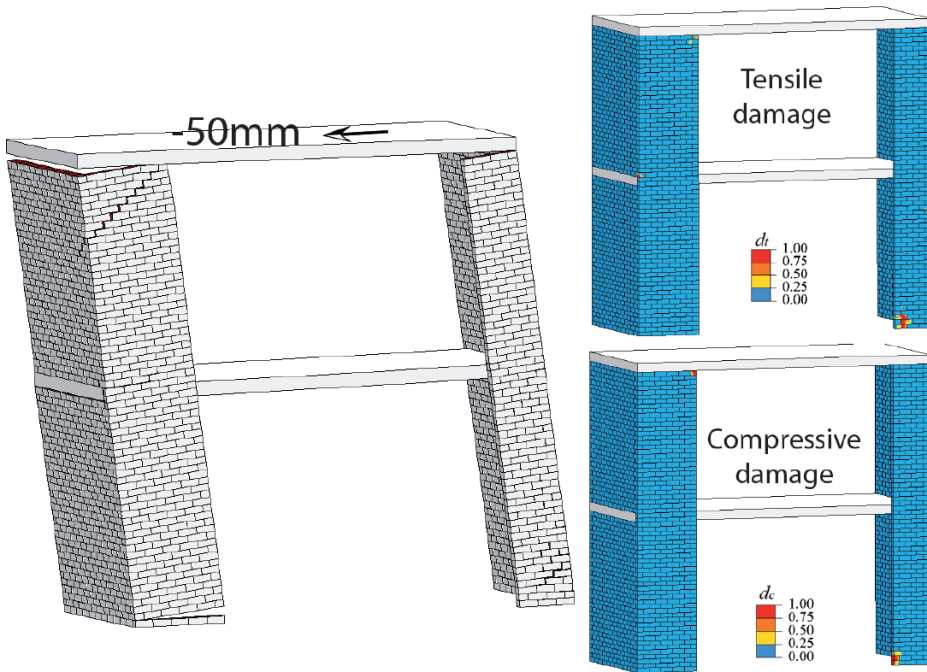
Figure 118: Numerical monotonic simulation in the negative direction: deformed shape at -50mm (left) and tensile and compressive damage variables contour plots.
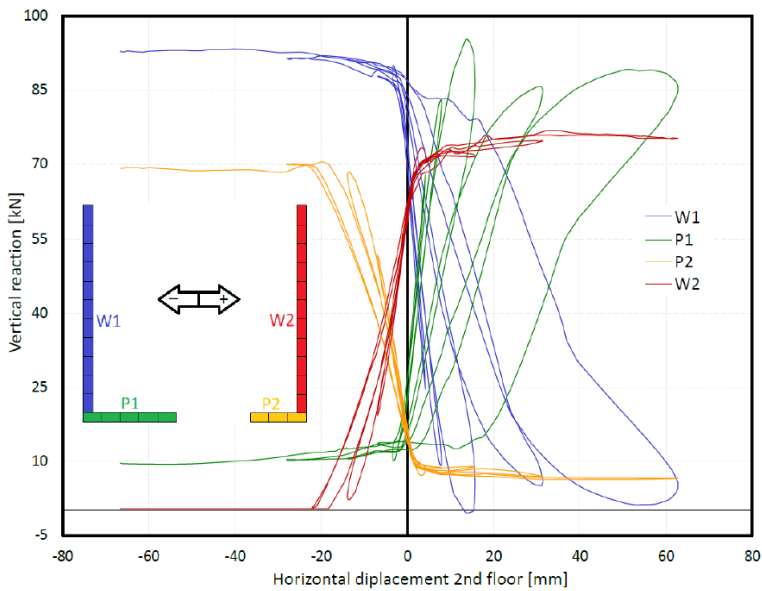
Figure 119: Numerical cyclic reduced analysis: resultant of the vertical reaction for the walls depending on the horizontal displacement of the second floor.

6.4   HISTORIC BARREL VAULTS UNDERGOING DIFFERENTIAL SETTLEMENTS

Masonry vaults have been an efficient and fire-proof roofing method in pre-modern structures, reaching a wide variety of configurations that may not always be easy to understand in terms of performance and safety. The study of simple barrel vaults can provide a base for the understanding of load paths under various support conditions, letting insight to be built for more complex forms (cross vaults, net vaults etc). Gothic barrel vaults in particular are formed by the extrusion of an arch (generatrix) along a linear distance (directrix). As with any arch based construction, the vault produces an outward thrust along its edge and there are several mechanisms for absorbing this thrust. One is to make the wall exceedingly thick or add buttresses. Alternatively, a more elegant method is to build two or more vaults parallel to each other, canceling mutually the forces of their outward thrust. However, the amount of thrust also depends on the shape of the arch. For example, in [355], Romano and Ochsendorf showed that pointed vaults generate significantly smaller lateral thrust to their support than semi-circular ones and thus this shape can be used to build higher and more slender walls. Furthermore, pointed arches can span larger distance with the same structural thickness. By decreasing the lateral thrust at the wall, larger windows can be built to allow for more light in the building.

Although a lot of thought and wisdom has been put into the design of arches and vaults, unfortunately, today, most of the existing historic masonry vaults stand in a damaged (cracked) condition. The main reasons of such damage arise from aging of material, soil subsidence, support failure due to poor foundations. Earthquakes can also induce significant damage to masonry vaults [356], as the oscillations can produce relative displacements between the vaults' abutments [238]. In general, although masonry vaults have great strength to vertical uniform loads, their capability to withstand differential settlements of the abutments is extremely low. Differential settlements can derive from masonry material or soil degradation (e.g. due to stress concentrations, non-uniform soil stratigraphy, etc.). However, the challenge faced during structural inspection is that although the effects of an on-going process of deformation are clear (visible cracks) on the vault, the nature and origin of the on-going settlement may remain unknown to the surveyor.

Today, several numerical tools are available for the structural analysis of vaults (Chapter 2).

Geometry-based approaches (Section 2.7) can follow the lower-bound (static approach [228, 232, 236]) or the upper-bound (kinematic approach [357, 243]) theorems of limit analysis. These approaches are considerably effective to evaluate the stability of vaults and domes. However, their capability to analyze vaults undergoing differential settlements is still under investigation.

Continuum approaches (Section 2.6) consider masonry as a homogeneous material in which the constitutive law is described in a phenomenological way [238, 358, 145]. These approaches can support any kind of boundary conditions

at the vault's abutments. However, the reliability of continuum constitutive laws for historic masonry vaults is still under study.

Finally, block-based approaches (Section 2.6) consider the structure as an assembly of separate blocks which can interact through specific laws. This approach represents the most accurate analysis tool [359, 90, 89, 360], even if the description of a historic vault block-by-block is still challenging and computationally demanding.

In this section, the effects of differential settlements on historic masonry barrel vaults are investigated. An efficient 3D non-standard contact-based distinct blocks model, based on the advances presented in the previous sections (6.2-6.3), is implemented to reproduce experiments on a scaled pointed barrel vault specimen (representative of late medieval barrel vaults from Scotland), under non-uniform differential settlement [361]. The choice of Scottish vaults is because they follow a specific typology during 15th century and they are plain yet very well built. Firstly, the numerical model is used to simulate the experimental campaign. The numerical results validate the experiments in terms of crack pattern and transverse-longitudinal deformation profiles. This makes possible further analyses to gain an insight on the effects of several plausible uniform and non-uniform settlement patterns on a representative historic barrel vault. Various settlement patterns were simulated and the complex failure mode of the vault investigated. This study could help analysts in understanding the nature of on-going deformation processes in historic masonry vaults and consequently in assisting engineers in the design of strengthening strategies.

It is well-known that size effects arise when cohesion and friction between blocks is conceived. Furthermore, the structural response could be also affected by the variation of the density of the material, when friction between blocks is supposed. However, full-scale experimental tests on masonry vaults are often prohibitive due to high costs of materials and equipment [362]. Therefore, scale models are usually adopted for the qualitative understanding of the structural response of masonry vaults. Indeed, the experimental set-up considered in this study aimed to qualitatively understand the mechanics of Gothic barrel vaults undergoing non-uniform settlements, without quantitative conclusions. Particularly, the experimental test considered in this study has been found to be appealing to evaluate the potentialities of the block-based modeling approach which accounts for both cohesion and friction between blocks. Indeed, if the numerical results are found to be consistent with the experimental outcomes of the test on a scale model, it is reasonable to assume that the numerical approach can be used for quantitative predictions on full-scale actual masonry vaults as well.

6.4.1 Scottish Gothic vaults

Barrel vaults in collegiate (private) churches in late-medieval Scotland (15 century) are a quite well-defined group in terms of their character, design and structural scheme (Figure 120), so they are a comprehensive typology and case study.

They may have origins in secular architecture, especially castles and tower-houses [363], where usually their spatial articulation and decoration (ribs) would denote higher status, but strength and fire-proofing were equally attractive. When applied to single volume churches though, the scheme does not borrow the solid envelope that contained the thrust very effectively there but relies on buttresses to let windows, which usually open below springing level, so the geometry of the barrel is not disturbed. Their geometric study [364, 365] shows pointed profiles largely generated within an equilateral triangle. Parallel ribs divide them into bays and often mask construction breaks (as was found during the repair works in Bothwell in 2014-16, Figure 120(a)). Consequently, there is no roof truss above them and flagstones cover the vault, laid directly on a rubble fill on the extrados or possibly diaphragm walls (called *frenelli* in Italy), adding a substantial load on the vault.

(a)   (b)

(c)   (d)
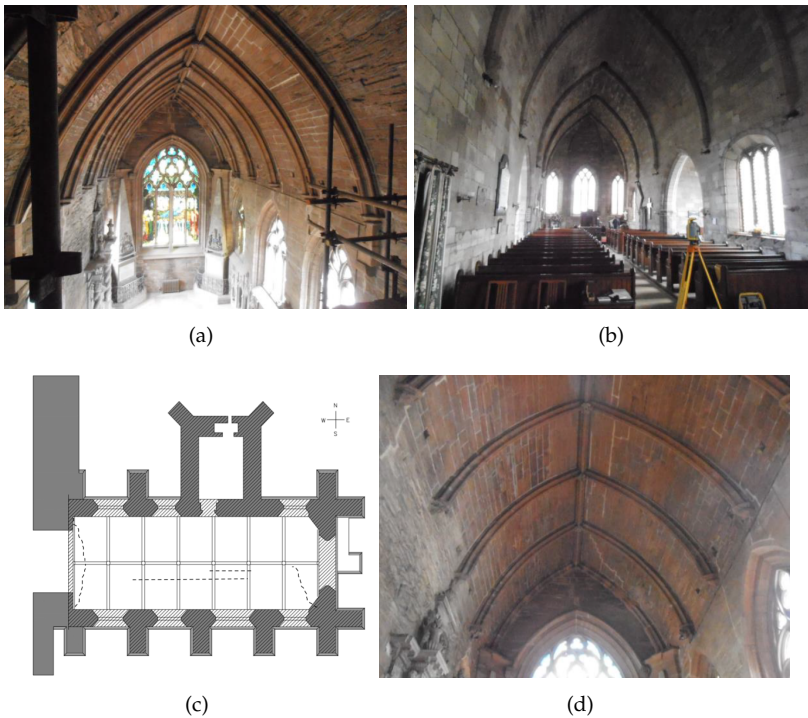
Figure 120: (a) The earliest (Bothwell 1398) and (b) latest (Ladykirk 1500) examples of barrel vaults in late-medieval Scotland churches. (c) Crack pattern in Bothwell due to deformation in the South wall from [366] and its appearance at the East end of the interior (following repairs in 2016), (settlement caused at the right-hand corner).

Considering the construction evolution since the earliest (1398) to the latest (1500) examples, it can be observed that pier buttresses contain the thrust and become thicker and safer towards the end of the period (e.g. Ladykirk, Figure

120(b)). Construction also improves in its visual expression, using polished ashlar (Crichton in 1449, Seton in 1478). Measured surveys [364] have shown precision in the execution of the form and very little deformation. This was not the case of the Bothwell church though (Figure 120(a)), which has suffered differential settlement on its South side (Figure 120(c)), as the foundations had slipped outwards and the clay under the south-east corner had settled significantly, and had to undergo repair and bracing (2014-16). The horizontal spread component of this vault was examined first [365] in an experimental and analytical program of a homogeneous model and then the vertical settlement only in a masonry-replica model [366], showing the vulnerability of the scheme to such instability. The two damage patterns were quite similar as well, which makes repair to a certain extent easier to plan.

6.4.2 *Experimental tests*

An attempt was made to construct a representative in geometry model of the barrel vault in the quire (choir) of Bothwell. A measured survey of the vault was carried out by the church once realized its geometry was slightly skewed and cracks started opening due to settlement over the years across the less braced South edge. A 1/12 scale was chosen for the construction of the model in the laboratory as it was convenient for the shaping of the blocks and the experimental set-up. To focus on the study of the original form of the Bothwell barrel vault, its shape was kept simple and symmetric. This resulted in a model of an interior span equal to 508 mm and a rise of 317 mm, keeping the length of the vault as 1,400 mm. The vault was composed of a series of equal in size varnished wooden units, bonded by a lime-based mortar. The length of the wooden blocks scaled a representative block of the original vault and the height to width ratio was 2/3. Mortar was composed of 3:1 (sand-lime). Then, glue and water were added. This mixture was used in previous experiments involving cross vaults [362] and it has been found to be convenient for construction reasons [366].

The model vault was subjected to a vertical displacement of one of the corners producing a linear displacement along its edge (Figure 121(a)). The right side of the vault was fixed while the left back corner was pinned so that the rest of the left side of the vault could rotate freely, following displacement imposed at the left front corner. Such experimental procedure has been designed to represent asymmetric differential settlement which often occurs in such structures. The vault was subjected to asymmetric settlement until collapse, which occurred at displacement of the left-hand corner of 132 mm or 42% of the rise of the vault.

During testing, a crack appeared after a settlement of 30 mm spreading longitudinally from the left front edge of the vault (Figure 121(b)) and in the next stages the crack propagated quickly until the mid-span of the vault. At a settlement of 45 mm, the section of the vault along the crack began to separate and deflect visibly, while a diagonal shear crack began to form at the intrados, starting from the back-right edge and spreading at roughly 45 degrees angle towards the apex. This was
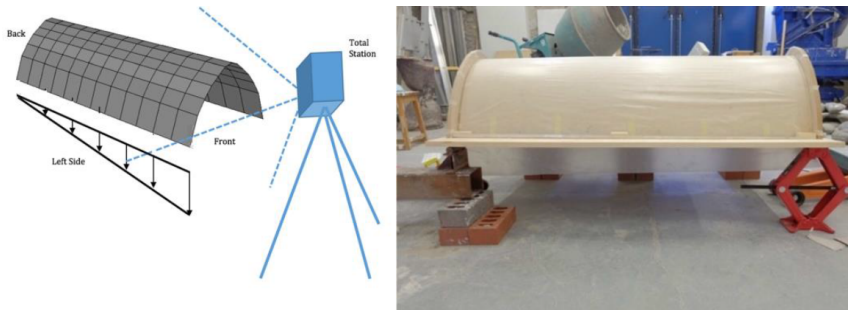
(a)

(b)   (c)   (d)

Figure 121: (a) Experimental set-up and cracks observed in the experiment: (b) initial cracks and crack pattern at the end of the test - (c) corner view and (d) top view [366].

accompanied by a crack along the apex spreading longitudinally from the back edge of the vault. At a settlement of 75 mm, the two cracks met, forming a hinge at the apex with the resulting triangular portion of the vault detaching from the lower vault structure. The test was continued until full collapse of the structure. Several small longitudinal cracks developed from the front of the vault near the apex. As the vault approached full collapse, a crack formed on the front extrados of the vault of the right side near the springing and propagated down the entire length, forming a hinge. In addition, another diagonal crack formed beginning at the front of the vault at 45 degrees angle. This joined with a longitudinal crack on the extrados and progressed to meet the first diagonal crack at the apex. Figures 121(c)-121(d) show the diagonal crack just before the vault collapsed.

6.4.3 *Numerical strategy and verification*

The experimental test above-described is modeled through the numerical approach presented in Section 6.3. The assembly of the blocks used to model the Gothic barrel vault is shown in Figure 122(a) and the adopted mesh (which has been found by a good compromise between accuracy and computational effort, see Section 6.2) is shown in Figure 122(b).

(a)

(b)
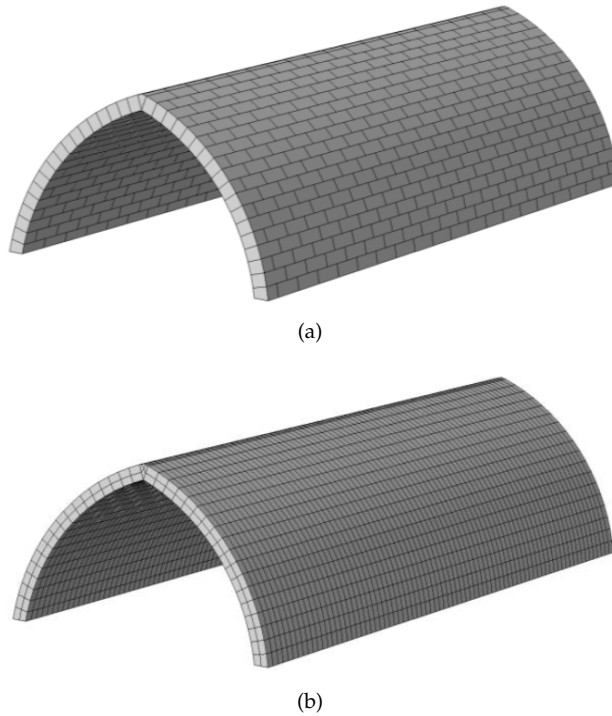
Figure 122: Contact-based distinct block model of the vault: (a) assembly of the blocks, and (b) and adopted mesh.

The block-based model herein adopted concerns expanded blocks (which account for the mortar layer thickness as well) assembled by zero-thickness contact-based interfaces. Therefore, mortar layers are not explicitly modeled in this numerical approach, similarly to other well-known modeling strategies [53]. However, the vault's key was realized in the physical model through a thick wedge-shaped mortar layer, see Figure 121(b). This geometric feature could not be finely represented by the numerical model, given the assumption at the basis of the modeling approach (i.e. any mortar layer explicitly modeled). Therefore, an approximation on the geometry of the vault's key was needed, and fictitious wedge-shaped blocks in the key stone were conceived.

In general, the model can be characterized by a nonlinear plastic-damage behavior of the block, as pursued in Sections 6.2-6.3 to reproduce the response of

brick. However, since in this case the experimental set-up was made by timber blocks, for simplicity the blocks have been described by means of an isotropic linear elastic material law, adopting the values 520 kg/m^3, 9 GPa and 0.25 for density, Young's modulus and Poisson's coefficient, respectively. Since the experimental campaign [366] did not investigate the mechanical response of mortar joints, the mechanical characterization of the contact behavior has been primarily carried out using the parameters calibrated in Sections 6.2-6.3 from small-scale tests. In particular, three different settings (S1, S2 and S3) of the main mechanical parameters, i.e. f_t in tension and c in shear, have been considered by keeping constant the ratio $f_t/c = 1.5$, which appears quite a common value as per [324]. In particular, the values of f_t and c in S2, which seem rather realistic, have been reduced four times (S1) and increased five times (S3) to realize their influence in the global structural response. The mechanical parameters used in the numerical simulations are collected in Table 22.

Table 22: Mechanical parameters used in the numerical simulations. When more than one value is given in a cell, the first value refers to the simulation S1, the second to S2 and the third to S3.

Tensile behavior		Shear behavior	
f_t [MPa]	0.0075, 0.03, 0.15	c [MPa]	0.005, 0.02, 0.1
u_k [mm]	1.0	tanϕ [\]	0.5
ζ [\]	8	δ_k [mm]	1.0
K_{nn} [N/m^3]	75·10^9	ξ [\]	4
		μ [\]	0.5
		K_{ss} [N/m^3]	7.5·10^9

Given that no mechanical characterization was available for the mortar used in the experiments, the linear elastic material properties adopted for the blocks have been also used for the wedge-shaped blocks in the key stone, for simplicity. However, other preliminary analyses were performed, by using typical values of mortar Young's modulus from the literature, showing a negligible influence of this aspect on the mechanical response of the vault.

The model in Figure 122(b), after the application of the gravity load, had a non-uniform vertical settlement imposed on its left side, following the scheme depicted in Figure 121(a). The settlement has been incrementally applied to the base nodes of one side of the vault, while clamped boundary conditions have been considered for the nodes of the other side of the vault. Basically, the constraints adopted in the model attempted to follow those of the experimental test, which had no diaphragms on either end (arches) and no dead load was applied in the test during the settlement (apart from the vault's own weight).

The node displacements at the extrados of the front (see Figure 121(a) for reference) end of the vault, as well as the apex displacements of the whole vault, have been recorded and compared with the experimental data (Figure 123).

Figure 123 compares the experimental and numerical deformation of the front end and the apex vertical displacement at three subsequent vertical settlements (i.e. 45mm, 75mm and 132mm) showing good agreement. In particular, the three different parameter settings (S1, S2 and S3) show very slight differences, suggesting that the absolute values of tensile strength and cohesion of the interfaces do not considerably influence the failure mode and the crack pattern of the vault subjected to differential settlements, giving robustness to the adopted modeling approach.

The numerical crack pattern at the end of simulation S2 (vertical settlement equal to 132 mm) is shown in Figure 124, and is in good agreement with the actual one (Figure 121). Only few small deviations can be noted, as the one on the left of the apex, where the experimental test shows a fast-developing detachment [366] while in the numerical model this failure is smoother and results suggest the generation of a hinge (Figure 123). Also, in all of the simulation, upwards vertical displacements of the apex are recorded in the sections close to the back end of the vault (Figure 123), while the experimental profile shows upwards displacement only for large settlements (e.g. 132 mm). To this regard, it has to be pointed out that the experimental recording of displacements by means of the total station (Figure 121(a)) was challenging or impossible for the points close to the back end of the vault due to the set-up. Therefore, all things considered, the FE model can be considered validated by the good match.

6.4.4 *Further numerical insights*

Further analyses were carried out to gain insight on the effects of several plausible uniform and non-uniform settlement patterns on a representative historic barrel vault model. In particular, vertical, horizontal, diagonal, inward and outward settlements are considered. The representative mechanical setting S2 has been adopted in all the analyses. The failure modes are summarized in Figure 125 (uniform settlements) and Figure 126 (non-uniform settlements) according to the imposed settlement pattern (left column in Figure 125 and Figure 126).

In general, the failure modes of uniform settlements (Figure 125) could be also suitably predicted by an arch model, as, in this case, the bonding of the structure along the longitudinal axis plays a marginal role. Conversely, the masonry bonding plays a fundamental role in non-uniform settlements, leading to complex crack patterns (Figure 126).

As expected, uniform horizontal settlements (outward and inward, Figure 125) lead to symmetric crack patterns. In particular, diffuse longitudinal cracks are recorded in the extrados close to the abutments and in the intrados close to the apex for an outward settlement. Quite the opposite is recorded for an inward settlement. More localized cracks are observed in the other cases (Figure 125 and Figure 126).

As can be noted in Figure 126, the failure modes of non-uniform vertical, outward horizontal and outward diagonal settlements are quite similar. On the one

hand, this pools the effects of these settlements and simplifies the detection, as the exactness on the origin of the settlement is less required. On the other hand, however, an accurate knowledge on the active settlement appears more complicated as these three settlements have similar effects.

Different failure modes are, instead, observed for non-uniform inward horizontal and inward diagonal settlements Figure 126. Indeed, although they are both characterized by an inward horizonal component of the settlement, the non-uniform inward diagonal settlement shows a crack in the extrados of the fixed side, while the non-uniform horizontal settlement shows a crack in the extrados of the active side.

Obviously, the described scenario could be further enriched by analysing other cases with different settlements and/or by considering also more complex boundary conditions to account for the effect of adjacent structural elements. By way of example, the presence of a diaphragm wall along the back end of the vault could be simulated by adopting, for simplicity, clamped boundary conditions in the nodes on the back side (Figure 125). The crack pattern of the analysis with fixed back non-uniform vertical settlement is depicted in Figure 125. As can be noted, although quite similar to the crack pattern of the non-uniform vertical settlement simulation (Figure 126), several cracks arise close to the clamped side. In particular, this outcome was not visible in the non-uniform vertical settlement (Figure 126), suggesting that the effect of a diaphragm wall on the damage pattern of a vault could result in cracks in the proximity of the diaphragm wall (Figure 125). A similar damage pattern was observed in Bothwell (Figure 120(a)) in the West side close to the West diaphragm wall, indicating a complex and sensible interaction of the vault with adjacent vertical structures.

(a)

(b)

(c)
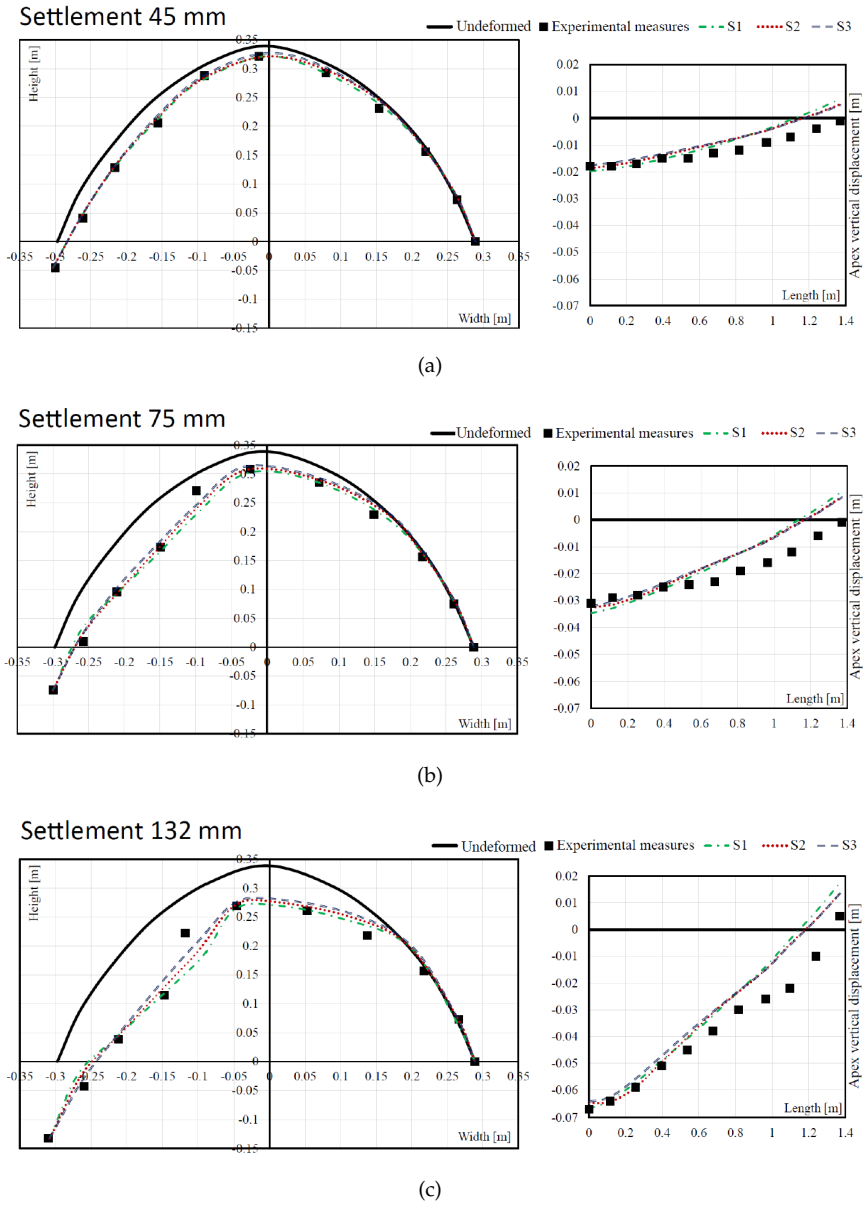
Figure 123: Comparison between experimental and numerical deformation of the front end (left) and apex vertical displacement (right) at three subsequent vertical settlements: (a) 45mm, (b) 75mm and (c) 132mm.

(a)

(b)

(c)
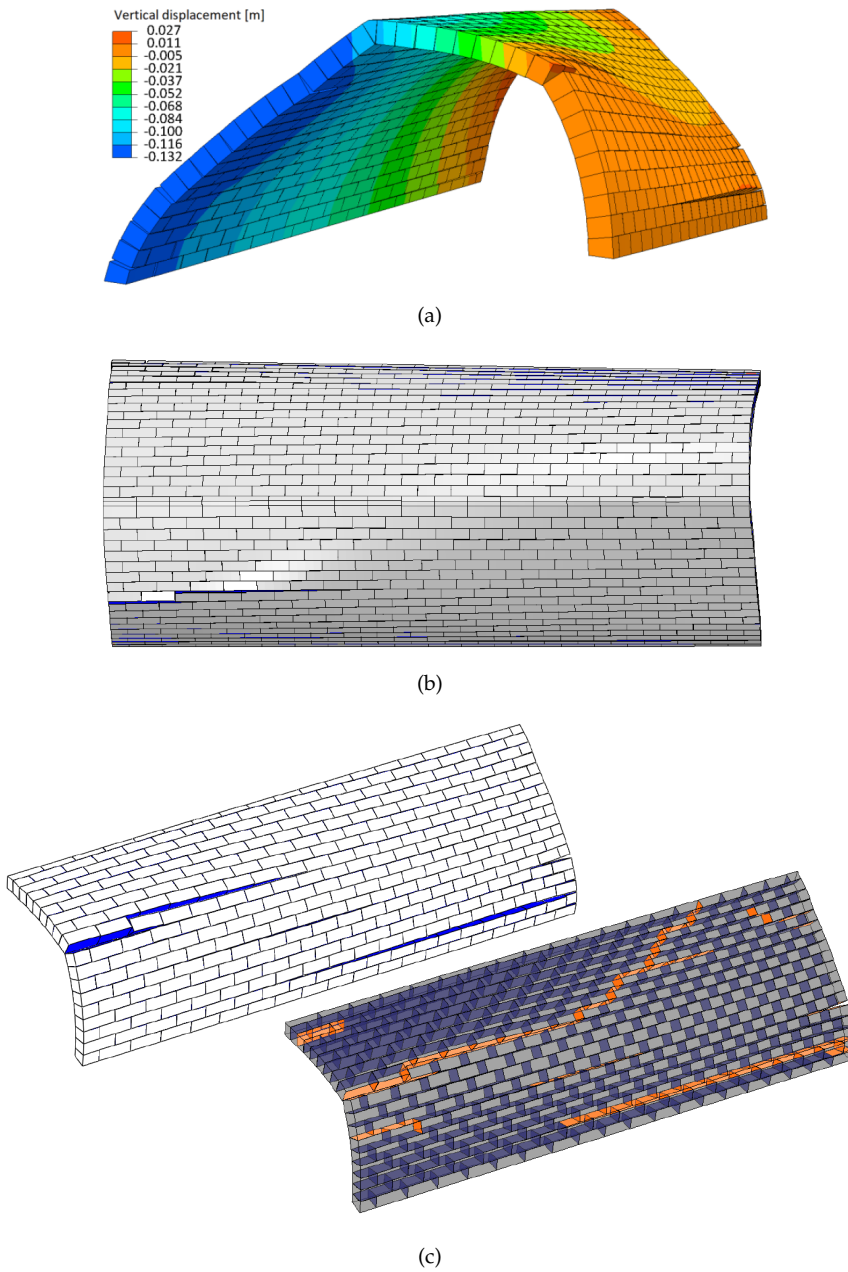
Figure 124: Numerical crack pattern at the end of simulation S2: (a) vertical displacement contour plot, (b) main failures in a top view and (c) interfaces which exhibited failure of the vault side opposite to the settlement.
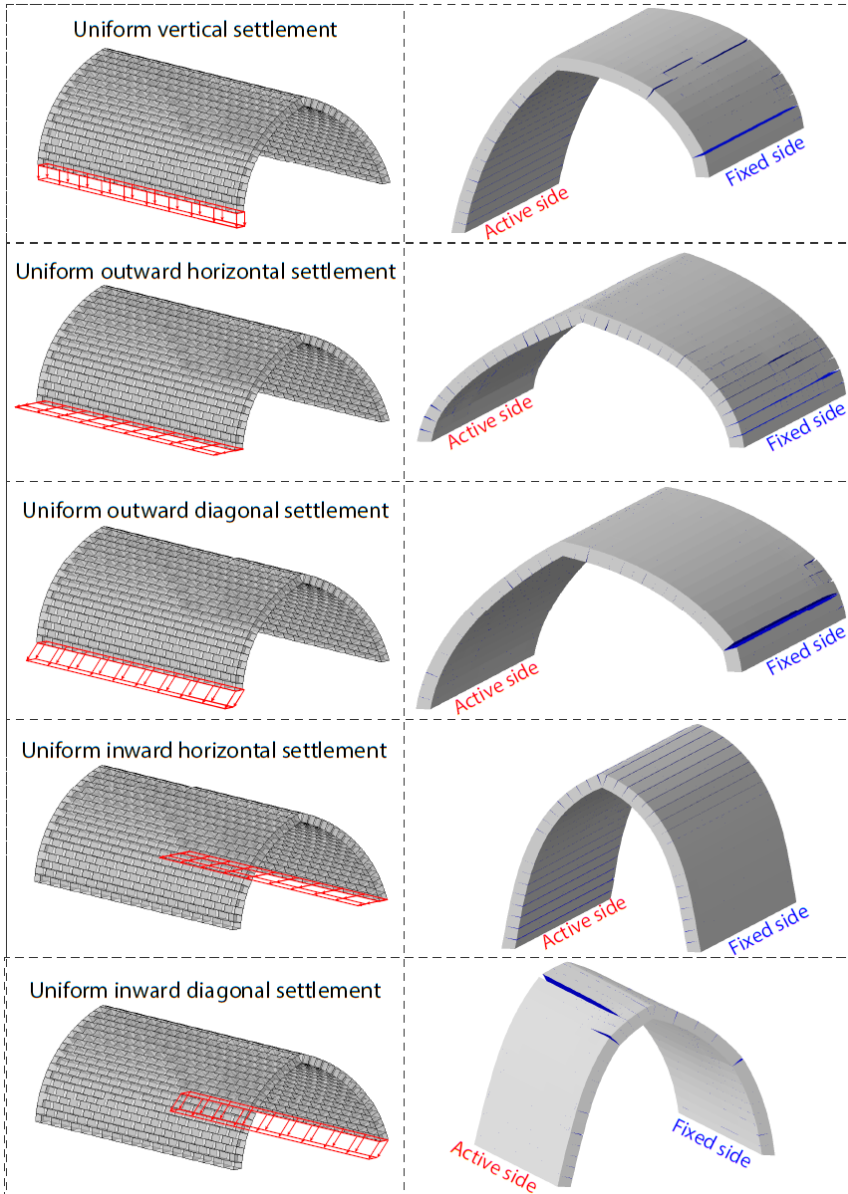
Figure 125: Summary of crack patterns for uniform settlements.
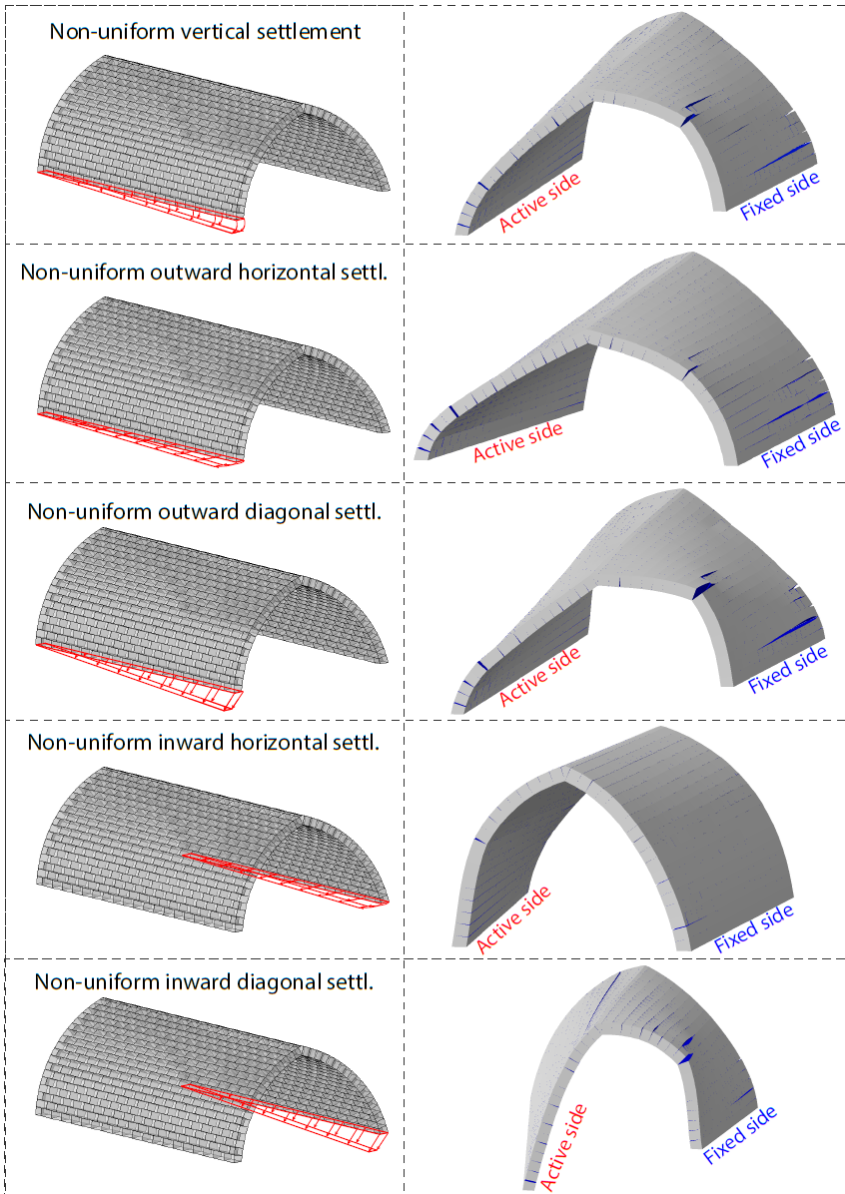
Figure 126: Summary of crack patterns for non-uniform settlements.
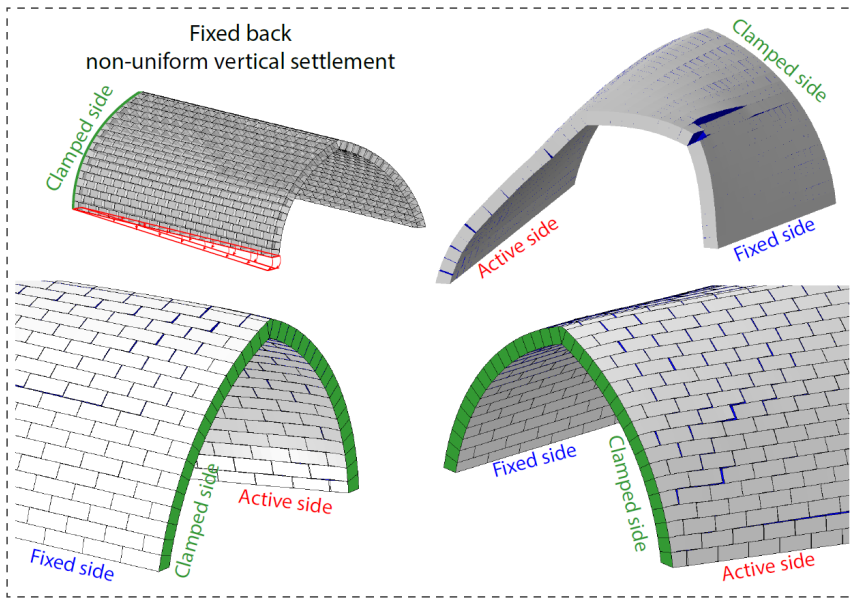
Figure 127: Fixed back non-uniform vertical settlement crack pattern.

6.5 CONCLUSIONS

In this chapter, a novel damaging block-based model to mechanically analyze masonry has been proposed. Two main versions of the model has been developed and validated.

According to the first version of the modeling approach proposed, masonry is represented by textured units consisting of one brick and few mortar layers composed of 3D solid FEs obeying to plastic-damage constitutive laws. This permits to represent the brick and mortar mechanical behavior when cracking and/or crushing occur. Textured units are assembled, accounting for any actual 3D through-thickness arrangement of masonry (including walls with openings, multi-leaf walls, etc.), by means of zero-thickness cohesive-frictional interfaces based on the contact penalty method. This permits to account for the brick-mortar bond failures both in tension and shear.

The contact behavior appeared to be consistent with experimental outcomes on small-scale masonry specimens. The results of numerical analyses carried out to investigate both the in-plane and the out-of-plane responses of brick-masonry panels up to collapse has been presented and compared with experimental outcomes. From this comparison, it was shown that the use of the proposed modeling approach allows the accurate representation of the masonry behavior both in the in-plane and out-of-plane responses. The results achieved demonstrate the significant potential of the proposed approach.

According to the second version of the modeling approach proposed (which substantially represented an extension of the first version to the cyclic behavior), solid 3D FEs governed by a plastic-damage constitutive law in tension and compression have been used to model the blocks (without mortar layers), while a cohesive-frictional contact-based formulation has been developed to simulate their cyclic interaction.

The mechanical characterization of this model can be easily carried out, as it requires only simple monotonic tests on small-scale masonry specimens. A strategy for the comprehensive mechanical characterization of the mechanical properties of the numerical model from these small-scale experiments has been proposed.

A comprehensive experimental campaign on calcium silicate brick masonry specimens has been used to validate the proposed calibration procedure, and to assess the accuracy of the modeling approach at structural level. Once defined the mechanical parameters from small-scale tests, they have been used in the simulation of in-plane and out-of-plane cyclic tests on masonry walls made of the same material. An overall good agreement between the numerical results and the experimental outcomes has been observed both in the in-plane and out-of-plane responses. This allowed to validate the model as well as the strategy proposed for its mechanical characterization.

Furthermore, a cyclic pushover test on a full-scale terraced masonry house has been simulated using the same mechanical parameters calibrated from small-scale tests. Good results have been obtained, showing the reliability of the model. Given the accuracy of the model and its capability to explicitly account for structural details such as running bonds, toothing between walls, the actual masonry texture, etc, which can be crucial in the structural response, the model can also be used to interpret the results of full-scale complex experimental tests.

Finally, the efficiency of the model is also shown by its limited computational effort. Indeed, although a full-scale terraced masonry house has been considered, all the analyses have been performed on a commercial laptop in a reasonable amount of time. By way of example, the average time needed for the monotonic pushover analyses on the full-scale terraced house, carried out on a laptop equipped with a processor Intel®Core^{TM} i7-6500U CPU @ 2.50GHz and 16GB RAM, was 2 hours and 9 minutes.

Therefore, although some further advances in the robustness of the solving algorithm should be developed, the model here proposed represents an efficient and reliable tool to analyse the cyclic behavior of masonry structures.

Finally, the second version of the model proposed have been used to evaluate the effects of differential settlements on historic masonry barrel vaults. A 3D block-by-block model has been developed to reproduce experiments on a scaled pointed barrel vault specimen, representative of late medieval barrel vaults in Scotland, undergoing non-uniform differential settlement.

Firstly, good agreement is observed between the experimental and numerical results in terms of crack pattern and transverses-longitudinal deformation pro-

files, capturing the major longitudinal cracks close to the applied settlement and also those at the other end of the vault.

Then, further analyses have been carried out to gain insight on the effects of several plausible uniform and non-uniform settlement patterns. All the failure modes have been collected according to the imposed settlement pattern. This summary of results, although preliminary, could help analysts in understanding the nature of the on-going deformation process in historic masonry vaults. The design of strengthening strategies can be made in the spirit of the "minimum intervention" principle to guarantee conservation is precise to the problems addressed or even considering not canceling a deformation if it is proved to represent a significant phase or inherent design fault of the vault.

Further aspects, such as the influence of the nonlinear behavior of the units, the dead load and the thickness of the vaults, the masonry bonding as also the segmentation of a vault (as masked by the ribs in Bothwell) should be investigated and collected in a more comprehensive matrix.

On a final note, it has to be pointed out that the assemblies of blocks studied in this chapter have been manually built. This operation, although rather simple for periodic regular textures, may become very time consuming for complex or irregular textures (e.g. vaults). To this aim, automatic routines (e.g. UEL [308]) could be used to directly generate the assembly of blocks.

CONCLUSIONS

In this thesis, some recent advances in computational analysis of masonry structures have been presented. In particular, this thesis attempted to fill the gap in the following open issues which arise when dealing with numerical modeling of masonry structures: (i) How to create the mesh of a structure if its geometry is extremely complex and irregular, as for historic masonry buildings? (ii) How to perform the seismic analysis of historic masonry buildings which are typically composed of several interacting units? (iii) How to evaluate the stability of leaning masonry structures with irregular geometries? (iv) How to accurately and efficiently represent the complex mechanical behavior of masonry? Essentially, the advancements pursued in the framework of mesh generation procedures for historic monumental buildings, analysis of seismically interacting structures, analysis of leaning historic structures, and block-based modeling of masonry structures, have been shown and discussed.

Firstly, a comprehensive review of the existing modeling strategies for masonry structures has been presented (Chapter 2), together with a novel classification of these strategies. This classification consisted of four categories (block-based models, continuum models, geometry-based models, and macroelement models) and attempted to put in order the wide scientific production on this field, although a fully coherent collocation of all the modeling approaches was substantially impossible due to the peculiar features of each solution proposed.

Then, two mesh generation procedures have been proposed (Chapter 3) to transform 3D point clouds into 3D solid finite element models of historic monumental buildings. The first approach, called CLOUD2FEM, consisted in the slicing and subsequent stacking of the geometry. An increase of the level of automation in the mesh generation process has been observed and a large reduction in the required time in comparison to CAD-based modeling procedures has been achieved. The validation of the method has been performed on the San Felice sul Panaro fortress, which embodies all the typical complexities of historic monumental buildings. The second approach, called watertight meshing, considered the structure as a watertight surface and eventually fills the volume. Although not always applicable to historic buildings, e.g. in case of inner spaces, rooms, furniture, doors, windows, etc., this procedure represented a very fast solution for the direct and fully automatic mesh generation of a geometrically irregular masonry building.

Additionally, a computational procedure based on the use of nonlinear static analyses has been developed (Chapter 4) to assess the response of seismically interacting historic masonry structures. The procedure required a numerical model of the entire aggregation of units (to explicitly consider the interaction effects among these latter), the execution of modal analysis to define the modes involv-

ing the dynamic response of each unit and their modal shapes, the execution of a series of pushover analyses (one for each unit) by applying time by time the load pattern fitted according to the identified modal shapes, and the conversion of the pushover curve of each unit into the corresponding capacity curve of the equivalent SDOF system, to perform the seismic verification. The procedure has been then applied to a case-study, the medieval fortress in San Felice sul Panaro, significantly damaged by the 2012 Emilia earthquake. The results were good in terms of comparison between the damage experienced by the structure and the one predicted (evaluated computing a ductility demand required by the actual seismic event), showing the potential of the proposed procedure. Given such promising results, the application of the procedure could be extended in the future to other kinds of complex monumental structure (e.g. palaces in aggregate).

Furthermore, a computational procedure based on upper-bound finite element limit analysis has been developed (Chapter 5) to undertake stability analysis of leaning historic masonry structures, estimating their critical inclination angle. To demonstrate the effectiveness of the procedure, the SW leaning ruined tower of the Caerphilly castle has been employed as a case study. It emerged that the tower in its actual condition is not far from its collapse. Indeed, an additional inclination of the structure by $1.5°$ appears to be critical. The proposed procedure is characterized by a high degree of automation and could be effectively utilized to assess the stability of historic structures at a national scale and provide useful information to engineers and managers to classify the structural health condition of historic assets in their care. Although the procedure proposed represents a novel solution for evaluating the stability of extant masonry structures, it could be enriched with an adaptive mesh enhancement in the framework of a multi-step strategy.

Finally, a damaging block-based model formulated in the context of contact mechanics has been developed (Chapter 6) for the computational analysis of masonry structures. The model has been validated through the comparison against in-plane and out-of-plane experimental tests on masonry walls, as well as cyclic pushover tests on a full-scale masonry house. In addition, the developed block-based model has been also used to investigate the response of historic barrel vaults undergoing differential settlements. The proposed damaging block-based model appeared effectively efficient, accurate and versatile. Furthermore, the capability of explicitly accounting for structural details such as running bonds, toothing between walls, the actual 3D masonry texture, etc, appears crucial in the structural analysis of masonry structures.

Although apparently disconnected, the different advances achieved in this thesis can be combined together to provide an advanced framework for the computational analysis of masonry structures. Basically, the outcomes of the mesh generation procedures proposed in Chapter 3 can be used within the structural analysis procedures proposed in this thesis, as shown in Chapter 4 and Chapter 5. Furthermore, although the block-based model presented in Chapter 6 has been only utilized on relatively simple structures so far, it could be used, in theory,

within the structural analysis procedures developed in Chapter 4 and Chapter 5 for monumental historic buildings.

Future developments of the computational tools presented in this thesis could include:

- The mesh generation procedures (Chapter 3) could be coupled with the block-based model developed in Chapter 6. Particularly, the solid volume obtained by these procedures could be automatically filled, by means of ad-hoc routines, with certain periodic textures of solid blocks, following the mechanical formulation of the block-based model of Chapter 6. However, this approach could result extremely computational demanding for the contemporary workstations when dealing with large-scale historic structures.

- The block-based model of Chapter 6 could be easily extended to the analysis of FRP- and FRCM-strengthened masonry structures. Indeed, the contact-based interface formulation developed in Chapter 6 appears particularly favorable to model the bond behavior between masonry and the reinforcement.

- The contact-based interface formulation developed in Chapter 6 could be also utilized to analyze the displacement capacity of masonry structures with pre-assigned collapse mechanisms (deduced, for instance, from the outcomes of limit analysis).

PLASTIC-DAMAGE MODEL

The main features of the plastic-damage model developed by Lee and Fenves [136] are here summarized. Isotropic degradation damage is assumed and, if a scalar degradation damage variable $0 \leqslant d < 1$ is used to represent the isotropic damage and the concepts of strain decomposition and effective stress are employed, then the Cauchy stress tensor $\boldsymbol{\sigma}$ becomes:

$$\boldsymbol{\sigma} = (1-d)\,\overline{\boldsymbol{\sigma}} = (1-d)\,\mathbf{E}_0\,(\boldsymbol{\varepsilon}-\boldsymbol{\varepsilon}^{\mathbf{p}})\,, \tag{26}$$

where $\overline{\boldsymbol{\sigma}}$ is the effective stress tensor, $\mathbf{E}_0$ is the initial undamaged elastic stiffness tensor, $\boldsymbol{\varepsilon}$ is the strain tensor and $\boldsymbol{\varepsilon}^{\mathbf{p}}$ is the plastic part of the strain tensor.

The plastic strain rate is obtained from a plastic potential Φ defined in the effective-stress space:

$$\dot{\boldsymbol{\varepsilon}^{\mathbf{p}}} = \dot{\lambda}\frac{\partial \Phi\,(\overline{\boldsymbol{\sigma}})}{\partial \overline{\boldsymbol{\sigma}}}, \tag{27}$$

where $\dot{\lambda}$ is the plastic multiplier ($\dot{\lambda} \geqslant 0$). To control dilatancy, a nonassociative flow rule is considered. Particularly, the plastic strain rate is obtained by a flow rule generated by a Drucker-Prager type plastic potential, which, in terms of effective stresses, has the form:

$$\Phi = \sqrt{(\epsilon f_{t0} \tan\psi)^2 + 3J_2\,(\overline{\boldsymbol{\sigma}})} + \frac{1}{3}I_1\,(\overline{\boldsymbol{\sigma}})\tan\psi\,, \tag{28}$$

being I_1 the first invariant of the stress tensor, J_2 the second invariant of the stress deviator, f_{t0} the initial uniaxial tensile strength, ϵ a smoothing constant generally assumed equal to 0.1 [325], and ψ the dilatancy angle of the quasi-brittle material, typically assumed equal to $10°$ in agreement with experimental evidences and previous numerical models [325, 141].
The stress admissibility condition reads as:

$$F\,(\overline{\boldsymbol{\sigma}}, f_{ft}, f_{fc}) \leqslant 0, \tag{29}$$

where f_{ft} and f_{fc} are uniaxial tensile and compressive strength functions depending on two hardening variables k_t and k_c:

$$f_{ft}\,(k_t) = [1 - d_t\,(k_t)]\,\overline{f_{ft}}\,(k_t)\,, \qquad f_{fc}\,(k_c) = [1 - d_c\,(k_c)]\,\overline{f_{fc}}\,(k_c)\,, \tag{30}$$

being $\overline{f_{ft}}\,(k_t)$ and $\overline{f_{fc}}\,(k_c)$ the uniaxial tensile and compressive strengths in the effective-stress responses and the scalar damage variables $d_t\,(k_t)$ and $d_c\,(k_c)$ functions of the hardening variables. The degradation damage variable d in (26)

is then written as a function of the stress state and the scalar damage variable d_t and d_c as:

$$d = 1 - (1 - s_t d_t)(1 - s_c d_c). \tag{31}$$

where s_t and s_c are functions of the stress state that are introduced to model stiffness recovery effects associated with stress reversals. Assuming that the material fully recovers the compressive stiffness, they are defined according to the following relationships:

$$s_t = 1 - H(\sigma_{uniaxial}), \qquad s_c = 1 - (1 - H(\sigma_{uniaxial})) \tag{32}$$

where

$$H(\sigma_{uniaxial}) = \begin{cases} 1 & \text{if } \sigma_{uniaxial} \geqslant 0 \\ 0 & \text{if } \sigma_{uniaxial} < 0 \end{cases} \tag{33}$$

being $\sigma_{uniaxial}$ the uniaxial stress (positive in tension). Assuming, for instance, an initially undamaged material in compression ($d_c = 0$), the degradation damage variable d becomes

$$d = 1 - (1 - (1 - (1 - H(\sigma_{uniaxial})))d_t) \tag{34}$$

where in tension $H(\sigma_{uniaxial}) = 1$ and, therefore, $d = d_t$ (as expected); whereas in compression $H(\sigma_{uniaxial}) = 0$ and, therefore, $d = 0$, the material fully recovers the compressive stiffness (which in this case is the initial undamaged stiffness, $E = E_0$). Furthermore, d in (31) fulfils the condition $0 \leqslant d < 1$ and equals d_t when $d_c = 0$ (uniaxial tensile case) and d_c when $d_t = 0$ (uniaxial compressive case). Consequently, the uniaxial strength functions (30) can be written as:

$$f_{ft} = (1 - d)\overline{f_{ft}}, \qquad f_{fc} = (1 - d)\overline{f_{fc}}. \tag{35}$$

Being $\mathbf{k} = [k_t, k_c]^T$, the plastic-damage model employs the yielding surface (Figure 128) proposed in [135] and further developed in [136], which has, in the effective-stress space, the form:

$$F = \frac{1}{1-\alpha}\left[\alpha I_1(\overline{\boldsymbol{\sigma}}) + \sqrt{3J_2(\overline{\boldsymbol{\sigma}})} + \beta(\mathbf{k})\langle\overline{\sigma}_{max}\rangle - \gamma\langle-\overline{\sigma}_{max}\rangle\right] + \overline{f_{fc}}(k_c) = 0, \tag{36}$$

where $\overline{\sigma}_{max}$ is the algebraically maximum principal stress in the effective-stress space, α and γ are dimensionless constants and $\beta(\mathbf{k})$ is a function of the hardening variables. The constant α depends on the ratio f_{b0}/f_{c0} between the biaxial initial compressive strength f_{b0} and the uniaxial initial compressive strength f_{c0} through the relationship $\alpha = [(f_{b0}/f_{c0}) - 1]/[2(f_{b0}/f_{c0}) - 1]$. Typically, $f_{b0}/f_{c0} = 1.16$, which implies $\alpha = 0.12$ [135]. The constant γ appears only in triaxial compression and is defined as $\gamma = 3(1 - \rho)/(2\rho - 1)$, where the constant ρ represents the ratio of the second stress invariant on the tensile meridian to that
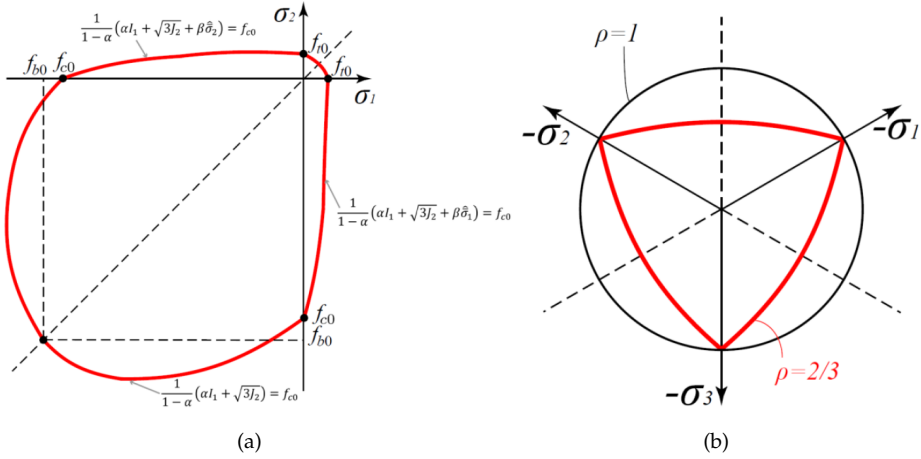
Figure 128: Plastic-damage model yielding surface in: (a) plain stress and (b) the deviatoric plane.

on the compressive meridian at initial yield. Typically, $\rho = 2/3$, which leads to $\gamma = 3$ [135]. Finally, $\beta\,(\mathbf{k})$ is assumed to depend on the hardening variables by the relationship $\beta\,(\mathbf{k}) = -\overline{f_{fc}}\,(k_c)\,/\overline{f_{ft}}\,(k_t)\,(1-\alpha) - (1+\alpha)$.

The evolution of the hardening variables is expressed in terms of the eigenvalues of the effective stress and plastic strain rate tensors, collected, respectively, in $\widehat{\overline{\sigma}}$ and $\widehat{\dot{\varepsilon}^p}$, as:

$$\dot{\mathbf{k}} = \dot{\lambda}\mathbf{h}\left(\widehat{\overline{\sigma}}, \mathbf{k}, g_t, g_c\right)\frac{\partial\Phi\left(\widehat{\overline{\sigma}}\right)}{\partial\widehat{\overline{\sigma}}} = \mathbf{h}\left(\widehat{\overline{\sigma}}, \mathbf{k}, g_t, g_c\right)\widehat{\dot{\varepsilon}^p}, \tag{37}$$

being

$$\mathbf{h}(\widehat{\overline{\sigma}}, \mathbf{k}, g_t, g_c) = \left[\begin{array}{ccc} r(\widehat{\overline{\sigma}})f_{ft}(k_t)/g_t & 0 & 0 \\ 0 & 0 & (1-r(\widehat{\overline{\sigma}}))f_{fc}(k_c)/g_c \end{array}\right], \tag{38}$$

where the scalar quantity $r(\widehat{\overline{\sigma}})$ is a weight factor ($0 \leqslant r \leqslant 1$) defined as $r(\widehat{\overline{\sigma}}) = \frac{\sum_{i=1}^{3}\langle\widehat{\overline{\sigma}}_i\rangle}{\sum_{i=1}^{3}|\widehat{\overline{\sigma}}_i|}$, and the quantities g_t and g_c are the dissipated energy densities in tension and compression, respectively. These are derived from the tensile G_t and compressive G_c fracture energies, which are primary mechanical properties of the material, following the relationships:

$$g_t = G_t/l_{eq}, \quad g_c = G_c/l_{eq}, \tag{39}$$

being l_{eq} the localization zone size (characteristic length) defined as

$$l_{eq} = \alpha_h\sqrt{V_e} = \alpha_h(\sum_{\rho=1}^{n_\rho}\sum_{\xi=1}^{n_\xi}\sum_{\eta=1}^{n_\eta}\det J w_\rho w_\xi w_\eta), \tag{40}$$

where w_ρ, w_ξ and w_η are the weight factors of the Gaussian integration scheme, J the Jacobian of the transformation, V_e the element area and α_h a modification factor that depends on the typology of the finite element used. In this way, the mesh size does not significantly influence the material response.

Generally, the values of the fracture energies (G_t and G_c), which are primary material parameters that have to be inputted in the model, can be defined either in a direct way, i.e. by directly specifying their values, or in an indirect way, i.e. by the point-by-point specification of the inelastic stress-strain uniaxial curves in tension and compression. Typically, the point-by-point specification of the inelastic stress-strain uniaxial curves in tension and compression is preferred as it allows to specify a residual strength (both in tension and compression) which greatly helps the convergence of the solving algorithm in case of softening

[1] M. Como, *Statics of Historic Masonry Constructions*. Springer, 2013.

[2] A. W. Hendry, *Structural Masonry*. Macmillan Education UK, 1998.

[3] A. Page, "The biaxial compressive strength of brick masonry.," *Proceedings of the Institution of Civil Engineers*, vol. 71, no. 3, pp. 893–906, 1981.

[4] A. Page, W. Samarasinghe, and A. Hendry, "The in-plane failure of masonry. A review," in *Proc. Br. Ceram. Soc.*, no. 30, p. 90, 1982.

[5] A. Page, "The strength of brick masonry under biaxial tension-compression," *International journal of masonry construction*, vol. 3, no. 1, pp. 26–31, 1983.

[6] G. Magenes and G. M. Calvi, "In-plane seismic response of brick masonry walls," *Earthquake engineering & structural dynamics*, vol. 26, no. 11, pp. 1091–1112, 1997.

[7] C. Calderini, S. Cattari, and S. Lagomarsino, "In-plane strength of unreinforced masonry piers," *Earthquake Engineering & Structural Dynamics*, vol. 38, no. 2, pp. 243–267, 2009.

[8] K. Beyer, "Peak and residual strengths of brick masonry spandrels," *Engineering Structures*, vol. 41, pp. 533–547, 2012.

[9] S. Petry and K. Beyer, "Influence of boundary conditions and size effect on the drift capacity of urm walls," *Engineering Structures*, vol. 65, pp. 76–88, 2014.

[10] F. Messali and J. Rots, "In-plane drift capacity at near collapse of rocking unreinforced calcium silicate and clay masonry piers," *Engineering Structures*, vol. 164, pp. 183–194, 2018.

[11] A. M. D'Altri, S. de Miranda, G. Castellazzi, and V. Sarhosis, "A 3D detailed micro-model for the in-plane and out-of-plane numerical analysis of masonry panels," *Computers & Structures*, vol. 206, pp. 18–30, 2018.

[12] L. Facconi, F. Minelli, and F. J. Vecchio, "Predicting uniaxial cyclic compressive behavior of brick masonry: New analytical model," *Journal of Structural Engineering*, vol. 144, no. 2, p. 04017213, 2018.

[13] E. Sassoni, C. Mazzotti, and G. Pagliai, "Comparison between experimental methods for evaluating the compressive strength of existing masonry buildings," *Construction and Building Materials*, vol. 68, pp. 206–219, 2014.

[14] M. Kržan, S. Gostič, S. Cattari, and V. Bosiljkov, "Acquiring reference parameters of masonry for the structural performance analysis of historical buildings," *Bulletin of earthquake engineering*, vol. 13, no. 1, pp. 203–236, 2015.

[15] F. Messali, R. Esposito, S. Jafari, G. Ravenshorst, P. Korswagen, and J. G. Rots, "A multiscale experimental characterization of dutch unreinforced masonry buildings," in *Proceedings of the 16th European conference on earthquake engineering, 16ECEE*, 2018.

[16] A. Borri, G. Castori, M. Corradi, and E. Speranzini, "Shear behavior of unreinforced and reinforced masonry panels subjected to in situ diagonal compression tests," *Construction and Building Materials*, vol. 25, no. 12, pp. 4403–4414, 2011.

[17] R. Lumantarna, D. T. Biggs, and J. M. Ingham, "Compressive, flexural bond, and shear bond strengths of in situ new zealand unreinforced clay brick masonry constructed using lime mortar between the 1880s and 1940s," *Journal of Materials in Civil Engineering*, vol. 26, no. 4, pp. 559–566, 2014.

[18] D. McCann and M. Forde, "Review of NDT methods in the assessment of concrete and masonry structures," *NDT & E International*, vol. 34, no. 2, pp. 71–84, 2001.

[19] V. Bosiljkov, V. Bokan-Bosiljkov, B. Strah, J. Velkavr, and P. Cotič, "Review of innovative techniques for the knowledge of cultural assets (geometry, technologies, decay)," *PERPETUATE (EC-FP7 project), Deliverable D6*, 2010.

[20] A. Borri, M. Corradi, G. Castori, and A. De Maria, "A method for the analysis and classification of historic masonry," *Bulletin of Earthquake Engineering*, vol. 13, no. 9, pp. 2647–2665, 2015.

[21] M. Tondelli, M. Rota, A. Penna, and G. Magenes, "Evaluation of uncertainties in the seismic assessment of existing masonry buildings," *Journal of Earthquake Engineering*, vol. 16, no. sup1, pp. 36–64, 2012.

[22] "Recommendations for the analysis, conservation and structural restoration of architectural heritage, International scientific committee for analysis and restoration of structures of architectural heritage, ratified as ICOMOS document by the General Assembly in Zimbabwe," 2003.

[23] "Eurocode 8 - Design of structures for earthquake resistance. Part 3: Assessment and retrofitting of buildings, Brussels, Belgium.," 2005.

[24] "Direttiva del Presidente del Consiglio dei Ministri 9 febbraio 2011. Valutazione e riduzione del rischio sismico del patrimonio culturale con riferimento alle Norme tecniche per le costruzioni di cui al D.M. 14/01/2008."

[25] "Guide for the structural rehabilitation of heritage buildings, prepared by CIB commission W023 – Wall structures.," 2010.

[26] S. Cattari, S. Lagomarsino, V. Bosiljkov, and D. D'Ayala, "Sensitivity analysis for setting up the investigation protocol and defining proper confidence factors for masonry buildings," *Bulletin of Earthquake Engineering*, vol. 13, no. 1, pp. 129–151, 2015.

[27] J. Haddad, S. Cattari, and S. Lagomarsino, "Sensitivity and preliminary analyses for the seismic assessment of Ardinghelli Palace," in *Structural Analysis of Historical Constructions*, pp. 2412–2421, Springer, 2019.

[28] A. Chiozzi, N. Grillanda, G. Milani, and A. Tralli, "UB-ALMANAC: An adaptive limit analysis NURBS-based program for the automatic assessment of partial failure mechanisms in masonry churches," *Engineering Failure Analysis*, vol. 85, pp. 201–220, 2018.

[29] G. Castellazzi, A. D'Altri, G. Bitelli, I. Selvaggi, and A. Lambertini, "From laser scanning to finite element analysis of complex buildings by using a semi-automatic procedure," *Sensors*, vol. 15, no. 8, pp. 18360–18380, 2015.

[30] G. Castellazzi, A. M. D'Altri, S. de Miranda, and F. Ubertini, "An innovative numerical modeling strategy for the structural analysis of historical monumental buildings," *Engineering Structures*, vol. 132, pp. 229–248, 2017.

[31] M. Korumaz, M. Betti, A. Conti, G. Tucci, G. Bartoli, V. Bonora, A. G. Korumaz, and L. Fiorini, "An integrated terrestrial laser scanner (TLS), deviation analysis (DA) and finite element (FE) approach for health assessment of historical structures. A minaret case study," *Engineering Structures*, vol. 153, pp. 224–238, 2017.

[32] A. M. D'Altri, G. Milani, S. de Miranda, G. Castellazzi, and V. Sarhosis, "Stability analysis of leaning historic masonry structures," *Automation in Construction*, vol. 92, pp. 199–213, 2018.

[33] M. Cerone, G. Croci, and A. Viskovic, "The structural behaviour of colosseum over the centuries," in *More than two thousand years in the history of architecture*, 2000.

[34] G. Macchi, G. Ruggeri, M. Eusebio, and M. Moncecchi, "Structural assessment of the leaning tower of pisa," in *IABSE Reports*, pp. 401–401, IABSE Internationa Association for Bridge, 1993.

[35] M. J. DeJong, B. Belletti, M. A. Hendriks, and J. G. Rots, "Shell elements for sequentially linear analysis: Lateral failure of masonry structures," *Engineering Structures*, vol. 31, no. 7, pp. 1382–1392, 2009.

[36] J. G. Rots, B. Belletti, and S. Invernizzi, "Robust modeling of RC structures with an "event-by-event" strategy," *Engineering Fracture Mechanics*, vol. 75, no. 3-4, pp. 590–614, 2008.

[37] J. N. Reddy, *An Introduction to Nonlinear Finite Element Analysis*. Oxford University Press, 2004.

[38] R. W. Clough and J. Penzien, *Dynamics of Structures*. Computers and Structures, Incorporated, 2003.

[39] J. Heyman, "The stone skeleton," *International Journal of Solids and Structures*, vol. 2, no. 2, pp. 249–279, 1966.

[40] M. Angelillo, ed., *Mechanics of Masonry Structures*. Springer Vienna, 2014.

[41] S. Huerta, "Mechanics of masonry vaults: The equilibrium approach," SAHC 2001, 2001.

[42] A. Giuffrè and C. Carocci, "Statica e dinamica delle costruzioni murarie storiche," pp. 539–598, 1993.

[43] F. Marmo and L. Rosati, "Reformulation and extension of the thrust network analysis," *Computers & Structures*, vol. 182, pp. 104–118, 2017.

[44] A. Chiozzi, G. Milani, and A. Tralli, "A genetic algorithm NURBS-based new approach for fast kinematic limit analysis of masonry vaults," *Computers & Structures*, vol. 182, pp. 187–204, 2017.

[45] P. B. Lourenço, "Computations on historic masonry structures," *Progress in Structural Engineering and Materials*, vol. 4, no. 3, pp. 301–319, 2002.

[46] P. Roca, M. Cervera, G. Gariup, and L. Pela', "Structural analysis of masonry historical constructions. classical and advanced approaches," *Archives of Computational Methods in Engineering*, vol. 17, no. 3, pp. 299–325, 2010.

[47] S. Lagomarsino and S. Cattari, "PERPETUATE guidelines for seismic performance-based assessment of cultural heritage masonry structures," *Bulletin of Earthquake Engineering*, vol. 13, no. 1, pp. 13–47, 2015.

[48] A. W. Page, "Finite element model for masonry," *Journal of the Structural Division*, vol. 104, no. 8, pp. 1267–1285, 1978.

[49] K. M. Dolatshahi and M. Yekrangnia, "Out-of-plane strength reduction of unreinforced masonry walls because of in-plane damages," *Earthquake Engineering & Structural Dynamics*, vol. 44, no. 13, pp. 2157–2176, 2015.

[50] E. Minga, L. Macorini, and B. A. Izzuddin, "A 3D mesoscale damage-plasticity approach for masonry structures under cyclic loading," *Meccanica*, vol. 53, no. 7, pp. 1591–1611, 2018.

[51] A. M. D'Altri, F. Messali, J. Rots, G. Castellazzi, and S. de Miranda, "A damaging block-based model for the analysis of the cyclic behaviour of full-scale masonry structures," *Engineering Fracture Mechanics*, 2018 (In Press).

[52] H. R. Lotfi and P. B. Shing, "Interface model applied to fracture of masonry structures," *Journal of structural engineering*, vol. 120, no. 1, pp. 63–80, 1994.

[53] P. B. Lourenço and J. G. Rots, "Multisurface interface model for analysis of masonry structures," *Journal of Engineering Mechanics*, vol. 123, no. 7, pp. 660–668, 1997.

[54] C. Sandoval and O. Arnau, "Experimental characterization and detailed micro-modeling of multi-perforated clay brick masonry structural response," *Materials and Structures*, vol. 50, no. 1, 2016.

[55] S. Calderón, C. Sandoval, and O. Arnau, "Shear response of partially-grouted reinforced masonry walls with a central opening: Testing and detailed micro-modelling," *Materials & Design*, vol. 118, pp. 122–137, 2017.

[56] R. Senthivel and P. Lourenço, "Finite element modelling of deformation characteristics of historical stone masonry shear walls," *Engineering Structures*, vol. 31, no. 9, pp. 1930–1943, 2009.

[57] D. V. Oliveira and P. B. Lourenço, "Implementation and validation of a constitutive model for the cyclic behaviour of interface elements," *Computers & structures*, vol. 82, no. 17-19, pp. 1451–1461, 2004.

[58] L. Gambarotta and S. Lagomarsino, "Damage models for the seismic response of brick masonry shear walls. Part I: The mortar joint model and its applications," *Earthquake engineering & structural dynamics*, vol. 26, no. 4, pp. 423–439, 1997.

[59] G. Alfano and E. Sacco, "Combining interface damage and friction in a cohesive-zone model," *International Journal for Numerical Methods in Engineering*, vol. 68, no. 5, pp. 542–582, 2006.

[60] F. Parrinello, B. Failla, and G. Borino, "Cohesive–frictional interface constitutive model," *International Journal of Solids and Structures*, vol. 46, no. 13, pp. 2680–2692, 2009.

[61] G. Formica, V. Sansalone, and R. Casciaro, "A mixed solution strategy for the nonlinear analysis of brick masonry walls," *Computer Methods in Applied Mechanics and Engineering*, vol. 191, no. 51-52, pp. 5847–5876, 2002.

[62] D. Malomo, R. Pinho, and A. Penna, "Using the applied element method for modelling calcium silicate brick masonry subjected to in-plane cyclic loading," *Earthquake Engineering & Structural Dynamics*, vol. 47, no. 7, pp. 1610–1630, 2018.

[63] S. Casolo, "Modelling the out-of-plane seismic behaviour of masonry walls by rigid elements," *Earthquake engineering & structural dynamics*, vol. 29, no. 12, pp. 1797–1813, 2000.

[64] A. Orduña, "Non-linear static analysis of rigid block models for structural assessment of ancient masonry constructions," *International Journal of Solids and Structures*, vol. 128, pp. 23–35, 2017.

[65] D. Baraldi and A. Cecchi, "Discrete approaches for the nonlinear analysis of in plane loaded masonry walls: Molecular dynamic and static algorithm solutions," *European Journal of Mechanics-A/Solids*, vol. 57, pp. 165–177, 2016.

[66] D. Baraldi and A. Cecchi, "A full 3D rigid block model for the collapse behaviour of masonry walls," *European Journal of Mechanics-A/Solids*, vol. 64, pp. 11–28, 2017.

[67] L. Macorini and B. Izzuddin, "A non-linear interface element for 3D mesoscale analysis of brick-masonry structures," *International Journal for Numerical Methods in Engineering*, vol. 85, no. 12, pp. 1584–1608, 2011.

[68] C. Chisari, L. Macorini, C. Amadio, and B. Izzuddin, "An inverse analysis procedure for material parameter identification of mortar joints in unreinforced masonry," *Computers & Structures*, vol. 155, pp. 97–105, 2015.

[69] C. Chisari, L. Macorini, C. Amadio, and B. A. Izzuddin, "Identification of mesoscale model parameters for brick-masonry," *International Journal of Solids and Structures*, 2018.

[70] E. Minga, L. Macorini, and B. Izzuddin, "Enhanced mesoscale partitioned modelling of heterogeneous masonry structures," *International Journal for Numerical Methods in Engineering*, vol. 113, no. 13, pp. 1950–1971, 2018.

[71] Y. Zhang, L. Macorini, and B. A. Izzuddin, "Mesoscale partitioned analysis of brick-masonry arches," *Engineering Structures*, vol. 124, pp. 142–166, 2016.

[72] A. J. Aref and K. M. Dolatshahi, "A three-dimensional cyclic meso-scale numerical procedure for simulation of unreinforced masonry structures," *Computers & Structures*, vol. 120, pp. 9–23, 2013.

[73] B. V. Wilding, K. M. Dolatshahi, and K. Beyer, "Influence of load history on the force-displacement response of in-plane loaded unreinforced masonry walls," *Engineering Structures*, vol. 152, pp. 671–682, 2017.

[74] K. M. Dolatshahi and A. J. Aref, "Multi-directional response of unreinforced masonry walls: Experimental and computational investigations," *Earthquake Engineering & Structural Dynamics*, vol. 45, no. 9, pp. 1427–1449, 2016.

[75] K. M. Dolatshahi, M. T. Nikoukalam, and K. Beyer, "Numerical study on factors that influence the in-plane drift capacity of unreinforced masonry walls," *Earthquake Engineering & Structural Dynamics*, vol. 47, no. 6, pp. 1440–1459, 2018.

[76] J. S. Kuang and Y. Yuen, "Simulations of masonry-infilled reinforced concrete frame failure," *Proceedings of the Institution of Civil Engineers: Engineering and Computational Mechanics*, vol. 166, no. 4, p. 179, 2013.

[77] P. C. Miglietta, E. C. Bentz, and G. Grasselli, "Finite/discrete element modelling of reversed cyclic tests on unreinforced masonry structures," *Engineering Structures*, vol. 138, pp. 159–169, 2017.

[78] V. Sarhosis, K. Bagi, J. V. Lemos, and G. Milani, *Computational Modeling of Masonry Structures Using the Discrete Element Method*. IGI Global, 2016.

[79] P. A. Cundall and O. D. Strack, "A discrete numerical model for granular assemblies," *geotechnique*, vol. 29, no. 1, pp. 47–65, 1979.

[80] P. A. Cundall, "UDEC-A generalised distinct element program for modelling jointed rock.," tech. rep., Cundall (Peter) Associates Virginia Water (England), 1980.

[81] E. Çaktı, Ö. Saygılı, J. V. Lemos, and C. S. Oliveira, "Discrete element modeling of a scaled masonry structure and its validation," *Engineering Structures*, vol. 126, pp. 224–236, 2016.

[82] C. Papantonopoulos, I. Psycharis, D. Papastamatiou, J. Lemos, and H. Mouzakis, "Numerical prediction of the earthquake response of classical columns using the distinct element method," *Earthquake Engineering & Structural Dynamics*, vol. 31, no. 9, pp. 1699–1717, 2002.

[83] T. Bui, A. Limam, V. Sarhosis, and M. Hjiaj, "Discrete element modelling of the in-plane and out-of-plane behaviour of dry-joint masonry wall constructions," *Engineering Structures*, vol. 136, pp. 277–294, 2017.

[84] V. Sarhosis and Y. Sheng, "Identification of material parameters for low bond strength masonry," *Engineering Structures*, vol. 60, pp. 100–110, 2014.

[85] J. V. Lemos, "Discrete element modeling of masonry structures," *International Journal of Architectural Heritage*, vol. 1, no. 2, pp. 190–213, 2007.

[86] A. R. Tóth, Z. Orbán, and K. Bagi, "Discrete element analysis of a stone masonry arch," *Mechanics Research Communications*, vol. 36, no. 4, pp. 469–480, 2009.

[87] J. Simon and K. Bagi, "Discrete element analysis of the minimum thickness of oval masonry domes," *International Journal of Architectural Heritage*, vol. 10, no. 4, pp. 457–475, 2016.

[88] T. Forgács, V. Sarhosis, and K. Bagi, "Minimum thickness of semi-circular skewed masonry arches," *Engineering Structures*, vol. 140, pp. 317–336, 2017.

[89] G. Lengyel, "Discrete element analysis of gothic masonry vaults for self-weight and horizontal support displacement," *Engineering Structures*, vol. 148, pp. 195–209, 2017.

[90] D. Foti, V. Vacca, and I. Facchini, "DEM modeling and experimental analysis of the static behavior of a dry-joints masonry cross vaults," *Construction and Building Materials*, vol. 170, pp. 111–120, 2018.

[91] G.-H. Shi, "Discontinuous deformation analysis: A new numerical model for the statics and dynamics of deformable block structures," *Engineering computations*, vol. 9, no. 2, pp. 157–168, 1992.

[92] A. Thavalingam, N. Bicanic, J. Robinson, and D. Ponniah, "Computational framework for discontinuous modelling of masonry arch bridges," *Computers & structures*, vol. 79, no. 19, pp. 1821–1830, 2001.

[93] M. Jean, "The non-smooth contact dynamics method," *Computer methods in applied mechanics and engineering*, vol. 177, no. 3-4, pp. 235–257, 1999.

[94] J. J. Moreau, "Unilateral contact and dry friction in finite freedom dynamics," in *Nonsmooth mechanics and Applications*, pp. 1–82, Springer, 1988.

[95] A. Rafiee and M. Vinches, "Mechanical behaviour of a stone masonry bridge assessed using an implicit discrete element method," *Engineering Structures*, vol. 48, pp. 739–749, 2013.

[96] A. Rafiee, M. Vinches, and C. Bohatier, "Application of the nscd method to analyse the dynamic behaviour of stone arched structures," *International Journal of Solids and Structures*, vol. 45, no. 25-26, pp. 6269–6283, 2008.

[97] G. Lancioni, D. Gentilucci, E. Quagliarini, and S. Lenci, "Seismic vulnerability of ancient stone arches by using a numerical model based on the non-smooth contact dynamics method," *Engineering Structures*, vol. 119, pp. 110–121, 2016.

[98] V. Beatini, G. Royer-Carfagni, and A. Tasora, "A regularized non-smooth contact dynamics approach for architectural masonry structures," *Computers & Structures*, vol. 187, pp. 88–100, 2017.

[99] A. A. Munjiza, *The combined finite-discrete element method*. John Wiley & Sons, 2004.

[100] H. Smoljanović, N. Živaljić, and Ž. Nikolić, "A combined finite-discrete element analysis of dry stone masonry structures," *Engineering structures*, vol. 52, pp. 89–100, 2013.

[101] H. Smoljanović, N. Živaljić, Ž. Nikolić, and A. Munjiza, "Numerical analysis of 3D dry-stone masonry structures by combined finite-discrete element method," *International Journal of Solids and Structures*, vol. 136, pp. 150–167, 2018.

[102] H. Smoljanović, Ž. Nikolić, and N. Živaljić, "A combined finite–discrete numerical model for analysis of masonry structures," *Engineering fracture mechanics*, vol. 136, pp. 1–14, 2015.

[103] S. S. Ali and A. W. Page, "Finite element model for masonry subjected to concentrated loads," *Journal of structural engineering*, vol. 114, no. 8, pp. 1761–1784, 1988.

[104] M. Petracca, L. Pelà, R. Rossi, S. Zaghi, G. Camata, and E. Spacone, "Micro-scale continuous and discrete numerical models for nonlinear analysis of masonry shear walls," *Construction and Building Materials*, vol. 149, pp. 296–314, 2017.

[105] D. Addessi and E. Sacco, "Nonlinear analysis of masonry panels using a kinematic enriched plane state formulation," *International Journal of Solids and Structures*, vol. 90, pp. 194–214, 2016.

[106] R. Serpieri, M. Albarella, and E. Sacco, "A 3D microstructured cohesive–frictional interface model and its rational calibration for the analysis of masonry panels," *International Journal of Solids and Structures*, vol. 122, pp. 110–127, 2017.

[107] C. Baggio and P. Trovalusci, "Limit analysis for no-tension and frictional three-dimensional discrete systems," *Journal of Structural Mechanics*, vol. 26, no. 3, pp. 287–304, 1998.

[108] C. Baggio and P. Trovalusci, "Collapse behaviour of three-dimensional brick-block systems using non-linear programming," *Structural Engineering and Mechanics*, vol. 10, no. 2, p. 181, 2000.

[109] M. Ferris and F. Tin-Loi, "Limit analysis of frictional block assemblies as a mathematical program with complementarity constraints," *International Journal of Mechanical Sciences*, vol. 43, no. 1, pp. 209–224, 2001.

[110] D. Sutcliffe, H. Yu, and A. Page, "Lower bound limit analysis of unreinforced masonry shear walls," *Computers & Structures*, vol. 79, no. 14, pp. 1295–1312, 2001.

[111] A. Orduña and P. B. Lourenço, "Three-dimensional limit analysis of rigid blocks assemblages. Part I: Torsion failure on frictional interfaces and limit analysis formulation," *International Journal of Solids and Structures*, vol. 42, no. 18-19, pp. 5140–5160, 2005.

[112] A. Orduña and P. B. Lourenço, "Three-dimensional limit analysis of rigid blocks assemblages. Part II: Load-path following solution procedure and validation," *International Journal of Solids and Structures*, vol. 42, no. 18-19, pp. 5161–5180, 2005.

[113] M. Gilbert, C. Casapulla, and H. Ahmed, "Limit analysis of masonry block structures with non-associative frictional joints using linear programming," *Computers & structures*, vol. 84, no. 13-14, pp. 873–887, 2006.

[114] F. Portioli, C. Casapulla, L. Cascini, M. D'Aniello, and R. Landolfo, "Limit analysis by linear programming of 3D masonry structures with associative friction laws and torsion interaction effects," *Archive of Applied Mechanics*, vol. 83, no. 10, pp. 1415–1438, 2013.

[115] F. Portioli, C. Casapulla, M. Gilbert, and L. Cascini, "Limit analysis of 3D masonry block structures with non-associative frictional joints using cone programming," *Computers & Structures*, vol. 143, pp. 108–121, 2014.

[116] G. Milani, "3d upper bound limit analysis of multi-leaf masonry walls," *International Journal of Mechanical Sciences*, vol. 50, no. 4, pp. 817–836, 2008.

[117] G. Milani, K. Beyer, and A. Dazio, "Upper bound limit analysis of meso-mechanical spandrel models for the pushover analysis of 2d masonry frames," *Engineering Structures*, vol. 31, no. 11, pp. 2696–2710, 2009.

[118] G. Milani, F. Zuccarello, R. Olivito, and A. Tralli, "Heterogeneous upper-bound finite element limit analysis of masonry walls out-of-plane loaded," *Computational Mechanics*, vol. 40, no. 6, pp. 911–931, 2007.

[119] A. Cavicchi and L. Gambarotta, "Two-dimensional finite element upper bound limit analysis of masonry bridges," *Computers & structures*, vol. 84, no. 31-32, pp. 2316–2328, 2006.

[120] K. F. Abdulla, L. S. Cunningham, and M. Gillie, "Simulating masonry wall behaviour using a simplified micro-model approach," *Engineering Structures*, vol. 151, pp. 349–365, 2017.

[121] C. Zhai, X. Wang, J. Kong, S. Li, and L. Xie, "Numerical simulation of masonry-infilled rc frames using xfem," *Journal of Structural Engineering*, vol. 143, no. 10, p. 04017144, 2017.

[122] G. Del Piero, "Constitutive equation and compatibility of the external loads for linear elastic masonry-like materials," *Meccanica*, vol. 24, no. 3, pp. 150–162, 1989.

[123] G. Maier and A. Nappi, "A theory of no-tension discretized structural systems," *Engineering Structures*, vol. 12, no. 4, pp. 227–234, 1990.

[124] M. Angelillo, "A finite element approach to the study of no-tension structures," *Finite Elements in Analysis and Design*, vol. 17, no. 1, pp. 57–73, 1994.

[125] G. Alfano, L. Rosati, and N. Valoroso, "A numerical strategy for finite element analysis of no-tension materials," *International Journal for Numerical Methods in Engineering*, vol. 48, no. 3, pp. 317–350, 2000.

[126] M. Cuomo and G. Ventura, "A complementary energy formulation of no tension masonry-like solids," *Computer Methods in Applied Mechanics and Engineering*, vol. 189, no. 1, pp. 313–339, 2000.

[127] M. Lucchesi, C. Padovani, and G. Pasquinelli, "Thermodynamics of no-tension materials," *International Journal of Solids and Structures*, vol. 37, no. 45, pp. 6581–6604, 2000.

[128] M. Bruggi, "Finite element analysis of no–tension structures as a topology optimization problem," *Structural and Multidisciplinary Optimization*, vol. 50, no. 6, pp. 957–973, 2014.

[129] M. Bruggi and A. Taliercio, "Analysis of no-tension structures under monotonic loading through an energy-based method," *Computers & Structures*, vol. 159, pp. 14–25, 2015.

[130] M. Bruggi and A. Taliercio, "Analysis of 3D no-tension masonry-like walls," in *European Mechanics Society ESMC 2018*, 2018.

[131] A. Hillerborg, M. Modéer, and P.-E. Petersson, "Analysis of crack formation and crack growth in concrete by means of fracture mechanics and finite elements," *Cement and concrete research*, vol. 6, no. 6, pp. 773–781, 1976.

[132] J. G. Rots and R. De Borst, "Analysis of mixed-mode fracture in concrete," *Journal of Engineering Mechanics*, vol. 113, no. 11, pp. 1739–1758, 1987.

[133] A. Dragon and Z. Mroz, "A continuum model for plastic-brittle behaviour of rock and concrete," *International Journal of Engineering Science*, vol. 17, no. 2, pp. 121–137, 1979.

[134] K. Løland, "Continuous damage model for load-response estimation of concrete," *Cement and Concrete Research*, vol. 10, no. 3, pp. 395–402, 1980.

[135] J. Lubliner, J. Oliver, S. Oller, and E. Onate, "A plastic-damage model for concrete," *International Journal of Solids and Structures*, vol. 25, no. 3, pp. 299–326, 1989.

[136] J. Lee and G. L. Fenves, "Plastic-damage model for cyclic loading of concrete structures," *Journal of engineering mechanics*, vol. 124, no. 8, pp. 892–900, 1998.

[137] H. Lotfi and P. Shing, "An appraisal of smeared crack models for masonry shear wall analysis," *Computers & structures*, vol. 41, no. 3, pp. 413–425, 1991.

[138] J. Toti, V. Gattulli, and E. Sacco, "Nonlocal damage propagation in the dynamics of masonry elements," *Computers & Structures*, vol. 152, pp. 215–227, 2015.

[139] A. M. D'Altri, G. Castellazzi, and S. de Miranda, "Collapse investigation of the Arquata del Tronto medieval fortress after the 2016 Central Italy seismic sequence," *Journal of Building Engineering*, vol. 18, pp. 245–251, 2018.

[140] G. Bartoli, M. Betti, and A. Vignoli, "A numerical study on seismic risk assessment of historic masonry towers: A case study in San Gimignano," *Bulletin of Earthquake Engineering*, vol. 14, no. 6, pp. 1475–1518, 2016.

[141] G. Castellazzi, A. M. D'Altri, S. de Miranda, A. Chiozzi, and A. Tralli, "Numerical insights on the seismic behavior of a non-isolated historical masonry tower," *Bulletin of Earthquake Engineering*, vol. 16, no. 2, pp. 933–961, 2018.

[142] M. Valente and G. Milani, "Seismic assessment of historical masonry towers by means of simplified approaches and standard FEM," *Construction and Building Materials*, vol. 108, pp. 74–104, 2016.

[143] M. Betti and A. Vignoli, "Numerical assessment of the static and seismic behaviour of the basilica of Santa Maria all'Impruneta (Italy)," *Construction and Building Materials*, vol. 25, no. 12, pp. 4308–4324, 2011.

[144] G. Milani and M. Valente, "Failure analysis of seven masonry churches severely damaged during the 2012 Emilia-Romagna (Italy) earthquake: Non-linear dynamic analyses vs conventional static approaches," *Engineering Failure Analysis*, vol. 54, pp. 13–56, 2015.

[145] G. Fortunato, M. F. Funari, and P. Lonetti, "Survey and seismic vulnerability assessment of the baptistery of san giovanni in tumba (Italy)," *Journal of Cultural Heritage*, vol. 26, pp. 64–78, 2017.

[146] A. Elyamani, P. Roca, O. Caselles, and J. Clapes, "Seismic safety assessment of historical structures using updated numerical models: The case of Mallorca cathedral in spain," *Engineering Failure Analysis*, vol. 74, pp. 54–79, 2017.

[147] M. Betti and L. Galano, "Seismic analysis of historic masonry buildings: The vicarious palace in Pescia (Italy)," *Buildings*, vol. 2, no. 2, pp. 63–82, 2012.

[148] S. Tiberti, M. Acito, and G. Milani, "Comprehensive fe numerical insight into finale emilia castle behavior under 2012 emilia romagna seismic sequence: Damage causes and seismic vulnerability mitigation hypothesis," *Engineering Structures*, vol. 117, pp. 397–421, 2016.

[149] S. Degli Abbati, A. M. D'Altri, D. Ottonelli, G. Castellazzi, S. Catteri, S. de Miranda, and S. Lagomarsino, "Seismic assessment of interacting structural units in complex historic masonry constructions by nonlinear static analysis," *Computers & structures*, 2019 (In Press).

[150] L. Pelà, A. Aprile, and A. Benedetti, "Seismic assessment of masonry arch bridges," *Engineering Structures*, vol. 31, no. 8, pp. 1777–1788, 2009.

[151] P. Zampieri, M. A. Zanini, and C. Modena, "Simplified seismic assessment of multi-span masonry arch bridges," *Bulletin of Earthquake Engineering*, vol. 13, no. 9, pp. 2629–2646, 2015.

[152] S. Saloustros, L. Pelà, and M. Cervera, "A crack-tracking technique for localized cohesive–frictional damage," *Engineering Fracture Mechanics*, vol. 150, pp. 96–114, 2015.

[153] S. Saloustros, L. Pelà, M. Cervera, and P. Roca, "An enhanced finite element macro-model for the realistic simulation of localized cracks in masonry structures: A large-scale application," *International Journal of Architectural Heritage*, vol. 12, no. 3, pp. 432–447, 2018.

[154] P. B. Lourénço, R. De Borst, and J. G. Rots, "A plane stress softening plasticity model for orthotropic materials," *International Journal for Numerical Methods in Engineering*, vol. 40, no. 21, pp. 4033–4057, 1997.

[155] P. B. Lourénço, J. G. Rots, and J. Blaauwendraad, "Continuum model for masonry: Parameter estimation and validation," *Journal of structural engineering*, vol. 124, no. 6, pp. 642–652, 1998.

[156] J. Lopez, S. Oller, E. Onate, and J. Lubliner, "A homogeneous constitutive model for masonry," *International Journal for Numerical Methods in Engineering*, vol. 46, no. 10, pp. 1651–1671, 1999.

[157] L. Berto, A. Saetta, R. Scotta, and R. Vitaliani, "An orthotropic damage model for masonry structures," *International Journal for Numerical Methods in Engineering*, vol. 55, no. 2, pp. 127–157, 2002.

[158] L. Pelà, M. Cervera, and P. Roca, "Continuum damage model for orthotropic materials: Application to masonry," *Computer Methods in Applied Mechanics and Engineering*, vol. 200, no. 9-12, pp. 917–930, 2011.

[159] L. Pelà, M. Cervera, and P. Roca, "An orthotropic damage model for the analysis of masonry structures," *Construction and Building Materials*, vol. 41, pp. 957–967, 2013.

[160] L. Pelà, M. Cervera, S. Oller, and M. Chiumenti, "A localized mapped damage model for orthotropic materials," *Engineering Fracture Mechanics*, vol. 124, pp. 196–216, 2014.

[161] E. Reyes, J. Gálvez, M. Casati, D. Cendón, J. Sancho, and J. Planas, "An embedded cohesive crack model for finite element analysis of brickwork masonry fracture," *Engineering Fracture Mechanics*, vol. 76, no. 12, pp. 1930–1944, 2009.

[162] G. Milani, S. Casolo, A. Naliato, and A. Tralli, "Seismic assessment of a medieval masonry tower in northern Italy by limit, nonlinear static, and full dynamic analyses," *International Journal of Architectural Heritage*, vol. 6, no. 5, pp. 489–524, 2012.

[163] B. Pantò, F. Cannizzaro, S. Caddemi, and I. Caliò, "3d macro-element modelling approach for seismic assessment of historical masonry churches," *Advances in Engineering Software*, vol. 97, pp. 40–59, 2016.

[164] B. Pantò, I. Caliò, and P. Lourenço, "A 3D discrete macro-element for modelling the out-of-plane behaviour of infilled frame structures," *Engineering Structures*, vol. 175, pp. 371–385, 2018.

[165] A. Anthoine, "Derivation of the in-plane elastic characteristics of masonry through homogenization theory," *International Journal of Solids and Structures*, vol. 32, no. 2, pp. 137–163, 1995.

[166] N. Cavalagli, F. Cluni, and V. Gusella, "Strength domain of non-periodic masonry by homogenization in generalized plane state," *European Journal of Mechanics-A/Solids*, vol. 30, no. 2, pp. 113–126, 2011.

[167] A. Taliercio, "Closed-form expressions for the macroscopic in-plane elastic and creep coefficients of brick masonry," *International Journal of Solids and Structures*, vol. 51, no. 17, pp. 2949–2963, 2014.

[168] I. Stefanou, K. Sab, and J.-V. Heck, "Three dimensional homogenization of masonry structures with building blocks of finite strength: A closed form strength domain," *International Journal of Solids and Structures*, vol. 54, pp. 258–270, 2015.

[169] G. Milani, "Simple lower bound limit analysis homogenization model for in- and out-of-plane loaded masonry walls," *Construction and Building Materials*, vol. 25, no. 12, pp. 4426–4443, 2011.

[170] E. Sacco, D. Addessi, and K. Sab, "New trends in mechanics of masonry," *Meccanica*, vol. 53, no. 7, pp. 1565–1569, 2018.

[171] E. Bertolesi, G. Milani, and S. Casolo, "Homogenization towards a mechanistic rigid body and spring model (HRBSM) for the non-linear dynamic analysis of 3D masonry structures," *Meccanica*, vol. 53, no. 7, pp. 1819–1855, 2018.

[172] M. Petracca, L. Pelà, R. Rossi, S. Oller, G. Camata, and E. Spacone, "Regularization of first order computational homogenization for multiscale analysis of masonry structures," *Computational mechanics*, vol. 57, no. 2, pp. 257–276, 2016.

[173] L. Leonetti, F. Greco, P. Trovalusci, R. Luciano, and R. Masiani, "A multi-scale damage analysis of periodic composites using a couple-stress/Cauchy multidomain model: Application to masonry structures," *Composites Part B: Engineering*, vol. 141, pp. 50–59, 2018.

[174] S. Pietruszczak and X. Niu, "A mathematical description of macroscopic behaviour of brick masonry," *International Journal of Solids and Structures*, vol. 29, no. 5, pp. 531–546, 1992.

[175] S. Briccoli Bati, G. Ranocchiai, and L. Rovero, "A micromechanical model for linear homogenization of brick masonry," *Materials and Structures*, vol. 32, no. 1, pp. 22–30, 1999.

[176] R. Masiani and P. Trovalusci, "Cosserat and Cauchy materials as continuum models of brick masonry," *Meccanica*, vol. 31, no. 4, pp. 421–432, 1996.

[177] I. Stefanou, J. Sulem, and I. Vardoulakis, "Three-dimensional Cosserat homogenization of masonry structures: Elasticity," *Acta Geotechnica*, vol. 3, no. 1, pp. 71–83, 2008.

[178] A. Cecchi and K. Sab, "A multi-parameter homogenization study for modeling elastic masonry," *European Journal of Mechanics-A/Solids*, vol. 21, no. 2, pp. 249–268, 2002.

[179] A. Cecchi and K. Sab, "A homogenized reissner–mindlin model for orthotropic periodic plates: Application to brickwork panels," *International Journal of Solids and Structures*, vol. 44, no. 18-19, pp. 6055–6079, 2007.

[180] M. Mistler, A. Anthoine, and C. Butenweg, "In-plane and out-of-plane homogenisation of masonry," *Computers & Structures*, vol. 85, no. 17-18, pp. 1321–1330, 2007.

[181] A. Drougkas, P. Roca, and C. Molins, "Analytical micro-modeling of masonry periodic unit cells–elastic properties," *International Journal of Solids and Structures*, vol. 69, pp. 169–188, 2015.

[182] A. Cecchi, G. Milani, and A. Tralli, "Validation of analytical multiparameter homogenization models for out-of-plane loaded masonry walls by means of the finite element method," *Journal of Engineering Mechanics*, vol. 131, no. 2, pp. 185–198, 2005.

[183] M. Kawa, S. Pietruszczak, and B. Shieh-Beygi, "Limit states for brick masonry based on homogenization approach," *International Journal of Solids and Structures*, vol. 45, no. 3-4, pp. 998–1016, 2008.

[184] P. De Buhan and G. De Felice, "A homogenization approach to the ultimate strength of brick masonry," *Journal of the Mechanics and Physics of Solids*, vol. 45, no. 7, pp. 1085–1104, 1997.

[185] A. Zucchini and P. Lourenço, "A micro-mechanical model for the homogenisation of masonry," *International Journal of Solids and Structures*, vol. 39, no. 12, pp. 3233–3255, 2002.

[186] A. Zucchini and P. B. Lourenço, "A coupled homogenisation–damage model for masonry cracking," *Computers & structures*, vol. 82, no. 11-12, pp. 917–929, 2004.

[187] X. Wei and H. Hao, "Numerical derivation of homogenized dynamic masonry material properties with strain rate effects," *International Journal of Impact Engineering*, vol. 36, no. 3, pp. 522–536, 2009.

[188] A. Cecchi and K. Sab, "Discrete and continuous models for in plane loaded random elastic brickwork," *European Journal of Mechanics-A/Solids*, vol. 28, no. 3, pp. 610–625, 2009.

[189] N. Cavalagli, F. Cluni, and V. Gusella, "Evaluation of a statistically equivalent periodic unit cell for a quasi-periodic masonry," *International Journal of Solids and Structures*, vol. 50, no. 25-26, pp. 4226–4240, 2013.

[190] G. Milani, P. B. Lourenço, and A. Tralli, "Homogenised limit analysis of masonry walls, Part I: Failure surfaces," *Computers & structures*, vol. 84, no. 3-4, pp. 166–180, 2006.

[191] G. Milani, P. Lourenço, and A. Tralli, "Homogenization approach for the limit analysis of out-of-plane loaded masonry walls," *Journal of structural engineering*, vol. 132, no. 10, pp. 1650–1663, 2006.

[192] A. Cecchi, G. Milani, and A. Tralli, "A reissner–mindlin limit analysis model for out-of-plane loaded running bond masonry walls," *International Journal of Solids and Structures*, vol. 44, no. 5, pp. 1438–1460, 2007.

[193] A. Cecchi and G. Milani, "A kinematic fe limit analysis model for thick english bond masonry walls," *International Journal of Solids and Structures*, vol. 45, no. 5, pp. 1302–1331, 2008.

[194] M. Godio, I. Stefanou, K. Sab, J. Sulem, and S. Sakji, "A limit analysis approach based on Cosserat continuum for the evaluation of the in-plane strength of discrete media: Application to masonry," *European Journal of Mechanics-A/Solids*, vol. 66, pp. 168–192, 2017.

[195] G. Milani, P. B. Lourenço, and A. Tralli, "Homogenised limit analysis of masonry walls, Part II: Structural examples," *Computers & structures*, vol. 84, no. 3-4, pp. 181–195, 2006.

[196] G. Milani, P. Lourenço, and A. Tralli, "3d homogenized limit analysis of masonry buildings under horizontal loads," *Engineering Structures*, vol. 29, no. 11, pp. 3134–3148, 2007.

[197] S. Casolo, "Modelling in-plane micro-structure of masonry walls by rigid elements," *International Journal of Solids and Structures*, vol. 41, no. 13, pp. 3625–3641, 2004.

[198] S. Casolo and F. Pena, "Rigid element model for in-plane dynamics of masonry walls considering hysteretic behaviour and damage," *Earthquake engineering & structural dynamics*, vol. 36, no. 8, pp. 1029–1048, 2007.

[199] L. C. Silva, P. B. Lourenço, and G. Milani, "Nonlinear discrete homogenized model for out-of-plane loaded masonry walls," *Journal of Structural Engineering*, vol. 143, no. 9, p. 04017099, 2017.

[200] E. Papa, "A unilateral damage model for masonry based on a homogenisation procedure," *Mechanics of Cohesive-frictional Materials: An International Journal on Experiments, Modelling and Computation of Materials and Structures*, vol. 1, no. 4, pp. 349–366, 1996.

[201] R. Luciano and E. Sacco, "Homogenization technique and damage model for old masonry material," *International Journal of Solids and Structures*, vol. 34, no. 24, pp. 3191–3208, 1997.

[202] R. Luciano and E. Sacco, "A damage model for masonry structures," *European Journal of Mechanics-A/Solids*, vol. 17, no. 2, pp. 285–303, 1998.

[203] L. Gambarotta and S. Lagomarsino, "Damage models for the seismic response of brick masonry shear walls. Part II: The continuum model and its applications," *Earthquake engineering & structural dynamics*, vol. 26, no. 4, pp. 441–462, 1997.

[204] S. Pietruszczak and R. Ushaksaraei, "Description of inelastic behaviour of structural masonry," *International Journal of Solids and Structures*, vol. 40, no. 15, pp. 4003–4019, 2003.

[205] C. Calderini and S. Lagomarsino, "A micromechanical inelastic model for historical masonry," *Journal of Earthquake Engineering*, vol. 10, no. 04, pp. 453–479, 2006.

[206] A. Zucchini and P. B. Lourenço, "A micro-mechanical homogenisation model for masonry: Application to shear walls," *International Journal of Solids and Structures*, vol. 46, no. 3-4, pp. 871–886, 2009.

[207] E. Sacco, "A nonlinear homogenization procedure for periodic masonry," *European Journal of Mechanics-A/Solids*, vol. 28, no. 2, pp. 209–222, 2009.

[208] S. Marfia and E. Sacco, "Multiscale damage contact-friction model for periodic masonry walls," *Computer Methods in Applied Mechanics and Engineering*, vol. 205, pp. 189–203, 2012.

[209] T. J. Massart, R. H. J. Peerlings, and M. G. D. Geers, "An enhanced multiscale approach for masonry wall computations with localization of damage," *International Journal for Numerical Methods in Engineering*, vol. 69, no. 5, pp. 1022–1059, 2007.

[210] A. Bacigalupo and L. Gambarotta, "Second-order computational homogenization of heterogeneous materials with periodic microstructure," *ZAMM-Journal of Applied Mathematics and Mechanics/Zeitschrift für Angewandte Mathematik und Mechanik*, vol. 90, no. 10-11, pp. 796–811, 2010.

[211] A. Bacigalupo and L. Gambarotta, "Computational two-scale homogenization of periodic masonry: Characteristic lengths and dispersive waves," *Computer Methods in Applied Mechanics and Engineering*, vol. 213, pp. 16–28, 2012.

[212] D. Addessi, S. Marfia, E. Sacco, and J. Toti, "Modeling approaches for masonry structures," *The Open Civil Engineering Journal*, vol. 8, no. 1, 2014.

[213] G. Salerno and G. de Felice, "Continuum modeling of periodic brickwork," *International Journal of Solids and Structures*, vol. 46, no. 5, pp. 1251–1267, 2009.

[214] S. Casolo, "Macroscopic modelling of structured materials: Relationship between orthotropic Cosserat continuum and rigid elements," *International Journal of Solids and Structures*, vol. 43, no. 3-4, pp. 475–496, 2006.

[215] D. Addessi, E. Sacco, and A. Paolone, "Cosserat model for periodic masonry deduced by nonlinear homogenization," *European Journal of Mechanics-A/Solids*, vol. 29, no. 4, pp. 724–737, 2010.

[216] M. L. De Bellis and D. Addessi, "A Cosserat based multi-scale model for masonry structures," *International Journal for Multiscale Computational Engineering*, vol. 9, no. 5, p. 543, 2011.

[217] D. Addessi and E. Sacco, "A multi-scale enriched model for the analysis of masonry panels," *International Journal of Solids and Structures*, vol. 49, no. 6, pp. 865–880, 2012.

[218] B. Mercatoris and T. Massart, "A coupled two-scale computational scheme for the failure of periodic quasi-brittle thin planar shells and its application to masonry," *International Journal for Numerical Methods in Engineering*, vol. 85, no. 9, pp. 1177–1206, 2011.

[219] M. Petracca, L. Pelà, R. Rossi, S. Oller, G. Camata, and E. Spacone, "Multi-scale computational first order homogenization of thick shells for the analysis of out-of-plane loaded masonry walls," *Computer Methods in Applied Mechanics and Engineering*, vol. 315, pp. 273–301, 2017.

[220] S. Brasile, R. Casciaro, and G. Formica, "Multilevel approach for brick masonry walls–part I: A numerical strategy for the nonlinear analysis," *Computer Methods in Applied Mechanics and Engineering*, vol. 196, no. 49-52, pp. 4934–4951, 2007.

[221] S. Brasile, R. Casciaro, and G. Formica, "Multilevel approach for brick masonry walls–part II: On the use of equivalent continua," *Computer Methods in Applied Mechanics and Engineering*, vol. 196, no. 49-52, pp. 4801–4810, 2007.

[222] E. Reccia, L. Leonetti, P. Trovalusci, and A. Cecchi, "A multi-scale/multi-domain model for the failure analysis of masonry walls: A validation with a combined FEM/DEM approach.," *International Journal for Multiscale Computational Engineering*, 2018.

[223] F. Greco, L. Leonetti, R. Luciano, and P. N. Blasi, "An adaptive multiscale strategy for the damage analysis of masonry modeled as a composite material," *Composite Structures*, vol. 153, pp. 972–988, 2016.

[224] O. Lloberas-Valls, D. Rixen, A. Simone, and L. Sluys, "Multiscale domain decomposition analysis of quasi-brittle heterogeneous materials," *International Journal for Numerical Methods in Engineering*, vol. 89, no. 11, pp. 1337–1366, 2012.

[225] D. O'Dwyer, "Funicular analysis of masonry vaults," *Computers & Structures*, vol. 73, no. 1-5, pp. 187–197, 1999.

[226] A. Andreu, L. Gil, and P. Roca, "Computational analysis of masonry structures with a funicular model," *Journal of Engineering Mechanics*, vol. 133, no. 4, pp. 473–480, 2007.

[227] P. Block, T. Ciblac, and J. Ochsendorf, "Real-time limit analysis of vaulted masonry buildings," *Computers & structures*, vol. 84, no. 29-30, pp. 1841–1852, 2006.

[228] P. Block and J. Ochsendorf, "Thrust network analysis: A new methodology for three-dimensional equilibrium," *Journal of the International Association for shell and spatial structures*, vol. 48, no. 3, pp. 167–173, 2007.

[229] P. Block and L. Lachauer, "Three-dimensional (3d) equilibrium analysis of gothic masonry vaults," *International Journal of Architectural Heritage*, vol. 8, no. 3, pp. 312–335, 2014.

[230] P. Block and L. Lachauer, "Three-dimensional funicular analysis of masonry vaults," *Mechanics Research Communications*, vol. 56, pp. 53–60, 2014.

[231] M. Fantin and T. Ciblac, "Extension of thrust network analysis with joints consideration and new equilibrium states," *International Journal of Space Structures*, vol. 31, no. 2-4, pp. 190–202, 2016.

[232] F. Fraternali, "A thrust network approach to the equilibrium problem of unreinforced masonry vaults via polyhedral stress functions," *Mechanics Research Communications*, vol. 37, no. 2, pp. 198–204, 2010.

[233] M. Angelillo, E. Babilio, and A. Fortunato, "Singular stress fields for masonry-like vaults," *Continuum Mechanics and Thermodynamics*, vol. 25, no. 2-4, pp. 423–441, 2013.

[234] M. Angelillo, "Static analysis of a guastavino helical stair as a layered masonry shell," *Composite Structures*, vol. 119, pp. 298–304, 2015.

[235] A. Fraddosio, N. Lepore, and M. D. Piccioni, "Lower bound limit analysis of masonry vaults under general load conditions," in *Structural Analysis of Historical Constructions*, pp. 1090–1098, Springer, 2019.

[236] F. Marmo and L. Rosati, "Reformulation and extension of the thrust network analysis," *Computers & Structures*, vol. 182, pp. 104–118, 2017.

[237] F. Marmo, D. Masi, and L. Rosati, "Thrust network analysis of masonry helical staircases," *International Journal of Architectural Heritage*, pp. 1–21, 2018.

[238] A. M. D'Altri, G. Castellazzi, S. de Miranda, and A. Tralli, "Seismic-induced damage in historical masonry vaults: A case-study in the 2012 Emilia earthquake-stricken area," *Journal of Building Engineering*, vol. 13, pp. 224–243, 2017.

[239] A. Giuffrè, *Letture sulla meccanica delle murature storiche*. Kappa, 1991.

[240] "Ordinanza del Presidente del Consiglio dei Ministri (OPCM). Norme tecniche per il progetto, la valutazione e l'adeguamento sismico degli edifici," 2005.

[241] "Circolare 2009. Circolare n. 617 del 02/02/2009. Istruzioni per l'applicazione delle nuove Norme Tecniche per le Costruzioni di cui al D.M. del 14/01/2008."

[242] "NTC2008, Norme Tecniche per le Costruzioni, D.M. 14/01/2008."

[243] G. Milani, "Upper bound sequential linear programming mesh adaptation scheme for collapse analysis of masonry vaults," *Advances in Engineering Software*, vol. 79, pp. 91–110, 2015.

[244] A. Chiozzi, G. Milani, and A. Tralli, "A genetic algorithm NURBS-based new approach for fast kinematic limit analysis of masonry vaults," *Computers & Structures*, vol. 182, pp. 187–204, 2017.

[245] A. Chiozzi, G. Milani, N. Grillanda, and A. Tralli, "A fast and general upper-bound limit analysis approach for out-of-plane loaded masonry walls," *Meccanica*, vol. 53, no. 7, pp. 1875–1898, 2018.

[246] E. Quagliarini, G. Maracchini, and F. Clementi, "Uses and limits of the equivalent frame model on existing unreinforced masonry buildings for assessing their seismic risk: a review," *Journal of Building Engineering*, vol. 10, pp. 166–182, 2017.

[247] N. Augenti, "Seismic behaviour of irregular masonry walls," in *Proceedings of the 1st European Conference on Earthquake Engineering and Seismology*, 2006.

[248] M. Berti, L. Salvatori, M. Orlando, and P. Spinelli, "Unreinforced masonry walls with irregular opening layouts: reliability of equivalent-frame modelling for seismic vulnerability assessment," *Bulletin of earthquake engineering*, vol. 15, no. 3, pp. 1213–1239, 2017.

[249] B. Calderoni, E. A. Cordasco, A. Sandoli, V. Onotri, and G. Tortoriello, "Problematiche di modellazione strutturale di edifici in muratura esistenti soggetti ad azioni sismiche in relazione all'utilizzo di software commerciali," *Atti del XVI convegno ANIDIS. L'Aquila. Italia*, 2015.

[250] M. Dolce, "Schematizzazione e modellazione degli edifici in muratura soggetti ad azioni sismiche," *L'Industria delle costruzioni*, vol. 25, no. 242, pp. 44–57, 1991.

[251] S. Lagomarsino, A. Penna, A. Galasco, and S. Cattari, "Tremuri program: An equivalent frame model for the nonlinear seismic analysis of masonry buildings," *Engineering Structures*, vol. 56, pp. 1787–1799, 2013.

[252] F. L. Moon, T. Yi, R. T. Leon, and L. F. Kahn, "Recommendations for seismic evaluation and retrofit of low-rise URM structures," *Journal of structural engineering*, vol. 132, no. 5, pp. 663–672, 2006.

[253] F. Parisi and N. Augenti, "Seismic capacity of irregular unreinforced masonry walls with openings," *Earthquake Engineering & Structural Dynamics*, vol. 42, no. 1, pp. 101–121, 2013.

[254] F. Parisi, G. P. Lignola, N. Augenti, A. Prota, and G. Manfredi, "Rocking response assessment of in-plane laterally-loaded masonry walls with openings," *Engineering Structures*, vol. 56, pp. 1234–1248, 2013.

[255] S. Lagomarsino, D. Camilletti, S. Cattari, and S. Marino, "In plane seismic response of irregular URM walls through equivalent frame and finite element models," in *Recent Advances in Earthquake Engineering in Europe: 16th European Conference on Earthquake Engineering-Thessaloniki 2018*, pp. 123–151, Springer, 2018.

[256] R. Siano, P. Roca, G. Camata, L. Pelà, V. Sepe, E. Spacone, and M. Petracca, "Numerical investigation of non-linear equivalent-frame models for regular masonry walls," *Engineering Structures*, vol. 173, pp. 512–529, 2018.

[257] M. Tomaževič, "The computer program POR," *Report ZRMK*, 1978.

[258] B. Calderoni, P. Marone, and M. Pagano, "Modelli per la verifica statica degli edifici in muratura in zona sismica," *Ingegneria sismica*, vol. 3, pp. 19–27, 1987.

[259] G. Magenes and A. Fontana, "Simplified non-linear seismic analysis of masonry buildings," in *Proc. Br. Masonry Soc. No. 8*, pp. 190–195, 1998.

[260] A. J. Kappos, G. G. Penelis, and C. G. Drakopoulos, "Evaluation of simplified models for lateral load analysis of unreinforced masonry buildings," *Journal of structural Engineering*, vol. 128, no. 7, pp. 890–897, 2002.

[261] P. Roca, C. Molins, and A. R. Marí, "Strength capacity of masonry wall structures by the equivalent frame method," *Journal of structural engineering*, vol. 131, no. 10, pp. 1601–1610, 2005.

[262] G. G. Penelis, "An efficient approach for pushover analysis of unreinforced masonry (urm) structures," *Journal of Earthquake Engineering*, vol. 10, no. 03, pp. 359–379, 2006.

[263] Y. Belmouden and P. Lestuzzi, "An equivalent frame model for seismic analysis of masonry and reinforced concrete buildings," *Construction and Building Materials*, vol. 23, no. 1, pp. 40–53, 2009.

[264] L. Pasticier, C. Amadio, and M. Fragiacomo, "Non-linear seismic analysis and vulnerability evaluation of a masonry building by means of the sap2000 v. 10 code," *Earthquake engineering & structural dynamics*, vol. 37, no. 3, pp. 467–485, 2008.

[265] E. Grande, M. Imbimbo, and E. Sacco, "A beam finite element for nonlinear analysis of masonry elements with or without fiber-reinforced plastic (frp) reinforcements," *International Journal of Architectural Heritage*, vol. 5, no. 6, pp. 693–716, 2011.

[266] D. Addessi, A. Mastrandrea, and E. Sacco, "An equilibrated macro-element for nonlinear analysis of masonry structures," *Engineering Structures*, vol. 70, pp. 82–93, 2014.

[267] D. Addessi, D. Liberatore, and R. Masiani, "Force-based beam finite element (fe) for the pushover analysis of masonry buildings," *International Journal of Architectural Heritage*, vol. 9, no. 3, pp. 231–243, 2015.

[268] D. Liberatore and D. Addessi, "Strength domains and return algorithm for the lumped plasticity equivalent frame model of masonry structures," *Engineering Structures*, vol. 91, pp. 167–181, 2015.

[269] S. Lagomarsino, A. Penna, A. Galasco, and S. Cattari, "TREMURI program: Seismic analyses of 3D masonry buildings," *Release 2.0, University of Genoa (mailto: tremuri@gmail. com)*, 2012.

[270] S. Cattari and S. Lagomarsino, "Masonry structures," 2013.

[271] S. Cattari, D. Camilletti, S. Lagomarsino, S. Bracchi, M. Rota, and A. Penna, "Masonry italian code-conforming buildings. part 2: nonlinear modelling and time-history analysis," *Journal of Earthquake Engineering*, vol. 22, no. sup2, pp. 2010–2040, 2018.

[272] E. Raka, E. Spacone, V. Sepe, and G. Camata, "Advanced frame element for seismic analysis of masonry structures: Model formulation and validation," *Earthquake Engineering & Structural Dynamics*, vol. 44, no. 14, pp. 2489–2506, 2015.

[273] S.-Y. Chen, F. Moon, and T. Yi, "A macroelement for the nonlinear analysis of in-plane unreinforced masonry piers," *Engineering Structures*, vol. 30, no. 8, pp. 2242–2252, 2008.

[274] L. Gambarotta and S. Lagomarsino, "On the dynamic response of masonry panels," in *Masonry Mechanics between theory and practice, Proc. Nat. Conf., Messina, 18-20 september 1996*, pp. 451–462, 1996.

[275] A. Brencich and S. Lagomarsino, "A macroelement dynamic model for masonry shear walls," in *Computer methods in structural masonry*, pp. 67–75, 1998.

[276] A. Penna, S. Lagomarsino, and A. Galasco, "A nonlinear macroelement model for the seismic analysis of masonry buildings," *Earthquake Engineering & Structural Dynamics*, vol. 43, no. 2, pp. 159–179, 2014.

[277] I. Caliò, M. Marletta, and B. Pantò, "A new discrete element model for the evaluation of the seismic behaviour of unreinforced masonry buildings," *Engineering Structures*, vol. 40, pp. 327–338, 2012.

[278] I. Caliò and B. Pantò, "A macro-element modelling approach of infilled frame structures," *Computers & Structures*, vol. 143, pp. 91–107, 2014.

[279] C. Chácara, F. Cannizzaro, B. Pantò, I. Caliò, and P. B. Lourenço, "Assessment of the dynamic response of unreinforced masonry structures using a macroelement modeling approach," *Earthquake Engineering & Structural Dynamics*, 2018.

[280] G. Rinaldin, C. Amadio, and L. Macorini, "A macro-model with nonlinear springs for seismic analysis of urm buildings," *Earthquake Engineering & Structural Dynamics*, vol. 45, no. 14, pp. 2261–2281, 2016.

[281] A. A. Mobarake, M. Khanmohammadi, and S. Mirghaderi, "A new discrete macro-element in an analytical platform for seismic assessment of unreinforced masonry buildings," *Engineering Structures*, vol. 152, pp. 381–396, 2017.

[282] H. Xu, C. Gentilini, Z. Yu, H. Wu, and S. Zhao, "A unified model for the seismic analysis of brick masonry structures," *Construction and Building Materials*, vol. 184, pp. 733–751, 2018.

[283] J. Martínez, A. Soria-Medina, P. Arias, and A. F. Buffara-Antunes, "Automatic processing of terrestrial laser scanning data of building façades," *Automation in Construction*, vol. 22, pp. 298–305, 2012.

[284] M. Stavroulaki, B. Riveiro, G. Drosopoulos, M. Solla, P. Koutsianitis, and G. E. Stavroulakis, "Modelling and strength evaluation of masonry bridges using terrestrial photogrammetry and finite elements," *Advances in Engineering Software*, vol. 101, pp. 136–148, 2016.

[285] C. Ordóñez, J. Martínez, P. Arias, and J. Armesto, "Measuring building façades with a low-cost close-range photogrammetry system," *Automation in Construction*, vol. 19, no. 6, pp. 742–749, 2010.

[286] A. D. Styliadis, "Digital documentation of historical buildings with 3-d modeling functionality," *Automation in Construction*, vol. 16, no. 4, pp. 498–510, 2007.

[287] B. Riveiro, M. Solla, I. De Arteaga, P. Arias, and P. Morer, "A novel approach to evaluate masonry arch stability on the basis of limit analysis theory and non-destructive geometric characterization," *Automation in construction*, vol. 31, pp. 140–148, 2013.

[288] G. Milani, Y. W. Esquivel, P. B. Lourenço, B. Riveiro, and D. V. Oliveira, "Characterization of the response of quasi-periodic masonry: Geometrical investigation, homogenization and application to the Guimarães castle, Portugal," *Engineering Structures*, vol. 56, pp. 621–641, 2013.

[289] S. Saloustros, L. Pelà, P. Roca, and J. Portal, "Numerical analysis of structural damage in the church of the Poblet monastery," *Engineering Failure Analysis*, vol. 48, pp. 41–61, 2015.

[290] L. Kudela, U. Almac, S. Kollmannsberger, and E. Rank, "Direct numerical analysis of historical structures represented by point clouds," in *Euro-Mediterranean Conference*, pp. 64–75, Springer, 2018.

[291] A. Guarnieri, N. Milan, and A. Vettore, "Monitoring of complex structure for structural control using terrestrial laser scanning (TLS) and photogrammetry," *International Journal of Architectural Heritage*, vol. 7, no. 1, pp. 54–67, 2013.

[292] I. Lubowiecka, J. Armesto, P. Arias, and H. Lorenzo, "Historic bridge modelling using laser scanning, ground penetrating radar and finite element methods in the context of structural dynamics," *Engineering Structures*, vol. 31, no. 11, pp. 2667–2676, 2009.

[293] L. Truong-Hong and D. F. Laefer, "Validating computational models from laser scanning data for historic façades," *Journal of Testing and Evaluation*, vol. 41, no. 3, pp. 481–496, 2013.

[294] L. Truong-Hong and D. F. Laefer, "Octree-based, automatic building façade generation from LiDAR data," *Computer-Aided Design*, vol. 53, pp. 46–61, 2014.

[295] T. Hinks, H. Carr, L. Truong-Hong, and D. F. Laefer, "Point cloud data conversion into solid models via point-based voxelization," *Journal of Surveying Engineering*, vol. 139, no. 2, pp. 72–83, 2012.

[296] M. Korumaz, M. Betti, A. Conti, G. Tucci, G. Bartoli, V. Bonora, A. G. Korumaz, and L. Fiorini, "An integrated terrestrial laser scanner (TLS), deviation analysis (DA) and finite element (FE) approach for health assessment of historical structures. A minaret case study," *Engineering Structures*, vol. 153, pp. 224–238, 2017.

[297] J. Sienz, I. Szarvasy, E. Hinton, and M. Andrade, "Computational modelling of 3D objects by using fitting techniques and subsequent mesh generation," *Computers & Structures*, vol. 78, no. 1-3, pp. 397–413, 2000.

[298] A. Borri and A. Grazini, "Diagnostic analysis of the lesions and stability of Michelangelo's David," *Journal of Cultural Heritage*, vol. 7, no. 4, pp. 273–285, 2006.

[299] H. Edelsbrunner, D. Kirkpatrick, and R. Seidel, "On the shape of a set of points in the plane," *IEEE Transactions on information theory*, vol. 29, no. 4, pp. 551–559, 1983.

[300] A. Moreira and M. Y. Santos, "Concave hull: A k-nearest neighbours approach for the computation of the region occupied by a set of points," 2007.

[301] G. Castellazzi, P. Krysl, L. Rojas, and T. W. Cranford, "Assessment of the effect of natural and anthropogenic aquatic noise on vaquita (Phocoena sinus) through a numerical simulation," in *The Effects of Noise on Aquatic Life*, pp. 307–309, Springer, 2012.

[302] G. Taubin, "Curve and surface smoothing without shrinkage," in *Computer Vision, 1995. Proceedings., Fifth International Conference on*, pp. 852–857, IEEE, 1995.

[303] L. Scognamiglio, L. Margheriti, F. M. Mele, E. Tinti, A. Bono, P. De Gori, V. Lauciani, F. P. Lucente, A. G. Mandiello, C. Marcocci, *et al.*, "The 2012 Pianura Padana Emiliana seimic sequence: Locations, moment tensors and magnitudes," *Annals of Geophysics*, vol. 55, no. 4, 2012.

[304] S. Cattari, S. D. Abbati, D. Ferretti, S. Lagomarsino, D. Ottonelli, and A. Tralli, "Damage assessment of fortresses after the 2012 Emilia earthquake (Italy)," *Bulletin of Earthquake Engineering*, vol. 12, no. 5, pp. 2333–2365, 2013.

[305] G. Castellazzi, A. M. D'Altri, S. de Miranda, F. Ubertini, G. Bitelli, A. Lambertini, I. Selvaggi, and A. Tralli, "A mesh generation method for historical monumental buildings: An innovative approach," in *ECCOMAS congress 2016—Proceedings of the 7th European congress on computational methods in applied sciences and engineering*, pp. 409–416, 2016.

[306] E. Bassoli, L. Vincenzi, A. M. D'Altri, S. de Miranda, M. Forghieri, and G. Castellazzi, "Ambient vibration-based finite element model updating of an earthquake-damaged masonry tower," *Structural Control and Health Monitoring*, vol. 25, no. 5, p. e2150, 2018.

[307] M. Kazhdan and H. Hoppe, "Screened Poisson surface reconstruction," *ACM Transactions on Graphics (ToG)*, vol. 32, no. 3, p. 29, 2013.

[308] *Abaqus 6.14 Documentation–Theory Guide, Dassault Systèmes*.

[309] S. Fang and H. Chen, "Hardware accelerated voxelization," *Computers & Graphics*, vol. 24, no. 3, pp. 433 – 442, 2000.

[310] W. Jakob, M. Tarini, D. Panozzo, and O. Sorkine-Hornung, "Instant field-aligned meshes.," *ACM Transactions on Graphics*, vol. 34, no. 6, pp. 189–1, 2015.

[311] S. G. Barsanti and G. Guidi, "A geometric processing workflow for transforming reality-based 3d models in volumetric meshes suitable for fea," *The International Archives of Photogrammetry, Remote Sensing and Spatial Information Sciences*, vol. 42, p. 331, 2017.

[312] D. F. Renn, *Caerphilly Castle*. Cadw: Welsh Historic Monuments, 1989.

[313] O. Prizeman, V. Sarhosis, A. M. D'Altri, C. J. Whitman, and G. Muratore, "Modelling from the past: the leaning southwest tower of Caerphilly castle 1539-2015," *ISPRS Annals of Photogrammetry, Remote Sensing and Spatial Information Sciences*, vol. 4, pp. 221–227, 2017.

[314] E. Coïsson, D. Ferretti, and E. Lenticchia, "Analysis of damage mechanisms suffered by Italian fortified buildings hit by earthquakes in the last 40 years," *Bulletin of Earthquake Engineering*, vol. 15, no. 12, pp. 5139–5166, 2017.

[315] P. Fajfar, "Analysis in seismic provisions for buildings: Past, present and future," *Bulletin of Earthquake Engineering*, vol. 16, no. 7, pp. 2567–2608, 2017.

[316] F. Minghini, E. Bertolesi, A. Del Grosso, G. Milani, and A. Tralli, "Modal pushover and response history analyses of a masonry chimney before and after shortening," *Engineering Structures*, vol. 110, pp. 307–324, 2016.

[317] F. Minghini, G. Milani, and A. Tralli, "Seismic risk assessment of a 50m high masonry chimney using advanced analysis techniques," *Engineering Structures*, vol. 69, pp. 255–270, 2014.

[318] "ASCE/SEI 41-13, Seismic evaluation and retrofit of existing buildings, Reston, Virginia, 2014."

[319] P. Fajfar, "Capacity spectrum method based on inelastic demand spectra," *Earthquake Engineering & Structural Dynamics*, vol. 28, no. 9, pp. 979–993, 1999.

[320] S. A. Freeman, "The capacity spectrum method," in *Proceedings of the 11th European conference on earthquake engineering, Paris*, 1998.

[321] G. Guerrini, F. Graziotti, A. Penna, and G. Magenes, "Improved evaluation of inelastic displacement demands for short-period masonry structures," *Earthquake Engineering & Structural Dynamics*, vol. 46, no. 9, pp. 1411–1430, 2017.

[322] S. Casolo, V. Diana, and G. Uva, "Influence of soil deformability on the seismic response of a masonry tower," *Bulletin of Earthquake Engineering*, vol. 15, no. 5, pp. 1991–2014, 2017.

[323] F. de Silva, F. Ceroni, S. Sica, and F. Silvestri, "Non-linear analysis of the Carmine bell tower under seismic actions accounting for soil–foundation–structure interaction," *Bulletin of Earthquake Engineering*, pp. 1–34, 2017.

[324] R. Van der Pluijm, A. A. Hamid, and H. G. Harris, "Shear behaviour of bed joints," in *6th North American Masonry Conference, 6-9 June 1993, Philadelphia, Pennsylvania, USA*, pp. 125–136, Technomic Publ. Co., 1993.

[325] G. Milani, M. Valente, and C. Alessandri, "The narthex of the Church of the Nativity in Bethlehem: A non-linear finite element approach to predict the structural damage," *Computers & Structures*, vol. 207, pp. 3–18, 2018.

[326] V. Turnšek and F. Čačovič, "Some experimental results on the strength of brick masonry walls," in *Proc. of the 2nd International Brick Masonry Conference*, pp. 149–156, 1971.

[327] V. Turnšek and P. Sheppard, *The shear and flexural resistance of masonry walls*. 1980.

[328] C. A. Blandon and M. Priestley, "Equivalent viscous damping equations for direct displacement based design," *Journal of earthquake Engineering*, vol. 9, no. sup2, pp. 257–278, 2005.

[329] G. Grünthal, "European macroseismic scale 1998," tech. rep., European Seismological Commission (ESC), 1998.

[330] J. B. Burland, M. Jamiolkowski, and C. Viggiani, "The stabilisation of the leaning tower of Pisa," *Soils and foundations*, vol. 43, no. 5, pp. 63–80, 2003.

[331] F. Pisanò, C. G. Di Prisco, and R. Lancellotta, "Soil-foundation modelling in laterally loaded historical towers," *Géotechnique*, vol. 64, no. 1, p. 1, 2014.

[332] M. Marchi, R. Butterfield, G. Gottardi, and R. Lancellotta, "Stability and strength analysis of leaning towers," *Géotechnique*, vol. 61, no. 12, pp. 1069–1079, 2011.

[333] J. Heyman, "Leaning towers," *Meccanica*, vol. 27, no. 3, pp. 153–159, 1992.

[334] W. Addis, *Building: 3000 years of design engineering and construction*. Phaidon London/New York, 2007.

[335] D. Abruzzese, L. Miccoli, and J. Yuan, "Mechanical behavior of leaning masonry Huzhu Pagoda," *Journal of Cultural Heritage*, vol. 10, no. 4, pp. 480–486, 2009.

[336] G. Milani, R. Shehu, and M. Valente, "Role of inclination in the seismic vulnerability of bell towers: FE models and simplified approaches," *Bulletin of Earthquake Engineering*, vol. 15, no. 4, pp. 1707–1737, 2017.

[337] K. Krabbenhoft, A. V. Lyamin, M. Hjiaj, and S. W. Sloan, "A new discontinuous upper bound limit analysis formulation," *International Journal for Numerical Methods in Engineering*, vol. 63, no. 7, pp. 1069–1088, 2005.

[338] S. Sloan and P. Kleeman, "Upper bound limit analysis using discontinuous velocity fields," *Computer methods in applied mechanics and engineering*, vol. 127, no. 1-4, pp. 293–314, 1995.

[339] "IBM ILOG CPLEX Optimizer. Available at: https://www-01.ibm.com/software/commerce/optimization/cplex-optimizer/."

[340] R. Weyler, J. Oliver, T. Sain, and J. Cante, "On the contact domain method: A comparison of penalty and lagrange multiplier implementations," *Computer Methods in Applied Mechanics and Engineering*, vol. 205, pp. 68–82, 2012.

[341] M. Godio, I. Stefanou, and K. Sab, "Effects of the dilatancy of joints and of the size of the building blocks on the mechanical behavior of masonry structures," *Meccanica*, vol. 53, no. 7, pp. 1629–1643, 2018.

[342] R. van der Pluijm, "Material properties of masonry and its components under tension and shear," in *Proceedings 6th Canadian Masonry Symposium, 15-17 June 1992, Saskatoon, Canada*, pp. 675–686, University of Saskatchewan, 1992.

[343] A. M. D'Altri, C. Carloni, S. de Miranda, and G. Castellazzi, "Numerical modeling of FRP strips bonded to a masonry substrate," *Composite Structures*, vol. 200, pp. 420–433, 2018.

[344] A. Vermeltfoort and T. Raijmakers, "Deformation controlled meso shear tests on masonry piers-Part 2. Draft report, Department of BKO, TU Eindhoven," 1993.

[345] N. G. Chee Liang, "Experimental and theoretical investigation of the behaviour of brickwork cladding panel subjected to lateral loading. Ph.D. thesis University of Edinburgh," 1996.

[346] H. B. Kaushik, D. C. Rai, and S. K. Jain, "Stress-strain characteristics of clay brick masonry under uniaxial compression," *Journal of materials in Civil Engineering*, vol. 19, no. 9, pp. 728–739, 2007.

[347] R. Esposito, K. Terwel, G. Ravenshorst, H. Schipper, F. Messali, and J. Rots, "Cyclic pushover test on an unreinforced masonry structure reseambling a typical Dutch terraced house," in *16th World Conference on Earthquake, WCEE*, pp. 9–13, 2017.

[348] F. Messali, G. Ravenshorst, R. Esposito, and J. Rots, "Large-scale testing program for the seismic characterization of Dutch masonry walls," in *Proc. 16th World Conf. EE, Santiago, Chile*, 2017.

[349] S. Casolo and G. Milani, "Simplified out-of-plane modelling of three-leaf masonry walls accounting for the material texture," *Construction and Building Materials*, vol. 40, pp. 330–351, 2013.

[350] J. Hallquist, G. Goudreau, and D. Benson, "Sliding interfaces with contact-impact in large-scale Lagrangian computations," *Computer methods in applied mechanics and engineering*, vol. 51, no. 1-3, pp. 107–137, 1985.

[351] R. Atkinson, B. Amadei, S. Saeb, and S. Sture, "Response of masonry bed joints in direct shear," *Journal of Structural Engineering*, vol. 115, no. 9, pp. 2276–2296, 1989.

[352] A. Formisano and A. Marzo, "Simplified and refined methods for seismic vulnerability assessment and retrofitting of an italian cultural heritage masonry building," *Computers & Structures*, vol. 180, pp. 13–26, 2017.

[353] S. Jafari, J. G. Rots, R. Esposito, and F. Messali, "Characterizing the material properties of Dutch unreinforced masonry," *Procedia engineering*, vol. 193, pp. 250–257, 2017.

[354] S. Jafari and R. Esposito, "Material tests for the characterisation of replicated calcium silicate brick masonry. Delft University of Technology. Report number C31B67WP1-9, version 01, 14 November 2016.."

[355] A. Romano and J. A. Ochsendorf, "The mechanics of Gothic masonry arches," *International Journal of Architectural Heritage*, vol. 4, no. 1, pp. 59–82, 2010.

[356] G. Ramaglia, G. Lignola, and A. Prota, "Collapse analysis of slender masonry barrel vaults," *Engineering Structures*, vol. 117, pp. 86–100, 2016.

[357] E. Milani, G. Milani, and A. Tralli, "Limit analysis of masonry vaults by means of curved shell finite elements and homogenization," *International Journal of Solids and Structures*, vol. 45, no. 20, pp. 5258–5288, 2008.

[358] G. Creazza, R. Matteazzi, A. Saetta, and R. Vitaliani, "Analyses of masonry vaults: A macro approach based on three-dimensional damage model," *Journal of Structural Engineering*, vol. 128, no. 5, pp. 646–654, 2002.

[359] G. Milani, M. Rossi, C. Calderini, and S. Lagomarsino, "Tilting plane tests on a small-scale masonry cross vault: Experimental results and numerical simulations through a heterogeneous approach," *Engineering Structures*, vol. 123, pp. 300–312, 2016.

[360] I. Caliò, F. Cannizzaro, and M. Marletta, "A discrete element for modeling masonry vaults," vol. 133, pp. 447–452, 2010.

[361] A. M. D'Altri, S. de Miranda, G. Castellazzi, V. Sarhosis, J. Hudson, and D. Theodossopoulos, "Historic barrel vaults undergoing differential settlements," *Submitted for publication*, 2019.

[362] C. Carfagnini, S. Baraccani, S. Silvestri, and D. Theodossopoulos, "The effects of in-plane shear displacements at the springings of gothic cross vaults," *Construction and Building Materials*, vol. 186, pp. 219–232, 2018.

[363] R. Fawcett, "Barrel-vaulted churches in late medieval Scotland," *Architecture and Interpretation. Essays for Eric Fernie, Boydell & Brewer: Martlesham*, 2012.

[364] D. Theodossopoulos, "Stone barrel vaulting in late medieval churches in Scotland," in *Proceedings of the First Conference of the Construction History Society*, p. 403, 2015.

[365] D. Theodossopoulos, N. Makoond, and A. Lily, "The effect of boundary conditions on the behaviour of pointed masonry barrel vaults: Late gothic cases in Scotland," *The Open Construction and Building Technology Journal*, vol. 10, no. Suppl 2: M8, pp. 274–292, 2016.

[366] J. Hudson and D. Theodossopoulos, "Gothic barrel vaults under differential settlement: The effects of boundary conditions and FRP on structural behaviour," vol. 747, pp. 496–503, 2017.